Fabrication and Properties of IR Transparent Ceramic Materials Using Sol-Gel Derived Powders

Thesis

Submitted in Partial Fulfillment of the Requirements

for the Award of the Degree of

DOCTOR OF PHILOSOPHY

in

METALLURGICAL AND MATERIALS ENGINEERING

by

RAJENDRAN SENTHIL KUMAR

(Roll No. 717138)

Under the supervision of

Dr. Asit Kumar Khanra

Associate Professor

National Institute of Technology Warangal,
Warangal, Telangana State, India

Dr. Roy Johnson

Scientist – G & Associate Director

International Advanced Research Centre for
Powder Metallurgy and New Materials (ARCI)
Hyderabad, Telangana State, India

DEPARTMENT OF METALLURGICAL AND MATERIALS ENGINEERING

NATIONAL INSTITUTE OF TECHNOLOGY WARANGAL,

WARANGAL – 506 004, TELANGANA STATE, INDIA

April - 2021

DEPARTMENT OF METALLURGICAL AND MATERIALS ENGINEERING

NATIONAL INSTITUTE OF TECHNOLOGY

WARANGAL – 506 004 (T.S.) INDIA

CERTIFICATE

This is to certify that the work presented in the thesis entitled **"Fabrication and Properties of IR Transparent Ceramic Materials Using Sol-Gel Derived Powders"** which is being submitted by **Mr. R. Senthil Kumar (Roll No: 717138),** is a bonafide work submitted to National Institute of Technology, Warangal in partial fulfillment of the requirements for the award of the degree of **Doctor of Philosophy** in **Metallurgical and Materials Engineering Department.**

To the best of my knowledge, the work incorporated in the thesis has not been submitted to any other university or institute for the award of any other degree or diploma.

Dr. Asit Kumar Khanra	**Dr. Roy Johnson**	**Dr. Asit Kumar Khanra**
Thesis Internal Supervisor	Thesis External Supervisor Scientist – G & Associate Director	Head of the Department

Thesis Approval for Ph.D.

The Thesis entitled **"Fabrication and Properties of IR Transparent Ceramic Materials Using Sol-Gel Derived Powders"** by **Mr. R. Senthil Kumar (Roll No: 717138),** is approved for the degree of Doctor of Philosophy.

Examiners

_____

_____

_____

Supervisor

_____

_____

_____

Chairman

_____

Declaration

This is to certify that the research work presented in the thesis entitled **"Fabrication and Properties of IR Transparent Ceramic Materials Using Sol-Gel Derived Powders"** is a bonafide work done by me under the supervision of **Dr. Asit Kumar Khanra,** NITW and **Dr. Roy Johnson,** ARCI and was not submitted elsewhere for the award of any degree. I declare that this written submission represents my ideas in my own words and where others' ideas or words have not been included, I have adequately cited and referenced the original sources. I also declare that I have adhered to all principles of academic honesty and integrity and have not misrepresented or fabricated or falsified any idea/ data/ fact/ source in my submission. I understand that any violation of the above will be a cause for disciplinary action by the Institute and can evoke penal action from the sources which have thus not been properly cited or from whom proper permission has not been taken when needed.

(Signature)

R. Senthil Kumar

Roll No. 717138

Date: 30/April/2021

Acknowledgements

First, I praise my Father, the almighty God who hold my hands constantly and provide everything that I have in this life. Likewise, I thank the servant of God who had strengthened and guided me in the will of God. Secondly, I would like to express my sincere thanks my parents N. Rajendran and R. Sulochana who have sacrificed their life and brought me to the stages of pursuing this doctoral course. Similarly, I convey my heartfelt gratitude to my brothers R. Saravanan and R. Vengadeson who have shared the family burdens and helped me building my carrier. Further, I would like to share my thankfulness to my wife, Dr. I. Sophia Rani who stood beside, moved me in every difficult stages, and travelled along with me throughout this research journey. In addition, I express my thanks for my daughters, Ms. Sharon and Ms. Shalom, my stress busters and energy boosters who have helped me to stand firm during my hardships in this journey.

On the other hand, concerning the professional component, I would like to express my sincere gratitude to my guide, Dr. Roy Johnson, Associate Director, ARCI, Hyderabad, for his proficient support and advices in my research carrier. His insightful knowledge and suggestions in the field of transparent ceramics helped me a lot to accomplish the objectives targeted in this thesis. Similarly, I would like to express my gratefulness to my internal guide, Dr. Asit Kumar Khanra, Associate Professor, NIT Warangal for his constant support right from the beginning of this course registration. He is one among the best guide at NIT Warangal who had given me complete freedom to carry out the research activities. In addition, his vast professional experience guided me to achieve every milestones in this research journey. I also wish to express my heartfelt thanks to Dr. G. Padmanabham, Director, ARCI, Hyderabad, for the grant of opportunity to register this course and provided all the facilities to carry out the research and

development activities. Further, I would like to acknowledge the technical supports extended by Dr. Y. Srinivasa Rao, Scientist F, Team Leader, Centre for Ceramic Processing, ARCI.

Further, I extend my gratitude to all my DSC members Dr. G.V.S. Nageswara Rao, Dr. R. Arockia Kumar, Dr. V. Sreedevi and Dr. Abdul Azeem for their continuous support. In addition, I wish to express my thanks to all the fellow research scholars at NITW who have helped me at various stages in this research tenure. Likewise, I would like to express my thankful heart to Dr. V. Ganapathy, Research Scientist, ARCI, for expending his precious time for me to carry out all the micrographic analyses. In addition, I wish to acknowledge my fellow scientist Dr. Srinivasan Anandan, Dr. S. Kumar, Dr. S. Chandra Shekar and Dr. K. Murugan for their constant technical inputs and supports in writing my research articles and this thesis.

Finally, I would like to express my thankfulness to Mr. A. Satya Narayana, Technician D and the research scholars and trainees who have worked in the Centre for ceramic processing for their constant technical assistance throughout this research journey.

R. Senthil Kumar

Abstract

Transparent ceramic materials are new class of advanced materials exhibiting excellent optical and mechanical characteristics attracting attention in substantial field of applications including high-pressure lamp envelops, host for lasers, peep windows for spaceships, ballistic armors, supersonic missile domes etc. Various single crystal materials such as sapphire and poly crystalline materials such as ZnS, ZnSe, sub-micron Al_2O_3, $MgAl_2O_4$ Spinel, Y_2O_3, Aluminum oxynitride (AlON) etc. have been developed to meet the demands in such applications. In spite of exhibiting excellent optical and mechanical properties, single crystal materials are still less preferred than the polycrystalline transparent ceramic materials owing to various practical inconveniences involved in fabrication such as sluggish growth rate, high temperature requirements and extreme production costs. On the other hand, the need is exponentially increasing for the polycrystalline transparent materials specifically the sub-micron Al_2O_3, AlON, Spinel and Y_2O_3 due to their versatility in fabrication, less processing temperatures and low production costs in addition to their benefits of exhibiting equivalent physical, mechanical and optical properties similar to single crystals. However, all these specified materials are still under current research to explore their scientific significance, improve their excellence, and enhance their potential properties to encounter futuristic requirements.

In view of these aspects, the present research work selected four transparent materials such as sub-micron Al_2O_3, Spinel, Y_2O_3 and Aluminum oxynitride (AlON) for the study. Currently, most of the research and development as well as the production of these materials utilize optical grade commercial starting powders due to their stringent specifications such as ultra – high purity and appropriate particle size and size distribution. The powders with these rigid qualities are extremely expensive that escalate the costs of the eventual products. Therefore, the present investigation attempts to synthesize the requisite starting powders for all the selected materials

through a facile sol – gel technique. Further, the study continued to evaluate the suitability of the synthesized powders for the fabrication of transparent Al_2O_3, Spinel, Y_2O_3 and Aluminum oxynitride (AlON) materials. Extensive investigations were carried out during and after the synthesis of the optical grade starting powders in terms of their phase, particle size, purity, morphology etc. Similarly, numerous studies were carried out to optimize the fabrication process of producing sintered transparent materials followed by the characterization at various stages of fabrication. Finally, the transparent ceramic materials such as Al_2O_3, Spinel, Y_2O_3 and AlON fabricated in this study were compared with the existing and best – reported materials in terms of their physical, chemical, mechanical and optical properties.

Interestingly, remarkable milestones have been achieved in all the selected materials. For instance, ultra-fine α- Al_2O_3 powder having particle size in the range between 20 and 40 nm was synthesized in the present study, which was successfully used for producing transparent sub-micron Al_2O_3. The transparent Al_2O_3 produced in the current study exhibited real inline transparency up to 87% in the mid-wave infrared region (3 – 5 µm), which is at par with the transparency of single crystal sapphire in those regions. The average sintered grain size was about 800 nm and the Vickers hardness reached up to 20.5 GPa which is even superior than the hardness of sapphire whose values are in the order of 18.5 GPa.

Outstanding results were obtained in the case of spinel ceramics. A novel sol-gel approach was followed for the synthesis of highly reactive, ultra-fine and ultra-pure spinel powders. The particle size of the powder synthesized in the present study was in the order of 18 to 20 nm. The sintered articles produced using this powder exhibited 100% theoretical density at temperatures as low as 1400°C. These results are extremely exceptional compared with the outcomes reported in most of the existing spinel fabrication processes where those approaches reached temperatures up to 1800°C for achieving similar densification. Due to the superior sinterability of spinel fabricated in the current study, the average sintered grain size retained in

the range of 500 nm. On the other hand, most of the currently existing conventional transparent spinel have grain sizes in the order of 200 µm. The Vickers hardness of the spinel produced in this study escalated up to 16.2 GPa which is 40% superior to the values achieved for the conventional transparent spinel. The IR transparency in the region between 3 and 5 µm was about 86% which are at par with the theoretical transmissions.

In case of transparent Y_2O_3, a facile methodology of synthesizing highly reactive, round-edged, Sulphur–free nano Y_2O_3 powders to fabricate submicron IR transparent yttria ceramics having a unique combination of superior optical and mechanical properties are reported for the first time. Homogenous nucleation and controlled growth enabled the development of non – aggregated particles with narrow size distribution. The powder exhibited excellent sinterability reaching near-theoretical density at temperatures around 1400°C in air. Sintered specimens showed average grain sizes closer to 700 nm. Post-sinter hot isostatic pressing eliminated the residual porosity from the sintered samples leading to exhibit IR transmissions up to 84% in the 2.0 – 9.0 µm regions, equivalent to single crystal Y_2O_3. Improved transparency and mechanical properties are attributed to the absence of secondary phases resulting from Sulphur additives employed in the hitherto reported processes. Transparent Y_2O_3 ceramic developed in this study is a promising candidate for solid-laser hosts, IR transparent domes, and uncooled – thermal – window applications by its superior optical and mechanical properties.

In addition to the above, investigations were carried out to synthesize nano AlON powder through aqueous sol-gel processing. Appropriate quantities of Aluminum Nitride (AlN) powder and aqueous boehmite sol were mixed to obtain molecular stoichiometry of AlON. In this process, the AlN deteriorated into its hydrated compounds in the aqueous sol due to its intrinsic hydrolysis tendency and hindered AlON formation. Extensive investigations were carried out to analyze the behaviour of AlN during the processing of sol-gel AlON. Hydrolysis of AlN in the aqueous sol-gel medium was circumvented by subjecting AlN to a surface modification

process. The homogeneously dispersed Al_2O_3 sol and AlN mixture was further gelled, dried, and heat treated at temperatures between 1600°C and 1850°C for the formation of AlON powder. AlON phase formation was confirmed through XRD investigations, and its physical and microstructural properties were also evaluated through FESEM and TEM analyses. Through this process, AlON powder with an average particle size of 490nm was successfully synthesized during the study. This process is suitable for producing AlON powder in bulk quantities. The powders were further shaped and sintered at 1950°C in a flowing argon atmosphere to produce transparent AlON specimens. The optically polished AlON specimens exhibited transmissions up to 84% in 3 – 5 µm wavelength regions and their mechanical properties were at par with the best – published data.

CONTENTS

List of Figures

List of Tables

CHAPTER - I

Introduction

1.1 Introduction to transparent ceramics

Polycrystalline ceramic materials are solid, inorganic, non-metallic materials that are usually shaped from their powders followed by sintering for densification. The commonly seen ceramic products such as floor tiles, sanitary wares and electrical insulators are optically opaque in nature, which means that they do not allow the light to pass through their bodies. In terms of light transmitting characteristics, ceramic materials are classified into three categories namely opaque, translucent and transparent ceramics. As mentioned above, the materials such as sanitary wares are classified under opaque ceramics as they forbid transmissions of light waves through them. On the other hand, certain products like the high-pressure lamp envelop, the incident light pass through partially through its body and therefore categorized as translucent ceramics. The third category is the transparent ceramics, which are relatively a new category of advanced materials that allows the maximum passage of electromagnetic radiations (EMR) through their bodies. Ceramic materials exhibiting high inline optical transparency to the wavelengths specifically in the visible to IR regions finds wide range of applications such as host for laser windows, super market scanners, high – temperature furnace pyrometer windows, orthodontic parts, artificial gems, bullet – proof armors, radomes and domes for high speed supersonic and hypersonic missiles [1 – 11].

Incident of electromagnetic radiations (EMR) on materials causes photon interactions followed by transition of electrons between valance and conduction bands. Materials with band gap lower than 1.8 eV exhibit high electron excitation for the incident energy of photons ($E = h\nu$) causing optical absorption and makes a material opaque to EMR waves.

Energy of the photon = $h\nu = hc/\lambda$---------- (1)

h = Planck's Constant = 6.626×10^{-34} Js. = 4.13×10^{-15} eV.

ν = frequency of incident light

c = speed of the light

λ = wavelength of the incident beam

The materials with no transition of valence electrons in to the orbitals exhibit no absorption of incident radiations and allow the light to pass through its body. In this context, materials with band gap above 3.1 eV are transparent to electromagnetic waves. Materials with band gap between 1.8 eV and 3.1 eV exhibit partial light transmissions and considered as translucent bodies. Therefore, materials with bandgap larger than 3.1 eV are ideal candidate for the optical transmission applications [12]. Figure 1.1 schematically shows the classification of ceramic materials based on their response to optical interactions.

1.2 Importance of polycrystalline transparent ceramics

On one hand, single crystal ceramic materials are the best class of transparent materials in terms of their optical characteristics as they do not contain any internal obstacles for the transmission of light. Various materials such as sapphire (Al_2O_3), yttrium aluminum garnet (YAG), Y_2O_3 etc. show superior inline transmissions in the entire UV to IR region (~200 nm to ~9.0 µm) compared to the polycrystalline transparent materials. However, the fabrication of single crystals requires very high temperatures, sophisticated facilities and consume large amount of time for their growths.

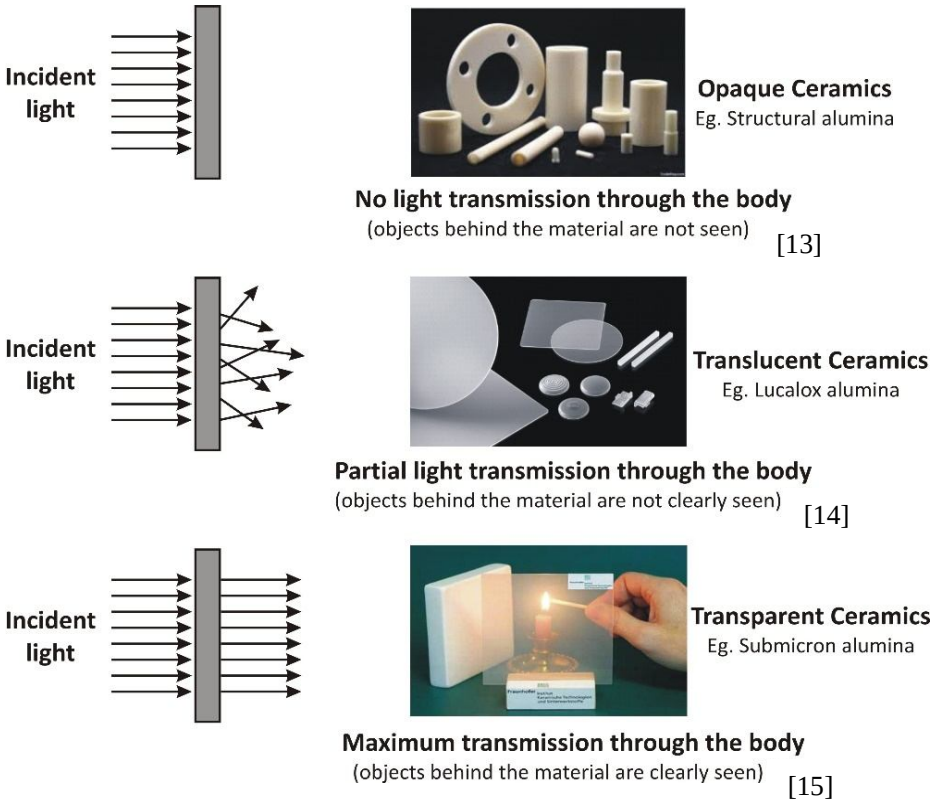

Fig. 1.1 Classification of ceramics based on optical interactions

These extreme processing conditions are leading to exorbitant fabrication costs. Moreover, the size of the single crystals is determined by their lattice structures and therefore ineffective to produce near – net and complex shaped articles such as domes. In such cases, dome shaped articles are scooped out of large sizes crystals through diamond grinding. These additional machining requirements further increase the cost of the single crystal products [16]. Other problems of single crystals include difficulties of producing in large scales and mechanical brittleness.

Therefore, polycrystalline transparent materials receives huge attraction as an alternate for the single crystal materials due to various advantages such as near – net shaping capabilities, ability to produce simple and complex shaped products, low temperature processing, large – scale production facilities and minimal necessity for grinding and polishing. These versatile advantages make the polycrystalline transparent ceramic materials highly economical

compared to the single crystal materials. Moreover, in the present days, with very careful and controlled fabrication techniques, the polycrystalline materials are produced with optical transmissions equivalent to single crystals. Therefore, polycrystalline transparent ceramic materials are likely preferred compared to single crystal ceramics. However, the knowledge on the phenomenon of the light transmission physics through the ceramic body is very much required for the successful fabrication of polycrystalline transparent ceramic materials. The following sections provide the gist of mechanisms on the interactions of light with the ceramic materials so that one can have the required precautions while fabricating the transparent ceramic materials.

1.3 The physics of light transmission in polycrystalline ceramics

Incident EMR on polycrystalline materials undergo various optical corollaries such as reflection, refraction, scattering, absorption and transmission based on the surface and the microstructural characteristics of the material. Fig. 1.2 shows various optical events occurring during the light transmission through a polycrystalline material.

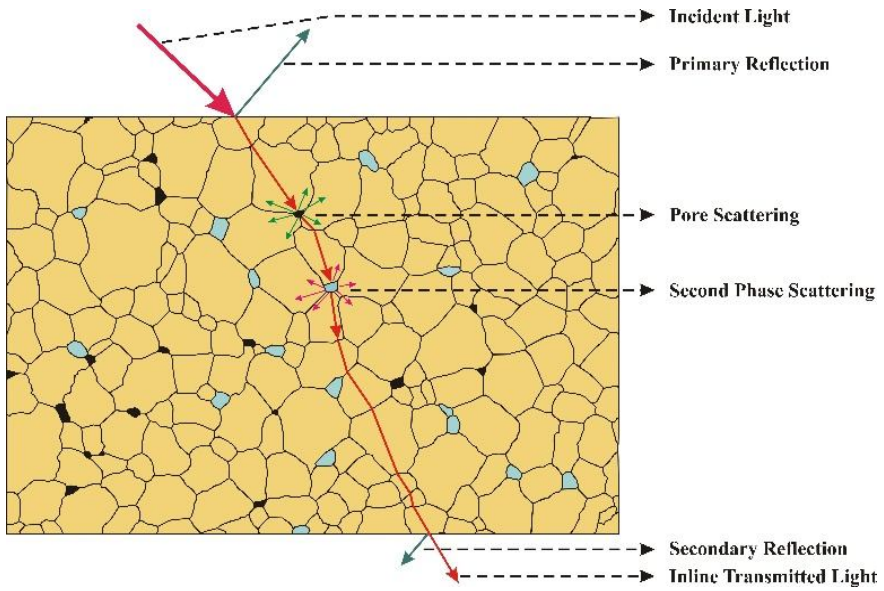

Fig. 1.2 Light Transmission phenomenon through polycrystalline ceramics.

The relation between transmissivity and other optical parameters as per the following Lambert – Beer equation is

$T = I/I_0 = (1 - R_s^2) \exp(-C_{sca}\, t)$ ---------- (2)

Where,

T is the total transmission

I is the intensity of the transmitted light

I_0 is the intensity of the incident light

R_s is the total surface reflection

C_{sca} is the effective scattering coefficient

t is the sample thickness

1.3.1 Loss of reflection

R_s describes the reflection losses at both the sides of the material which is expressed as

$$R_s = \frac{2R'}{1 + R'} \qquad R' = \left(\frac{n-1}{n+1}\right)^2 \quad \text{---------- (3)}$$

Where n is the refractive index of the sample

Therefore the inherent theoretical limit for the transmission of any material is

$$T_{th} = (1 - R') = \frac{2n}{n^2+1} \quad \text{---------- (4)}$$

From the equation (4), it is evident that the material having high refractive index exhibit less theoretical transmissions. Moreover, this equation is valid only for the materials having extreme physical and chemical homogeneity.

1.3.2 Absorption coefficient

For the heterogeneous materials, the parameter called absorption or the scattering coefficient (C_{sca}) additionally influence the transmissions as per the following equation.

$C_{sca} = \alpha + S_{im} + S_{op}$ ---------- (5)

Where

α is the absorption term due to transition of electrons. This term has minimum effect for the large band gap materials (band gap > 3.1 eV)

S_{im} is scattering term due to structural inhomogeneity such as pores, grain boundaries and second phases

S_{op} is another scattering component evolve due to crystallographic anisotropy. This term is invalid for the optically isotropic cubic crystalline materials such as spinel, Y_2O_3 and AlON. However, this term is important for the anisotropic polycrystalline materials such as Al_2O_3. α – Al_2O_3 exhibit hexagonal crystal structure with lattice parameters at a = 4.754 Å and c = 12.99 Å and at a wavelength of 600 nm, its refractive index for the ordinary ray is 1.768 (polarisation perpendicular to the c – axis) and for the extraordinary ray is 1.760 (polarisation parallel to the c – axis) [17]. The refractive index difference of 0.008 induce birefringence for the incident light at every grain boundaries and diminish the quantum of in-line transmission. Therefore, to circumvent the birefringence effect and gain the transparency, the sintered grains of alumina is restricted to the sizes lesser than the wavelength of the incident light.

1.3.3 Scattering Loss

Transmission losses due to scattering (S_{im}) for a material occur from both external rough surfaces and internal structural infirmities. Surface grinding and optical grade polishing eliminates the scattering losses from uneven surfaces. However, combating scattering from the

internal sections require cautious manufacturing skills to develop engineered microstructures free from elements such as porosity, second phases and impurities, non-stoichiometric regions having different refractive index [18 – 19]. Peelan *et al.* suggested the following expression on scattering coefficient ϒ for pore scattering in terms of the total porosity [20].

$$\Upsilon_{pore} = \frac{p}{\frac{4}{3}\pi r_{pore}^{3}} C_{sca.pore} \qquad \text{---------- (6)}$$

Where,

C_{sca} is the scattering cross section of one spherical pore

p is the total porosity

r is the radius of the pore

Apetz *et al.* used the above expression and calculated the effect of the porosity content in terms of the optical transmission and reported that even the porosity of only 0.1% reduce the inline transmissions from 86% to 1% and the content of 0.01% porosity diminish the transmissions to 35% [14]. Yamashita *et al.* studied the effect of pore size on the percentage of in-line transmission and reported that 1000 ppm of pores having the size of 0.1 µm completely collapse the degree of transparency [21]. In the case of imaging applications using longer wavelengths, only thin widows tolerate pore sizes smaller than 100nm [22]. Reducing pore size by half bring down the Rayleigh scatter by one order of magnitude [23]. Therefore, pore concentrations and their size reductions become a major goal for a successful fabrication of transparent materials.

Scattering due to second phases and impurities are controlled by selecting ultra-high pure raw materials having purity above 99.99% and avoiding inclusions of contaminations at various levels of processing such as milling, drying, sintering and post sintering etc. Densification is encouraged without any assistance of sintering aids or otherwise in the ppm levels to avoid any

grain boundary segregations. Transparent ceramics are indeed expensive compared to other ceramics materials due to these boundaries of using extremely high-pure raw materials and stringent processing conditions.

1.3.4 Absorption edges

Apart from the bandwidth selection, materials exhibit transmissions to EMR at a specific range of wavelengths. For e.g. having the bandwidth of 8.8 eV, single crystal sapphire exhibit transmissions for the entire wavelength region from 140 nm to about 7.0 µm as shown in fig. 1.3. Beyond these boundaries, the sapphire shows absorption of light. At the UV end, the absorption is due to the excitation of valence electrons into orbitals for the wavelengths <140nm. On the IR region of the spectrum, the absorption is not due to excitation of electrons but is associated with the small energy differences in the vibrational and rotational states of molecules, amorphous networks or lattices [8]. $MgAl_2O_4$ spinel exhibit absorption edges at~ 190 nm and the UV end and closer to 6 µm at the IR wavelengths [17].

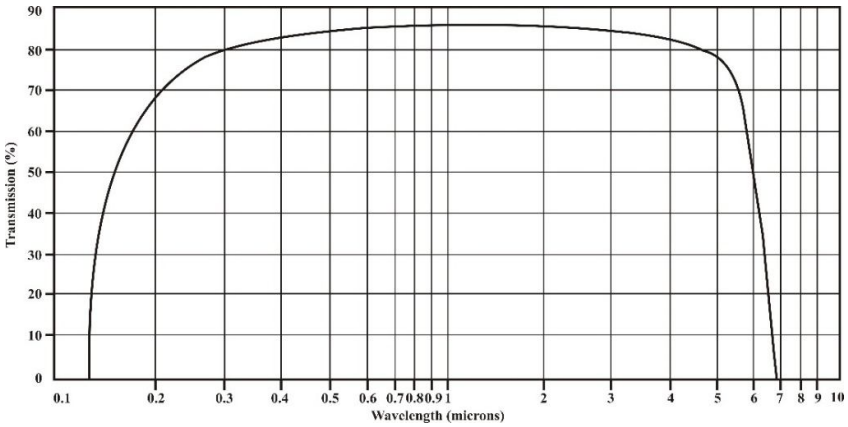

Fig. 1.3 Transmission spectrum of single crystal sapphire [24]

1.4 High performance transparent ceramic materials

In the current scenario, transparent ceramic materials such as sapphire, submicron – Al_2O_3, $MgAl_2O_4$ spinel, Y_2O_3, aluminum oxynitride (AlON), ZnS and ZnSe are majorly used for

various visible and IR transparent applications. Among these, ZnS and ZnSe are less preferred for the applications with extreme service environments such as high-speed missile domes and bulletproof armor materials due to their inherent poor mechanical properties. Therefore, the rest of the candidates are considered as high performance materials because of their combination of superior optical and mechanical properties. Still, sapphire is preferred in limited quantities do to their extreme costs and slow production rate. Therefore, the materials such as submicron – Al_2O_3, $MgAl_2O_4$ spinel, Y_2O_3 and aluminum oxynitride (AlON) takes a long leap and considered as ideal candidates for most of the presently required high performance applications. Table 1.1 compares the physical, chemical, mechanical and optical properties of various transparent ceramic materials [12].

Properties	**ZnSe**	**ZnS**	**Sapphire**	**Sub - µm Al_2O_3**	**$MgAl_2O_4$ Spinel**	**AlON**	**Y_2O_3**
Crystal Structure	Cubic	Cubic	Hexagonal	Hexagonal	Cubic	Cubic	Cubic
Density (g/cc)	5.27	4.08	3.986	3.986	3.58	3.69	5.031
Flexural Strength (MPa)	55	103	350	480	250	240	160
Hardness (Hv) (Kg/mm^2)	100 - 115	200 - 220	1600 - 1800	2000-2300	1300-1400	1350-1380	630-650
K_{IC} ($MPa.m^{1/2}$)	0.5	0.8 – 0.9	2.6	3.5	1.9	2.0	0.7
Range of Transmission	0.6 – 18	0.4 – 12	0.2 – 5.5	0.2 – 5.5	0.2 – 6.0	0.2 – 5.5	0.25-9.0
% of RIT (3 – 6 µm)	65 – 66	70 – 71	84 – 86	84 – 86	84 – 87	85 – 86	82 – 84
Process Methodology	CVD	CVD	Crystal Growth	Powder Metallurgy	Powder Metallurgy	Powder Metallurgy	Powder Metallurgy

Table 1.1 Typical characteristics of various transparent ceramic materials

As shown in the table 1.1, the materials other than ZnS and ZnSe exhibit superior IR transmissions ranging closer to 85% that are ideal for obtaining IR images with improved

resolution. Figure 1.4 compares various transparent ceramic materials with respect to their IR transmission characteristics [25]. It may be noted that the transmission characteristics of various polycrystalline materials are highly competing with that of the single crystal sapphire materials.

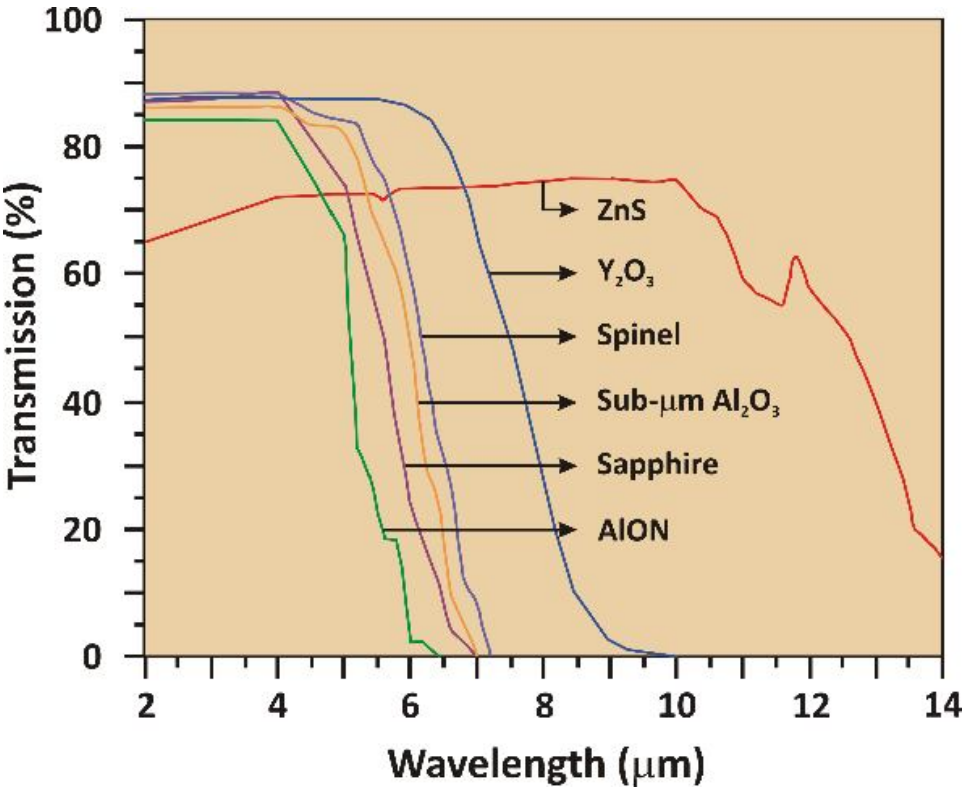

Fig. 1.4 IR Transmission spectrum of various ceramic materials

1.5 Challenges of manufacturing transparent ceramics

Unlike the fabrication of traditional ceramic materials, manufacturing transparent ceramics follow stringent processing conditions starting from the selection of raw materials until to the final stages of grinding and polishing. The following prerequisites require constant attention at every levels for the efficacious manufacturing of these transparent materials.

1.5.1 Selection of raw materials

Selecting the appropriate starting powders is the fundamental key for fabricating transparent ceramics with superior optical and mechanical properties. Therefore, most of the investigators employed standard commercial powders having purity of at least 99.99% for their processes [3, 7 – 8, 15]. However, due to extreme costs and restricted supplies of these commercial powders, researchers explored in finding the other suitable techniques for synthesizing these starting powders for their fabrication of transparent ceramics. In this context, various powder processing techniques such as chemical precipitation, combustion synthesis, sol-gel method, co-precipitation, flame spray pyrolysis, Pechini precipitation, freeze-drying, hydrolysis assisted synthesis, acid dissolution and precipitation etc. [26 – 49] have been investigated.

However, transparent ceramics derived through commercial powders exhibited relatively superior physical, chemical, mechanical and optical properties. For example, transparent submicron Al_2O_3 having IR transparency equivalent to single crystal sapphire is developed using commercial Al_2O_3 powders [50]. Similarly, excellent results on transparent spinel were mostly obtained with commercial spinel powders [51 – 54]. This is probably due to their coherent combinations of physical and chemical characteristics such phase purity, ultra – fine sizes (100 – 200 nm), narrow size particle distribution, round edged morphology, high reactivity, outstanding particle homogeneity and excellent inter – particle coordination.

Therefore, the exploration is still under progress for producing starting powders having properties equivalent or better than the commercially available optical grade powders. Moreover, there is a real need for finding the ideal synthesis technique that can produce optical grade powders in large scales. However, synthesizing such optical grade powders having consistent and coherent physical and chemical properties is still a challenging task.

1.5.2 Flawless green processing and controlled densification

Apart from the usage of suitable starting powders, adapting the appropriate fabrication technique is equally important for the successful fabrication of transparent ceramic materials. For instance, fabricating materials such as submicron – Al_2O_3, $MgAl_2O_4$ spinel, Y_2O_3 and aluminum oxynitride (AlON) require strict processing parameters to gain the maximum inline transparency. Manufacturing green bodies with high degree of homogeneities is necessary for avoiding development of structural defects such as micro cracks and laminations. Similarly, extreme control on densification is also required to obtain flawless sintered microstructures. According to the source and characteristics of the starting powders, researchers employed various green fabrication techniques such as compaction, cold isostatic pressing, slip casting, gel casting, hydrolysis assisted casting, pressure/ vacuum casting. Similarly, several sintering techniques such as conventional air sintering, vacuum sintering, hydrogen sintering, pressure assisted sintering, hot forging, spark plasma sintering, flash sintering, hot pressing and hot isostatic pressing were followed for densification. Eventually, the sintered materials were carefully ground and polished at the external surfaces to eliminate surface scattering and gaining the maximum optical transparency.

Therefore, apart the challenges involved with synthesis of powders, stringent challenges persist in converting the powders in to real optical components having properties equivalent to the theoretical standards and at par with the best values reported in the literatures.

1.6 Scope for the present study

The era of research and development in the field of transparent ceramic materials started just in the years of 1960s and their exploration gained momentum in the recent decades [55]. Therefore, immense potential areas still exist in this emerging domain for developing novel methodologies of synthesizing optical grade ceramic powders and further fabricating

transparent ceramic materials therefrom. For example, there is a necessity for a process of synthesizing ultra – high pure and ultra – fine Al_2O_3 powders suitable for producing transparent submicron Al_2O_3 products. Similarly, investigations report that the existing commercial spinel powders and Y_2O_3 powders suffer with inherent Sulphur contaminations [17, 42 – 43] due to the limitations in the existing synthesis procedures. These contaminations inhibit spinel and Y_2O_3 from exhibiting their intrinsic optical transmissions. Therefore, there is a definite necessity for the improved methodology for producing optical grade spinel and Y_2O_3 powders free from Sulphur contaminations. Moreover, the existing literatures fabricating submicron transparent spinel materials undisclosed the procedures followed for the spinel powders due to technical and commercial reasons. Therefore, the present study explored the possibilities of synthesising optical grade spinel powders suitable for producing submicron grained transparent spinel. Likewise, in the area of AlON materials, the starting AlON powders are mostly synthesized using non-aqueous processing techniques due to the inherent hydrolysis tendency of AlON precursors in the water medium. Additionally, non-aqueous synthesis processing is highly expensive and hazardous to the environments. Therefore, there is an obvious need for the development of novel aqueous processing methods for synthesizing AlON powders, which would be economical and friendly to the environments.

Apart from the development of novel methodologies of synthesizing optical grade ceramic powders, optimization of a suitable fabrication technique is also required for the transformation of these powders into transparent articles.

1.7 Objectives of the present investigation

- The prime objective of the present investigation is to develop a facile processing methodologies using sol – gel techniques to produce a series of optical grade powders such as Al_2O_3, $MgAl_2O_4$ spinel, Y_2O_3 and aluminum oxynitride.

- Another objective of the investigation is to synthesize powders with at least 99.99% of phase purity.
- Another objective of the investigation is to synthesize powders with particle size ≤ 100 nm
- Another objective of the investigation is to develop the synthesis technique that are scalable for bulk productions
- Another objective of the investigation is to synthesize highly reactive powders that are mostly sinterable at temperatures around 1400°C
- Another objective of the study is to shape the articles through compaction routes
- Another objective of the study is to obtain the sintered grain sizes in the submicron regions
- Another objective of the study is to sinter the components using minimum or without any inclusions of sintering additives
- Another objective of the study is to produce a series of transparent ceramic articles such as Al_2O_3, $MgAl_2O_4$ spinel, Y_2O_3
- Another objective of the study is to synthesize AlON powders aqueous sol – gel methods followed by fabrication of transparent AlON ceramics
- Another objective of the present study is to systematically characterize the synthesized powders and transparent articles and compare them with the present global standards

1.8 Outline of the thesis

This thesis consists of eight chapters. First chapter provides a brief introduction on transparent ceramics, classification of ceramics based on optical interference, the physics behind the transmission of light in polycrystalline ceramics, introduction on currently pursued transparent ceramic materials. Further, it discuss the major challenges involved in fabricating transparent

ceramic materials and provides the gist of methodologies that are explored hitherto for their fabrication. Also the chapter details the scope for the further research and development and lists various objectives of the present study to develop various transparent ceramic materials such as Al_2O_3, $MgAl_2O_4$ spinel, Y_2O_3 and AlON.

The second chapter details the intense literature survey conducted to cover various approaches and methodologies adapted to date for fabricating transparent ceramic materials such as transparent alumina, spinel, yttria and AlON. The details include the history and evolution of these ceramic materials, various techniques followed for synthesizing starting powders, methods of forming green shapes and procedures followed for their densification. In addition, the chapter covers various properties achieved for these materials in terms of their physical, chemical, optical and mechanical properties.

The third chapter includes the fundamentals and advantages of sol – gel techniques chosen for synthesizing optical grade Al_2O_3, $MgAl_2O_4$ spinel, Y_2O_3 and AlON powders. Additionally, the chapter explains the fabrication instruments used for manufacturing transparent articles and the characterization tools employed for analyzing the synthesized powders and sintered transparent ceramic materials. Besides, the chapter also outlines the fundamentals of the characterization techniques use for the present invesigations.

Fourth to seventh chapters explain the actual works carried out for synthesizing various optical grade powders and fabricating those to transparent ceramic materials. Accordingly, the fourth chapter details on synthesizing optical grade Al_2O_3 powders through sol – gel techniques. Further, it describes the methodologies adapted for shaping the powders and transforming the green components into dense IR transparent articles. Moreover, the chapter covers all the systematic characterization techniques used for confirming the achieved properties and discusses their standards with respect to the reported values.

The fifth chapter reveals the procedures employed for synthesizing optical grade, nano – spinel powders through sol – gel techniques followed by their systematic characterization at every stages of processing. Further, the chapter explains the methodologies adapted for fabricating transparent spinel materials from the synthesized spinel powders. In addition, the shaped and sintered materials followed detailed characterizations in order to confine the fabrication techniques to obtain transparent spinel materials.

Chapter 6 explains the novel formulations involved in synthesizing phase pure, nano – Y_2O_3 powders using sol – gel methodology. The chapter details the systematic characterization techniques utilized for the analysis of synthesized powders and covers the entire procedures followed for their fabrication into transparent yttria. The chapter also compares the standards of presently produced transparent yttria with the existing transparent yttria materials.

Chapter 7 reports the novel aqueous sol – gel methodologies adapted for synthesizing submicron AlON powders. The chapter details the various challenges encountered in synthesizing AlON powders in water medium. Further, the chapter details the methodologies carried out to counter attack the challenges and explain the appropriate procedures to produce AlON powders through environmental friendly aqueous processing. In addition, the chapter details the fabrication of transparent AlON materials and compare their properties with the best – published AlON materials.

Chapter 8 summarize the entire thesis providing the overall gist of the characteristics of synthesized powders and the sintered components. In addition, it also provides the scope for further investigations that can be carried out to improve the current processing techniques.

References

1. R. L. Coble, Transparent alumina and method of preparation, U. S. Pat. No. 3026210, Mar 20, 1962.
2. A. Krell, T. Hutzler, and J. Klimke, Transparent Ceramics for Structural Applications, Ber. Dtsch. Keram. Ges., 84 (2007) E41– 49
3. A. Krell, P. Blank, H. Ma, T. Hutzler, and M. Nebelung, Processing of high – density sub micrometer Al_2O_3 for new applications, J. Am. Ceram. Soc.86 (2003) 546 - 553
4. A. Muta, G. Toda, T. Noro, and C. Yamazaki, Use of Yttria – Magnesia mixtures to produce highly transparent sintered alumina bodies, U. S. Pat. No. 3711585, Jan 16, 1973
5. A. Krell, and E. Strassburger, High purity submicron α – alumina armor ceramics: design, manufacture and ballistic performance, Ceram. Transactions: In proceeding of the ceramic armor materials by design symposium., 134 (2001) 463 – 471
6. D.T. Jiang, D. M. Hulbert, U. A. Tamburini, T. Ng, D. Land, and A. K. Mukherjee, Optically transparent polycrystalline Al_2O_3 produced by spark plasma sintering, J. Am. Ceram. Soc.91 (2008) 151 – 154
7. A. Krell, J. Klimke, and T. Hutzler, Advanced spinel and sub - μm Al_2O_3 for transparent armor applications, J. Eur. Ceram. Soc.29 (2009) 275 - 281
8. A. Krell, T. Hutzler, and J. Klimke, Transmission physics and consequences for material selection, manufacturing and applications, J. Eur. Ceram. Soc. 29 (2009) 207 - 221
9. E. Strassburger, Ballistic testing of transparent armor ceramics, J. Eur. Ceram. Soc.,29 (2009) 267–273
10. E. A. Maguire Jr. and R. L. Gentilman, Press Forging Small Domes of Spinel, Am. Ceram. Soc. Bull, 60 (1981) 255 – 256

11. D. W. Roy and J. L. Hastert, Polycrystalline $MgAl_2O_4$ spinel for high temperature windows, Ceram. Engg. Sci. Proc., 4 (1983) 502 – 509
12. R. Johnson, P. Biswas, P. Ramavath, R.S. Kumar, G. Padmanabham, Transparent polycrystalline ceramics: An overview, Trans. Indian Ceram. Soc. 71 (2012) 73 – 85
13. P. Biswas, R. Senthil Kumar, P. Ramavath, V. Mahendar, G. V. N. Rao, U. S. Hareesh, R. Johnson, Effect of post CVD thermal treatments on crystallographic orientation, microstructure, mechanical and transmission Properties of ZnS Ceramics, J. Alloys Compd. 496 (2010) 273 – 277
14. R. Apetz, and M. P. B. Van Bruggen, Transparent alumina; a light scattering model, J. Am. Ceram. Soc. 86 (2003) 480– 486
15. A. Krell, P. Blank, H.Ma, and T. Hutzler, Transparent sintered corundum with high hardness and strength, J. Am. Ceram. Soc.86 **(**2003) 12–18
16. D. C. Harris, A peek into the history of sapphire crystal growth, Window and Dome Technologies and Materials VIII, Proc. SPIE, 5078, 1 – 11 (2003).
17. M. E. Thomas, S. K. Andersson, R. M. Sova and R. I. Joseph, Frequency and temperature dependence of the refractive index of sapphire, Infrared phys. Technol. 39 (1998) 235 – 249
18. M. R. Merac, H. Kleebe, M. M. Muller and I. E. Reimanis, Fifty years of research and development coming to fruition; unraveling the complex interactions during processing of transparent magnesium aluminate ($MgAl_2O_4$) spinel, J. Am. Ceram. Soc., 96 (2013) 3341–3365
19. S. Ma, W. Q. Quek, Q. F. Li, Y. F. Zhang, J. Y. H. Fuh and L. Lu, Sintering of translucent alumina, J. Mater. Process Technol. 209 (2009) 4711 – 4715
20. J.G.J. Peelen, and R. Metselaar, Light scattering by pores in polycrystalline materials: Transmission properties of alumina, J. Appl. Phys. 45 (1974) 216 – 220

21. I. Yamashita, H. Nagayamma and K. Tsukuma, Transmission properties of translucent polycrystalline alumina, J. Am. Ceram. Soc. 91 [8] (2008) 2611 – 2616

22. A. Krell, K. Waetzig, and J. Klimke, Influence of the structure of MgO–n. Al_2O_3 spinel lattices on transparent ceramics processing and properties, J. Eur. Ceram. Soc., 32 (2012) 2887– 2898

23. M. Suarez, A. Fernandez, R. Torrecillas, and J. L. Menendez, Sintering to Transparency of Polycrystalline Ceramic Materials, in Sintering of Ceramics – New Emerging Techniques, Edited by A. Lakshmanan. InTech, Rijeka, (2012) 527– 552

24. Saint Gobain Sapphire, The clear advantage for IR windows, Saint – gobain crystals, www.saphikon.com, (2010) 1 – 8

25. P. Hogan, T. Stefanik, C. Willingham and R. Gentilman, Transparent yttria for IR windows and domes – past and present, ADM201976, 10thDoDEM Windows Symposium May 19, Norfolk, VV, 2004

26. O. H. Kwon, C. S. Nordahl, and G. L. Messing, Sub micrometer transparent alumina by sinter forging seeded γ – Al_2O_3 powders, J. Am. Ceram. Soc.78 (1995) 491 – 494

27. A. Krell, P. Obenaus, Grain shape in sintered submicrometer alumina, J. Eur. Ceram. Soc. 18 (1998) 1 – 13

28. H. Ma and A. Krell, Synthesis and processing of Nano – α – Al_2O_3 powders, Key Engg. Mater. 206 – 213 (2002) 43 – 46

29. C. R. Bickmore, K. F. Waldner, D. R. Treadwell and R. M. Laine, Ultrafine spinel powders by flame spray pyrolysis of magnesium aluminum double alkoxide, J. Am. Ceram. Soc. 79 (1996) 1419 – 1423

30. A. Goldstein, A. Goldenberg, Y. Yeshurun and M. Hefetz, Transparent $MgAl_2O_4$ spinel from a powder prepared by flame spray pyrolysis, J. Am. Ceram. Soc., 91 (2008) 4141–4144

31. C. T. Mathew, S. Solomon and J. K. Thomos, Structural, optical and vibrational characterization of infrared – transparent nanostructured $MgAl_2O_4$ synthesized by a modified combustion technique, Mater. Tod. Proc. 2 (2015) 954 – 958

32. J. Rufner, D. Anderson, K.Benthem and R. H. R. Castro, Synthesis and sintering behavior of ultrafine (<10 nm) magnesium aluminate spinel nanoparticles, J. Am. Ceram. Soc., 96 (2013) 2077–2085

33. D. Lepkova, A. Batarjav, B. Samuneva, Y. Ivanova and L. Georgieva, Preparation and properties of ceramics from magnesium spinel by sol-gel technology, J. Mater. Sci. 26 (1991) 4861-4864

34. T. Shiono, K. Shiono, K. Miyamoto and G. Pezzoti, Synthesis and characterization of $MgAl_2O_4$ spinel powder from a heterogeneous alkoxide solution containing MgO powder, J. Am. Ceram. Soc. 83 (2000) 235 – 237

35. M. Barj, J. F. Bocquet, K. Chhor and C. Pommier, Submicronic $MgAl_2O_4$ powder synthesis in supercritical ethanol, J. Mater. Sci. 27 (1992) 2187 – 2192

36. O. Varnier, N. Hovanian, A. Larbot, P. Bergez, L. Cot and J. Charpin, Sol-gel synthesis of magnesium aluminum spinel from a heterometallic alkoxide, Mater. Res. Bull. 29 (1994) 479 – 488

37. R. Cook, M. Kochis, I. Reimanis and H. Kleebe, A new powder production route for transparent spinel windows: powder synthesis and window properties, Window and Dome Technologies and Materials IX, Proc. SPIE, 5786 (2005) 41 – 47

38. C.T. Wang, L. S. Lin and S. J. Yang, Preparation of $MgAl_2O_4$ spinel powders via freeze – drying of alkoxide precursors, J. Am. Ceram. Soc. 75 (1992) 2240 – 2243

39. S. S. Balabanov, V. E. Vaganov, E. M. Gavrishchuka, V. V. Drobotenko, D. A. Permin, and A. V. Fedin, Effect of magnesium-aluminum isopropoxide hydrolysis conditions

on the properties of magnesium-aluminate spinel powders, Inorg. Mater. 50 (2014) 830 – 836

40. S.S. Balabanov, R.P. Yavetskiy, A.V. Belyaev, E.M. Gavrishchuk, V.V. Drobotenko, I.I. Evdokimov, A.V. Novikova, O.V. Palashov, D.A. Permin, V.G. Pimenov, Fabrication of transparent $MgAl_2O_4$ ceramics by hot-pressing of sol-gel-derived nano powders, Ceram. Inter. 41 (2015) 13366–13371
41. N. Saito, S. Matsuda and T. Ikegami, Fabrication of transparent yttria ceramics at low temperature using carbonate-derived powder, J. Am. Ceram. Soc., 81 (1998) 2023–2028
42. T. Ikegami, T. Mori, Y. Yamija, S. Takenouchi, T. Misawa and Y. Moriyoshi, Fabrication of transparent yttria ceramics through the synthesis of yttrium hydroxide at low temperature and doping by sulfate ions, J. Ceram. Soc. Jpn. 107 (1999) 297 – 299
43. T. Ikegami, J. G. Li, T. Mori and Y. Moriyoshi, Fabrication of transparent yttria ceramics by the low-temperature synthesis of yttrium hydroxide, J. Am. Ceram. Soc., 85 (2002) 1725–1729
44. J. Mouzon, T. Lindback and M. Oden, Influence of agglomeration on the transparency of yttria ceramics, J. Am. Ceram. Soc., 91 (2008) 3380–3387
45. W. K. Jung, H. J. Ma, S. W. Jung and D. K. Kim, Effects of calcination atmosphere on monodispersed spherical particles for highly optical transparent yttria ceramics, J. Am. Ceram. Soc., DOI: 10.1111/jace.14776 (2017) 1876 – 1884
46. H. Eilers, Fabrication, optical transmittace, and hardness of IR – transparent ceramics made from nanophase yttria, J. Eur. Ceram. Soc. 27 (2007) 4711 – 4717
47. W. K. Jung, H. J. Ma, Y. Park and D. K. Kim, A robust approach for highly transparent Y_2O_3 ceramics by stabilizing oxygen defects, Script. Mater. 137 (2017) 1 – 4

48. Z. Huang, X. Sun, Z. Xiu, S. Chen and C. T. Tsai, Precipitation synthesis and sintering of yttria nanopowders, Mater. Lett. 58 (2004) 2137 – 2142

49. J. Mouzon T. Lindback and M. Oden, Influence of agglomeration on the transparency of yttria ceramics, J. Am. Ceram. Soc. 91 (2008) 3380 – 3387

50. A. Krell, G. Baur, and C. Dahne, Transparent sintered sub - μm Al_2O_3 with IR transmittivity equal to sapphire; pp. 199 – 207 in Window and dome technologies VIII, Vol.5078, Proceedings of SPIE, Edited by Randal.W. Tustiston., *et al.* SPIE—The International Society for Optical Engineering, Orlando, 2003

51. G. Gilde, P. Patel, and P. Patterson, Evaluation of hot pressing and hot isostatic pressing parameters on the optical properties of spinel, J. Am. Ceram. Soc., 88 (2005) 2747–2751

52. A. A. DiGiovanni, L. Fehrenbacher, D. W. Roy, Hard transparent domes and windows from magnesium aluminate spinel, Window and Dome Technologies and Materials IX, Proc. SPIE, 5786, 56–63 (2005).

53. T. J. Mroz, T. M. Hartnettb, J. M. Wahlb, L. M. Goldmanb, J. Kirschc, and W. R. Lindbergd, Recent advances in spinel optical ceramic, Window and Dome Technologies and Materials IX, Proc. SPIE, 5786, 64 – 70 (2005)

54. A.Goldstein, A.Goldenberg and M.Vulfson, Development of a technology for the obtainment of fine grain size, transparent $MgAl_2O_4$ spinel parts, J. Ceram. Sci. Tech. 02 (2011) 1 – 8

55. M. C. L. Patterson, A. A. DiGiovanni, L. Fehrenbacher and D. W. Roy, Spinel - gaining momentum in optical applications, Window and Dome Technologies and Materials IX, Proc. SPIE, 5078, 71 – 79 (2003)

CHAPTER - II

Literature Review

This chapter reviews the prior arts and various investigations extensively carried out in the areas of Al_2O_3, $MgAl_2O_4$ spinel, Y_2O_3 and AlON transparent ceramic materials.

2.1 Transparent Al_2O_3

Transparent sub-µm Al_2O_3 attracts huge attention in the field of transparent ceramics due to its exclusive and excellent intrinsic properties such as as superior hardness, high flexural strength, resistance to chemical attack, high thermal shock resistance and transparency from visible to mid-IR (1-6 µm) wavelength regions. These unique combinations of properties extended its applications in wide range of areas including discharge lamp envelopes, windows for lasers, armor materials, orthodontic parts and artificial gems [1 – 9]. In addition, their utilization extends as IR transparent radomes and dome materials in the advanced supersonic missiles to confront severe and harsh aerodynamic environments [10]. In the present scenario, sub-µm Al_2O_3 is the hardest and the strongest among all the transparent ceramic materials.

2.1.1 Coarse grained translucent Al_2O_3

Numerous studies have been carried out on transparent Al_2O_3 for several decades due to its immense potential characteristics and the investigations are constantly progressing until today to acquire its maximum competencies. The sintered polycrystalline Al_2O_3 was considered as an opaque material until R.L. Coble exposed its capability of transmissions to light during 1960. According to the U.S. Patent 3026210, Coble *et al*. developed the transparent Al_2O_3 by mixing finely divided alumina particles with 0.5% MgO and compacted the mixture at a pressure of about 50 tons per square inch to produce the green discs. The shaped discs were

pre-heated at 1000°C – 1200°C and further sintered at 1700°C – 1950°C under vacuum or hydrogen environment to obtain completely sintered body. According to this method, the sintered and polished articles having 0.5 mm thickness showed transmissions up to 79% at 4.9 µm wavelengths [1].

Muta and his group disclosed a method of making transparent Al_2O_3 employing alumina powders having particle sizes ranging from 0.1 µm and mixtures of 0.1% of MgO and 0.25% of Y_2O_3 as sintering aids. These powders were compacted and pre-sintered in air at 1000°C – 1600°C and subsequently sintered at 1700°C – 1900°C under vacuum or hydrogen atmosphere. The sintered articles having 0.5 mm thickness showed inline transmissions of at least 60% in the wavelength region between 320 µm and 1100 µm [2].

Alternatively, Greber *et al*. produced transparent Al_2O_3 for ceramic lamp tubes using aluminum oxide monohydrate as a starting material. This method involves mixing of aluminum alkoxides in alcohol at 80°C with the appropriate quantity of MgO additive. The mixture was hydrolyzed in water and peptized using acid vapors followed by distillation and drying. The as-dried powder consisting 12 – 25% of acid content was compacted and sintered in vacuum or hydrogen atmosphere above 1850°C for 24 hours. The high purity aluminum alkoxide was selected for this method to avoid the inclusions of any harmful secondary phases such as SiO_2, Fe_2O_3, Mn_2O_3 etc. that may cause severe reaction with sodium vapors during the operation of high-pressure lamps [11].

Amato *et al*. evaluated the effects of powder morphology with respect to the final densification by preparing the starting powders using freeze and spray drying techniques. The compacted green samples were sintered at 1700°C under vacuum for 2 hours and further heat treated at 1900°C in vacuum for a period between 2 and 24 hours to obtain density very closer to

theoretical values. The sintered samples after grinding and polishing to 0.5 mm thickness showed transmissions up to 70% in the 2 – 5 μm wavelength region [12].

Wei *et al.* modified the sintering additives and the sintering atmosphere (mixtures of hydrogen and argon) and produced transluscent alumina [13 – 14]. Quihong *et al.* attempted to dope La_2O_3 for studying its effect on enhancing the densification of Al_2O_3 and added concentrations up to 0.3 wt% along with 0.1 wt% of MgO. They shaped the green samples through CIPing at 200 MPa pressures and sintered at 1700 – 1750°C for a period up to 15 hours in H_2 atmosphere. The samples exhibited transmissions up to 50% in the IR- regions [15].

All the above-mentioned methods succeeded in achieving transparency by eliminating the pore element from their sintered bodies. The samples were heat treated to very high temperatures that is above 1800°C for the complete removal of pores. Al_2O_3 bodies at these temperatures not only attained densification but also experienced severe grain growth with the average grain sizes exceeding 10 – 20 μm. At these magnitudes of grain sizes, Al_2O_3 turn out to be translucent for the incident lights due to its birefringence scattering.

Yamashita *et al.* simulated the in-line and total forward transmissions of the translucent polycrystalline alumina as a function of pore size, pore volume, grain size and degree of birefringence. He derived a theoretical expressions using Mie scattering model [16] and correlated the results with his experimental values. His model express that the quantum of porosity significantly influence both the total forward and in-line transmissions whereas the grain size affects only the in-line transmissions and have no considerable impact on total forward transmissions [17].

2.1.2 Submicron transparent Al_2O_3

Understanding these drawbacks associated with the larger grain sizes, subsequent researchers initiated to improve the process to obtain eventual sintered grain sizes less than 1.0 μm to avoid

the birefringence losses. Accordingly, Peelan *et al*. attempted to sinter Al_2O_3 using hot press [HP] technique at temperatures lesser than 1450°C. The sintered grain sizes were retained to around 1.0 µm due to the lower densification temperatures and thus the transparency was improved up to 80 – 81 % at 2.5 µm wavelengths for 0.5 mm thick body. However, the report reveals that the sintered bodies still left with traces of residual pores having sizes around 0.2 µm [18 – 19]. These pores have induced inline scattering as per the Mie theory [20 – 21] and restrained the sintered body from exhibiting transparency beyond 80%. The experimental studies further conducted by Peelan *et al*. detailed the effect of such pores towards the transmission of light in Al_2O_3 [22].

Later, Mizuta *et al.* produced translucent alumina through low temperature sintering using commercially available α- Al_2O_3 powder (Tamicron TM-DA Grade, Taimei Chemicals Co., Ltd., Nagano, Japan). The powder was reported to be 99.99% pure and the average particle size was around 400 nm. Due to very fine particle size and large specific area (14 m^2/g), the slip casted green samples attained reasonable densification (no density values were reported on sintered samples) at temperatures around 1240°C for 2hours. The samples were further pressed hot isostatically at temperatures between 1200°C to 1400°C to obtain theoretically dense samples. The average grain size after HIPing was found to be around 5.0 µm for the samples HIPed at 1250°C and the samples exhibited transmissions up to 46% in the visible to infrared regions [23].

Subsequently, O.H. Kwon and co-workers developed the first sub-micron grained transparent alumina through sinter forging technique using sol gel derived γ-alumina as a starting powders seeded with 1.5 wt% α-alumina. The powder was highly agglomerated and therefore the hot forge method was used for sintering the samples. They have achieved complete densification at temperatures as low as 1250°C. It was reported that the sample was light grey in colour, which is presumably due to the carbon contaminations from their graphite dies or due to the

oxygen deficiencies or because of the addition of TiO_2 dopants. The average grain size was reported as 0.43 µm. Though the samples after forging exhibited theoretical densities up to 100% (values are not discussed) with 0.43 µm average grain sizes, the transparency was not improved beyond 50 % in the IR region [24]. Kumagai *et al*. proposed the concept of α-alumina seeding in the boehmite sol to improve the transformation kinetics of Al_2O_3 for the conversion of θ phase to α phase during heat treatments. In addition, the seeds acted as nucleation sites for θ to α transformation at lower temperatures. Besides, they also inhibit the formation of vermicular microstructure and encourage the formation of equiaxed isotropic grain structures. Moreover, the seeds retain the sintered grain sizes in the sub-micron region [25 – 26].

In view of the above, many conducted various studies on improving densification and reducing the sintered grain sizes using alumina seeds. Krell *et al*. utilised very fine commercially available Al_2O_3 powder and achieved relative densities above 99% T.D. and grain sizes around 0.5 µm. The samples were prepared by gel casting and pressure assisted filtration casting and sintered at 1300°C to 1350°C. He studied various advantages of sub-micron grained sintered Al_2O_3 in terms of their mechanical properties and reported that the Al_2O_3 having 400 nm average grain sizes exhibit significant improvements in the hardness reaching the values above 20 GPa and flexural strengths above 900 MPa [27]. Additionally, he also studied the effect of sintered grain shapes with respect to the usage of sol-gel derived powder and reported that the sol-gel derived powders favoured the formation of equiaxed grain structures [28]. Ma *et al*. showed that the seeding of α – Al_2O_3 or diaspore (Al-O-OH) in the chemical precipitation synthesis of alumina powder produce equiaxed Al_2O_3 particles having particle sizes between 25 – 100 nm. The green discs from these powders exhibited relative density of 99% at 1285°C having grain sizes around 600 nm [29]. However, the powders obtained from these synthesis routes exhibited inferior properties in terms of relative densities and sintered grain sizes compared to the gel-casted samples derived using commercial Al_2O_3 powders (Tamicron TM-

DA Grade, Taimei Chemicals Co., Ltd., Nagano, Japan) [28]. An another investigation showed that it is not the most fine grained nano powders promote finest sintered microstructure but the powders with extremely homogeneous particle co-ordination in the green bodies encourage low temperature densification and favor the achievement of nano microstructures [30 – 32]. This would be the plausible reason for why most of the investigators selected commercial Al_2O_3 powders rather than their in-house synthesized powders for the processing of transparent Al_2O_3.

Echeberrira *et al.* attempted to fabricate dense Al_2O_3 through sinter-HIP processing using nanoscale alumina powders from various commercial suppliers. Shaping was carried out using compaction and pressure filtration techniques and the samples were sintered to obtain closed porosities and further HIPed at 1250°C at a pressure of 150 MPa. The HIPed specimens showed an average grain size of 0.45 µm and hardness up to 24 GPa [33]. Laine *et al.* synthesized nano $\alpha - Al_2O_3$ having particle size between 30 – 80 nm through liquid-flame spray pyrolysis technique. The sintered samples from these powders exhibited density above 99.5% with the final grain sizes around 500 nm [34]. All these investigations [27 – 30, 33 – 34] evaluated the enhancement in properties relating to ultra-fine sintered microstructures and however, not conducted any investigations related to optical transparencies.

Godlinski *et al*. utilized controlled float packing method for the fabrication of alumina green bodies using commercial alumina powders. As per this method, the colloidal suspensions of alumina was allowed to settle based on their particle and agglomerate sizes. The tunings between electrostatic and electro-steric repulsions in the suspensions initiated the settlement of coarser particles followed by the ultra-fine and equivalent sized particles. Through this method, they produced homogeneous, dense green compacts, and sintered without any dopants at 1275°C. The average grain size after sintering was 0.4 µm and the sintered samples after polishing to 0.5 mm thickness showed transparency up to 15% in the visible regions [35].

Cheng *et al*. employed microwave-sintering for his fabrication of transparent alumina. High purity (99.99%) commercial alumina powders (Baikolox CR 10, Baikowski International, North Carolina) having mean particle sizes of 150 nm was compacted using cold isostatic press (CIP) at 280 MPa pressures. They pre-heated the compacted pellets at 1100°C for the removal of residual binders and further sintered under hydrogen atmosphere using microwave energy having 6 kW microwave power source. They observed the enhanced rate of grain growth for the samples sintered using microwave assistance and found their samples partially converted to single crystals. The samples exhibited transmissions up to 70% at 2.5 µm wavelength region [9, 36].

All the above-mentioned methods employed various techniques to fabricate transparent alumina materials. However, until 2003, no investigations reported the achievement of transparency above 80% in the wavelength regions between 0.2 to 6 µm.

Later in 2003, Apetz *et al.* reported the fabrication of sub-micron transparent Al_2O_3 having high-inline transparency up to 83% in the wavelength region around 2.0 µm. Aqueous suspensions of α – alumina powders having mean particle sizes of 150 nm was shaped through slip or pressure casting and sintered at 1250°C in air to obtain closed porosity. The sintered samples further subjected to HIPing at 1200°C – 1400° C in argon atmosphere at 200 MPa pressures to obtain transparent bodies. The report discussed the light transmission behaviour in the sintered sub-micron polycrystalline Al_2O_3 in detail and compared it with the transmissions of coarse-grained Al_2O_3. They indicated that the real-inline transmissions drastically reduce from 80 % to < 10 percentage when the sintered grains escalated from 500 nm to 3.0 µm. In addition, they emphasized that the existence of residual porosity in the sintered body can have a prominent effect on the transmissions of light where even the presence of 0.1% of residual porosities can completely deteriorate the transparency [37].

Simultaneously, Krell *et al.* reported the manufacturing of complex hollow components and large flat transparent windows of completely sintered and HIPed alumina shaped through aqueous gel-casting techniques. Commercially available TM-DAR corundum powder (purity > 99.99%, average particle size 0.2 µm, Boehringer Ingelheim Chemicals, Tokyo) was made into aqueous slurries having solid concentrations between 76 – 78 wt %. Ultra-fine ZrO_2 particles up to 0.2 wt % was used for pinning the grain growth and 0.03 wt % of MgO was added as sintering aid. The green samples, sintered at 1240°C – 1250°C in air for 2 hours achieved 97% T.D and further HIPed at temperatures between 1150°C and 1400°C at 200 MPa pressures showed theoretical densities above 99.9%. The average grain sizes of HIPed samples varied between 0.5 and 0.6 µm and exhibited hardness up to 21 GPa. The 0.8 mm thick polished samples exhibited very high inline transmissions up to 86% in the 3 – 5 µm region and about 59% in the visible regions. The report claimed that their transparent Al_2O_3 exhibit transparency equal to the single crystal sapphire in the 3 – 5 µm wavelength regions [38 – 39]. Qi *et al.* also followed the similar process as Krell *et al.* using gel casting, sintering and HIPing techniques to fabricate 1.0 mm thick transparent Al_2O_3 having sintered grain sizes around 1.0 µm with a reasonable optical transparency (values are not discussed) [40].

Yamashita *et al.*[17], Apex *et al.* [31] and Krell *et al.* [37, 41] reported in detail on how the hexagonal crystallography of polycrystalline alumina cause birefringence reflection at every grain boundary junctions and diminish the real inline transmissions significantly. On the other hand, Mao *et al.* attempted to align the orientation of c-axes of alumina parallel to each other to circumvent the effect of birefringence. They have conceived this idea from the earlier work reported by Suzuki *et al.* [42] where the application of magnetic field of 10 tesla align the c-axes of alumina parallel to the direction of magnetic field. Accordingly, they applied a strong magnetic field of 12 tesla during slip casting and sintered the shaped bodies at 1850°C in H_2 atmosphere for 3 hours. The sintered bodies exhibited aligned crystal structure and showed the

grain sizes between 30 – 40 µm. Though the grains have grown very large, the 0.8 mm thick polished samples showed no birefringence scattering and exhibited inline transmissions up to 55% in the visible regions [43].

Granger *et al.* patented his method of fabricating transparent alumina through the U.S. Patent No. 2009/0137380 A1 [44]. According to his approach, combinations of various sintering additives such as Sm_2O_3, CaO and TiO_2 were mixed with commercial alumina powder for the preparation of aqueous suspensions followed by casting, sintering and HIPing at temperatures around 1250°C. The sintered grain sizes retained between 200 nm and 1.5 µm with the in-line transmissions up to 83% in the wavelength region between 2.5 µm and 4.5 µm. Further, Parish *et al.* disclosed a method of achieving improved transmissions equivalent to single crystal sapphire in the IR wavelength region. His approach followed preparing aqueous suspensions of alumina using commercial alumina powder (100% α – phase, 99.97% pure and particle sizes less than 500nm) together with the sintering aids such as MgO, Y_2O_3, and ZrO_2 having concentrations between 25 to 3000 ppm. He used the pressure casting or filter casting techniques for shaping the green components and sintering in H_2 atmosphere at temperatures above 1200°C for densification and HIPing at 1200°C under pressures of 100 – 200 bars for complete elimination of pores. The final polished samples having 0.8mm thickness showed in-line transmissions up to 88.9% at 4.0 µm wavelength region [45]. Though his approaches have, no much deviation from the methods discussed above, the attempt of sintering in H_2 atmosphere have plausibly enhanced the rate of pore mobility from the sintering microstructures and favoured low temperatures densification and further achieving improved transmissions.

Biswas *et al.* attempted to introduce La_2O_3 doping and fabricated transparent alumina using commercial alumina powders. The aqueous suspensions of alumina was casted, pressure-less sintered and HIPed at 1350°C for 5 hours. The addition of La_2O_3 up to 0.1 wt % concentrations enhanced the visible transparency to 50% compared to the un-doped alumina which has showed

transmissions up to 30%. IR transparency in the wavelength regions between 3 – 5 µm showed no major effect with respect to La_2O_3 addition [46].

Drdlikova *et al.* modified the surface of the commercial alumina powder through plasma treatment and introduced NO_x and CO_x species on the particle surface. They used these molecule charges for dispersing alumina and prepared stable aqueous suspensions for casting. In addition, suspensions were prepared through conventional methods employing electro-static forces (dispersion using acid molecules and adjusting the pH for stabilization) and electro-steric forces using commercially available dispersing agents such as Darvan – CN (R.T.Vanderbilt Co., Inc., Norwalk, CT, USA). All these suspensions were casted, dried and sintered at 1380°C and 1500°C and HIPed at 1200°C to 1250°C at 200 MPa pressures for 3 hours. In contrast to their expectations, transparent alumina produced using plasma treated powders showed poor transmissions (up to 36%) compared to the untreated powders (up to 57%) in the visible regions [47].

Drdlik *et al.* explored the effect of erbium doping on the optical, mechanical and fracture behaviour of transparent alumina. They have doped erbium ions having concentrations between 0.1 and 0.15 at.% in the aqueous suspensions of commercial alumina powder and casted for making green samples. The samples attained densification through two-step sintering in air. The step followed the heating to 1440°C from RT, cooled without a hold, and dwelled at 1280°C for 10 hours to gain the closed porosity stage. The samples were further HIPed at 1280°C under 200 MPa pressure in argon to achieve optical transparency. The studies report that the erbium atoms supress the grain growth and confine the average size to 0.3 µm. The polished samples without erbium doping exhibited transmissions up to 60 % and the doped samples showed decrement in the transparency to 56%, which is due to the segregation of erbium atoms at the grain boundaries. However, the erbium atoms slightly enhanced the hardness to 27 GPa than that of the un-doped version (26 GPa) [48].

From the above discussions, it is evident that almost every investigators utilized only the commercial alumina powders for their processing and attempted to shape the green components using various techniques such as compaction, cold isostatic pressing, slip casting, gel casting, pressure casting, filer pressing etc. Further, the densification is achieved through conventional air sintering, two – stage sintering, hydrogen sintering, HP and HIP etc. Most of these approaches have the versatility of fabricating components having larger sizes and complex shapes such as armour windows, domes and ogive radomes. For e.g., Krell *et al.* reported the fabrication of larger flat windows of dimension of 100mm X 100mm X 0.8mm (Length X Breadth X Thickness) and hollow lamp envelop through gel casting [38] and Ceranova corporation exhibit their capabilities of making domes and ogive radomes probably through pressure casting techniques [49].

Apart from these methodologies, some investigators attempted fabricating transparent alumina using spark plasma sintering (SPS) techniques. Various processing features such as rapid rate of heating (> 150°C/ min), minimum holding period at peak temperatures (usually about 3 to 10 minutes) and simultaneous application of heat and pressure attract researchers to utilize this technique for gaining low temperature densification and extremely fine-grained microstructures. In spite of several studies conducted on alumina using SPS techniques to reduce the sintered grain sizes less than 0.4 μm [50 – 54], no optical transparency was achieved in any attempts probably due to the presence of residual porosities.

Kim *et al.* reported the first transparent alumina sample fabricated through controlled SPS sintering. As per their approach, they compacted commercial Al_2O_3 powder (Tamicron TM-DA Grade, Taimei Chemicals Co., Ltd., Nagano, Japan) at 80 MPa pressures and heated the sample in two different heating rates. The first stage from 600°C to 1000°C treated with the rate of 25°C/ min and the second increment up to 1150°C received the rate of 8°C/ min. Samples with a rapid heating rate of 100°C/ min up to 1150°C was also prepared for

comparison. The samples heat-treated under controlled heating rate exhibited densifications up to 99.97% with the mean grain sizes of 0.27 µm and the samples with abrupt heating rate exhibited opacity due to the occlusions of intergranular porosities. The polished samples having thickness of 0.88 mm exhibited in-line transmissions up to 70% at 1.6 µm wavelengths [55]. They further extended their study and explored the effect of heating rate with respect to the percentage of transmissions and reported that the slow heating rate (2°C/ min) improve the transmissions compared to the faster heating rates (100°C/ min) [56]. They also given identical explanations like Yamashita *et al*. [17] on the influences of pore size, grain size and microstructural defect with respect to the transmissions of their SPS samples [57].

Jiang *et al*. also conducted similar experiments like Kim *et al.* [55 – 57] using the same commercial alumina powder and achieved transmittance up to 85% in the 3 – 5 µm regions [58]. Instead of usual dry compaction of the powders, Aman *et al.* attempted using slip casted green samples for the SPS studies and reported achieving 45% transmissions at 0.9 µm wavelengths [59]. Chakravarthy *et al.* studied the influences of applied stress on the densification and the optical transparency of alumina by varying the SPS load from 150 – 275 MPa and obtained transmissions closer to 85% in the 3 – 5 µm regions for the maximum loaded samples. Instead of conventional graphite dies, they utilized SiC moulds for their compaction for withstanding the enhanced applied stress [60]. Jin *et al.* pre-treated the as-received powder alumina powder (HFF5, Shangai Wusong Chemical Co. Ltd., Shanghai, China) with hydrofluoric acid for de-agglomeration and conducted SPS experiment at temperatures between 1250°C and 1350°C. They showed that the de-agglomerated powders exhibiting better in-line transparency around 50% in the visible region [61]. Lallemant *et al.* conducted similar exercises like Aman *et al.* [59] and included additional shaping techniques such as filter pressing and cold isostatic pressing for preparing the green samples for their SPS studies. The

samples from all the pre-shaped samples presented real inline transmissions of 53% in the 0.64-μm wavelengths [62].

Grasso *et al.* increased the applied stress over Chakravarthy *et al.* reaching loads above 400 MPa using moulds made of carbon fibre composites. They could sinter the samples with minimum grain growth having sizes as low as 107 nm that were slightly larger than their particle sizes (130 nm) of the starting powder (Super TM-DAR, Taimei Chemicals Co. Ltd., Japan). The transparency reached to the levels of 65.4% in the visible regions due to the ultra-fine sintered grain sizes [63]. Ratzker *et al.* further extended the applied load between 650 and 800 MPa using a hybrid graphite – SiC moulds and obtained enhanced visible transparency of about 68% [64].

Though the transparent alumina samples fabricated through SPS techniques exhibited improved optical and mechanical properties compared to the fore-mentioned processing techniques, the SPS processing still have many inherent deficiencies. For instance, this process is not versatile for fabricating larger sized components and complex shaped articles. Moreover, this technique is highly oriented for academic studies and not preferred for major practical applications. Apart from these realities, one can observe that even for all the SPS studies, the investigators selected only the commercial alumina powders from various resources and no studies utilized any in-house synthesized alumina powders for the fabrication of transparent alumina.

Considering the critical demands on the need of ultra-fine and ultra-pure alumina powders suitable for high performance transparent alumina fabrication, the present study presents a facile sol–gel route to synthesize the alumina powder having ultra-high purity and ultra-fine particle sizes in the range around 20 – 40 nm. The process exhibited high control on inter-particle homogeneity for shaping green bodies and showed excellent sinterability at

temperatures around 1350 – 1400°C. The sintered specimens transformed to exhibit optical transparency after HIPing. The synthesized powders and the sintered specimens were extensively characterized for elucidating their physical, microstructural, mechanical and optical properties. The details of the powder synthesis and the fabrication of transparent alumina are presented in detail in chapter 4.

2.2 Transparent $MgAl_2O_4$ spinel

The next material selected in this study is transparent $MgAl_2O_4$ spinel. Transparent magnesium aluminate spinel is cubic and optically isotropic materials carries excellent intrinsic characteristics such as high strength, hardness, low scatter and broadband optical transparency up to 86% in the region between 0.2 µm and~7.0 µm. These combinations of properties makes spinel as an ideal candidate for infrared domes and windows for missiles, optical lenses, transparent armours, host material for lasers, super-market scanning windows, scratch proof watch casings, optical heat exchangers, pyrometer windows for high-temperature and high-pressure furnaces etc. [65]. Fabrication of transparent grade spinel articles involve various processing steps comprising appropriate selection of ultra-pure, highly-reactive starting powders, fabrication of homogeneous, defect-free green bodies, sintering the shaped components with high degree of densification and elimination of last 0.01% of porosity from the sintered bodies [66].

2.2.1 History on development of transparent spinel

J.J. Ebelman reported the first synthetic spinel crystals during 1848. In the early 1960, Navias *et al.* attempted for a vapor transport technique for the fabrication of spinel materials [67]. However, the research and development activities on powder to transparent spinel through HP technique initiated in the late 1960s [68]. In the year 1969, General electric co. fabricated transparent spinel with 60% infrared transmissions using hydrogen sintering at temperatures

around 1900°C [69 – 71]. During 1970s, Don *et al.* at Coors Ceramics hot forged the spinel powder containing 0.8 wt % Li_2O and 2 wt % SiO_2 to obtain 1.0 mm thick samples having visible transmissions closer to 76%. The grain size varied between 0.2 µm and 60 µm. Later, in 1977, Raytheon research division developed transparent spinel using fusion cast method for fabricating infrared dome for the advanced short-range missile. However, due to the residual stresses, most of the fused cast bodies developed cracks during cooling [72 – 76]. In Parallel, Applied Physics Laboratory at Johns Hopkins University and Honeywell Systems Research Centre Works conducted tests on high temperature optical properties of transparent spinel supplied by Coors in the years 1980 [77]. In the mid of 1980s, Raytheon research division reported fabrication of spinel domes and windows through HP method in large scales having transmissions closer to theoretical values (86%) with a bimodal grain sizes distributed in the ranges around 4 µm and 65µm [78]. In early 1990s, the characteristic analysis were carried out for measuring microwave properties, high temperature infrared transmission and fracture resistance test [79 – 81]. In the mid of 1990s, spinel fabricated through rate controlled sintering followed by hot isostatic pressing exhibited grain sizes in the range between 20 – 40 µm embedded in the matrix of 2 – 3 µm sized grains [82]. Even until the years of 2000, spinel fabrication process suffered in obtaining consistent transparency due to inconsistency in the properties of spinel powders supplied by Baikowski International. Moreover, the literature had very little information on consistent sintering and fabrication of transparent spinel materials [83 – 85].

2.2.2 Conventional coarse-grained transparent spinel

Apart from the existence of single crystal spinel, the polycrystalline transparent spinel started its expedition as a coarse-grained material having average grain sizes above 10 µm. As mentioned above, the genesis of fabricating spinel focused on obtaining consistent optical

transparency majorly through HP and HIPing procedures at temperatures in the range between 1600°C – 1900°C.

In continuance to the fore-mentioned reports, in the year 2005, Gilde *et al.* evaluated the optical properties of spinel produced through HP + HIPing. The spinel powder (Baikowski, S30-CR) and 0.75 wt% LiF were blended together and hot pressed at temperatures between 1620°C and 1650°C at 20 MPa pressures followed by hot isostatic pressing at temperatures of 1500°C – 1900°C with a pressures between 100 MPa and 200 MPa. The grains after HIPing grown to the sizes above 100 µm at these temperatures and the samples showed IR transmissions closer to 82% [86]. Simultaneously, DiGiovanni *et al.* produced transparent spinel blanks and domes through HP + HIP or pressureless sintering (PLS) + HIP routes and reported that the HP+HIP method delivered consistent quality in terms of transmissions closer to 87% in the IR regions [87].

Mroz *et al.* at Surmet Corporation developed high quality transparent spinel at large scales through powder compaction + PLS + HIP route and produced a nominal 5" to 6" diameter discs and lenses. The average transmissions in the IR regions varied between 82 and 84%. The microstructure revealed bimodal grain distribution with the grain sizes as large as 100 µm and contained traces of foreign inclusions of sizes in the range of 10 µm to several hundred microns in diameter. Mroz *et al.* further reported that the larger grains acted as stress concentrators and significantly affected the strength of their material and therefore emphasized for the necessity of fine-grained spinel to improve the mechanical properties [88].

Goldstein *et al.* examined the densification characteristics of spinel powders produced through flame spray pyrolysis supplied by Nanocerox, Ann Arbor, MI. The powder contained soft agglomerates with the average particle size closer to 0.84 µm. The isostatically compacted specimens sintered at 1400°C for a prolonged period of 80 hours and HIPed at 1700°C

exhibited the average grain size of 17 µm and transmissions up to 84% in the IR regions. The samples showed hardness (HV_5) up to 12.8 GPa [89].

Biswas *et al.* employed an uncommon shaping methodology called methylcellulose based thermal gelation technique for fabricating transparent flat spinel discs and honeycomb-like structures. $MgAl_2O_4$ powder from Baikowski made into high solid loaded aqueous suspensions with 0.2% of methylcellulose. The casted samples gained 99% relative density upon sintering at 1700°C and achieved 100% densification upon HIPing at 1800°C under 195 MPa pressure. The final samples exhibited an average grain size of 40 µm and a hardness of 13.2 GPa. The visible transmissions reached closer to 80% at 650 µm wavelength regions [90].

2.2.3 Fabrication of transparent spinel using precursors

Apart from the practice of using commercial spinel powders, several attempts continued on fabricating spinel components using various precursors. Two variants of approaches such as single stage and two stage processing followed for fabrication. Single stage process involved shaping of green components using spinel precursors and obtaining densification through reactive sintering in a single heat treatment whereas the two-stage process comprises the synthesis of spinel powders in the first stage followed by shaping and sintering in the second stage.

2.2.3.1 Spinel through reactive sintering

Fabricating transparent spinel through single stage approach practised rarely due to the occurrence of volume expansion between 5 and 8 % [91 – 92] during phase formation prior to sintering. In spite of this challenge, researchers explored various techniques of handling this obstacle and produced spinel to various levels of transparency. Shimada *et al.* included part of commercial spinel powders in the mixture of alumina and MgO and sintered the cold isostatically pressed compacts up to 1550°C for 3 to16 h in air followed by HIPing up to

1800°C at a pressure of 150 MPa for 1 hour in argon atmosphere. The samples exhibited transmissions closer to theoretical values [93]. Frage *et al.* according to his U.S. Patent No. 2009/ 0297851 A1 produced transparent spinel through field assisted sintering technique. The mixtures of alumina and MgO with 0.5 to 2.0 wt % LiF was heated initially to 1600°C for phase transformation followed by application of pressures up to 100 MPa for densification. The sintered body exhibited transmissions around 75 % in the visible region and Vickers hardness closer to 14 GPa [94]. Krell *et al*. and Esposito *et al.* also conducted similar studies and reported comparable results for their reactive sintered transparent spinel [95 – 96]. A recent studies conducted by Han *et al*. report that the usage of $\gamma - Al_2O_3$ to minimize the volume expansion issues compared to $\alpha - Al_2O_3$. However, spinel produced with $\gamma - Al_2O_3$ suffered with severe abnormal grain growth and pores trapped in the intergranular sites resulted in poor optical transmissions [97]. Their subsequent studies addressed this issue by varying the molecular ratio between $\gamma - Al_2O_3$ and MgO to the alumina rich region (n = 1.5) and produced transparent spinel by sintering at 1500°C and HIPing at 1600°C. The HIPed samples exhibited an average grain sizes around 4 μm [98]. Sutorik *et al.* used $Mg(OH)_2$ instead of MgO for their alumina rich spinel (n = 2.0, 2.5) and produced pre-sintered body through hot pressing at 1600°C under 20 MPa presure followed by post-HIPing at 1850°C under 200 MPa pressure. The combination of HP+HIP improved the visible transmissions of about 82% with the hardness around 11.0 GPa [99]. Few other trails on reactive sintering achieved moderate transparency lesser than 60% in the visible regions [100 – 101]. Apart from the volume expansion related issues, spinel through reactive sintering require very high sintering temperatures causing exorbitant grain growth to the sizes up to 622 μm [102]. Therefore, the reactive sintered spinel materials generally exhibited poor mechanical properties.

2.2.3.2 Spinel through two-stage process

As mentioned earlier, two-stage process involve synthesizing spinel powders using organo-metal or oxide precursors followed by shaping and sintering for final densification. This section spotlights the processes involving powder synthesis followed by fabrication of transparent spinel components and therefore excludes the methods involving commercial spinel powders though they are classified under two-stage process. The powder synthesis received major attention due to the constant demand of improved, consistent and cost-effective spinel powders alternative to commercial powders. In those aspects, researchers explored several methods such as flame spray pyrolysis [103 – 104], combustion technique [105], Pechini and co-precipitation methods [106], sol-gel of metal alkoxides or inorganic salts [107 – 111] and freeze-drying [112] for the synthesis of high purity and ultrafine spinel powders.

Among these methods, very few processes developed powders suitable for fabricating transparent spinel with appreciable level of optical transparency. For instance, the spinel powder produced through sol-gel method by Cook *et al.* [111] obtained densification through hot pressing at 1550°C under a pressure of 5000 psi. With 1% aid of LiF, the samples exhibited broadband transmissions up to 86% in the visible to IR regions. Balabanov *et al.* produced spinel powders through non-aqueous sol-gel methods. Hot pressing of powders at temperatures around 1600°C under 48 MPa pressure produced transparent spinel with optical transparency around 80% in the IR regions and grain sizes around 40 μm [112 – 115].

2.2.4 Transparent spinel with finer microstructures

Though the fore-mentioned spinel materials exhibited high levels of optical transparency, their moderate mechanical properties due to the coarser microstructures limited their applications in the harsher environments. Moreover, spinel with larger grain sizes exhibited poor thermal shock resistance [116]. Therefore, throughout the evolution of fabricating transparent spinel, a

resurgent interest engendered various research communities for the development of transparent spinel having finer microstructures. Being an emerging material, the information regarding the synthesis of spinel powders for the fabrication of submicron spinel is closely guarded and not available in the open literatures.

Spinel is extremely difficult to sinter at lower temperatures due to (a) low oxygen lattice diffusion, which requires very high densification temperatures, (b) volatilization of Mg/MgO that causes variations in molecular stoichiometry, (c) propensity for grain coarsening due to surface-energy anisotropy and (d) extreme sensitivity to impurities, processing parameters, additives and the size and shape of the components. In spite of all these challenges, investigators explored the possibilities of achieving grain sizes closer or lesser than 1.0 µm.

In this context, Gazza *et al.* reported the fabrication of transparent spinel having sintered grain sizes closer to 1.0 µm [117]. His method comprised vacuum hot pressing of commercial spinel powder of purity above 99.9% and a particle size of about 1.0 µm at a temperature of 1500°C with the pressure of about 6000 psi. The increment in the temperature beyond 600°C until the maximum temperature had a pause at every 50°C for an hour. As per the report, the final samples sintered without any grain growth and retained its grain sizes around 1.0 µm. Lu *et al.* attempted for the same cause and achieved grain sizes around 100nm through high-pressure hot pressing [118]. However, both of the attempts did not provide the expected degree of appreciable transparency.

Tsukuma *et al.* employed finer spinel powder with a particle size of 150 nm supplied by Taimei Chemical Industry, Japan for developing transparent spinel with the expectation of achieving final grain sizes closer to 1 µm. The powder mixed with B_2O_3 of various concentration from 0.005 to 0.5 mass percentages was compacted cold isostatically at 200 MPa and vacuum sintered at 1250°C – 1400°C for 2 hours followed by HIPing at 1300°C under 150 MPa

pressure. The amount of B_2O_3 and the sintering temperature played crucial roles in controlling the microstructure refinement. Eventually, the samples with 0.15% of B_2O_3 exhibited transparency up to 81% in the visible regions. The samples exhibited grain sizes between 1.0 and 2.0 µm, which was much closer to their expected values [119].

Even in the years 2009, the hunt for a consistent high quality spinel powders was continued and the activities continued simultaneously for developing spinel with ultra-fine grain sizes less than 0.5 µm and RIT closer to the theoretical maximum (spinel with these combination of characteristics is hereafter termed as advanced spinel). In this context, Krell *et al.* attempted for developing advanced spinel using three variants of powders. The first investigation employed commercial spinel powders, while the next route utilized in-house produced powders and the third approach involved reactive sintering using high-purity Al_2O_3 powder mixed with MgO powder. The sintered spinel from commercial powders exhibited grain sizes in the range of 0.4 to 0.6 µm with the optical transparency closer to 85%. The next method of employing in-house spinel powders (produced by an undisclosed chemical synthesis) produced sintered spinel with grain sizes further reduced to 0.37 µm with the RIT near to 83%. The hardness of this fine-grained spinel reached to the values up to 15 GPa which is on par with the hardness of single crystal sapphire. The third approach involving reactive sintering demanded the usual high fabrication temperatures (>1500°C) and produced coarse microstructures and transmissions up to 80% [120]

Simultaneously, Goldstein *et al.* improved their earlier process [89] by selecting a coarser spinel powder from Nanocerox, Ann Arbor, MI, having surface area of 30 m^2/g produced by flame pyrolysis technique. The cold isostatically pressed compacts without any sintering additives attained densification above 99% of relative density at temperatures closer to 1400°C. Similar densifications achieved at 1800°C in their earlier attempts due to highly agglomerated starting powders whereas, in their present investigation, the low agglomerated starting powders

explained the earlier densification. Sintered samples of the improved version exhibited grain sizes in the sub-micron regions of dimensions averaged to 0.45 µm. The HIPed samples (1320°C/ 3 hours) at 2mm thickness exhibited high optical transparency having RIT around 80% in the visible region [121]. Further, Goldstein *et al.* reported that the process described by Krell *et al.* [5, 120] was presented in a general manner and do not allow any reproducibility due to the non-disclosure of the nature of processing and the quantity of sintering additives [121].

In another study, Krell *et al.* explored the densification characteristics of spinel powders synthesized through methods such as thermal decomposition of ammonium carbonates, flame spray pyrolysis and thermal decomposition of alum salts. The initial particle size of the powders varied between 53 nm and 120 nm based on the synthesis procedures. Gel casting and cold isostatic pressing processes produced green samples. At the end of their investigations, green samples from flame pyrolysis powders having purity of 99.995% and particle size of 53 nm attained 97% relative density at temperatures as low as 1260°C and the complete densification attained up on HIPing at 1260°C. The HIPed specimens with an average grain size of 340 nm showed transmissions up to 84% in the visible regions. Though the powders through flame spray pyrolysis technique exhibited, the ultimate characteristics of producing transparent spinel having high inline transmissions coupled with ultra-fine microstructures, Krell *et al.* reported that the costs of the powders were exorbitantly high, which was around 3000 % higher than the relative costs of alumina powders of equivalent purities [122]. Spinel powders with such extreme cost does not favor large scale and economical productions.

Consecutively, Mroz *et al.* reported on fabricating transparent spinel with properties equivalent to the values reported by Krell *et al.* The development utilized their undisclosed proprietary process for fabricating transparent spinel with average grain sizes as fine as 370 nm. Their unrevealed process utilized Y_2O_3 as sintering additives for grain refinement. The report

contained no further information regarding the characteristics of the starting powder, shaping and sintering techniques. The samples exhibited transmissions closer to theoretical values (~86 %) in the 3 – 5 µm wavelength regions with the hardness ($HV_{2.5}$) reaching to 16.8 GPa [123].

Few of the investigators [124 – 126], termed their spinel powders highly-reactive or highly-sinterable based on the densification temperatures where they obtain theoretical densities above 98% at temperatures lower than 1600°C. Accordingly, the spinel powder synthesized in this study is termed as highly-reactive as they showed superior sinterable characteristics reaching greater than 98% theoretical densities at temperatures closer to 1400°C.

2.2.4.1 Transparent spinel through exploratory sintering techniques

As mentioned in the earlier sections, the inherent issues in achieving transparency were mostly resolved from the year 1990s and the focus was shifted towards process optimization, cost reduction and improving mechanical properties, mainly through grain size reductions. Accordingly, spinel has been produced by various sintering techniques such as PLS [70 – 71, 127 – 128], HP [72, 75, 111, 129 – 132], HP+HIP [86 – 87, 100 – 101, 133 – 135] and PLS+HIP [5, 87 – 88, 93, 119, 122, 133, 136-137]. Among these techniques, most of the commercial manufacturers employ HP+HIP and PLS + HIP, for their production due to the versatilities of producing larger and complex shape components.

However, few research groups explored the other sintering methods such as SPS [138 – 146], flash sintering [147] and field assisted sintering [94] techniques. In specific, SPS method facilitate faster and pressure assisted densification at relatively lower temperatures leading to finer sintered microstructures compared to other techniques. For instance, Bonnefont *et al.* selected three kinds of spinel powder with surface areas varying between 22 – 31 m^2/g supplied by Baikowski, USA (S30CR, S30XCR and SA30XCR). The average crystallite size of the powders ranged from 50 – 80 nm. The powders attained densification at temperatures around

1300°C with the sintered grain sizes averaged around 250 nm for the grade S30CR and the grain size varied between 350 nm and 450 nm for the grades S30XCR and SA30XCR respectively. The inline transmission varied between 80 – 84% at the wavelength of 2.5 µm and exhibited poor visible transparency due to the existence of pores in the microstructures [143]. Most of the SPS investigations resulted similar fine-grained microstructures with the RIT closer to theoretical values. In spite of having such capacities of producing transparent spinel with superior microstructural characteristics, the inherent deficiencies of SPS related to producing large and complex shaped components limit this technique for commercial productions. Flash and field assisted sintering techniques also exhibit similar shortcomings and therefore limited to the academic exploratory studies.

From the observation after the detailed literature survey, commercial spinel powders played in a major portion of investigations for producing transparent spinel. The inevitable Sulphur contamination and formation of micro opaque spots in the transparent samples is still unresolved from commercial Baikowski powders [148 – 149] and the powders through flame pyrolysis method suffer with exorbitant production costs [122]. Limited investigations report utilization of spinel powders produced through their indigenous undisclosed methods for the manufacturing of transparent spinel with relatively superior physical, mechanical and optical properties [15, 18, 21, 50]. Therefore, the demand persist until today for the powder synthesis methodology to produce highly-reactive spinel powders having superior characteristics such as ultra-high purity above 99.99% and particle sizes ≤ 100nm. It is an added benefit if the spinel powders exhibit high-sinterability at temperatures ≤ 1400°C and show sintered microstructures with submicron grain sizes. The interest will grow further if the powder is produced through scalable and economically feasible processes.

In these aspects, the present study proposes the synthesis of highly-reactive $MgAl_2O_4$ spinel nano powders ($MgO.nAl_2O_3$, $n \approx 1$) through a facile sol-gel process. The powder exhibited

ultrafine particles having size around 20 nm with homogeneous round edged morphology. The compacted green bodies exhibited superior sinterability at temperatures around 1375°C without any assistance of sintering additives. In addition, the sintered + HIPed samples showed the average grain sizes around 500 nm with outstanding inline transmissions up to 84% in the 3 – 5 µm wavelength region. The method involve powder synthesis, shaping of green bodies, sintering, HIPing and their corresponding characterizations in terms of their physical, chemical, microstructural, mechanical and optical properties are presented in detail in chapter 5.

2.3 Transparent Yttria Ceramics

The next material chosen for the present investigation is transparent Y_2O_3 ceramics. Polycrystalline yttrium oxide is another cubic structured, optically isotropic ceramic material exhibiting superior resistance to corrosion, high refractoriness and transparent to electromagnetic radiations from ultra-violet to mid IR regions. Due to such excellent chemical, thermal and optical properties, it is widely used for various applications such as host material for high power lasers and scintillators, envelops for high-intensity-discharge lamps, IR transparent domes and windows [150 – 151]. In addition, transparent Y_2O_3 is an exclusive material exhibiting broader absorption edge relative to other competitive transparent materials such as sapphire, AlON and spinel. The IR transmission limits of Y_2O_3 extends up to 9 µm while the other candidates exhibit transmissions closer to 7 µm. Moreover, the maximum IR transmissions extends up to 6.5 µm for Y_2O_3 ceramics whereas the maximum transmission shoulder drops and absorptions begins at the wavelengths around 4.5 to 5 µm for the rest of the competing materials [152]. For heated domes or windows, these absorptions become emissions that reduce the signal to noise response of the seekers leading to poor image qualities. On the other hand, Y_2O_3 remains transparent beyond 5.0 µm and the heated Y_2O_3 domes do not reradiate into MWIR detectors for the ranges up to 6.5 µm and therefore relatively increase the

acquisition range and produce superior image qualities [153]. These exclusive qualities state Y_2O_3 as a leading candidate for strategic applications.

The fabrication of transparent Y_2O_3 materials starts with the ultra-high purity powders obtained from two major resources. Some approaches produced transparent Y_2O_3 using commercially available powders while the rest have attempted to synthesize their own powders for their investigation. Relatively, the latter method produced Y_2O_3 with consistent and superior transmission properties compared to the former one. However, the second route involved with multiple powder-processing modules comprising appropriate selection of ultra-pure precursors, suitable methodology for producing highly reactive, ultra-pure, single-phase Y_2O_3 powders having extreme inter-particle coordination. Apart from the powder synthesis, the successive processes also require precise control on fabricating homogeneous, defect free green bodies that is sinterable with homogeneous microstructures free from any optical interventions such as pores, impurities and secondary phases [32].

2.3.1 Genesis of development on transparent Y_2O_3

Single crystal transparent Y_2O_3 have been grown by flame fusion method in the early 1960s but relatively in small due to its higher melting temperatures (2410°C) [154]. However, since the material is optically isotropic, the development inclined towards the fabrication of its polycrystalline form in the late 1960s with the Brisette *et al.* producing a partially transparent Y_2O_3 disc through thermo-mechanical hot-forging techniques. The sintered density of the forged samples exceeded above 99% of T.D. exhibiting the Knoop hardness closer to 857 kg/mm^2 [155]. Subsequently, Anderson *et al.* at General electric research laboratory reported the improved version of transparent Y_2O_3 called Yttralox by doping 10% of ThO_2 and sintering at 2200°C. The resulted material containing grain size in the range between 10 – 50 µm exhibited appreciable levels of transparency [156]. Later, Lefever *et al.* fabricated transparent

Y_2O_3 through vacuum press forging at 950°C using liquid assisted sintering using LiF additives. The average grain size of the final material retained around 3 µm and the optical transparency of 1.0 mm thick sample reached to the levels of single crystal Y_2O_3 exhibiting transmissions up to 84% in the 2 – 8 µm wavelength regions. The material showed hardness up to 800 Kg/mm^2 for the Knoop indentation at 100g load [157]. Further, Dutta *et al.* produced transparent Y_2O_3 specimens using commercial Y_2O_3 powders by vacuum hot pressing at a pressure of 5000 – 7000 psi and at temperatures between 1300 – 1500°C without any assistance of sintering additives. The samples exhibited average grain sizes around 1.0 µm with the specular transmissions close to 84% in the 2 – 8 µm regions. The hardness reached the values up to 900 Kg/mm^2 due to the finer grain sizes [158]. Tsukuda *et al.* attempted for a hydrogen sintering approach at temperatures around 2270°C and produced transparent Y_2O_3 without any sintering additives and pressure assistance [159].

Later in 1980s, Rhodes *et al.* synthesized 8 – 12 mol percentage of La_2O_3 doped Y_2O_3 powders through acid dissolution and co-precipitation technique and developed transparent Y_2O_3 using transient solid-state diffusion sintering at temperatures around 2170°C under hydrogen atmosphere. The average grain size of this pressure-less sintered material enlarged above 50 µm due to very high sintering temperatures and showed real inline transparency less than 80% in the 3 – 8 wavelength regions [160].

In the early 1985, Raytheon research divison, U.S.A developed transparent yttria missile domes utilizing sinter + HIP approach to fabricate 100% dense, pre-free ceramics at temperatures around 1700°C. The material produced with and without 0.1 mol % La_2O_3 doping exhibited similar RIT close to 84% in the 2 – 7 µm region [152].

2.3.2 Conventional coarse-grain transparent yttria

Most of the early stage investigations employed sintering at temperatures around 2000°C primarily due to coarser particle size of the starting powders [152]. In the later stages, the orientation of the investigations turned towards promoting densification of Y_2O_3 at relatively lower temperatures. Amongst, many have utilized commercially available Y_2O_3 powders [161 – 163] and the remaining attempted to synthesize their own powders following various techniques such as dissolution of Y_2O_3 powder in acids followed by precipitation and calcination [164 – 166] and precipitation of yttrium salts [167 – 171]. For instance, Mouzan *et al.* employed commercial Y_2O_3 powders of 99.99% purity having average particle sizes below 1 µm. The compacted green samples attained pre-densification at 1600°C in the vacuum atmosphere and the final densification through glass capsuled HIPing at temperatures between 1500°C and 1625°C under 200 MPa pressure. The HIPed specimens of 1.5mm thickness showed transparency up to 40% at 1.0 µm wavelength and contained grain sizes in the range of 150 µm with large volume of residual porosities at the intergranular sites. The powders contained large volume of hard agglomerates, induced heterogeneous nucleation and grain growth, and resulted to inferior densification [162]. He *et al.* utilized commercial nano yttria powders having particle sizes closer to 33 nm and produced green bodies using centrifugal consolidation. The green specimens sintered at 1700°C for 5 hours in vacuum exhibited inline transparency up to 55% at 0.8 µm wavelength at 1.5 mm thickness [163]. Willingham *et al.* evaluated Y_2O_3 powders from three various commercial suppliers with the aim of producing transparent Y_2O_3 at temperatures around 1400°C and obtaining sintered grain sizes close to 1.0 µm. The powders were compacted cold isostatically and sintered at 1650°C in air for 4 hours followed by HIPing at 1650°C at 200 MPa pressures for 4 hours. Out of three powders, one could reach to the levels of moderate transparency and rest remained optically opaque. The sample with moderate transparency also contained large volume of precipitate phases

consisting various impurities. Moreover, the samples exhibited sintered grains averaged to 60 µm, which was considerably larger than their initial goal of achieving grain sizes of 1.0 µm [153]. Eilers *et al.* also initiated his investigations to fabricate transparent Y_2O_3 with the goal of achieving 1µm final sintered grain sizes. Commercial Y_2O_3 powders having 99.95% purity and 30 – 50 nm particle sizes from Inframat Advanced Materials, CT, U.S.A, was used for this purpose. The powders pressed cold isostatically for shaping and sintered at 1600°C – 1700°C in air followed by HIPing at 1650°C at 203 MPa for 6 hours in argon atmosphere. However, their efforts could produce transparent Y_2O_3 with sintered grain sizes around 20 µm with RIT close to 60% at 1.0 µm wavelengths [172]. Jung *et al.* added 3-mol% of ZrO_2 as an oxygen supplier to Y_2O_3 to avoid occurrence of oxygen deficiency during vacuum sintering. The compacts of ZrO_2 added commercial Y_2O_3 powder obtained densification at temperatures around 1750°C followed by post annealing in air at 1250 – 1400°C for 5 hours to obtain optical transparency around 80% in the visible to IR regions [173].

Apart from such investigations involving commercial Y_2O_3 powders, the other approaches employing in-house synthesized powders also produced transparent Y_2O_3 with significant progress in terms of densification compared to the traditional methods. For example, the attempt of Saito *et al.* using their in-house produced carbonate-derived Y_2O_3 powders exhibited improved sinterability at temperatures around 1700°C. As per his approach, the carbonated Y_2O_3 precursor obtained phase purity to cubic Y_2O_3 at 1100° and exhibited particle sizes closer to 1.0 µm. Ammonium sulfate as a surface refiner was employed up to 0.05 wt% during the powder synthesis for the particle to gain round edged morphology. The green compacts attained complete densification at 1700°C, which is relatively lower than most of the above-mentioned traditional methods. The sintered specimens exhibited grain sizes near to 20 µm and optical transparency up to 40% at 1.2 µm wavelengths [167]. Their further investigations using Y_2O_3 powders derived from yttrium hydroxide rather from yttrium carbonate enhanced the

transparency to an extent (values are not discussed). However, the powders produced in this method suffered with Sulphur contaminations up to 50 ppm due to the addition of ammonium sulfate, which impeded the sintered bodies achieving theoretical transparencies [168 – 169].

Huang *et al.* carried out a process similar to Saito *et al.* and investigated the effect of pH of the precipitate on the final particle size and morphology. He concluded that the precipitate at pH 8 produced Y_2O_3 powders with favorable morphology to produce transparent Y_2O_3 at temperatures around 1700°C. The final samples exhibited grain sizes around 30 – 50 µm [174]. Wen *et al.* also followed the footprints of Saito and Huang *et al*. and investigated the effect of striking method during precipitation on the powder morphology. His exercises revealed that the powders produced through normal striking (adding ammonia to yttrium nitrate solution for effecting precipitation) exhibited higher sinterability than the powders derived through reverse striking (adding yttrium nitrate solution to ammonia for precipitation). The samples sintered at 1700°C exhibited grain sizes around 20 µm and RIT closed to 52% at 1.2 µm wavelengths [165].

Mouzon *et al.* investigated the influences of agglomeration of the starting Y_2O_3 powders on the densification and the optical transparency. The initial powders with various status of agglomeration were obtained through several drying techniques such as room temperature drying, freeze-drying, distillation drying etc. The compacted powders attained densification through sinter + HIP approach for obtaining transparency. Eventually, the powders with less agglomeration dried under room temperatures showed optical transparency up to 43% at 0.4 µm wavelengths and their grain sizes varied between 3 and 120 µm. The formation of wide range in grain sizes was probably due to the event of heterogeneous nucleation and grain growth corresponding to the state of agglomeration. In certain cases, the agglomeration induced abnormal grain diffusion leading to the entrapment of pores in the intragranular sites, which caused permanent obstruction for optical transmissions [175].

2.3.3 New generation, fine-grained transparent Y_2O_3

The fore-mentioned developments majorly focused on sintering Y_2O_3 to its theoretical densities and obtaining maximum optical transmissions for which the investigators employed very high sintering temperatures and pressures. These extreme processing environments facilitated to realizing their goals. However, the eventual dense material suffered with poor mechanical properties due to larger sintered grain sizes. Gentilman *et al*. recorded the grain sizes as large as 100 – 150 µm for their transparent Y_2O_3 due to their higher processing temperatures [176].

In the current scenario, there is a great demand for the transparent ceramic dome materials having improved mechanical properties to withstand extreme aerodynamic environments such as rain and sand erosion. Therefore, the current state of the art is fabricating Y_2O_3 with superior mechanical properties by controlling the sintered grain sizes in the submicron regions. By processing Y_2O_3 with ultra-fine, nano starting powders (< 100nm), and carefully controlling the shaping and sintering parameters, it should be possible to control the grain growth and retain the final grain sizes in the submicron levels [5, 121 – 122, 149, 177]. Various investigations explored the possibilities of sintering such high-refractory Y_2O_3 material at temperatures around 1400°C. In this context, Chen *et al*. proposed a two – stage – densification method for sintering Y_2O_3 in air at temperatures lower than the conventional sintering processes. This study investigated the feasibility of obtaining densification by suppressing the grain boundary migration while keeping the grain boundary diffusion active. As per this approach, the green compacts of Y_2O_3 were heated to a higher temperature (1310°C) for few minutes to initiate the grain boundary diffusion and the temperature was drastically reduced to lower levels (1150°C) and held for 20 hours to achieve complete densification without grain growth [178]. This study majorly focused on optimizing sintering mechanism to control the grain sizes and not conducted any studies related to optical transparency.

On the other hand, Serivalsatit *et al.* followed this sintering technique in vacuum for the development of transparent Y_2O_3 by adding post HIPing operations. As per his approach, the samples initially heated to 1500°C and held at that there for few minutes followed by immediate cooling to 1400°C with a dwell for 20 hours. The sintered samples obtained complete densification and transparency while HIPing at 1300°C under 206 MPa pressures [179 – 180]. The HIPed samples exhibited grain sizes around 350 – 400 nm with the optical transparency up to 80% in the 2.0 µm wavelength regions. Though this sintering technique enabled achieving low-temperature densification, the prolonged heating schedules are not energy efficient and economical. Though this technique claimed achieving low-temperature densification, in certain cases, this method showed inconsistency of achieving second-stage densification at lower temperatures [153]. Zhang *et al.* attempted the similar sintering technique in vacuum at relatively higher temperatures in the ranges around 1500 to 1550°C with the hold of 20 hours at peak temperatures for his fabrication and utilized alumina seeds up to 150 ppm to control high temperature grain growth. The alumina particles pinned the grains not to grow beyond the average size of 1.5 µm. The samples after post annealing at 1300°C for 10 hours exhibited transparency around 82% at the wavelengths closer to 1.5 µm [181]

Some researchers employed various additives such as LiF [157, 182], Tm_2O_3 & ZrO_2 & Al_2O_3 [161], La_2CO_3 [166], Er and Yb ions, ZrO_2 & Ho ions, Tm & ZrO_2 [180, 182 – 184] for promoting densifications and reducing sintering temperatures. Though these inclusions improved the densification significantly, in most of the cases, they exhibited numerous optical absorptions in the wavelength region between 0.25 and 8 µm plausibly due to their variance of refractive index with respect to Y_2O_3. These absorption bands considerably enhanced the noise levels and eventually reduced the resolution of the resultant IR image. Other sintering methodologies such as SPS [185 – 187] and hot pressing [188 – 189] were also adapted for obtaining low temperature densification. However, these methodologies are limited for

fabricating flat shapes and not suitable for large-scale productions and fabricating complex shapes such as domes and radomes.

From the above reported literatures, it is apparent that there is a need for an improved process for producing transparent Y_2O_3 ceramics. Accordingly, the present investigation comprises synthesis of highly reactive nano Y_2O_3 powders through a facile sol – gel technique followed by shaping and sintering. The process utilized a straightforward conventional air sintering method, which is economical for producing dense Y_2O_3. The samples exhibited superior densification at temperatures around 1350 – 1400°C. The samples after HIPing at 1400°C exhibited excellent IR transparency in the 2 – 8 μm regions with the high control on retaining sintered grain sizes in the submicron regions. The study on synthesizing Y_2O_3 powders and fabricating transparent Y_2O_3 followed by extensive characterization on their physical, chemical, mechanical and optical properties are presented in detail in chapter 6.

2.4 Aluminum Oxynitride

The current study also selected aluminum oxynitride for investigation and development. Aluminum oxynitride (AlON) is an optically isotropic and relatively a new material added in the group of transparent ceramics. By virtue of the cubic crystallography, it shows inline transmissions up to 86% in the 0.22 and 6 μm wavelength regions. Owing to its excellent optical and mechanical properties, the field of application diverges in various areas such as bullet-proof armors, windows for super market scanners, IR windows and domes, laser windows, ceramic semiconductors, ceramic lamp envelops and low-cost substitute for sapphire [190 – 191]. AlON exhibits 13 polytypoid forms with respect to various concentrations of AlN and exist as a single-phase γ – AlON with the reactions between Al_2O_3 and 28 – 40 mol % of AlN at temperatures above 1700°C form single phase [192].

2.4.1 A brief history on the evolution of AlON

In 1946, Yamaguchi *et al.* observed the formation of spinel structure for Al_2O_3 system thermally stabilized above 1000°C [193]. A detailed study on this polymorph during 1960s revealed that the stabilization of spinel was due to the inclusions of nitrogen atoms in the structures of Al_2O_3 [194]. In these periods, Adams *et al.* [195] and Long *et al.* [196] also reported various characteristics of oxynitride forming in the Al_2O_3 and AlN systems. However, major interest on AlON compounds was emerged with the report on fabricating SiAlON based ceramics [197]. Later in 1979, McCauley et al reported the first dense AlON specimen with possible traces of transparency. Their detailed investigations on phase relations and sintering behavior of AlON in the Al_2O_3 and AlN system showed that the cubic γ – AlON phase is compositionally centered at $\approx$ 35.7 mol % of AlN, which is equivalent to the molecular stoichiometry of 9 Al_2O_3 and 5 AlN [198 – 199]. These initial outcomes attracted Raytheon Company to have collaboration with James. W. McCauley to improve the processing and fabricating cubic AlON with high degree of transparency. Thereafter, Raytheon worked on the development on AlON for the next two decades and produced large AlON windows of sizes around 4" X 10"with superior transparency. In the year 2002, Surmet Corporation received the license from Raytheon and currently producing AlON windows on commercial scales [200].

2.4.2 Processing routes of AlON

Hitherto, AlON has been produced majorly through two approaches such as reactive sintering and two-stage sintering. The former method involve mixing of AlON precursors such Al_2O_3 and AlN powders at appropriate molecular proportions followed by compaction and sintering in a single firing process whereas the latter involve synthesizing AlON powders in the first thermal treatment followed by shaping of AlON powders and densification in the second heat treatment [201]. In most of the cases, the formation of single-phase γ – AlON follows the

solid-state reactions between Al_2O_3 and AlN at temperatures between 1700°C and 1800°C from the following reaction.

$9\ Al_2O_3 + 5\ AlN \rightarrow Al_{23}O_{27}N_5$ ---------- (1)

2.4.2.1 Reactive sintering of AlON

As mentioned above, the method of fabricating AlON through reactive sintering pursue simultaneous phase formation and densification. The first specimen of transparent AlON was fabricated by mixing $\gamma - Al_2O_3$ and 30 mol % AlN powders in ethanol medium followed by compaction and reactively sintered at temperatures around 2000°C in a flowing nitrogen atmosphere [198]. Similar exercise conducted by Willems *et al.* at 1850°C under 3.0 bar nitrogen pressures produced translucent AlON materials [202]. Cheng *et al.* explored the possibilities of coupling microwave energy for the synthesis of AlON from 67.5 mol % Al_2O_3 and 33.5 mol% AlN. His studies derived AlON phase at 1650°C. The samples attained 82 % of T.D. at these temperatures. Their further trails at temperatures around 1800°C improved the densification to reach the sintered density closer to 99.4% of T.D. [203 – 204]. Patel *et al.* induced transient liquid phase in the reactive sintering by increasing the sintering temperatures beyond the solidus line, which is about 1950°C to 2050°C to form a fraction of liquid phase of AlON for assisting densification [205]. Kumar *et al.* investigated the reactive sintering of AlON fabricated through aqueous colloidal forming techniques. As per their approach, the initial precursors such as Al_2O_3 and AlN powders went through a surface passivation procedure followed by shaping and densification at temperatures around 1950°C [201, 206]. Miller *et al.* also employed aqueous forming routes for shaping requisite mixture Al_2O_3 and AlN. They utilized the hydrolysis reactions of AlN for the solidification of green shapes and produced dense AlON samples through reactive sintering [207].

All these reactive sintering methods produce 100% phase pure γ – AlON at temperatures above 1600°C. However, in most of the cases, this route could not produce 100% dense AlON. Moreover, the sintered microstructures contained pores at both inter and intragranular sites. The plausible reason for this phenomenon is due to occlusion of Al_2O gas that is evolving from Al_2O_3 during the reduction reaction between alumina and AlN for forming AlON phase. Bandhyopadhyay *et al.* observed such volatile compounds of Al_2O_3 at temperatures above 1600°C under reduced atmospheric conditions [208]. Corbin *et al.* also observed such evolution of Al_2O vapors according to the following reactions [209].

$$Al_2O_{3\,(s)} + 2C_{\,(s)} \rightarrow Al_2O_{\,(g)} + 2CO \qquad \text{---------- (2)}$$

$$Al_2O_{3\,(s)} + Al_{\,(l)} \rightarrow 3\,Al_2O_{\,(g)} \qquad \text{---------- (3)}$$

Moreover, the occlusion of pores in the microstructure would occur if the rate of pore mobility were lesser than the rate of grain mobility during the event of reactive sintering and subsequent grain growth [207]. Though the entrapment of gas species due to the consequence of grain mobility may be controlled by manipulating the sintering schedules, the event of gas formation is still critical to put under control, as it is associated with the phase formation of AlON. The incidents of gas evolution and subsequent pore formations in the reactive sintering process are detrimental for obtaining completely dense, transparent AlON as they act as scattering sites for transmission of light. Therefore, most of the investigations on fabricating transparent AlON followed two-stage process of synthesizing AlON powders at temperatures between 1600°C and 1800°C in the first stage followed by milling of AlON powders, shaping and sintering in the second stage. In this route, the volatile gases such as Al_2O and CO have the scope to escape during the first stage of calcination and hence produce pore free microstructures in the successive heat treatments.

2.4.2.2 Synthesis of AlON powders

Investigators adapted various synthesis routes such as solid-state reactions, reduction etc. for producing single-phase γ – aluminum oxynitride powders for the fabrication of transparent AlON.

2.4.2.2.1 Carbothermal nitridation process

For instance, Gentilman *et al*. produced AlON powders through carbothermal nitridation technique by reacting γ– Al_2O_3 with carbon at 1550°C and 1850°C. As per this process, part of Al_2O_3 reacts with carbon produce AlN as an intermediate compound, which would further reacts with the remaining Al_2O_3 for forming the final AlON phase [210]. Rafaniello *et al.* followed the similar carbothermal nitridation technique and used α – Al_2O_3 and AlN as starting precursors [211]. Yawei *et al.* attempted for producing AlON at temperatures lower than its usual phase forming temperatures through carbothermal nitridation reaction of gibbsite and carbon black. A small proportion of MgO was used as a phase stabilizer to protect the AlON phase that was formed as an intermediate phase at temperatures around 1400 to 1600°C [212]. Ma *et al.* synthesized AlON powders through wet chemical processing using three variants of precursors of Al_2O_3 such as γ– Al_2O_3, Al $(OH)_3$ and ammonium aluminum carbonate hydroxide. These precursors were mixed with carbon black through direct mixing for the case of γ– Al_2O_3 and through co-precipitation for the cases of the remaining precursors. These mixtures were calcined at 1600°C to 1800°C for the carbothermal nitridation reactions to form AlON phase [213]. Apart from the selection of various precursors of Al_2O_3 investigation were carried out using various precursors of carbon as well for synthesizing AlON through carbothermal nitridation technique [214 – 219]. Regardless of employing various precursors of Al_2O_3 and carbon, the AlON powders derived through carbothermal nitridation technique

suffered with residual carbon contaminations [219 – 220]. Therefore, few other approaches were also explored for synthesizing AlON powders without utilizing carbon precursors.

2.4.2.2.2 Alumino – thermic reduction process

For example, Zhou *et al.* employed the mixture of 89% of γ – Al_2O_3 and 11% aluminum powders and calcined at 1800°C for 3 hours in the nitrogen atmosphere for the synthesis of AlON powders. The aluminum powders reduced to form AlN and further reacted with Al_2O_3 for the conversion of AlON phase [221]. Wang *et al.* followed similar technique for synthesizing their AlON powders and produced relatively superior in quality in terms of purity and phase [222]. Ruan *et al.* conducted identical exercise but in the atmosphere containing nitrogen and carbon monoxide mixtures and produced AlON powders in the whisker morphology [223]. Zientara *et al.* induced SHS reactions in the aluminum powders to react with α – Al_2O_3 for forming AlON particles having chain – like morphology [224]. Xidong *et al.* utilized aluminum powders as the reducing agent in their raw mix of Al_2O_3 and AlN powders and produced AlON powders at 1800°C in a flowing N_2 atmosphere [225].

2.4.2.2.3 Novel synthesis methods

Apart from the above – mentioned approaches, synthesis of AlON powders followed few novel methods as well. For instance, Labbe synthesized AlON powders using solid-state reactions between Al_2O_3 and BN powders at temperatures around 1700 – 1900°C in the argon atmosphere [226]. Another attempt on synthesizing AlON phase through chemical vapor deposition techniques produced non-stoichiometric AlON thin films [227]. Likewise, Fukuyama *et al.* explored the plasma arc melting technique to melt the precursors at high temperatures for forming AlON phase followed by quenching to obtain the powders [228]. However, this rapid technique found ineffective for producing powders in bulk quantities and

in certain cases borne inhomogeneous AlON powders mixed with residual Al_2O_3 and nitride phases [229 – 230].

2.4.2.2.4 Solid – state reactions between Al_2O_3 and AlN

Among the various methodologies of synthesizing γ – AlON powders, most of the studies employed solid-state reactions between Al_2O_3 and AlN due to various factors such as process simplicity, commercial availability of ultra – high pure Al_2O_3 and AlN precursors and formation of stoichiometric γ – AlON with minimum contaminations.

For example, Gentilman *et al.* used the mixtures comprising 63 – 70 mol % of α – Al_2O_3 and 37 – 30 mol% of AlN powders. The homogenously mixed powder was calcined at 1600 – 1750°C to form single-phase γ – AlON powder [231 – 232]. Many researchers for synthesizing AlON powders followed the alike footprints [233 – 234]. Bechelard *et al.* replaced a small proportion of α – Al_2O_3 with transition Al_2O_3 such as γ – Al_2O_3 and mixed with AlN to produce γ – AlON powders. The addition of transition Al_2O_3 intended for producing relatively softer granules of AlON after calcination [235].

In most of the procedures followed for synthesizing AlON, environmentally hazardous, non-aqueous liquids such as ethanol, isopropyl alcohol etc. were the medium used for mixing Al_2O_3 and AlN powders due to the hydrolysis tendency of AlN in aqueous medium. AlN reacts with water and disintegrate into its hydrolyzed compounds such as Al OOH and Al $(OH)_3$ through following reactions.

AlN reacts with water and converts into AlOOH, Al $(OH)_3$ and NH_3 compounds according to the following reactions:

$AlN + 2H_2O \rightarrow AlOOH + NH_3$ ---------- (4)

$NH_3 + H_2O \rightarrow NH_4^+ + OH^-$ ---------- (5)

$AlOOH + H_2O \rightarrow Al(OH)_3$ ---------- (6)

Such reactions collapse the molecular stoichiometry between Al_2O_3 and AlN and hinder the formation of single γ – AlON. Therefore, none of the investigators employed aqueous medium for synthesizing AlON powders using Al_2O_3 and AlN precursors. A recently reported sol – gel methodology also utilize acetonitrile and chloroform as solvents for synthesizing AlON powders [236].

Understanding the environmental hazards involved in the usage of non-aqueous liquids, in the present study, an attempt has been made to produce γ – AlON powders using the precursors processed through a simple aqueous sol-gel route. Appropriate quantities of Aluminum Nitride (AlN) powder and aqueous boehmite sol were mixed to obtain molecular stoichiometry of AlON. However, during the course of processing, AlN powders reacted with the aqueous boehmite sol and disintegrated into its hydrated compounds. Such reactions altered the initial molecular stoichiometry between boehmite and AlN formulated for the eventual AlON phase formation. Extensive investigations were carried out to analyse the behaviour of AlN during the sol-gel processing. Hydrolysis of AlN in the aqueous sol-gel medium was circumvented by subjecting AlN to a surface modification process. The homogeneously dispersed boehmite sol and AlN mixture was further gelled, dried, and heat treated at temperatures between 1600°C and 1850°C for the formation of AlON powder. AlON phase formation was confirmed through XRD investigations, and its physical and microstructural properties were also evaluated through FESEM and TEM analyses.

AlON powders produced through this technique are comparatively economical. This is because the source of Al_2O_3 utilized in this process is less expensive than the commercially available high pure Al_2O_3 powders, which were generally used in most of the existing AlON processing methods. Perhaps for the first time, AlON precursors were successfully processed through

aqueous sol-gel procedures and the AlON powders were eventually synthesized with an average particle size in the submicron region. This process is suitable for producing AlON powder in bulk quantities, and it can be used readily for further processes such as shaping and sintering to produce various optical products based on AlON. The complete investigations on producing AlON powders through the novel sol – gel method followed by the fabrication of transparent AlON are detailed in chapter 7.

References

1. R. L. Coble, Transparent alumina and method of preparation, U. S. Pat. No. 3026210, Mar 20, 1962.
2. A. Muta, G. Toda, T. Noro, and C. Yamazaki, Use of Yttria – Magnesia mixtures to produce highly transparent sintered alumina bodies, U. S. Pat. No. 3711585, Jan 16, 1973
3. A. Krell, and E. Strassburger, High purity submicron α – alumina armor ceramics: design, manufacture and ballistic performance, Ceram. Transactions: In proceeding of the ceramic armor materials by design symposium., 134 (2001) 463 – 471
4. E. Strassburger, Ballistic testing of transparent armor ceramics, J. Eur. Ceram. Soc.,29 (2009) 267–273
5. A. Krell, J. Klimke, and T. Hutzler, Advanced spinel and sub - µm Al_2O_3 for transparent armor applications, J. Eur. Ceram. Soc.29 (2009) 275 - 281
6. A. Krell, T. Hutzler, and J. Klimke, Transmission physics and consequences for material selection, manufacturing and applications, J. Eur. Ceram. Soc. 29 (2009) 207 – 221
7. D.T. Jiang, D. M. Hulbert, U. A. Tamburini, T. Ng, D. Land, and A. K. Mukherjee, Optically transparent polycrystalline Al_2O_3 produced by spark plasma sintering, J. Am. Ceram. Soc.91 (2008) 151 – 154

8. A. Krell, P. Blank, H. Ma, T. Hutzler, and M. Nebelung, Processing of high – density sub micrometer Al_2O_3 for new applications, J. Am. Ceram. Soc.86 (2003) 546 - 553
9. J. Cheng, D. Agarwal, and R. Roy, Method and apparatus for the preparation of transparent alumina ceramics by microwave sintering, U. S. Pat. No. 6812441 B2, Nov 2, 2004.
10. M. V. Parish, M. R. Pascucci, J. J. Gannon and D. C. Harris, Strength characteristics of transparent alumina and spinel ceramics, pp. 101790G-1 – 101790G-9 in Window and dome technologies XV, Vol.10179, Proceedings of SPIE, Edited by Brian J. Zelinski., *et al*. SPIE—The International Society for Optical Engineering, 2017
11. J. F. Greber, H. Melas, Method for the manufacture of transparent aluminum oxide ceramic, U. S. Pat. No. 4952539, Aug 28, 1990
12. I. Amato, F. Baudrocco and D. Martorana, Evaluation of freeze-drying and spray drying processes for preparing transparent alumina, Mater. Sci. Engg. 26 (1976) 73 – 78
13. G.C. Wei and W. H. Rhodes, Method of making translucent alumina articles, U. S. Pat. No. 4948538 (1990)
14. G. C. Wei and W. H. Rhodes, Sintering of translucent alumina in nitrogen – hydrogen gas atmosphere, J. Am. Ceram. Soc. 83 [7] (2000) 1641 – 1648
15. Y. Qiuhong, Z. Zhijiang, X. Jun and Z. Hongwei, Effect of L_2O_3 on microstructure and transmittance of transparent alumina ceramics, J. Rar. Ear. 24 (2006) 72 – 75
16. G. Mie, “Beitrage zur optic truber meiden, spezeill kolloidaler metallosungen, Ann. Phys. 330 [3] (1908) 377 – 445
17. I. Yamashita, H. Nagayamma and K. Tsukuma, Transmission properties of translucent polycrystalline alumina, J. Am. Ceram. Soc. 91 [8] (2008) 2611 – 2616
18. J.G.J. Peelen, Transparent hot – pressed alumina I: Hot pressing of alumina, Ceram. Inter. 5 (1979) 70 – 75

19. J.G.J. Peelen, Transparent hot – pressed alumina II Transparent Vs Translucent alumina, Ceram. Inter. 5 (1979) 115 – 119
20. H. C. Van de Hulst, Light scattering by small particles, Pp. xiii, 470 (Wiley, New York, 1957)
21. M. Kerker, The scattering of light and other electromagnetic radiation, Vol 16 in Physical Chemistry: A series of monograph (Academic, New York, 1969)
22. J.G.J. Peelen, and R. Metselaar, Light scattering by pores in polycrystalline materials: Transmission properties of alumina, J. Appl. Phys. 45 (1974) 216 – 220
23. H. Mizuta, K. Oda, Y. Shibasaki, M. Maeda, M.Machida, and K. Ohshima, Preparation of high strength and translucent alumina by hot isostatic pressing, J. Am. Ceram. Soc.75 (1992) 469 - 473
24. O. H. Kwon, C. S. Nordahl, and G. L. Messing, Sub micrometer transparent alumina by sinter forging seeded $\gamma - Al_2O_3$ powders, J. Am. Ceram. Soc.78 (1995) 491 – 494
25. M. Kumagai, and G. L. Messing, Enhanced densification of boehmite sol – gels by α – alumina seeding, Comm. Am. Ceram. Soc. (1984) C-230 – 231
26. M.Kumagai, and G. L. Messing, Controlled transformation and sintering of a boehmite sol – gel by α – alumina seeding, J. Am. Ceram. Soc. 68 (1985) 500 – 505
27. A. Krell, Improved hardness and hierarchic influences on wear in submicron sintered alumina, Mater. Sci. Engg. A 209 (1996) 156 – 163
28. A. Krell, P. Obenaus, Grain shape in sintered submicrometer alumina, J. Eur. Ceram. Soc. 18 (1998) 1 – 13
29. H. Ma and A. Krell, Synthesis and processing of Nano – α – Al_2O_3 powders, Key Engg. Mater. 206 – 213 (2002) 43 – 46

30. A. Krell, T. Hutzler and J. Klimke, Presentation on "Transparent armor: sintered Al_2O_3 Vs cubic materials" at specialist meeting AVT-122: Nanomaterials technology for military vehicle structural applications, Granada, Oct, 2005

31. A. Krell, T. Hutzler and J. Klimke, NATO – OTAN - nano materials technology for military vehicle applications, report entitled "Physics and technology of transparent ceramic armor: sintered Al_2O_3 Vs cubic materials", (2006) 14-1 – 14-10 http://www.dtic.mil/get-tr-doc/pdf?AD=ADA469603

32. A. Krell and J. Klimke, Effects of the homogeneity of particle coordination on solid-state sintering of transparent alumina, J. Am. Ceram. Soc. 89 (2006)1985 – 1992

33. J. Echeberria, J. Tarazona, J.Y. He, T. Butler and F. Castro, Sinter-HIP of α-alumina powders with sub-micron grain sizes, J. Eur. Ceram. Soc. 22 (2002) 1801 – 1809

34. R. M. Laine, J. C. Marchal, H. P. Sun and X. Q. Pan, Nano-α- Al_2O_3 by liquid-feed flame spray pyrolysis, Nat. Lett. 5 (2006) 710 – 712

35. D.Godlinski, M. Kuntz, and G. Grathwohl, Transparent alumina with sub micrometer grains by float packing and sintering, J. Am. Ceram. Soc.85 (2002) 2449 –2456

36. J. Cheng, D. Agarwal, Y. Zhang, and R. Roy, Microwave sintering of transparent alumina, Mater. Lett. 56 (2002) 587 – 592

37. R. Apetz, and M. P. B. Van Bruggen, Transparent alumina; a light scattering model, J. Am. Ceram. Soc. 86 (2003) 480– 486

38. A. Krell, P. Blank, H.Ma, and T. Hutzler, Transparent sintered corundum with high hardness and strength, J. Am. Ceram. Soc.86 **(**2003) 12–18

39. A. Krell, G. Baur, and C. Dahne, Transparent sintered sub - µm Al_2O_3 with IR transmittivity equal to sapphire; pp. 199 – 207 in Window and dome technologies VIII, Vol.5078, Proceedings of SPIE, Edited by Randal.W. Tustiston., *et al.* SPIE—The International Society for Optical Engineering, Orlando, 2003

40. L. Qi, J. Shen and W. Pan, The influence of sintering process on the microstructure of submicron alumina fabricated by gel casting, Key. Engg. Mater. 336 – 338 (2007) 1185 – 1187
41. A. Krell, T. Hutzler and J. Klimke, Transmission physics and consequences for materials selection, manufacturing and applications, J. Eur. Ceram. Soc. 29 (2009) 207 – 221
42. T. S. Suzuki, Y. Sakka and K. Kitazawa, Orientation amplification of alumina by colloidal filtration in a strong magnetic field, Adv. Eng. Mater. 3 (2001) 490 – 492
43. X. Mao, S. Wang, S. Shimai and J. Guo, Transparent, polycrystalline alumina ceramics with oriented optical axes, J. Am. Ceram. Soc. 91 [10] (2008) 3431 – 3433
44. B. G. Guillaume, S. Christophe, Sintered alumina product transparent to infrared radiation and in the visible region, U.S. Pat. No. 2009/0137380 A1, May 28, 2009
45. M. V. Parish, M. R. Pascucci, W. H. Rhodes, Polycrystalline alumina articles and methods of manufacture, U.S. Pat. No. 2010/0025896 A1, Feb, 2010
46. P. Biswas, M. Kiran Kumar, K. Rajeswari, R. Johnson and U.S. Hareesh, Transparent sub-micrometer alumina from lanthanum oxide doped common grade alumina powder, Ceram. Inter. 39 (2013) 9415–9419
47. K. Drdlikova, K. Maca, M. Slama and D. Drdlik, Transparent alumina ceramics: Effect of standard and plasma generated approaches in colloidal processing, J. Am. Ceram. Soc. (2019) https://doi.org/10.1111/jace.16630 , 01 – 08
48. D. Drdlik, K. Drdlikova, H. Hadraba and K. Maca, Optical, mechanical and fractographic response of transparent alumina ceramics on erbium doping, J. Eur. Ceram. Soc. (2019) http://dx.doi.org/10.1016/j.jeurceramsoc.2017.02.043, 01 – 06
49. M. V. Parish, Polycrystalline alumina for advanced infrared windows and domes, Ceranova corporation, NAVAIR public release 09 – 1234, page 1 – 6

50. S. H. Risbud, C. H. Shan, A. K. Mukherjee, M. J. Kim, J. S. Bow and R. A. Holl, Retention of nanostructure in aluminum oxide by rapid sintering at 1150°C, J. Mater. Res. 10 (1995) 237 – 239

51. L. A. Stanciu, V. Y. Kodash and J. R. Groza, Effects of heating rate on densification and grain growth during field-assisted sintering of α - Al_2O_3 and $MoSi_2$ powders, Metall. Mater. Trans. 32 A (2001) 2633 – 2638

52. G. D. Zhan, J. Kuntz, J. Wan, J. Garay and A. K. Mukherjee, Alumina based nano composites consolidated by spark plasma sintering, Scripta Mater. 47 (2002) 737 – 741

53. Z. Shen, M. Johnsson, Z. Zhao and M. Nygren, Spark plasma sintering of alumina, J. Am. Ceram. Soc. 85 (2002) 1921 – 1927

54. Y. Zhou, K. Hirao, Y. Yamauchi and S. Kanzaki, Densification and grain growth in pulse electric current sintering of alumina, J. Eur. Ceram. Soc. 24 (2004) 3465 – 3470

55. B. N. Kim, K. Higara, K. Morita, and H. Yoshida, Spark plasma sintering of transparent alumina, Scripta Mater. 57 (2007) 607 – 610

56. B. N. Kim, K. Higara, K. Morita and H. Yoshida, Effect of heating rate on microstructure and transparency of spark-plasma-sintered alumina, J. Eur. Ceram. Soc. 29 (2009) 323 – 327

57. B. N. Kim, K. Higara, K. Morita, H. Yoshida, T. Miyazaki, and Y. Kagawa, Microstructure and optical properties of transparent alumina, Acta Mater. 57 (2009), pp. 1319 – 1326

58. D.T. Jiang, D. M. Hulbert, U. A. Tamburini, T. Ng, D. Land, and A. K. Mukherjee, Optically transparent polycrystalline Al_2O_3 produced by spark plasma sintering, J. Am. Ceram. Soc.91 (2008) 151 – 154

59. Y. Aman, V. Garnier, and E. Djurado, Influence of green state processes on the sintering behavior and the subsequent optical properties of spark plasma sintered alumina, J. Eur. Ceram. Soc. 29 (2009) 3363 – 3370

60. D. Chakravarty, and G. Sundararajan, Effect of applied stress on IR transmission of spark plasma – sintered alumina, J. Am. Ceram. Soc. 93 (2010) , 951 – 953
61. X. Jin, L. Gao, and J. Sun, Highly transparent alumina spark plasma sintered from common – grade commercial powder: The effect of powder treatment, J. Am. Ceram. Soc. 93 (2010) 1232 – 1236
62. L. Lallemant, G. Fantozzia,V. Garniera and G. Bonnefonta, Transparent polycrystalline alumina obtained by SPS: Green bodies processing effect, J. Eur. Ceram. Soc. 32 (2012) 2909–2915
63. S. Grasso, H. Yoshida, H. Porwal, Y. Sakka and M. Recce, Highly transparent α – alumina obtained by low cost high pressure SPS, Ceram. Inter. 39 (2013) 3243 – 3248
64. B. Ratzker, A. Wanger, M. Sokol, S. Kulabukhov and M. P. Dariel, Optical and mechanical properties of transparent alumina fabricated by high-pressure spark plasma sintering, J. Eur. Ceram. Soc. 39 (2019) 2712 – 2719
65. I. Reimanis and H. K. Kleebe, A review on the sintering and microstructure development of transparent spinel ($MgAl_2O_4$), J. Am. Ceram. Soc., 92 (2009) 1472 – 1480
66. A. Goldstein and A. Krell, Transparent ceramics at 50: progress made and further prospects, J. Am. Ceram. Soc., 99 (2016) 3173 – 3197
67. L. Navias, Preparation and properties of spinel made by vapor transport and diffusion in the system $MgO\text{-}Al_2O_3$, J. Am. Ceram. Soc., 44 (1960) 434 – 446
68. D. C. Harris, History of development of polycrystalline optical spinel in the U. S., SPIE, 5786 (2005) 1 – 22
69. D. M. Chay, H. Palmour III, and W. W. Kreigel, Microstructure and room temperature mechanical properties of hot-pressed magnesium aluminate as described by quadratic multivariable analysis, J. Am. Ceram. Soc., 51 (1968) 10-16

70. A. Gatti, Development of a process for producing transparent spinel bodies, Final report contract N00019-69-C-0133, General electric co, Space division, Philedelphia, Pennsylvania, September 1969

71. R.J. Bratton, Translucent sintered $MgAl_2O_4$, J. Am. Ceram. Soc. 57 (1974) 283 – 286

72. D. W. Roy and J. L. Hastert, Method of manufacturing a transparent ceramic body, U.S. Pat. No. 3974249 – 264/ 65 (1976)

73. R. L. Gentilman, Fusion-Casting of Transparent Spinel, Am. Ceram. Soc. Bull. 60 (1981) 906-909

74. E. A. Maguire Jr. and R. L. Gentilman, Press Forging Small Domes of Spinel, Am. Ceram. Soc. Bull, 60 (1981) 255 – 256

75. D. W. Roy and J. L. Hastert, "Polycrystalline $MgAl_2O_4$ spinel for high temperature windows, Ceram. Engg. Sci. Proc., 4 (1983) 502 – 509

76. D. W. Roy and K. E. Green, "Transparent $MgAl_2O_4$ Spinel, A Broad Band Window Materials for Offensive Environments," Proc. SPIE, 1112 (1989) 2 – 8

77. M. E. Thomas, R. L. Joseph, and W. J. Tropf, Infrared Properties of Sapphire, Spinel and Yttria as a Function of Temperature, SPIE, 683 (1986) 41 – 48

78. T. M. Hartnett and R. L. Gentilman, Optical and mechanical properties of highly transparent spinel and AlON domes, Proc. SPIE, 505 (1984) 15-22

79. W. W. Ho, "Millimeter-Wave Dielectric Properties of Infrared Window Materials," Proc. SPIE, 750 (1987) 161-165.

80. C. M. Freeland, "High Temperature Transmission Measurements of IR Window Materials," Proc. SPIE, 929 (1988) 79 – 86.

81. A. Ghosh, K. W. White, M. G. Jenkins, A. S. Kobayashi, and R. C. Bradt, "Fracture Resistance of a Transparent Magnesium Aluminate Spinel," J. Am. Ceram. Soc. 74, (1991) 1624 – 1630.

82. M. L. Huckabee, M. J. Paisley, R. L. Russell, and H. Palmour III, RCS–Taking the Mystery Out of Densification Profiles, Am. Ceram. Soc. Bull. 73 (1994) 82-86

83. J. A. Cox, D. Greenlaw, G. Terry, K. McHenry, and L. Fielder, Infrared and Optical Transmitting Materials, SPIE, 683 (1986) 49 – 62

84. M. C. L. Patterson, D. W. Roy, and G. Gilde, Improvements in Optical Grade Spinel; Ninth DoD EM Windows Symposium, May 2002, Huntsville, AL.

85. G. R. Villalobos, J. S. Sanghera, and I. D. Aggarwal, Degradation of magnesium aluminum spinel by lithium fluoride sintering aid, J. Am. Ceram. Soc., 88 (2005) 1321–1322

86. G. Gilde, P. Patel, and P. Patterson, Evaluation of hot pressing and hot isostatic pressing parameters on the optical properties of spinel, J. Am. Ceram. Soc., 88 (2005) 2747–2751

87. A. A. DiGiovanni, L. Fehrenbacher, D. W. Roy, Hard transparent domes and windows from magnesium aluminate spinel, Window and Dome Technologies and Materials IX, Proc. SPIE, 5786, 56–63 (2005).

88. T. J. Mroz, T. M. Hartnettb, J. M. Wahlb, L. M. Goldmanb, J. Kirschc, and W. R. Lindbergd, "Recent advances in spinel optical ceramic", Window and Dome Technologies and Materials IX, Proc. SPIE, 5786, 64 – 70 (2005)

89. A. Goldstein, A. Goldenberg, Y. Yeshurun and M. Hefetz, "Transparent $MgAl_2O_4$ spinel from a powder prepared by flame spray pyrolysis", J. Am. Ceram. Soc., 91 (2008) 4141–4144

90. P. Biswas, K. Rajeswari, P. Ramavath, R. Johnson and H. S. Maiti, Fabrication of transparent spinel honeycomb structures by methyl cellulose–based thermal gelation processing, J. Am. Ceram. Soc., 96 (2013) 3042–3045

91. I. Ganesh, A Review on Magnesium Aluminate ($MgAl_2O_4$) Spinel: Synthesis, Processing, and Applications, Int. Mater. Rev., 58 (2013) 63–112

92. A. D. Mazzoni, M. A. Sainz, A. Caballero, and E. F. Aglietti, Formation and Sintering of Spinels ($MgAl_2O_4$) in Reducing Atmospheres, Mater. Chem. Phys. 78 (2002) 30 –37

93. M. Shimada, T. Endo, T. Saito and T. Sato, "Fabrication of transparent spinel polycrystalline materials", Mater. Lett. 28 [4] 413–415 (1996)

94. N. Frage, M. Dariel, S. Meir and S. Kalabuchov, "Single-stage thermal process for manufacturing transparent sintered spinel", U.S. Pat. No 2009/ 0297851 A1, Dec 3, (2009)

95. A. Krell, K. Waetzig and J. Klimke. Influence of the structure of $MgO{\cdot}nAl_2O_3$ spinel lattices on transparent ceramics processing and properties. J. Eur. Ceram. Soc. 32 (2012) 2887 – 2898.

96. L. Esposito, A. Piancastelli and P. Miceli, A thermodynamic approach to obtaining transparent spinel ($MgAl_2O_4$) by hot pressing. J. Eur. Ceram. Soc. 35 (2015) 651-661

97. D. Han, J. Zhang and P. Liu, Effect of polymorphism of Al_2O_3 on the sintering and microstructure of transparent $MgAl_2O_4$ ceramics. Opt. Mater. 71 (2017) 62-65.

98. D. Han, J. Zhang, P. Liu, G. Li and S. Wang, Densification and microstructure evolution of reactively sintered transparent spinel ceramics, Ceram. Inter. 44 (2018) 11101 – 11108

99. A. C. Sutorik, C. Cooper and G. Gilde, Visible light transparency for polycrystalline ceramics of $MgO.2Al_2O_3$ and $MgO.2.5Al_2O_3$ spinel solid solutions, J. Am. Ceram. Soc. 96 (2013) 3704 – 3707

100. A. F. Dericioglu and Y. Kagawa, "Effect of the Grain Boundary Micro-cracking on the Light Transmittance of Sintered Transparent $MgAl_2O_4$, J. Eur. Ceram. Soc., 23 (2003) 951–959

101. A. F. Dericioglu, A. R. Boccaccini, I. Dlouhy, and Y. Kagawa, Effect of Chemical Composition on the Optical Properties and Fracture Toughness of Transparent Magnesium Aluminate Spinel Ceramics, Mater. Trans. 46 (2005) 996–1003

102. K. Waetzig and A. Krell, The effect of composition on the optical properties and hardness of transparent Al-rich MgO. n Al_2O_3 spinel ceramics, J. Am. Ceram. Soc., 99 (2016) 946–953

103. C. R. Bickmore, K. F. Waldner, D. R. Treadwell and R. M. Laine, Ultrafine spinel powders by flame spray pyrolysis of magnesium aluminum double alkoxide, J. Am. Ceram. Soc. 79 (1996) 1419 – 1423

104. A. Goldstein, A. Goldenberg, Y. Yeshurun and M. Hefetz, Transparent $MgAl_2O_4$ spinel from a powder prepared by flame spray pyrolysis, J. Am. Ceram. Soc., 91 (2008) 4141–4144

105. C. T. Mathew, S. Solomon and J. K. Thomos, Structural, optical and vibrational characterization of infrared – transparent nanostructured $MgAl_2O_4$ synthesized by a modified combustion technique, Mater. Tod. Proc. 2 (2015) 954 – 958

106. J. Rufner, D. Anderson, K.Benthem and R. H. R. Castro, Synthesis and sintering behavior of ultrafine (<10 nm) magnesium aluminate spinel nanoparticles, J. Am. Ceram. Soc., 96 (2013) 2077–2085

107. D. Lepkova, A. Batarjav, B. Samuneva, Y. Ivanova and L. Georgieva, Preparation and properties of ceramics from magnesium spinel by sol-gel technology, J. Mater. Sci. 26 (1991) 4861-4864

108. T. Shiono, K. Shiono, K. Miyamoto and G. Pezzoti, Synthesis and characterization of $MgAl_2O_4$ spinel powder from a heterogeneous alkoxide solution containing MgO powder, J. Am. Ceram. Soc. 83 (2000) 235 – 237

109. M. Barj, J. F. Bocquet, K. Chhor and C. Pommier, Submicronic $MgAl_2O_4$ powder synthesis in supercritical ethanol, J. Mater. Sci. 27 (1992) 2187 – 2192

110. O. Varnier, N. Hovanian, A. Larbot, P. Bergez, L. Cot and J. Charpin, Sol-gel synthesis of magnesium aluminum spinel from a heterometallic alkoxide, Mater. Res. Bull. 29 (1994) 479 – 488

111. R. Cook, M. Kochis, I. Reimanis and H. Kleebe, A new powder production route for transparent spinel windows: powder synthesis and window properties, Window and Dome Technologies and Materials IX, Proc. SPIE, 5786 (2005) 41 – 47

112. C.T. Wang, L. S. Lin and S. J. Yang, Preparation of $MgAl_2O_4$ spinel powders via freeze – drying of alkoxide precursors, J. Am. Ceram. Soc. 75 (1992) 2240 – 2243

113. S. S. Balabanov, V. E. Vaganov, E. M. Gavrishchuka, V. V. Drobotenko, D. A. Permin, and A. V. Fedin, Effect of magnesium-aluminum isopropoxide hydrolysis conditions on the properties of magnesium-aluminate spinel powders, Inorg. Mater. 50 (2014) 830 – 836

114. S.S. Balabanov, R.P. Yavetskiy, A.V. Belyaev, E.M. Gavrishchuk, V.V. Drobotenko, I.I. Evdokimov, A.V. Novikova, O.V. Palashov, D.A. Permin, V.G. Pimenov, Fabrication of transparent $MgAl_2O_4$ ceramics by hot-pressing of sol-gel-derived nano powders, Ceram. Inter. 41 (2015) 13366–13371

115. S. S. Balabanov, A. V. Belyaev, A. V. Novikova, D. A. Permin, E. Ye. Rostokina, and R. P. Yavetskiy, Densification peculiarities of transparent $MgAl_2O_4$ ceramics— Effect of LiF sintering additive, Inorg. Mater. 54 (2018) 1045 – 1050

116. D. C. Harris, Materials for Infrared Windows and Domes, SPIE Optical Engineering Press, Bellingham, Washington U.S.A. (1999) pp. 1 – 429

117. G. E. Gazza and S. K. Dutta, Hot pressing of ceramic oxides to transparency by heating in isothermal increments, U. S. Pat. No. 3767745 (1973)

118. T. C. Lu, X. H. Chang, J. Q. Qi, X. J. Luo, Q. M. Wei, S. Zhu, K. Sun, J. Lian, and L. M. Wang, Low-temperature high-pressure preparation of transparent nano-crystalline $MgAl_2O_4$ ceramics, Appl. Phys. Lett., 88 (2006) 3 pp, 213120

119. K. Tsukuma, Transparent $MgAl_2O_4$ spinel ceramics produced by HIP post-sintering, J. Ceram. Soc. Jpn. 114 (2006) 802 – 806

120. A. Krell, T. Hutzler, and J. Klimke, Transparent Ceramics for Structural Applications, Ber. Dtsch. Keram. Ges., 84 (2007) E41– 49

121. A. Goldstein, A. Goldenberg, and M. Hefetz, Transparent polycrystalline $MgAl_2O_4$ spinel with submicron grains, by low temperature sintering, J. Ceram. Soc. Jpn. 117 (2009) 1281 – 1283

122. A. Krell, T. Hutzler, J. Klimke and A. Potthoff, Fine grained transparent spinel windows by the processing of different nano powders, J. Am. Ceram. Soc., 93 (2010) 2656–2666

123. T. Mroz and L. M. Goldman, A. D. Gledhill, D. Li and N. P. Padture, Nanostructured, infrared-transparent magnesium aluminate spinel with superior mechanical properties, Int. J. Appl. Ceram. Technol. 9 (2012) 83–90

124. J. Li, T. Ikegami and Y. Yajima, A wet chemical process yielding reactive magnesium aluminate spinel ($MgAl_2O_4$) powder, Ceram. Inter., 27 (2011) 481 – 489

125. S. Zhang, D. D. Jayaseelan, G, Bhattacharya and W. E. Lee, Molten salt synthesis of magnesium aluminate ($MgAl_2O_4$) powder, J. Am. Ceram. Soc. 89 (2006) 1724 – 1726

126. Y. Yuan, S. Zhang and W. You, Synthesis of $MgAl_2O_4$ spinel nanometer powder via biology polysaccharide assisted sol – gel process, J. Sol. Sci. Technol. 30 (2004) 223 - 227

127. P. Hing, Fabrication of translucent magnesium aluminate spinel and its compatibility in sodium vapour, J. Mater. Sci., 11 (1976) 1919 – 1926

128. J.-G. Li, T. Ikegami, J.-H. Lee, and T. Mori, Fabrication of translucent magnesium-aluminate spinel ceramics, J. Am. Ceram. Soc., 83 (2000) 2866 – 2868

129. M. R. Merac, I. E. Reimanis, C. Smith, H. J. Kleebe, and M. M. Muller, Effect of impurities and LiF additive in hot-pressed transparent magnesium aluminate spinel, Int. J. Appl. Ceram. Technol., 10 (2013) E33–E48

130. J. L. Hastert and D. W. Roy, Dome and window for missiles and launch tubes with high ultraviolet transmittance, U.S. Pat. No. 4,930,731, (1990)

131. K. Rozenburg and I. E. Reimanis, "Sintering kinetics of $MgAl_2O_4$ spinel doped with LiF, J. Am. Ceram. Soc., 92 (2008) 444 – 450

132. L. Esposito, A. Piancastelli, and S. Martelli, "Production and characterization of transparent $MgAl_2O_4$ perpared by hot pressing," J. Eur. Ceram. Soc., 33 (2013) 737 – 747

133. M. Y. Lei, C. X. Huang, and J. L. Sun, Effect of HIP on the properties and microstructure of transparent polycrystalline spinel, Key Eng. Mat., 336–338 (2007) 1200 – 1202.

134. A. C. Sutorik, G. Gilde, J. J. Swab, C. Cooper, R. Gamble, and E. Shanholtz, The production of transparent $MgAl_2O_4$ ceramic using calcined powder mixtures of $Mg(OH)_2$ and γ-Al_2O_3 or AlOOH, Int. J. Appl. Ceram. Technol., 9 (2011) 575 – 587

135. MER Corp., High strength, transparent, edge bonded IR spinel windows, NAVAIR Public Release 11-119, MER Corp., Tuscon, AZ, (2011)

136. J. Zhang, T. Lu, X. Chang, N. Wei, and W. Xu, Related mechanism of transparency in $MgAl_2O_4$ nano-ceramics prepared by sintering under high pressure and low temperature, J. Phys. D: Appl. Phys., 42 (2009) 1 – 5

137. A. C. Sutorik, G. Gilde, C. Cooper, J. Wright, and C. Hilton, The effect of varied amounts of LiF sintering aid on the transparency of alumina rich spinel ceramic with the composition $MgO–1.5Al_2O_3$, J. Am. Ceram. Soc. 95 (2012) 1807– 1810

138. N. Frage, S. Cohen, S. Meir, S. Kalabukhov, and M. P. Dariel, Spark plasma sintering (SPS) of transparent magnesium–aluminate spinel, J. Mater. Sci. 42 (2007) 3273 –3275

139. K. Morita, B.-N. Kim, K. Hiraga, and H. Yoshida, Fabrication of transparent $MgAl_2O_4$ spinel poly crystal by spark plasma-sintering process, Scripta Mater. 58 (2008)1114 –1117

140. C. Wang and Z. Zhao, Transparent $MgAl_2O_4$ ceramic produced by spark plasma sintering, Scripta Mater. 61 (2009) 193 – 196

141. S. Meir, S. Kalabukhov, N. Froumin, M. P. Dariel, and N. Frage, Synthesis and densification of transparent magnesium aluminate spinel by SPS processing, J. Am. Ceram. Soc. 2 (2009) 358 – 364

142. B. N. Kim, K. Morita, J. H. Lim, K. Hiraga, and H. Yoshida, Effects of preheating of powder before spark plasma sintering of transparent $MgAl_2O_4$ spinel, J. Am. Ceram. Soc. 93 (2010) 2158 – 2160

143. G. Bonnefont, G. Fantozzi, S. Trombert, and L. Bonneau, Fine-grained transparent $MgAl_2O_4$ spinel obtained by spark plasma sintering of commercially available nano powders, Ceram. Int. 38 (2012) 131– 141

144. K. Morita, B. Kim, H. Yoshida, and K. Hiraga, Spark-plasma-sintering condition optimization for producing transparent $MgAl_2O_4$ spinel polycrystal, J. Am. Ceram. Soc. 92 (2009) 1208–1216

145. A. Zegadi, M. Kolli, M. Hamidouche, and G. Fantozzi, Transparent $MgAl_2O_4$ spinel fabricated by spark plasma sintering from commercial powders, Ceram. Inter. 44 (2018) 18828 – 18835

146. H. Shahbazi, H. Shokrollahi, and M. Tataei, Gel casting of transparent magnesium aluminate spinel ceramics fabricated by spark plasma sintering (SPS), Ceram. Inter. 44 (2018) 4955 – 4960

147. H. Yoshida, P. Biswas, R. Johnson and M. K. Mohan, Flash-sintering of magnesium aluminate spinel ($MgAl_2O_4$) ceramics, J. Am. Ceram. Soc. 100 (2017) 554 – 562

148. M. R. Merac, H. Kleebe, M. M. Muller and I. E. Reimanis, Fifty years of research and development coming to fruition; unraveling the complex interactions during processing of transparent magnesium aluminate ($MgAl_2O_4$) spinel, J. Am. Ceram. Soc., 96 (2013) 3341–3365

149. A.Goldstein, A.Goldenberg and M.Vulfson, Development of a technology for the obtainment of fine grain size, transparent $MgAl_2O_4$ spinel parts, J. Ceram. Sci. Tech. 02 (2011) 1 – 8

150. C. Greskovich and J. P. Chernoch, Polycrystalline ceramic lasers, J. Appl. Phys., 44 (1973) 4599–606

151. C. Greskovich and S. Duclos, Ceramic scintillators, Annu. Rev. Mater. Sci., 27 (1997) 69-88

152. P. Hogan, T. Stefanik, C. Willingham and R. Gentilman, Transparent yttria for IR windows and domes – past and present, ADM201976, 10thDoDEM Windows Symposium May 19, Norfolk, VV, 2004

153. C.B. Willingham, J.M. Wahi, P.K. Hogan, L.C. Kupferberga, T.Y. Wong and A.M. Dea, Densification of nano-yttria powders for IR window applications, Window and Dome Technologies and Materials VIII, Vol. 5078, Proceedings of SPIE, Edited by R. W. Tustiston, SPIE, Orlando, FL (2003) 179 – 188.

154. R. A. Lefever, Flame fusion growth of C – type rare earth oxides, Rev. Sci. Intsr. 33 (1962) 769

155. L. A. Brisette, P. L. Burnett, R. M. Spriggs and T. Vasilos, Thermo-mechanically deformed Y_2O_3, J. Am. Ceram. Soc. Discussions and Notes, (1966) 165 – 166

156. R. C. Anderson, GE has transparent ceramic, Chem. & Engg. News, Oct. 17 (1966) 38

157. R. A. Lefever and J. Matsko, Transparent yttrium oxide ceramics, Mater. Res. Bull. 2 (1967) 865 – 869

158. S. K. Dutta and G. E. Gazza, Transparent Y_2O_3 by hot pressing, Mater. Res. Bull. 4 (1969) 791 – 796

159. Y. Tsukuda and A. Muta, Sintering of Y_2O_3 at high temperatures, J. Ceram. Soc. Jpn. 84 (1976) 585 – 589

160. W. H. Rhodes, Controlled transient solid second-phase sintering of yttria, J. Am. Ceram. Soc. 64 (1981) 13 – 19

161. J. Wang, J. Zhang, K. Ning, D. Luo, H. Yang, D. Yin, D. Tang and L. B. Kong, Densification of yttria transparent ceramics: The utilization of activated sintering, J. Am. Ceram. Soc., 99 (2016) 1671–1675

162. J. Mouzona, A. Maitre, L. Frisk, N. Lehto and M. Od´en, Fabrication of transparent yttria by HIP and the glass-encapsulation method, J. Eur. Ceram. Soc. 29 (2009) 311–316

163. J. He, X. D. Li, J. G. Li and X. D. Sun, Colloidal stability of aqueous suspensions of nano-yttria powders, Inter. J. Mater. Sci. Eng. 1 (2013) 28 – 31

164. H. Mingsheng, L. Jianbao, L. Hong, G. Gangfeng and L. Long, Fabrication of transparent polycrystalline yttria ceramics by combination of SPS and HIP, J. Rar. Ear., 24 (2006) 223 – 224

165. L. Wen, X. Sun, Q. Lu, G. Xu and X. Hu, Synthesis of yttria nano-powders for transparent yttria ceramics, Opt. Mater., 29 (2006) 239 – 245

166. Y. Huang, D. Jiang, J. Zhang and Q. Lin, Fabrication of transparent lanthanum-doped yttria ceramics by combination of two-step sintering and vacuum sintering, J. Am. Ceram. Soc., 92 (2009) 2883–2887

167. N. Saito, S. Matsuda and T. Ikegami, Fabrication of transparent yttria ceramics at low temperature using carbonate-derived powder, J. Am. Ceram. Soc., 81 (1998) 2023– 2028

168. T. Ikegami, T. Mori, Y. Yamija, S. Takenouchi, T. Misawa and Y. Moriyoshi, Fabrication of transparent yttria ceramics through the synthesis of yttrium hydroxide at low temperature and doping by sulfate ions, J. Ceram. Soc. Jpn. 107 (1999) 297 – 299

169. T. Ikegami, J. G. Li, T. Mori and Y. Moriyoshi, Fabrication of transparent yttria ceramics by the low-temperature synthesis of yttrium hydroxide, J. Am. Ceram. Soc., 85 (2002) 1725–1729

170. J. Mouzon, T. Lindback and M. Oden, Influence of agglomeration on the transparency of yttria ceramics, J. Am. Ceram. Soc., 91 (2008) 3380–3387

171. W. K. Jung, H. J. Ma, S. W. Jung and D. K. Kim, Effects of calcination atmosphere on monodispersed spherical particles for highly optical transparent yttria ceramics, J. Am. Ceram. Soc., DOI: 10.1111/jace.14776 (2017) 1876 – 1884

172. H. Eilers, Fabrication, optical transmittace, and hardness of IR – transparent ceramics made from nanophase yttria, J. Eur. Ceram. Soc. 27 (2007) 4711 – 4717

173. W. K. Jung, H. J. Ma, Y. Park and D. K. Kim, A robust approach for highly transparent Y_2O_3 ceramics by stabilizing oxygen defects, Script. Mater. 137 (2017) 1 – 4

174. Z. Huang, X. Sun, Z. Xiu, S. Chen and C. T. Tsai, Precipitation synthesis and sintering of yttria nanopowders, Mater. Lett. 58 (2004) 2137 – 2142

175. J. Mouzon T. Lindback and M. Oden, Influence of agglomeration on the transparency of yttria ceramics, J. Am. Ceram. Soc. 91 (2008) 3380 – 3387

176. R.L. Gentilman, M. Greenberg and T. Hartnett, Optically transparent yttrium oxide, U S Pat. No. 4761390 (1988)

177. R. S. Kumar, A. K. Khanra and R. Johnson, Processing and properties of sintered submicron IR transparent alumina derived through sol-gel method, J. Sol. Sci. Tech., 86 (2018) 374 – 382

178. I. W. Chen and X. H. Wang, Sintering dense nano crystalline ceramics without final-stage grain growth, Lett. Nat. 404 (2000) 168 – 172

179. K. Serivalsatit, B. Yazgan Kokuoz, B. Kokuoz, and J. Ballato, Nanograined highly transparent yttria ceramics, Opt. Lett. 34 (2009) 1033 – 1035

180. K. Serivalsatit, B. Kokuoz, B. Y. Kokuoz, M. Kennedy and J. Ballato, Synthesis, processing and properties of submicrometer-grained highly transparent yttria ceramics, J. Am. Ceram. Soc. 93 (2010) 1320 – 1325

181. L. Zhang, Y. Ben, J. Wu, H. Yang, C. Wong, Q. Zhang and H. Chen, Alumina assisted grain refinement and physical performance enhancement of yttria transparent ceramics by two-step sintering, Mater. Sci. Engg. A, 684 (2017) 466 – 469

182. H. Weglarz, A. Wajler, H. Tomaszewski, M. Mozdzonek and Z. Librant, Sintering studies of transparent yttria ceramics, Ceram. Mater. 63 (2011) 123 – 126

183. T. R. Hinklin, S. C. Rand and R. M. Laine, Transparent, poly crystalline upconverting nano ceramics: Towards 3 – D displays, Adv. Mater. 20 (2008) 1270 – 1273

184. J. Wang, K. Ning, J. Zhang, D. Luo, J. Ma, D. Yin, D. Tang and L. B. Kong, Rapid rate sintering of yttria transparent ceramics, J. Am. Ceram. Soc. 99 (2016) 1935 – 1942

185. H Zhang, B. N. Kim, K. Morita, H. Yoshida, K. Hiraga and Y. Sakka, Fabrication of transparent yttria by high-pressure spark plasma sintering, J. Am. Ceram. Soc., 94 (2011) 3206–3210

186. L. An, A. Ito and T. Goto, Transparent yttria produced by spark plasma sintering at moderate temperature and pressure profiles, J. Eur. Ceram. Soc., 32 (2012) 1035 – 1040

187. E. Korkmaz and F. Shahin, Fabrication of transparent yttria ceramics by spark plasma sintering, Act. Phys. Polo A., 131 (2017) 460 – 462

188. L. Gan, Y. J. Park, M. J. Park, H. Kim, J. M. Kim, J. W. Ko and J. W. Lee, Facile fabrication of highly transparent yttria ceramics with fine microstructures by a hot-pressing method, J. Am. Ceram. Soc., 98 (2015) 2002–2004

189. B. Li, X. Zheng and Z. F. Fu, Fast densification of nanocrystalline yttria ceramics without grain growth, Inter. J. Sel. Hig. Temp. Syn. 24 (2015) 14 – 20

190. J. M. Wahl, T. M. Hartnett, L. M. Goldman, R. Twedt, C. Warner, Recent advances on AlON optical ceramic; in window and dome technologies and materials IX, Vol. 5786, Proceedings of SPIE, Edited by R. W. Tustiston. SPIE, Bellingham, WA, (2005) 71 – 82

191. G.C. Wei, Transparent ceramic lamp envelope materials, J. Phys. D: Appl. Phys. 38 (2005) 3057 – 3065

192. J. W. McCauley and N. D. Corbin, High temperature reactions and microstructures in the Al_2O_3 – AlN system, Progress in nitrogen ceramics, ed. F.L. Rley, Martinus Nijhojj Pub., The Netherlands, 65 (1983) 111 – 118

193. G. Yamaguchi, Refractive power of the lower – valent aluminum ion (Al^+ or Al^{2+}) in the crystal. Bull. Chem. Soc. Jpn. 23 (1950) 89 – 90

194. G. Yamaguchi and H. Yanagida, Study on the reductive spinel – A new spinel formula AlN – Al_2O_3 instead of the previous one Al_3O_4, Chem. Soc. Jpn. Bull. 32 (1959) 1264 – 1265

195. I. Adams, T. R. Aucoin and G. A. Wolff, Luminescence in the system Al_2O_3 – AlN, J. Electro Chem. Soc. 109 (1962) 1050 – 1054

196. G. Long and L. M. Foster, Crystal phases in the system Al_2O_3 – AlN, J. Am. Ceram. Soc. 44 (1961) 255 – 258

197. K. H. Jack and W. I. Wilson, Ceramics based on the Si-Al-O-N and related systems, Nature. Phys. Sci. (London) 238 (1972) 28 – 29

198. J. W. McCauley and N. D. Corbin, Phase relations and reaction sintering of transparent cubic aluminum oxynitride spinel (AlON) 62 (1979) 476 – 479

199. J. W. McCauley and N. D. Corbin, Process for producing polycrystalline cubic aluminium oxynitride, U. S. Pat. No. 421400 (1980)

200. R. M. Sullivan, A historical view of AlON, ; in window and dome technologies and materials IX, Vol. 5786, Proceedings of SPIE, Edited by R. W. Tustiston. SPIE, Bellingham, WA, (2005) 23 – 32

201. R. Senthil Kumar, K. Rajeshwari, B. Praveen, U. S. Hareesh and R. Johnson, Processing of aluminum oxynitride through aqueous colloidal forming techniques, J. Am. Ceram. Soc. 91 (2010) 429 – 435

202. H. X. Willems, M. M. R. M. Hendrix, G. De with and R. Metsalaar, in Euro-ceramics II Vol 3, edited by G. Ziegler and H. Hausner (1991) 2443 – 2447

203. J. P. Cheng, D. Agarwal and R. Roy, Microwave synthesis of aluminum oxynitride, J. Mater. Sci. Lett. 18 (1999) 1989 – 1990

204. J. Cheng, D. Agarwal, Y. Zhang and R. Roy, Microwave reactive sintering to fully transparent aluminum oxynitride (AlON) ceramics, J. Mater. Sci. Lett. 20 (2002) 77 – 79

205. P. J. Patel, G. Gilde and J. W. McCauley, Transient liquid phase reactive sintering of aluminum oxynitride (AlON), U. S. Pat. No. 7045091 B1 (2006)

206. R. Senthil Kumar, U. S. Hareesh, P. Ramavath and R. Johnson, Hydrolysis control of alumina and AlN mixture for aqueous colloidal processing of aluminum oxynitride, Ceram. Inter. 37 (2011) 2583 – 2590

207. L.Miller and W.D.Kalpan, Water-based method for processing of aluminum oxynitride (AlON), Int. J. Appl. Ceram. Technol. 5 (2008) 641 – 648

208. S. Bandyopadhyay, G. Rixercer, F. Aldinger, S. Pal, K. Mukherjee and H. Maiti, Effect of rection parameters on AlON formation from Al_2O_3 and AlN, J. Am. Ceram. Soc. 85 (2002) 1010 – 1012

209. N. D. Corbin, The influence of carbon, nitrogen and argon on aluminum oxynitride spinel formation, M. S. Thesis, Department of Materials Science and Engineering, Massachusetts Institute of Technology, Cambridge, MA, 1982

210. E.A. Maguire, T. M. Hartnett and R.L. Gentilman, Method of producing aluminum oxynitride having improved optical characteristics, U.S. Pat. No. 4686070 (1987)

211. W.Rafaniello and B.Cutler, Preparation of sinterable cubic aluminum oxynitride by carbothermal nitridation of aluminium oxide, J. Am. Ceram. Soc. 10 (1981) C-128

212. L.Yawei, L.Nan and Y.Runzhang, Carbothermal reduction synthesis of aluminum oxynitride spinel powders at low temperatures, J. Mater. Sci. Lett 16 (1997) 185 – 186

213. F. Ma, J. Lei, Y. Shi, J. Xie and F. Lei, Synthesis of submicron powder by wet chemical processing, Adv. Mater. Res. 624 (2013) 42 – 46

214. X. Jin, L. Gao, J. Sun, Y. Liu and L. Gui, Highly transparent AlON presuurelessly sintered from powder synthesized by a novel carbothermal nitridation method, 95 (2012) 2801 – 2807

215. V. Sabaghi, F. Davar, M. H. Teherian, Ultrasonic – assisted preparation of AlON from alumina / carbon core – shell nano particle, Ceram. Inter. 45 (2019) 3350 – 3358

216. Y. Shan, P. Li, X. Sun, X. He, C. Hong, J. Xu and J. Li, Study on AlON phase evolution and densification behavior as a function of particle size and dopant amount, J. Eur. Ceram. Soc. 40 (2020) 3906 – 3917

217. Z. Feng, J. Qi and T. Lu, Highly – transparent AlON ceramic fabricated by tape – casting and pressureless sintering method, J. Eur. Ceram. Soc. 40 (2020) 1168 – 1173

218. Z. Feng, J. Qi, X. Huang, X. Guo, Y. Yu, X. Cao, Y. Wang, D. Wu, C. Meng and T. Lu, Planetary ball milling of AlON powder for highly transparent ceramics, J. Am. Ceram. Soc. 102 (2019) 2377 – 2389

219. X. Xie, Y. Wang, J. Qi, S. Wang, Z. Feng, G. Hou, W. Liu, W. Zhang, Q. Xu , T. Lu, Ethanol – water derived sucrose coated Al_2O_3 for sub-micrometer AlON powder synthesis, J. Am. Ceram. Soc. 99 (2016) 2601 – 2606

220. N. D. Corbin, Aluminum oxynitride spinel: a review, J. Eur. Ceram. Soc. 5 (1989) 143 – 154

221. J. Zhou, Z. Liao, J. Qi, W. Pang, Y. Wen, A new method for the preparation of transparent AlON ceramic, Key Eng. Mater. 368, 441 (2008)

222. Y. Wang, X. Xie, J. Qi, J. Wang, D. Wu, X. Guo, N. Wei and T. Lu, Two-step preparation of AlON transparent ceramics with powder synthesized by aluminothermic reduction and nitridation method, J. Mater. Res. 20 (2014) 2325 – 2331

223. G. Ruan, H. Xu, Z. Zhang, M. Yin, G. Xu and X. Zhan, New method of synthesizing aluminum oxynitride spinel powders, J. Am. Ceram. Soc. 96 (2013) 1706 – 1708

224. D. Zientara, M. M. Bucko and J. Lis, AlON – based materials prepared by SHS technique, J. Eur. Ceram. Soc. 27 (2007) 775 – 779

225. W. Xidong, W. Fuming and L. Wenchao, Synthesis, microstructures and properties of γ – aluminum oxynitride, Mater. Sci. Engg. A 324 (2003) 245 – 250

226. J. C. Labbe, A. Jeanne, G. Roult, Synthesis of gamma phase AlON by reaction of the BN/alumina system, Ceram. Int. 18 (1992) 81 – 84

227. E. A. Irene, V. J. Silvestri and G. R. Woolhouse, Some properties of chemically vapor deposited films of $Al_xO_yN_z$ on silicon, J. Elect. Mater. 4 (1975) 409 – 427

228. H. Fukuyama, W. Nakao, M. Susa and K. Nagata, New synthetic method of forming aluminum oxynitride by plasma arc melting, J. Am. Ceram. Soc. 82 (1999) 1381 – 1387

229. S. Balasubramanian, R. K. Sadangi, V. Shukla and B. H. Kear, Plasma reaction synthesis of alumina – aluminum oxynitride nano composite powders, Ceram. Trans. 148 (2004) 83 – 90

230. Y. Takao, K. Shuzenji and T. Tachibana, Preparation of aluminum oxynitride and nitride spherical powders via flame synthesis assisted by DC arc plasma, J. Am. Ceram. Soc. 91 (2008) 311 – 314

231. R.L. Gentilman, E.A. Maguire and L.E. Dolhert, Transparent aluminum oxynitride and method of manufacture, U.S. Pat. No. 4 520 116 (1985)

232. R.L. Gentilman, E.A. Maguire and L.E. Dolhert, Transparent aluminum oxynitride and method of manufacture, U.S. Pat. No. 4 720 362 (1988)

233. H. Li, P. Min, N. Song, A. Zhang, J. Zhou, H. Xian, H. Liu and J. Fang, Rapid synthesis of AlON powders by low temperature solid – state reaction, Ceram. Inter. 45 (2019) 8188 – 8194

234. R. Senthil Kumar and R. Johnson, Aqueous slip casting of Aluminum oxynitride, J. Am. Ceram. Soc. 99 (2016) 3220 – 3225

235. R, Bechelard, J. P. Disson and B. Morlhon, Optically transparent gamma – aluminum oxynitride powders and ceramic articles shaped therefrom, U. S. Pat. No. 5688730 (1997)

236. B. N. Beni and A. Alizadeh, Development of a new sol – gel route for the preparation of aluminum oxynitride nano – powders, 46 (2020) 913 – 920

CHAPTER - III

Experimental and Characterization Techniques

3.1 Introduction

The prime scope of the entire study comprises producing the spectrum of optical grade ceramic oxide powders such as Al_2O_3, $MgAl_2O_4$ spinel and Y_2O_3 followed by fabricating respective transparent solid materials using the synthesized powders. In addition, the scope includes to study the suitability of the current synthesizing technique for producing oxynitride powders such as Aluminium oxynitride (AlON) that are useful for fabricating dense AlON articles. This chapter describes the fundamentals of major processing and experimental tools used in the current investigations and provides a brief outline of the characterization techniques used for evaluating the materials in terms of their physical, chemical, microstructural, thermal, mechanical and optical properties.

3.2 Synthesis methodology and instrumentations

The entire study employed the sol – gel – processing techniques for the synthesis of all the optical grade powders followed by using various powder metallurgy processes to produce dense ceramic materials transparent to the electro – magnetic radiations, specifically in the 3 – 8 μm wavelength regions.

3.2.1 Sol – gel processing technique

Sol-gel process is generally a wet chemical process involving two major reactions. First reaction involve hydrolysis of the precursor in a basic or acidic medium. Second reaction is the polycondensation of the hydrolysed product. The starting materials used in the preparation of the sol are mostly the salts of an inorganic metals or metal organic compounds such as

alkoxides of metals. In a typical sol – gel process, the starting precursors subjected to various hydrolysis and precipitation reactions follow acid peptization to form a transparent to semi-transparent colloidal suspension known as sol, which would be further activated by means of pH modifiers to form a three-dimensional continuous liquid phase known as gel [1 – 2]. The outline of synthesizing nano ceramic powders through sol-gel method is schematically shown in fig. 3.1.

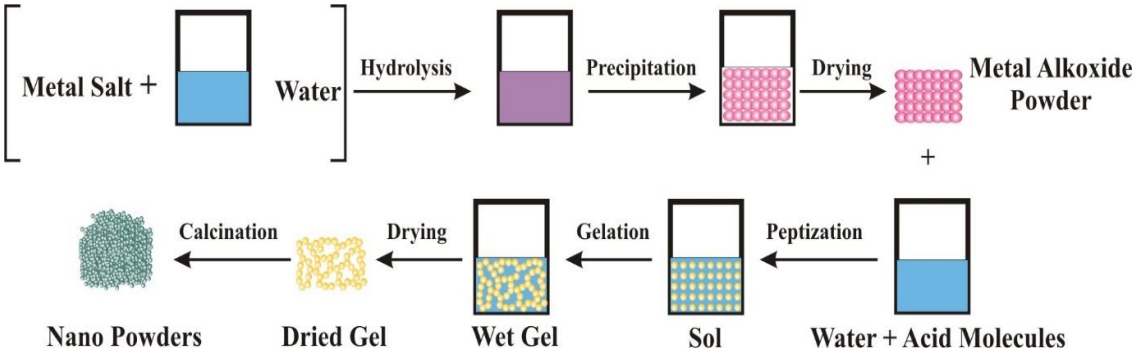

Fig. 3.1 Schematic of synthesizing ceramic nano powders through sol-gel method

Sol-gel is an ideal methodology for producing ultra – high pure and ultra – fine ceramic nano powders. The process is employed for synthesizing numerous ceramic oxide and non – oxide systems ranging from Al_2O_3, ZrO_2, TiO_2, SiO2, Mullite, AlN, SiC etc. for various functional and structural applications [3 – 9]. This method is attractive over other powder synthesis methods due to its versatility in controlling the size and the morphology of the powder particles and produce the required phase at relatively low temperatures. In addition, this methodology allow high control over molecular stoichiometry during the synthesis of powders having multicomponent compounds [10]. For example, in the present study, this process facilitated homogeneous and intimate mixing of Al_2O_3 and MgO precursors, which enabled the formation

of ultra – pure spinel phase. Moreover, this method is relatively more economical compared to the rest of the synthesis techniques.

3.2.2 Planetary ball milling

Planetary ball mill is a type of high-energy ball mill used to comminute and grind ceramic powders using various sizes of spherical balls placed in a ceramic vial. It works under the principles of impact and attrition and the size reduction takes place as the balls hit with each other and against the walls of the vial. It rotates in a planetary motion on a stationary platform and exhibit aggressive impact on the powder particles [11]. This method is highly effective for milling and mixing of nano-sized particles and relatively comminute at rapid rate due to very high speed of rotations ranging up to 500 RPM. Fig. 3.2 shows the picture and the schematic of planetary ball mill (Fritsch, Germany) used in this study. High purity alumina vials (>99.9%) of 500 ml capacity was used as a milling container and 2 mm alumina balls of purity above 99.95% was used as a milling media. High – pure milling tools were used to avoid the inclusions of milling contaminations in to the ceramic powders during milling operations.

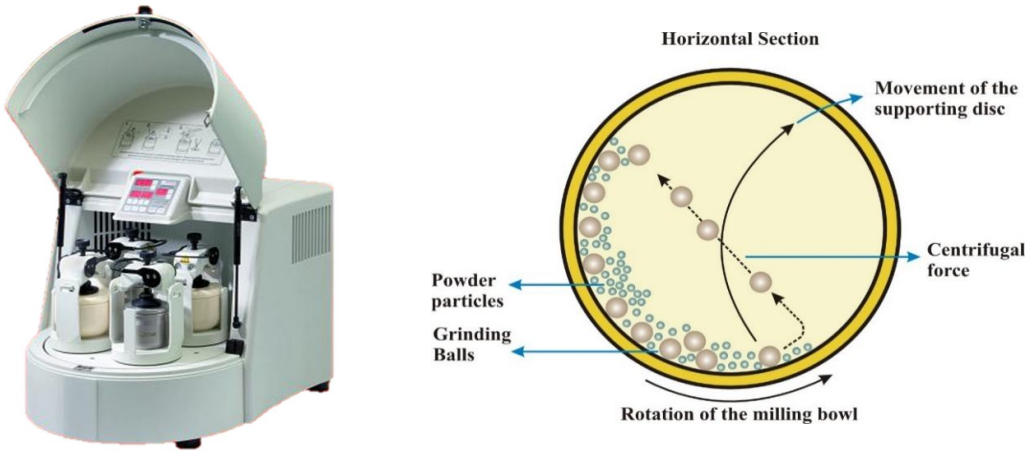

Fig. 3.2 Picture and the schematic of planetary ball mill

3.2.3 Cold isostatic press (CIP)

Cold isostatic compaction is a process used for shaping ceramic powders by applying homogenous hydrostatic pressures from all the directions by means of a liquid medium (water – oil emulsion). It is a simple process capable of producing high – integrity green shapes with homogeneous green density that exhibit minimal distortion or cracking during further hot deformation or sintering. In a typical practice, the ceramic powders or their preforms is placed in latex bag and sealed to prevent any external liquid entrapment. The moulded powder or the preforms would receive a homogenous isostatic pressures in the enclosed pressure vessel pumped with liquid. The increased pressure cause the flexible latex to collapse and transfer the pressure to the powders or preforms for compaction. The process is highly advantageous in terms of obtaining green parts with consistent shrinkage, low internal stress and versatile to produce simple and complex shaped components [12]. In the present process, the preforms such as uniaxially compacted pellets of ceramic powders obtained green densification above 55% of T.D. at pressures of 200 MPa after the cold isostatic compaction (Avure Technologies AB, Sweden). Fig. 3.3 shows the typical photograph and the schematic of the CIP used in this study.

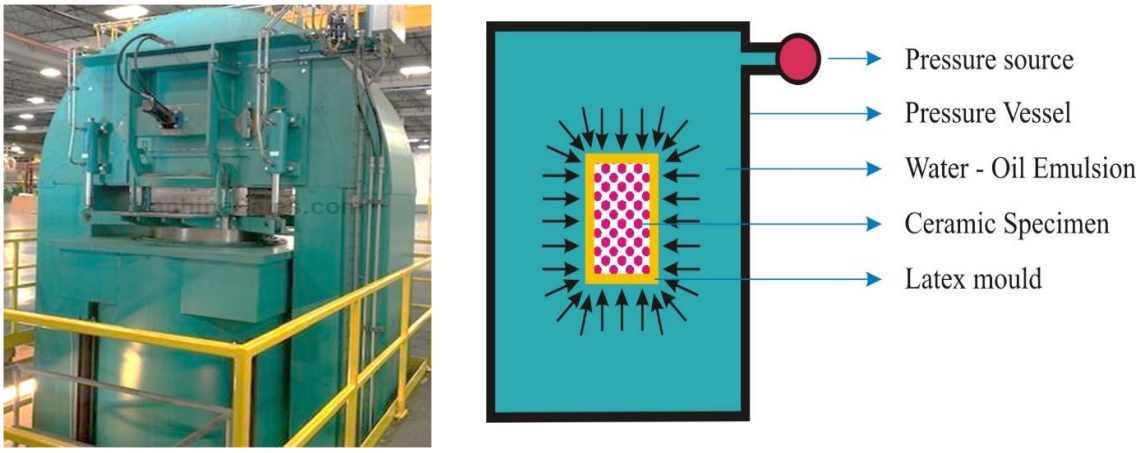

Fig. 3.3 Picture and the schematic of the cold isostatic press (CIP)

3.2.4 High temperature furnaces

A furnace is a heat-generating unit containing a controlled hot zone surrounded by or built around using high temperature refractory insulating materials. The source of heat is usually combustion of liquid or gaseous fuel or electrical energy applied through resistance heating or inductive heating. The heat that is generated in the furnace is usually measured by means of thermocouples, pyrometers, and the rate of heating and cooling is controlled by means of thyristors. In the present study, an air atmospheric furnace (Nabertherm, Germany) was used for synthesis of powders and densification of ceramic oxide systems such as Al_2O_3, spinel and Y_2O_3. In case of the studies on the oxynitride systems such as AlON, a controlled atmospheric furnace from MPA Industrie, France, was used. The furnace contain graphite-heating elements and lined with graphite wool insulations. The furnace is designed for the temperatures up to 2000°C and run under vacuum or under flowing nitrogen and argon atmospheres. Figure 3.4 shows the pictures of the air (fig. 3.4a) and the controlled atmospheric furnaces (fig. 3.4b) used in this investigation.

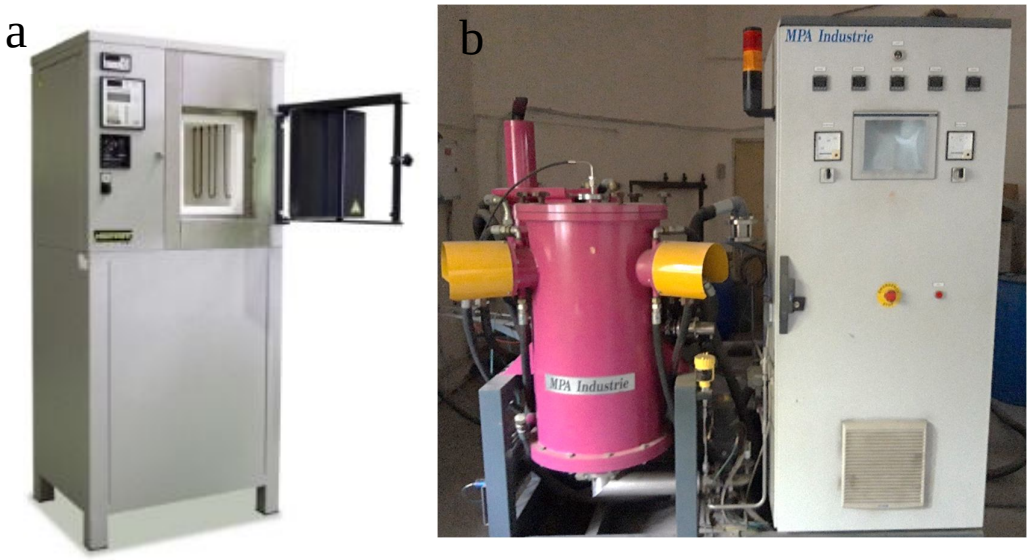

Fig. 3.4 Pictures of the air atmospheric (3.4a) and the controlled atmospheric (3.4b) furnaces

3.2.5 Hot isostatic press (HIP)

Hot isostatic pressing is a materials fabrication process in which a starting powder or a pre-sintered shape is simultaneously subjected to both high temperatures and isostatic pressures by means of gas medium [13]. HIPing of powders require an encapsulation, which is generally an evacuated glass or a metal envelop that flex at high temperatures and transfer the pressures to the powders for densification. On the other hand, the pre-sintered components with no open pore channels obtain densification without any assistance of clads or encapsulations. For the successful operation of HIP, three variables such as pressure, temperature and time require control and optimization. The HIP unit (American Isostatic Presses, U.S.A) utilised in this study is equipped with graphite-lined furnace having capacity to reach temperatures up to 2000°C and pressures up to 200 MPa under argon atmosphere. The equipment is built with monolith forged type pressure vessel and lids are supported with frame type yokes. In the present studies, the ceramic materials obtained densification above 96% T.D. to gain zero open porosities prior to the HIPing operations. Figure 3.5 shows the photograph and the schematic of the HIP unit utilized in this study.

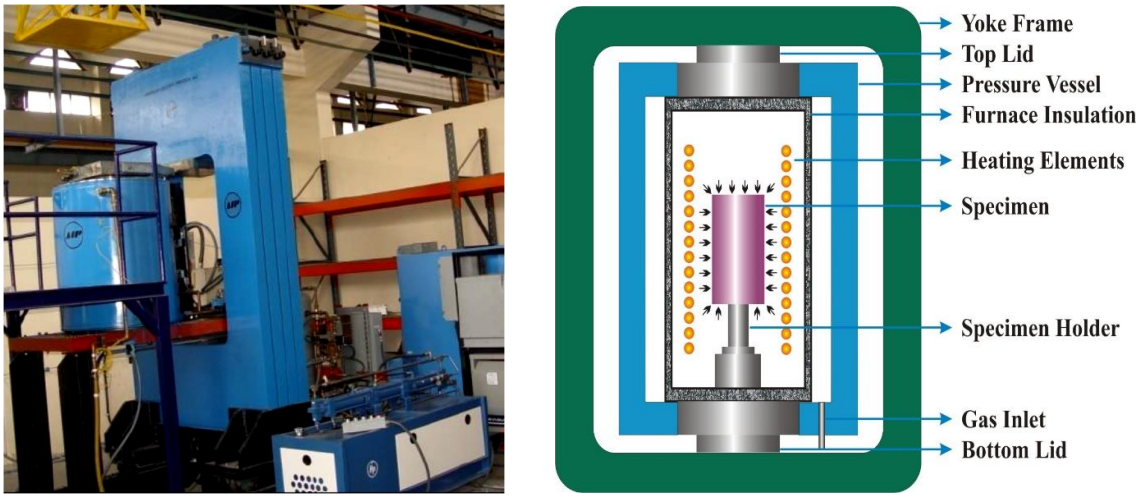

Fig. 3.5 Picture and the schematic of the hot isostatic press (HIP)

3.3 Characterization techniques

The optical grade ceramic powders and the dense IR transparent materials produced in the present studies were characterized for their physical, chemical, microstructural, mechanical and optical properties at the appropriate processing stages in order to orient the studies to successfully obtain the eventual objectives. The entire characterization techniques employed in this investigation is tabulated in table 3.1.

S. No	**Characterization Technique**	**Information acquired**	**Instrument details**
1	FESEM	Powder morphology, particle size, grain size and size distribution, crack propagation,	Hitachi, 3200S, FESEM, Tokyo, Japan Carl Zeiss Microscopy GmbH, Oberkochen, Germany
2	TEM	Powder morphology, particle size, SAED analysis, core – shell analysis, crystallization state	FEI, Technai G2, Netherlands
3	XRD	Phase analysis, crystallite size	D8, Bruker, Karlsruhe, Germany Rigaku Rapid – II Micro area XRD, Japan
4	TGDTA	Phase transformation temperatures, identification of temperature regions for various evaporation of water and other organic molecules	Netzsch STA 409C, Selb, Germany

S. No	Characterization Technique	Information acquired	Instrument details
5	Dilatometer	Sintering and shrinkage pattern analysis	DIL 402 C, Netzsch, Germany
6	Hardness	Vickers and Knoops Hardness	Leco, St. Joseph, MI
7	BET analysis	Surface area of the powders	Gemini, Micromeritics, U. S. A
8	FTIR analysis	Chemical bonding informations, Real inline optical transmission	Spectrum GX, Perkin Elmer, C.T, U.S.A Vertex 70, Bruker optic GnbH, Germany
9	Particle size analysis	Particle size and size distribution	Nano SZ, Malvern Instruments Ltd, UK
10	Viscosity	Viscosity of the sol and sol – seed mixtures	MCR 51, Anton Paar GmBH, Austria
11	Thermal conductivity	Thermal conductivity at temperatures from RT – 800°C	LFA, Netzsch, Germany
12	Archimedes Principles	Porosity and Density	LA 120S, Sartorius AG, Germany

Table 3.1. Details of the characterization techniques used in the entire investigation

3.3.1 Field emission scanning electron microscope (FE – SEM)

SEM works similar to optical microscopes but uses a strong electron beam for optical reflections. The field emission gun in the instrument provides tremendously focused high and low-energy electron beams and enables the work to be carried out at very low potential. It also improves larger spatial resolution and helps to minimize charging effect on non-conductive

samples such as ceramic materials. On the other hand, ceramic materials require a coating of gold film deposited through ion beam sputtering for improved conductivity on the surface for obtaining high – resolution images. The lens detectors used in FE-SEM work at higher resolution and lower acceleration potential for maximum efficiency. During the analysis, the electron beam focused on the sample surface under vacuum and scan over the surface of the sample. Electrons scattered from the surface of the sample fed to detector and to a cathode ray tube for imaging the surface information of the sample.

3.3.2 Transmission electron microscope

Max Knoll and Ernst Ruska first developed TEM during the year 1931. Transmission electron microscopy (TEM) facilitate higher spatial resolution down to the features at atomic scale (in the range of a few nanometres) using electron beam energies in the range of 100-400 keV. TEM technique uses a relatively high voltage electron beam compared to SEM analysis to obtain the image. It comprises a tungsten or LaB_6 filament or a field emission gun as source of electron beam, condenser lens, sample, objective lens projector lens, fluorescent screen, charged coupled device camera, monitor etc. High-energy electron beam collimated by magnetic lenses and passed through a sample kept under high vacuum. The transmitted beam form a magnified see - through image on a fluorescent screen (bright field imaging mode) for the observation. It is useful for analysing the morphology, particle size and shape, internal microstructures, twinning, coating thickness, crystallographic structure and the composition of the materials. The information on the atomic structure of the material obtained by recombining the transmitted beam. The techniques is highly versatile for obtaining features of selected area electron diffraction (SAED) pattern. In this study, parts of the crystalline regions diffract for the formation of the image and allow switching to diffraction pattern of a sample region simultaneously. It allows the determination of the exact crystal type and lattice distances of a phase in a material down to the area closer to 100 nm in diameter.

3.3.3 X – ray diffraction technique

X-ray diffraction methods are the most concrete methods for determining the crystal structures of the materials. It is very effective in identifying chemical compounds from their crystalline structure without providing any inputs on the chemical compositions of the chemical elements. Therefore, it is capable of analysing different compounds or phases of the same composition. For example, Al_2O_3 exists in various polymorph such as γ, δ, θ and α with the same chemical compositions. However, they vary in their respective crystal structures. For example, γ – Al_2O_3 exhibit cubic structures and α – Al_2O_3 exhibit hexagonal structures. In such conditions, X – ray techniques are the most effective tool for identification of the nature of the chemical compounds.

The X – ray tube generates the X- ray radiation having wavelengths ranging from a minimum λ, known as white or continuous X – rays in addition to few sharp characteristic X – rays that goes along with the continuous X – rays. The monochromatic radiation that are useful for X-ray characterization are these characteristic Kα and Kβ radiations. In the present study, Kα of 0.154052 nm produced from copper anode targets were used for analysis.

X – rays are electromagnetic waves of wavelengths in the order of 0.1 nm. The analysis is working under wave interferences where two light waves of same wavelength travelling in the same direction to produce constructive (nλ) and destructive interferences (nλ/2). X – ray beams incident on a crystalline solid undergo diffraction in the crystallographic planes and the deflection waves attain in phase by satisfying the following Bragg's relationship.

$$n\lambda = 2d \sin\theta \qquad \text{---------- (1)}$$

Where, λ is wavelength of X-rays, d is inter-planar spacing of parallel lattice planes, θ is diffraction angle.

The X – ray technique is also useful for finding the crystallite size using following Scherer formula and other crystal related information lattice energy, crystal defects, disorders etc.

$D = 0.9 \lambda (1.54052 Å) / \beta \cos (2\theta/2)$ ---------- (2)

Where, D is crystallite size, λ is wavelength of X-rays (0.154052 in our case), β is the full width half maximum (FWHM) in radians and θ is the phase position of the high intense peak.

3.3.4 Thermo – gravimetric and differential thermal analysis (TGDTA)

TGDTA is an analytic technique that measure properties or change in properties of materials as a function of temperature. These changes considered in the analysis are termed as thermal events. The properties that can change include dimensions, phase, mass and mechanical behaviour. In the present study, this technique was used as an important tool for the identification of mass changes from the dried gel with respect to raise in temperatures and provided details on temperatures of phase transformation from amorphous to crystalline state.

TG is mainly used to estimate the decomposition of materials by monitoring the change in mass with the increment in the calcination temperatures and DTA is widely used for examining the phase changes of materials. The analysis records the thermal events from room temperatures to the higher temperatures at which the reactions are expected. At room temperatures, the atoms of the material are in static positions and exhibit no vibration or rotation of atomic bonds. However, with the increasing temperature, the material gains thermal energy and initiates the vibrations and rotations of atomic bonds. At respective temperatures, the material undergo various reactions such as solid – phase transformation, glass transition, sublimation, evaporation, melting and decomposition. Events such as solid – phase transformation may occur for solids that have different crystalline phases at different temperature regions. For example, in our study, the alkoxides of Al_2O_3 such as AlOOH or $Al(OH)_3$ transforms to γ phase at temperatures around 650°C which is further converted to α phase at temperatures

closer to 1050°C. These events are generally exothermic reactions and therefore exhibit heat flow from the system to the surroundings and the reversal may occur in certain events such as thermal decomposition or evaporation.

The instrumentation of TGDTA analysis comprises a furnace in which a sample is heated or cooled in a controlled environment and a transducer through which the changes in properties in the material are monitored. The DTA instrument is designed to compare the difference in temperatures between the sample and reference using two respective thermocouples. The reference material is selected in such a criteria that it does not undergo any thermal events over the test temperature range and does not react with any of the component in the instrument. On the occurrence of a thermal event, there is a data generation of nonzero ΔT, which is negative for endothermic and positive for exothermic reactions. In the present study, the starting dried gel powders obtained heat treatment at the rate of 10°C during heating and cooling to obtain the thermal events.

3.3.5 Dilatometry studies

Dilatometry is the most effective technique for the analysis of CTE in bulk specimens and it can also be used to determine the rate of sintering, rate of shrinkage, phase transition temperatures and vacancy information. In this technique, the linear change of sample length is recorded as a function of temperature using a push rod and the LVDT (linear variable differential transformer) device. For the present investigation, sintered alumina specimen was used as a standard reference for calibration. In general, the recorded pattern is plotted between the ratio of change in length with the original length and temperature. The push rod that is connected to the tip of LVDT moves the tip horizontally either in a positive or in negative directions, based on the expansion or the shrinkage of the specimen with respect to the increment in temperatures. In addition, this analysis provides the data on rate of densification

based on various heating rate and derive the optimum sintering schedule for obtaining effective and maximum sintered densities. Fig. 3.6 shows the picture of the dilatometer used in the present studies.

Fig. 3.6. Picture of the dilatometer used in the current studies

3.3.6 BET surface area analysis

The Brunauer Emmer and Teller (BET) technique is useful for analysing the surface characteristics of the nano powders. It is effective in finding the surface area, pore size and the pore volume of the powders. The technique works on the amount of adsorbate gases by the surface area of the particles and liquid nitrogen is used as a medium of analysis. The powders typically undergo a degassing event at temperatures closer to 200 – 300°C under vacuum prior to the analysis. The surface area of the powder specimen is calculated using the following formula.

$$BET = 1/ [V_a (P_0 / P - 1)] \quad \text{---------- (3)}$$

Where, P and P_0 – the partial vapour pressure and saturated pressure of adsorbate gas respectively, V_a – volume of adsorbed gas at room temperature and atmospheric pressure.

3.3.7 FTIR spectroscopy

FTIR (Fourier Transform Infrared) spectroscopy is a technique used to obtain an infrared spectrum corresponding to the absorption or emission of a solid, liquid and gas molecules. It collects spectral – resolution data of the material over a wide range of wavenumbers ranging between 400 – 4000 cm^{-1} and provides data on optical absorption or transmissions in the wavelength regions between ≈ 1.5 – 25 µm. The powder samples require a material support, which is non-reactive to the incident rays. Therefore, the powder samples are usually dispersed in the KBr powders followed by uniaxial compaction to form a thin wafers of thickness around 200 – 300 µm for the analysis. The solid samples are usually flattened at both the sides and made parallel to each other for the analysis.

Two terminologies such as total forward (TFT) and in-line or real-inline transmissions (RIT) commonly used in the field of transparent ceramics express their degree of transparency. TFT includes contributions from both scattered and un-scattered light whereas the RIT is the measure of only the un-scattered light. In other words, the total intensity transmitted through a window is called TFT whereas that within a narrow cone (3°- 5°) along the incident direction is called RIT. The difference between these two terms is called diffuse transmittance or forward scatter. In the area of transparent ceramics, the materials with RIT above 95 % theoretical (or above 82.2 % actual measured transmissions) are termed as transparent whereas the materials with RIT below 95% are termed translucent [14].

In the literatures, a first qualitative evidence of transparency of materials is obtained through a simple observation. In this context, a right approach needs a distance of at least 1 cm between the background image and the sample to prove the degree of transparency. On the contrary, direct placement of samples on the printed background includes both the scattered and un-scattered transmission and therefore considered as an invalid demonstration of showing transparency [15].

In the present report, the samples placed at least 1 cm above the background text to show the degree of transparency. Fig. 3.7 shows the experimental setup used for the measuring the transparency. TFT measurements require a spectrophotometer equipped with an integrated reflecting sphere to reflect all the diffuse scattered and un-scattered light towards the detector. In case of RIT measurements, a laser diode delivers radiations with controlled wavelengths and the sample placed between the light source and the detector with the distance of at least 1 meter from the detector measure the transmissions in-line with the light source. Only RIT measurements of materials considered for optical imaging applications [16].

In the present study, we measure the RIT for our transparent ceramics specifically in the IR region between 2 – 5 µm using FTIR spectrophotometer.

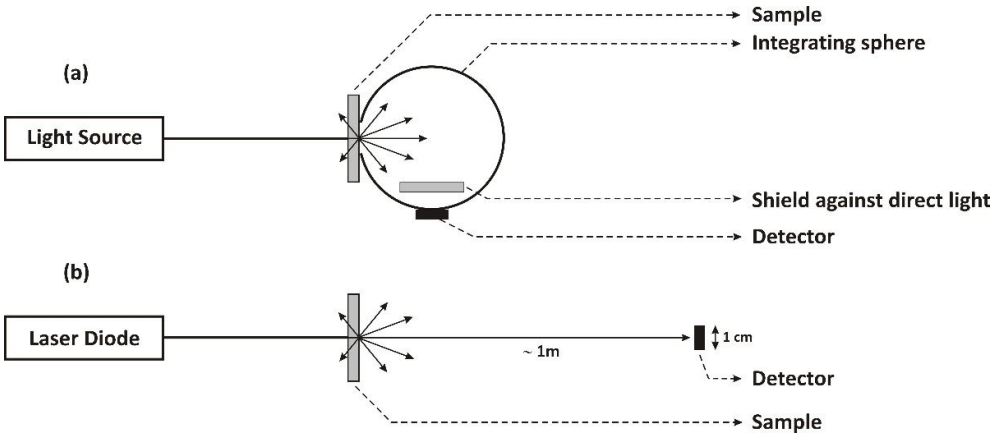

Fig. 3.7. Instrumentation for the measurement of (a) TFT and (b) RIT of transparent ceramic materials

3.3.8 Particle size analysis

The powders synthesized in this study characterized for their particle size distribution in order to estimate the range of distribution and for the mean particle sizes. The technique utilize photon correlation measurements on the homogenously suspended particle typically in the

water medium. The technique measures the angular variation in intensity of light scattered as a laser beam diffracts through the suspended particles. Larger particles diffracts at smaller angles while the smaller particles diffract the light wider. The angular scattering intensity data is further analysed to calculate the size of the particles based on their respective diffraction pattern using the Mie theory of light scattering assuming a volume equivalent to sphere. The technique employs the optical properties such as refractive index of the sample and the dispersant used. The final diameter of the particle is further calculated using the following Strokes – Einstein equation.

$D = K_B T / 6\pi\eta r$ ---------- (4)

Where D is diffusion coefficient, K_B is Boltzmann constant, T is absolute temperature, η is viscosity of the medium and r is particle diameter.

In the present studies 1 – 2 wt % of solid loaded aqueous suspension of powders were prepared using 0.5 % of Darvan – 821 A as a dispersant. The suspension was milled for a period of 12 hours in a ball mill. Alumina balls of 2 mm diameter was used for milling. The suspension was further diluted to the concentrations of 0.1 wt% followed by ultra-sonication for 30 minutes for the measurement of particle size analysis.

3.3.9 Viscosity

The analysis of viscosity was mainly used during the investigations of synthesizing AlON powders through aqueous sol – gel-processing technique as detailed in chapter 7. In principle, the viscosity of a liquid is a measure of its resistance to flow. Apart from the intrinsic flow properties, the viscosity of a liquid may vary by the additionally added substances such as powder particles. These particles collide each other and move at different velocities in the flowing fluid and alter or reduce the overall flow of the mixture. For example, the boehmite sol prepared in the study showed an initial viscosity of 0.01 Pa. s during the initial stage of

synthesizing AlON powders. However, the viscosity increased drastically to the values of 0.45 Pa. s after the addition of AlN particles to the sol. The increase in the viscosity was partly due to the addition of solid AlN particles in the liquid sol and majorly due to the hydrolysis reactions of AlN powders occurred in the aqueous sol. In the viscosity studies, 20 ml of sol was poured in a cylindrical cup and attached to the rotating cone shaped spindle for measuring the resistance to flow or the changes in viscosity.

3.3.10 Thermal conductivity

Thermal conductivity (λ) with the unit W/(m.K) is the measure of transport of energy in the form of heat through a body of mass due to temperature gradients. It is well known that the heat flows from higher end to the lower as per the second law of thermodynamics. The thermal conductivity of a material is calculated using the following equation

$$\lambda = \rho . C_p . \alpha \qquad \text{---------- (5)}$$

Where, ρ is density of the specimen measured by Archimedes principle, C_p is specific heat capacity and α is thermal diffusivity. In the present study, the sample of dimensions 10mm X 10mm X 1 mm was used for the analysis using laser flash technique. This technique is a kind of transient method that provides transitional thermal flow to the specimen and determines the characteristic of thermal conductivity with respect to temperatures. Fig. 3.8 shows the schematic setup of the laser flash technique and the principle used for measuring the thermal diffusivity. To conduct this study, a short laser energy pulse heats the top surface of a flat surfaced, parallel edged sample. The resulting change in temperature on the lower surface of the sample is measured by means of infrared detector. The raise in temperature with respect to time corresponds to the thermal energy diffusion along the thickness of the specimen. The thermal diffusivity α is calculated using the following equation

$$\alpha(T) = 0.1388 \text{ X } (d^2/t_{1/2}) \qquad \text{---------- (6)}$$

Where T is the temperature of measurement, d is thickness of the specimen and $t_{1/2}$ is time needed for the rear side of the specimen to reach half the maximum temperature [17].

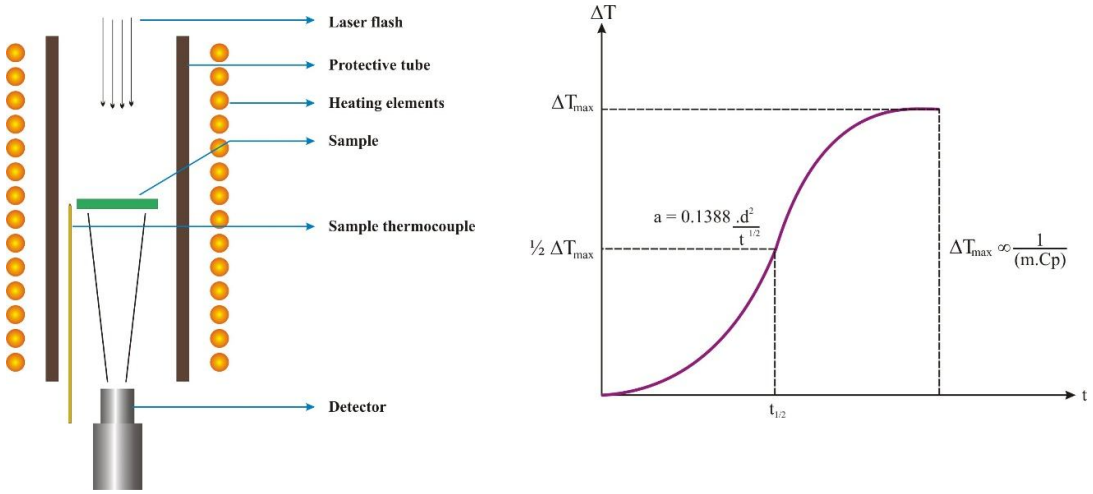

Fig. 3.8. Schematic and the temperature raise curve of laser flash method

3.3.11 Hardness and fracture toughness

Hardness is the property of resistance of material against plastic deformation achieved from indentation of a predetermined geometry indenter on a flat surface of a metal or ceramic under a fixed load. Based on the theoretical hardness and the physical geometry of a material, the test is conducted either with Vickers or with Knoop indentation. The indenter for the Vickers is a square – based pyramidal – shaped diamond with face angles of 136° while for the Knoop it is a rhombic – based pyramidal shaped diamond with edge angles of A = 172°30' and angles of B = 130° 0' as shown in fig. 3.9a and 3.9b respectively. The Knoop hardness reported with units of GPa is determined using the following equation [18].

$Hk = 0.014229 \text{ X } P/d^2$ ---------- (7)

Where, P is force in Newton and d is the length of the long diagonal of the indentation in mm.

The Vickers hardness reported with units in GPa is calculated based on the following equation

$$Hv = 0.0018544 \text{ X } P/d^2 \qquad \text{---------- (8)}$$

Where, P is force in Newton and d is the length of the long diagonal of the indentation in mm.

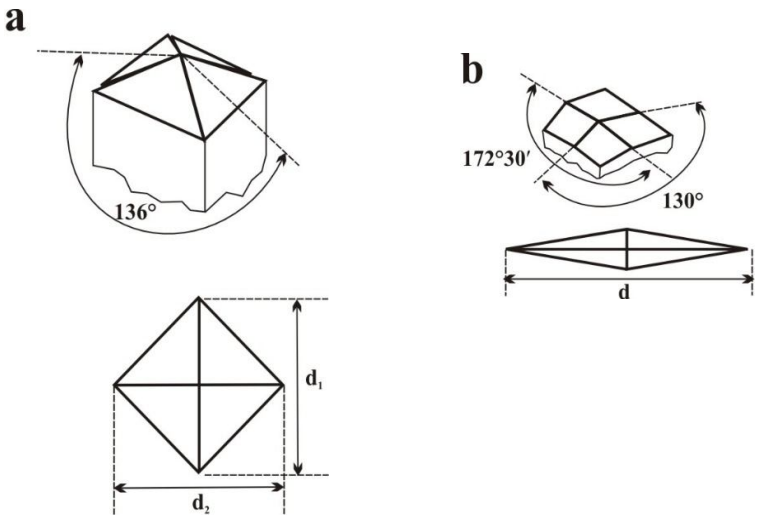

Fig. 3.9. Dimensions of the indenter used for the determination of (a) Vickers Hardness (Hv) and (b) Knoop Hardness (Hk)

The fracture toughness is the property of material that indicates its resistance to crack propagation under applied stress. It is a sign of the existence of the flaws in the sintered microstructure and shows the strengths of grain and grain boundaries. In the present study, fracture toughness was measured with the fractures that developed during indentation test using the Anstis principle [19] as per the following equation.

$$K_{IC} = 0.016 (E/H)^{1/2}(P/C^{3/2}) \qquad \text{---------- (9)}$$

Where, E is the Young's Modulus, H is Hardness, P is Applied Load and C is Half Penny Crack Length formed at the indent's corners during the hardness tests.

3.3.12 Archimedes Principle for density and porosity measurements

The porosity and the density of the sintered specimens were characterized using the Archimedes principles as per the ASTM standards B962 [20]. According to this standards, the test specimen is first weighed in air in the dried condition which is termed as dry weight (W_d). The sample is further subjected to boil in water for a period of at least one hour to fill the open pore channels of the sample. The weight in air after boiling is termed as soaked or wet weight (W_w). The weight of the wet sample in water (sample in submerged in water) is termed as suspended weight (W_s).

The porosity and the density of the sample is calculated using the following formula

$$\text{Porosity (\%)} = (W_w - W_d) \times 100 / (W_w - W_s) \quad \text{---------- (10)}$$

$$\text{Density (g/cc)} = W_d / (W_w - W_s) \quad \text{---------- (11)}$$

References

1. S. S. Pooyan, Sol – gel process and its application in nanotechnology, J. Polym. Engg. Technol. 13 (2005) 38 – 41
2. R. Asmatulu, Nano coatings for corrosion protection of aerospace alloys, Corr. Protect. Contr. Nanomater. Woodhead publishing series in metals and surface engineering, (2012) 357 – 374
3. J. Li, Y. Pan, C. Xiang, Q. Ge, J. Guo, Low temperature synthesis of ultrafine α – Al2O3 powder by a simple aqueous sol – gel process, Ceram. Inter. 32 (2006) 587 – 591

4. N. Mamana, A. D. Parralejo, A. L. Ortiz, F. S. Bajo and R. Caruso, Influence of the synthesis process on the features of Y_2O_3 stabilized ZrO_2 powders obtained by the sol – gel method, Ceram. Inter. 40 (2014) 6421 – 6426
5. J. Marugan, P. Christensen, T. Egerton and H. Purnama, Synthesis, characterization and activity of photocatalytic sol – gel TiO_2 and electrodes, Appl. Catal. B. Environ. 89 (2009) 273 – 283
6. Q. GuO, D. Huang, X. Kou, W. Cao and J. Li, Synthesis of disperse amorphous SiO_2 nano particles via sol – gel process, Ceram. Inter. 43 (2017) 192 – 196
7. Y. Zhang, Y. Ding, J. Gao and J. Yang, Mullite fibres prepared by sol – gel method using polyvinyl butyral, J. Eur. Ceram. Soc. 29 (2009) 1101 – 1107
8. Q. He, M. Quin, M. Huang, H. Wu, H. Lu, H. Wang, X. Mu, Y. Wang and X. Qu, Synthesis of highly sinterable AlN nano powders through sol – gel route by reduction – nitridation in ammonia, Ceram. Inter. 45 (2019) 14568 – 14575
9. A. Najafi, F. G. Fard, H. R. Rezaie and N. Ehsani, Synthesis and characterization of SiC nano powder with low residual carbon processed by sol – gel method, Pow. Technol. 219 (2012) 202 – 210
10. G. V. Aguilar, Introductory chapter: A brief semblance of the sol – gel method in research, Sol – gel method – Design and synthesis of new materials with interesting physical, chemical and biological properties, DOI: 10.5772/intechopen.82487 (2018) 1 – 6
11. D. S. Kumar, B. J. Kumar and H. M. Mahesh, Quantum nanostructures (QDs): An overview, Chapter 3, Synthesis of inorganic materials, Woodhead publishing (2018) 59 – 88
12. K. J. Morris, Cold isostatic pressing, Concise encylopedia of advanced ceramic materials, DOI: 10.1016/B978-0-08-034720-2.50031-9, (1991) 84 – 88

13. R. F. Davis, Hot isostatic pressing, Concise encylopedia of advanced ceramic materials, DOI: 10.1016/B978-0-08-034720-2.50061-7, (1991) 210 – 215
14. M. R. Merac, H. Kleebe, M. M. Muller and I. E. Reimanis, Fifty years of research and development coming to fruition; unraveling the complex interactions during processing of transparent magnesium aluminate ($MgAl_2O_4$) spinel, J. Am. Ceram. Soc., 96 (2013) 3341–3365
15. A. Krell, G. Baur, and C. Dahne, Transparent sintered sub - μm Al_2O_3 with IR transmittivity equal to sapphire; pp. 199 – 207 in Window and dome technologies VIII, Vol.5078, Proceedings of SPIE, Edited by Randal.W. Tustiston., *et al.* SPIE—The International Society for Optical Engineering, Orlando, 2003
16. A. Krell, T. Hutzler and J. Klimke, Transmission physics and consequences for materials selection, manufacturing and applications, J. Eur. Ceram. Soc. 29 (2009) 207 – 221
17. T. W. Lian, A. Kondo, M. Akoshima, H. Abe, T. Ohmura, W. H. Tuan and M. Naito, Rapid thermal conductivity measurement of porous thermal insulation material by laser flash method, Adv. Powd. Technol. 27 (2016) 882 – 885
18. Standard test method for micro indentation hardness of materials, ASTM E 384 – 05a, ASTM International, U. S. A
19. G. R. Anstis, P. Chantikul, B.R. Lawn and D.B. Marshall, A critical evaluation of indentation techniques for measuring fracture toughness: I, Direct crack measurements J. Am. Ceram. Soc., 64 (1986), 533 – 538
20. Standard test methods for density of compacted or sintered powder metallurgy (PM) products using Archimedes principle, ASTM B 962 – 08, ASTM International, U. S. A.

CHAPTER - IV

Fabrication and properties of IR transparent alumina

4.1 Introduction

Fabrication of transparent alumina ceramics having controlled sintered grain sizes in the sub-micron region require constant attention in every stage of processing. The prime key of manufacturing IR transparent alumina is synthesizing ultra-fine (≤100nm), ultra-pure (99.99%) and highly reactive alumina powders. In the present report, the powders with these characteristics and suitable for the fabrication of transparent ceramics is termed as optical grade powder. The next key comprises fabrication of defect free green bodies, sintering to obtain 97% of T.D. and retaining the average sintered grain sizes < 1 μm. The subsequent process involve reaching 100% densification without further increment in the grain sizes followed by optical surface polishing for the successful manufacturing of transparent alumina. The powder synthesized in this study was characterized for its morphology, particle size and phase purity and the transparent alumina was characterized for its physical, mechanical and optical properties.

4.2 Process highlights

- For the first time, sintered submicron alumina with high inline transparency in mid infrared region has been fabricated using sol–gel derived powders
- The powder was seeded with α – Al_2O_3 particles for enabling effective inter-particle coordination and improved densification
- Seeding with α – Al_2O_3 also assisted achieving equiaxed sintered grains

- Traces of γ - Al_2O_3 was retained in the synthesized powder for enhancing low temperature densification and controlling sintered grain sizes in the submicron regions
- The powder synthesized in this process is scalable and suitable for producing transparent alumina components
- IR transparent alumina fabricated in this study exhibited inline transmissions up to 87% in 3 – 5 μm region which is equivalent to the transmissions of single crystal sapphire
- The samples exhibited hardness closer to 20.5 GPa which is higher than the hardness of sapphire.
- Transparent alumina window of dimensions up to 80mm diameter and 0.9 mm thickness were produced in this study
- The method is suitable for producing simple and complex shaped components in large scales

4.3 Synthesis of optical grade α - alumina powder

In the present study, a facile route involving sol-gel processes was followed for the synthesis of optical grade α - alumina powder. The process includes various steps such as synthesis of boehmite sol, addition of seed particles, calcination etc. The boehmite sol preparation was performed using highly dispersible and commercially available boehmite powder (Disperal, Sasol Germany GmbH, Germany). Seeding the sol was executed using commercial α alumina powder from SM8, Baikowski Chemie, France. Table 4.1 shows the characteristics of these raw materials as per the specifications given by the supplier. Fig. 4.1 shows the flow chart of the entire procedure followed for the synthesis of optical grade alumina powder.

Characteristics (as per the suppliers specifications)	Boehmite	Alumina seeds
Manufacturer	Disperal, Sasol, Germany	SM-8, Baikowski Chemie, France
Particle Size (d_{50})	2.5 µm	0.4 µm
BET Surface Area (m^2/g)	180	14
Chemical Analysis	Al_2O_3 - 77%, Na_2O - 0.002%, Fe_2O_3 - 0.01%, SiO_2 - 0.012%	Fe-3ppm, Na-13ppm, Si-16ppm, Ca-2ppm, K-22ppm, Mg, Ti, Cr, Mn, Ni, Cu, Zn < 1ppm

Table 4.1: Characteristics of precursors

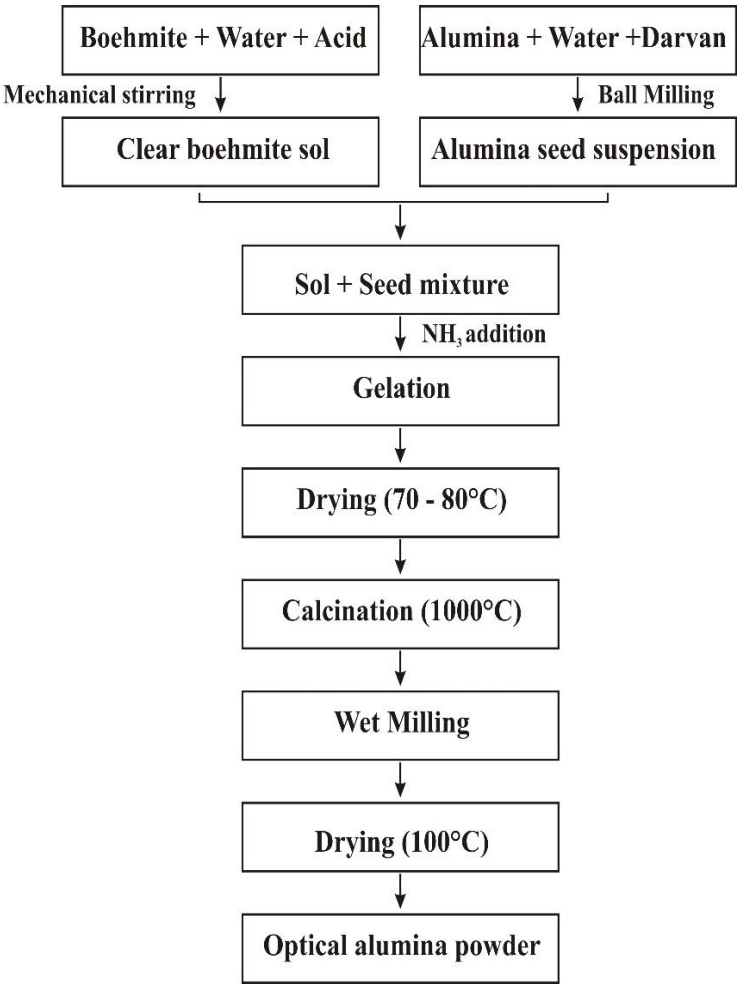

Fig. 4.1. Process flowchart for the synthesis of optical grade alumina powder

4.3.1 Preparation of boehmite sol

The process initiates with the mixing of boehmite powder with distilled water at 2:8 weight ratios under constant stirring conditions using mechanical stirrer at 30°C. Peptization was carried out after 1h stirring by dropwise addition of glacial acetic acid (Standard Reagents, India) to adjust the pH between 2 and 2.5 to obtain the stable sol. The sol was kept idle for a period of 24 hours for allowing the unreacted boehmite traces to settle. The supernant clear sol (fig. 4.2) was transferred to another container and used for the entire process. 10 g of clear sol was dried at 100°C and calcined at 1200°C in air to find out the actual content of $\alpha - Al_2O_3$ in the sol.

Glacial acetic acid for the peptization process was preferred due to its versatility in controlling the pH of the sol and its environmentally friendly properties. Controlled change or adjustment of pH during peptization process is necessary to obtain effectively suspended sol and govern the morphology and the particle size of the powders produced.

Fig. 4.2. Stable boehmite sol prepared in this study

4.3.2 Preparation of alumina seed suspension

α-alumina powder and water were mixed at 75:25 weight ratios using 1 % of Darvan 821A (R.T.Vanderbilt Co., Inc., Norwalk, CT, USA) as a dispersant. Mixing was carried out in a polyethylene container using high purity (>99.9%) alumina balls as milling media. High purity balls were used to avoid inclusion of any contaminations from grinding media during milling. The mixture was ball milled for 12 hours to obtain the homogeneous aqueous α-alumina suspension.

4.3.3 Alumina seeding and gelation

The clear boehmite sol was stirred for one hour using high speed mechanical stirrer followed by the addition of magnesium nitrate hexahydrate ($Mg(NO_3)_2.6H_2O$, Sigma Aldrich, U.S.A) having concentration corresponding to 300 ppm of MgO with respect to the final alumina content. MgO is used as a sintering aid in this study.

Under constant mechanical stirring conditions, dispersion of α-alumina seeds in the form of a suspension into sol was carried out. 1:9 was the dry weight ratio between the alumina from sol and alumina from suspension. Stirring was continued for 1h to obtain the homogeneous dispersion of seeds in the sol. Ammonia was added dropwise after 1h of dispersion to adjust the pH between 13 and 14 for effecting gelation.

4.3.4 Powder calcination

Drying the gel at 70 – 80°C in a hot air oven for 48h produced the dried hydrogel followed by calcination at 1000°C for 2h in the air atmosphere to obtain calcined alumina granules. The calcined alumina granules were further milled in the planetary ball mill (PM400, Retsch, Germany) at 200 rpm for 2h in ethanol medium. As a binder, one weight % of polyvinylpyrrolidone (PVP) (Sigma Aldrich, U.S.A) was added during milling. High pure (>99.9%) alumina jars and alumina balls were used for milling to avoid the inclusion of

contaminations during milling. The milled slurry was further dried at 70°C in air and sieved through a 100-mesh sieve to obtain optical grade alumina powder.

4.4 Fabrication of transparent alumina samples

The alumina powder was compacted uniaxially at 40 MPa pressure to produce samples having 30 mm diameter and 5 mm thickness. The shaped samples were further pressed cold isostatically at a pressure of 200 MPa for a period of 2 minutes and sintered at temperatures from 1200°C to 1400°C in air atmosphere for 1 hour to obtain densification. The heating and cooling rate was maintained as 5°C/minute. The sintered samples with no open porosity were further pressed hot isostatically (HIPed) at 1350°C for 5h in an argon atmosphere at 195 MPa pressure (American Isostatic Press Inc. U.S.A) to obtain transparent alumina samples. Fig. 4.3 shows the image of alumina samples at various stages of its processing such as (a) after compaction (green stage), (b) after air sintering and (c) after hot isostatic pressing. The HIPed samples were further ground and polished to the thickness of 0.9 mm using diamond suspensions of various grit sizes ranging between 15µm and 1µm to obtain optically transparent alumina samples.

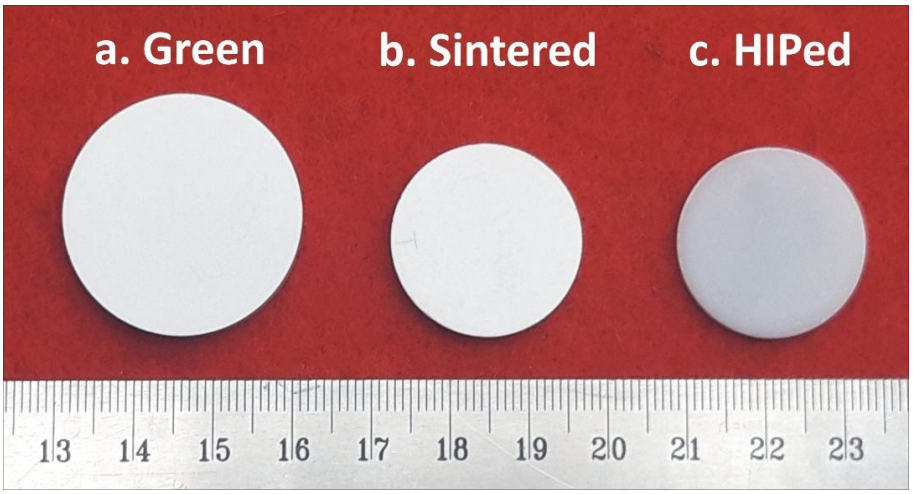

Fig. 4.3. Transparent alumina samples at various stage of processing
a. green, b. as – sintered, c. after HIPing

4.5 Materials Characterization

Microstructure analyses of the starting materials such as boehmite and seed alumina powder were carried out through high-resolution FE-SEM (Hitachi, 3200S, FESEM, Tokyo, Japan). The hydrogel obtained after drying process was subjected to TG-DTA analysis (Netzsch STA 409C, Selb, Germany) to estimate the phase transformation temperatures and optimize the calcination temperature of dried gel for synthesizing α - alumina powder. Confirmation of phase formation after calcination was carried out using XRD (D8, Bruker, Karlsruhe, Germany). The microstructure of alumina powder derived in the present method, and the seed distribution in the final alumina powder was studied using high-resolution FEG SEM and TEM (FEI, Technai G2, Netherlands) analyses.

Porosity and density characterizations of sintered and HIPed samples were carried out through Archimedes principle and their polished and thermally etched microstructures through FE-SEM. Hardness was measured by Vickers (Leco, St. Joseph, MI) indentation at 10 kg load and the inline transmission for the HIPed and polished alumina disc of 0.9 mm thickness was measured in the wavelength region between 1 and 6 μm using FTIR analyzer (Spectrum GX, Perkin Elmer, C.T, U.S.A).

4.6 Results and Discussions

4.6.1 Physical characteristics of starting precursors

Fig. 4.4 shows the powder morphology of starting precursors such as alumina seeds and boehmite powder. Fig. 4.4a shows the microstructure of α-alumina seeds, which are mostly un-agglomerated and round edged particles with the narrow particle size distribution in the range between 150 nm and 400 nm. Fig. 4.4b shows the characteristic microstructure of boehmite powder with the particles of random shapes and irregular morphology with a wide range of particle size distribution extending between 1 μm and 20 μm.

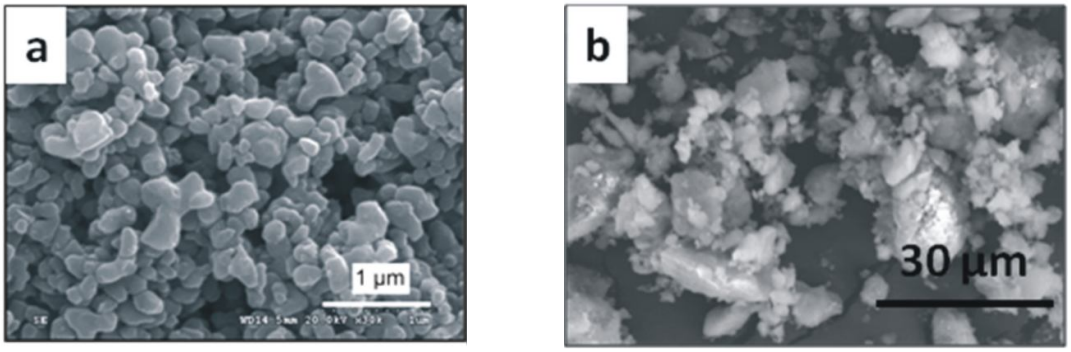

Fig. 4.4. Morphology of starting precursors

4.6.2 Thermal behaviour of dried hydrogel

Fig. 4.5 shows the TG-DTA curves recorded during the analysis of dried hydrogel powder. TG curve shows the weight loss in two stages where the initial weight loss at 100°C to 150°C corresponds to the loss of physically combined water. The subsequent weight loss at 460°C to 470°C was probably due to loss of chemically combined water. The weight loss in these temperature regions may also occur due to the reaction initiation for the formation of γ alumina. The DTA curve also complements the formation of γ phase where the initiation of phase formation starts at 460°C to 470°C. The exothermic peak at 550°C is the characteristic peak for γ alumina formation. Another exotherm at 1050°C without weight loss represents the transformation of alumina from γ to α phase. At these regions, γ alumina that is a cubic crystal completely transform to highly stable hexagonal α alumina [1]. As per the report by *Kumagai et al.*, retaining traces of γ alumina in the calcined α alumina acts as a nucleation sites and improves its reactivity and densification characteristics [2 – 3]. Therefore, in the present study, the dried hydrogel powder was calcined at little lower temperatures that is 1000°C. Lower calcination temperatures preserve few traces of gamma phase and further prevent the formation of hard granules in the final calcined alpha alumina powder.

The calcined α Al_2O_3 powder retained only traces of γ Al_2O_3 in order to obtain equiaxed grains after sintering. *Kumagai et al.*, observed vermicular or elongated sintered grains for the powders having larger volume of γ phase Al_2O_3 in the calcined powders. Sintered microstructure with equiaxed submicron grains circumvent the effect of birefringence scattering, which may be a notable concern with verimular or elongated grains.

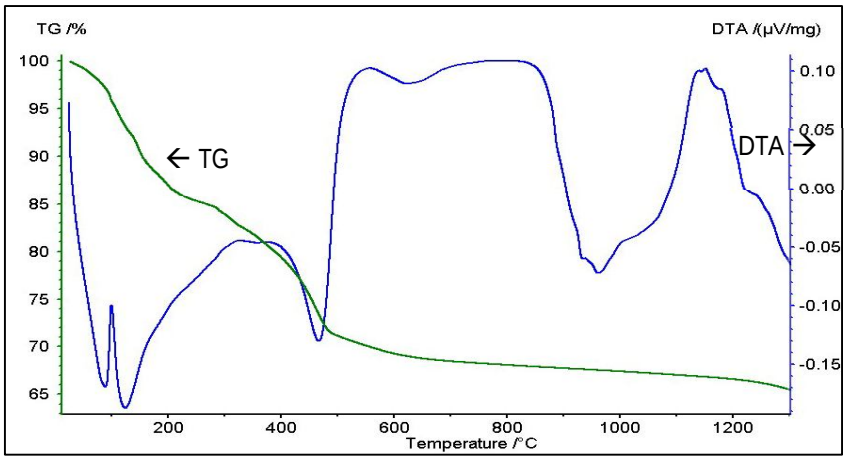

Fig. 4.5. TG-DT analysis of dried hydrogel powder

4.6.3 Phase formation studies

Fig. 4.6 shows the evolution of phase formation of dried hydrogel at its various stages of calcination. XRD pattern of hydrogel (Fig. 4.6a) dried at 100°C shows peaks corresponding to boehmite and alpha alumina seeds. At a calcination temperature of 600°C (Fig. 4.6b), XRD pattern shows the appearance of peaks corresponding to γ- alumina which is in agreement with the TG-DTA data for the formation of γ-phase at 550°C. The pattern also contains peaks corresponding to α-phase from alumina seeds. At a calcination temperature of 1000°C, significant parts of γ phase transformed to α-phase. Traces of γ-alumina stretch were still visible in the pattern that was not changed to α-phase alumina at this calcination temperature (Fig. 4.6c). As mentioned earlier, as nucleation sites, the traces of γ-phase were maintained in the calcined powder for enhanced densification of α-alumina.

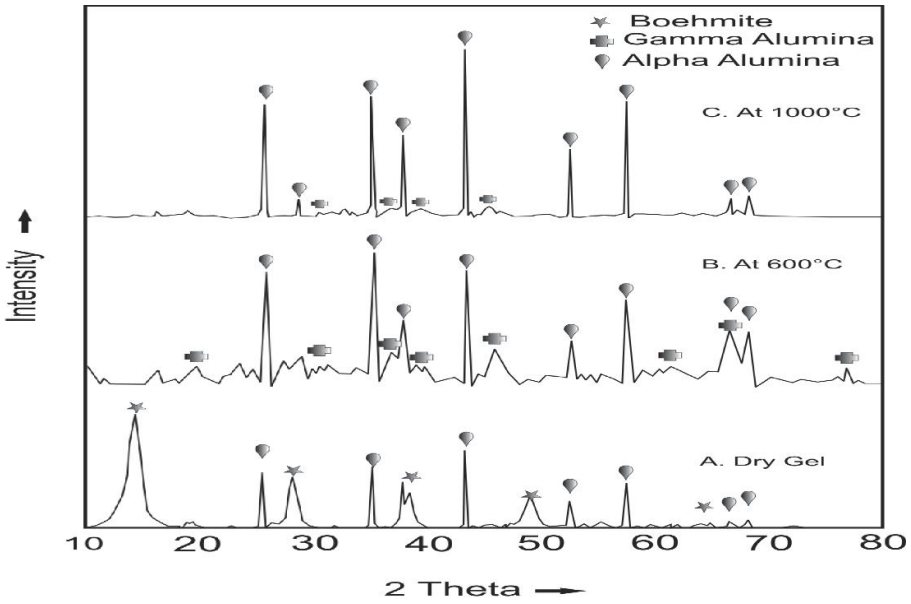

Figure 4.6. XRD analysis of dried hydrogel (a) as synthesized. (b) Calcined at 600°C, (c) Calcined at 1000°C

4.6.4 Alumina seeding and microstructure studies

Fig. 4.7 shows the microstructure of the powder calcined at 1000°C. The alumina particles derived from sol exhibit homogenous and narrow size distribution ranging between 20nm and 40nm as shown in fig. 4.7a. In addition, the seed alumina particles with particle size of 200 nm distributed homogeneously within the alumina powder particle matrix derived from sol. The particles exhibit curved edges, which is an important feature for obtaining improved inter-particle coordination during shaping [4 – 5].

Ultra-fine raw powders having particle sizes <100nm are ideal to initiate the further processing to produce sub-micron grained transparent polycrystalline alumina. Nano powders with such sizes possess strong surface curvature and exhibit higher surface diffusion and condensation activity to promote sintering. However, literature state that the active surface curvatures also favour strong agglomeration resulting in inhomogeneous pore distribution and retard tendency of densification [6]. This inherent character of the nano powders would be a possible reason

for most of the researchers to utilize coarser powders having the particle size of 200nm to produce high inline transparent alumina even though they are exorbitantly expensive [7 – 14].

However, the present study has succeeded in controlled densification and achieved the high inline transparency using powders having particle sizes less than 40 nm. The probable reason would be the addition of 10% α-alumina seeds that have reduced the substantial surface curvature activity to the extent to favour controlled densification. In addition, the seeds inclusion in the sol-gel processing enhanced low-temperature θ to α transformation. Literatures reports the concept of seeding for enhancing θ to α transformation at lower temperatures in sol-gel alumina processing [2 – 3, 15]. The seed concentration of 1 – 1.5 % was found to be sufficient for such conversion. Whereas, the present study utilized alumina seeds up to 10 weight % not only to enhance low-temperature θ to α transformation but also to improve the homogeneity of particle coordination and the packing factor. The homogenous particle coordination improves the green consolidation during shaping and enhances the densification at lower temperatures [16].

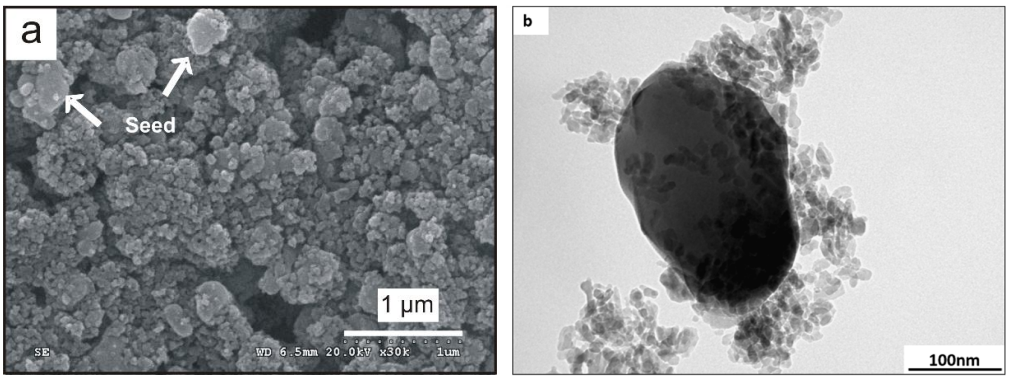

Fig. 4.7 Microstructure of alumina powder calcined at 1000°C (a) SEM analysis, (b) TEM analysis

TEM image of the calcined powder in fig. 4.7b confirms the 200nm sized seed particle surrounded by nano alumina powders having the size between 20 and 40nm. As we discussed above, this compositional mixture has assisted the nanoparticles to overcome their intense surface curvature activity and agglomeration tendency and favoured controlled densification.

4.6.5 Physical characterization of sintered and HIPed alumina samples

Fig. 4.8 shows the densification behaviour of green alumina samples as a function of sintering temperatures. The samples exhibited 90% theoretical density (T.D.) for the firing temperature of 1200°C and for 1300°C, the density enhanced to 95% of T.D. The samples exhibited traces open porosities up to 1 % and further increment of sintering temperatures to 1400°C removed all the open porosities. The samples exhibited theoretical densities up to 97% at these sintering temperatures. The steady rate of increment in the sintered density indicate the controlled rate of grain growth and gradual elimination of pores from the microstructures. Attaining such level of densification in air atmosphere is highly economical compared to the practices involving hydrogen sintering [14]. The samples with no open porosities can be HIPed without any encapsulation for the elimination of residual porosity. Encapsulation free HIPing procedures enhance the versatility of producing large and complex shape articles such as domes and radomes. Therefore, the present method of fabrication procedure is ideal for producing transparent alumina articles in larger production scales. The samples having 97% T.D. attained 100% T.D. after HIPing at 1350°C.

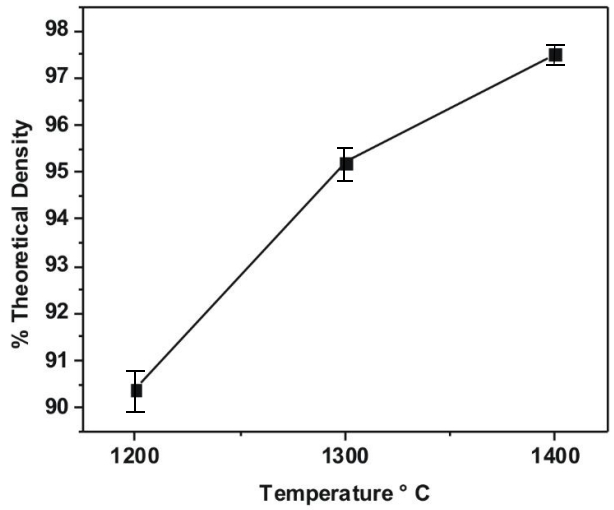

Fig. 4.8 Densification behaviour of alumina samples with respect to sintering temperature

4.6.6 Microstructural and mechanical characteristics of alumina samples

Fig. 4.9a shows the polished and thermally etched microstructure of the sample sintered at 1400°C. The microstructure shows clear grains and grain boundaries of alumina with no presence of impurities and second phases. However, traces of closed pores existed in the grain boundaries. Pores at intergranular sites indicate that the grains have grown under control rate whereas abnormal or discontinuous grain growth develop pores at intra-granular locations. The MgO added in the mixture prevented such discontinuous growths, restrained abnormal grain mobility and assisted controlled grain formations [17]. The microstructure shows that the grains with the average size of 800 nm with the distribution between 0.2 μm and 1.6 μm. However, presence of pores in the microstructures subside the light transmission due to scattering and makes the body opaque. Therefore, it is necessary to remove all the traces of pores to make the body transparent [18]. A conventional practice of increasing the sintering temperatures beyond 1400°C would have assisted the pore elimination in the present study. However, increasing sintering temperature leads to grain growth that further leads alumina in the direction of

translucency rather than transparency. Therefore, the present study utilized HIPing operation for removing pores without entertaining grain growth.

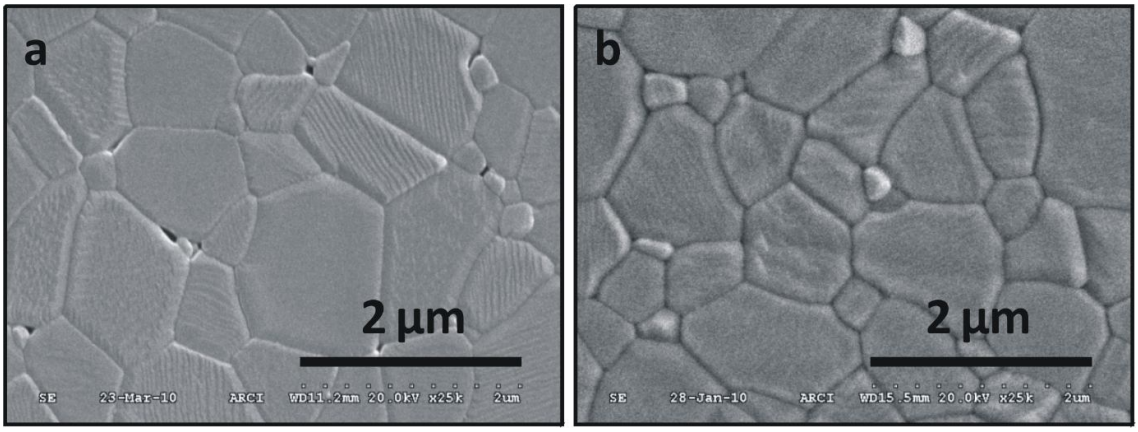

Fig. 4.9 Microstructure of samples (a) sintered at 1400°C, (b) Sintered at 1400°C and HIPed at 1350°C

Fig. 4.9b shows the microstructure of transparent alumina after HIPing at 1350°C with 195 MPa pressure. The microstructure indicates that the body with no presence of pores at intra or intergranular sites and exhibit complete densification to 100% T.D. HIPing eliminate the pores from the microstructures by squeezing them through the grain boundaries without causing any structural defects. In addition, since the HIPing temperature retained well below the sintering temperature, the samples after HIPing have not exhibited any grain growth. Therefore, the sintered grain sizes ranging between 0.2 µm and 1.6 µm with the mean size of 800 nm as shown in fig. 4.9a could be maintained even after the HIPing process.

The Vickers hardness of the polished sintered submicron alumina was found to be 18.5 GPa for the samples sintered at 1400°C which was increased further to 20.5 GPa after HIPing. These values are in agreement with the reported data for the HIPed submicron alumina. Moreover, these hardness values are said to be superior to the hardness of single crystal sapphire which is

about 18.5 GPa [9]. Studies of Krell et al. [9] and Kong et al. [32] also reported similar observations of higher hardness for polycrystalline transparent alumina. These observations can be attributed to the engineered grain boundary and grain size, which is complemented by the Hall Petch equation. Further, the absence of residual porosities achieved through hot isostatic pressing also contributes to the higher hardness observed.

4.6.7 Optical Characterizations

Fig. 4.10 shows the highly transparent sintered alumina disc fabricated in the present study.

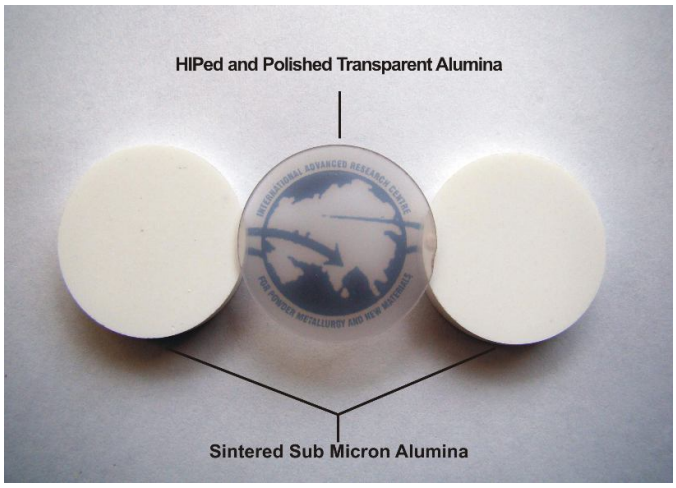

Fig. 4.10 Photograph of transparent alumina fabricated in this study (Centre), the samples at both the adjacent sides are the as-sintered alumina samples

The sample is placed above one inch from the printed background for confirming its degree of transparency. The white opaque samples at the adjacent sides are as – sintered at 1400°C for 1 hour in air. A remarkable change in the physical and optical appearance changing from opacity to transparency was observed after HIPing. It was evident that the nanoparticles of sizes less than 40nm could be successfully sintered to these levels of transparency through controlled densification using appropriate quantity of alumina seeds. The transparent disc placed in the

center in fig. 4.10 was obtained after HIPing and polishing to 0.9 mm thickness. The transparent sample was placed 1 cm above the surface of the underneath picture to exhibit the degree of transparency. Fig. 4.11 shows the IR transmission spectra of 0.9 mm thick polished transparent alumina sample obtained by the present method.

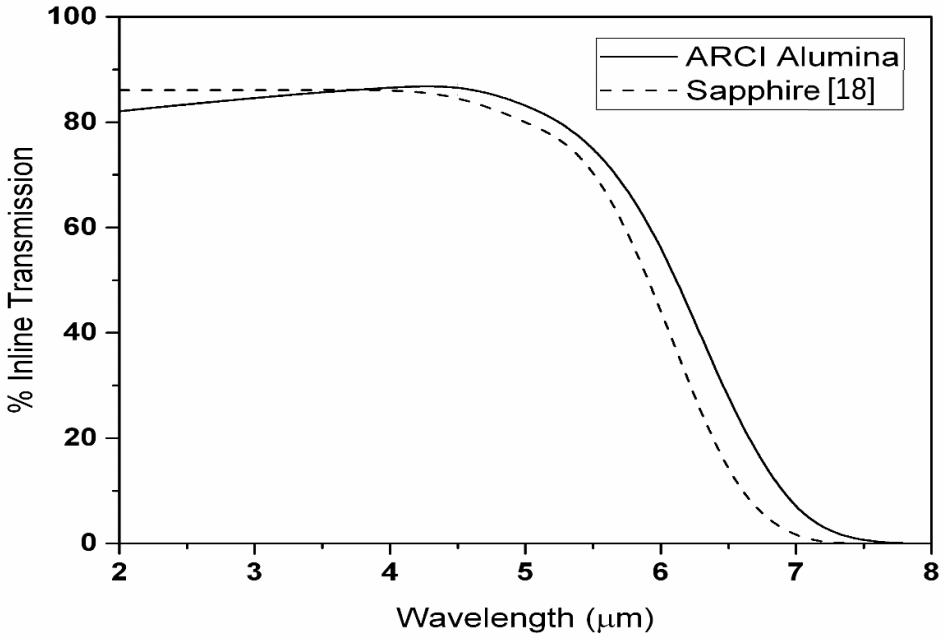

Fig. 4.11 IR transmission pattern of the transparent alumina (0.9mm thickness) fabricated in this study.

The transparent alumina samples show broadband transmission from 82 % to 87% between 2 and 5 μm regions with no remarks of any absorption peaks in the entire region proving that the material is free from any structural defects such as impurities, pores and second phases. The transparency reached to the levels of theoretical transmissions of alumina in the IR regions, which is at par with the transmissions of sapphire and as equivalent with the best transmissions hitherto reported for submicron alumina materials [11, 16, 18]. A slight decrement in the transmissions compared to the sapphire at the wavelength of 2 μm is attributed to the inherent declination characteristics of sub-micron alumina towards visible regions. To the best of our

knowledge, for the first time, the transparent alumina has been fabricated using sol-gel powders with an exceptional mechanical properties and superior optical transparency above 85% in the mid wave IR region.

The above work entitled “Processing and properties of sintered submicron IR transparent alumina derived through sol–gel method” has been published by **R. Senthil Kumar**, Asit Kumar Khanra and Roy Johnson in the journal of sol-gel science and technology 86 (2018) 374–382. https://doi.org/10.1007/s10971-018-4651-9

4.7 Summary

Highly reactive nano α – alumina powder for the fabrication of sub – micron transparent alumina has been successfully synthesized using a facile sol-gel approach. Appropriate addition of alumina seeds enhanced the inter-particle coordination and assisted the fabrication of flawless green bodies. MgO improved the low temperature densification to obtain 97% of T.D. at 1400°C and controlled the average grain growth to 0.8 µm. HIPing at 1350°C removed all the intergranular pores and transforming the sintered samples from opacity to optically transparent alumina with an exceptional mechanical and optical properties. The optically polished alumina samples having 0.9mm thickness fabricated in this study exhibited transmissions up to 87%, which is at par with transmissions of single crystal sapphire in mid-wave IR regions.

4.8 References

1. Lamouri S, Hamidouche M, Bouaouadja N, Bellhouchet H, Garnier V, Fantozzi G, Trelkat J F (2017) Bull Span Soc Ceram Glas 56: 47 – 54
2. M. Kumagai, and G. L. Messing, Enhanced densification of boehmite sol – gels by α – alumina seeding, Comm. Am. Ceram. Soc. (1984) C-230 – 231
3. M.Kumagai, and G. L. Messing, Controlled transformation and sintering of a boehmite sol – gel by α – alumina seeding, J. Am. Ceram. Soc. 68 (1985) 500 – 505
4. H. Ma and A. Krell, Synthesis and processing of Nano – α – Al_2O_3 powders, Key Engg. Mater. 206 – 213 (2002) 43 – 46
5. A. Krell and J. Klimke, Effects of the homogeneity of particle coordination on solid-state sintering of transparent alumina, J. Am. Ceram. Soc. 89 [6] (2006)1985 – 1992
6. A. Krell, T. Hutzler and J. Klimke, NATO – OTAN - nano materials technology for military vehicle applications, report entitled "Physics and technology of transparent ceramic armor: sintered Al_2O_3 Vs cubic materials", (2006) 14-1 – 14-10 http://www.dtic.mil/get-tr-doc/pdf?AD=ADA469603
7. A. Krell, P. Obenaus, Grain shape in sintered submicrometer alumina, J. Eur. Ceram. Soc. 18 (1998) 1 – 13
8. J. Echeberria, J. Tarazona, J.Y. He, T. Butler and F. Castro, Sinter-HIP of α-alumina powders with sub-micron grain sizes, J. Eur. Ceram. Soc. 22 (2002) 1801 – 1809
9. D.Godlinski, M. Kuntz, and G. Grathwohl, Transparent alumina with sub micrometer grains by float packing and sintering, J. Am. Ceram. Soc.85 (2002) 2449 –2456
10. J. Cheng, D. Agarwal, Y. Zhang, and R. Roy, Microwave sintering of transparent alumina, Mater. Lett. 56 (2002) 587 – 592
11. R. Apetz, and M. P. B. Van Bruggen, Transparent alumina; a light scattering model, J. Am. Ceram. Soc. 86 (2003) 480– 486

12. L. Qi, J. Shen and W. Pan, The influence of sintering process on the microstructure of submicron alumina fabricated by gelcasting, Key. Engg. Mater. 336 – 338 (2007) 1185 – 1187
13. B. G. Guillaume, S. Christophe, Sintered alumina product transparent to infrared radiation and in the visible region, U.S. Pat. No. 2009/0137380 A1, May 28, 2009
14. M. V. Parish, M. R. Pascucci, W. H. Rhodes, Polycrystalline alumina articles and methods of manufacture, U.S. Pat. No. 2010/0025896 A1, Feb, 2010
15. A. Krell, Improved hardness and hierarchic influences on wear in submicron sintered alumina, Mater. Sci. Engg. A 209 (1996) 156 – 163
16. A. Krell, T. Hutzler and J. Klimke, Presentation on "Transparent armor: sintered Al_2O_3 Vs cubic materials" at specialist meeting AVT-122: Nanomaterials technology for military vehicle structural applications, Granada, Oct, 2005
17. I. Amato, F. Baudrocco and D. Martorana, Evaluation of freeze-drying and spray drying processes for preparing transparent alumina, Mater. Sci. Engg. 26 (1976) 73 – 78
18. A. Krell, G. Baur, and C. Dahne, Transparent sintered sub - μm Al_2O_3 with IR transmittivity equal to sapphire; pp. 199 – 207 in Window and dome technologies VIII, Vol.5078, Proceedings of SPIE, Edited by Randal.W. Tustiston., *et al.* SPIE—The International Society for Optical Engineering, Orlando, 2003

CHAPTER - V

Fabrication and Properties of Sintered Submicron IR-Transparent Spinel Ceramics

5.1 Introduction

Transparent magnesium aluminate ($MgAl_2O_4$) spinel is a face-centered cubic, optically isotropic polycrystalline material transparent to electromagnetic radiations from ultraviolet through mid-IR wavelength regions. By virtue of its intrinsic combination of excellent optical transparency and exceptional mechanical characteristics, it attracts attention in various areas of applications including IR windows and domes, transparent armors, super-market scanning windows, scratchproof watch casings, optical heat exchangers, pyrometer windows for high temperature and high-pressure furnaces etc. [1]. Fabrication of transparent grade spinel body involve various processing steps comprising appropriate selection of ultra-pure, highly reactive starting powders, fabrication of homogeneous, defect free green bodies, sintering the shaped components with high degree of densification and elimination of last 0.01% of porosity from the sintered bodies [2]. As detailed in chapter 2, most of the spinel fabrication studies employed commercial spinel powders [3 – 24] and very few investigations utilized in-house synthesized spinel powders for producing transparent spinel [25 – 29]. Some have derived spinel powders through their undisclosed processing techniques for producing spinel with ultra-fine grain sizes less than 0.5 µm and RIT closer to the theoretical maximum (advanced transparent spinel) [30 – 32]. The studies infer that the routes involving powder synthesis followed by fabricating transparent spinel require stringent control over the powder characteristics such as phase purity, molecular stoichiometry, particle size and size distribution, morphology, sinterability etc. Various optimized factors includes choice of raw materials, processing route, mixing

methodology, calcination temperatures and milling parameters govern the eventual characteristics of the optical grade spinel powder.

Considering all the challenges involved in synthesizing the spinel powders, the present study employ the sol-gel process for powder synthesis followed by fabricating transparent spinel bodies. The investigations details the facile procedure for producing highly reactive, $MgAl_2O_4$ spinel nano powders ($MgO.nAl_2O_3$, $n \approx 1$) through an aqueous sol-gel processing technique. The powder synthesis methodology proposed in this study is having high control over molecular stoichiometry and suitable for commercial upscale. In brief, the method involves synthesizing stable boehmite sol in aqueous medium followed by homogenous mixing of MgO in the form of aqueous suspension. The mixture follows drying and calcination at temperatures between 600°C and 1100°C for 1 hour. XRD studies on the calcined powders confirmed the phase formation and SEM and TEM studies exhibited their physical characteristics. The optical grade spinel powders produced in this study showed ultra-fine particle sizes ranging around 20 nm with the specific area closer to 96 m^2/g. The powders shaped in the form of pellets through uniaxial pressing followed by cold isostatic pressing at 100 MPa and sintered in air at temperatures between 1300°C and 1400°C for densification. The sintered samples exhibited >98 % T.D with no assistance of sintering additives or dopants. The dense samples attained complete densification and exhibited transparency by subjecting them to hot isostatic pressing (HIPing) at 1400°C under 160 MPa pressure for producing transparent spinel. The HIPed samples with an average grain size of 505 nm exhibited RIT equivalent to theoretical values in the 3 – 5 µm wavelength region. The detailed characterization studies of the spinel powders and the dense samples evaluated their physical, microstructural, mechanical properties and optical properties.

5.2 Highlights of the study

- Highly reactive, $MgAl_2O_4$ spinel nano powders ($MgO.nAl_2O_3$, $n \approx 1$) have been synthesized through a facile aqueous sol-gel processing technique
- The powder synthesized in this study is free from Sulphur contaminations which is a prime contamination persists in the existing commercial spinel powders
- The procedure followed in this method is highly suitable for producing optical grade spinel powders in large quantity and found suitable for fabricating submicron grained transparent spinel ceramics
- The powder exhibited excellent sinterability at 1400°C reaching density above 98% of T.D. while most of the reported materials exhibit similar densities at temperatures above 1600°C
- Low temperature densification is achieved without any assistance of sintering aids whereas most of the current investigations employ LiF as an additive for low temperature densification
- The samples after HIPing retained the sintered grain sizes closer to 500 nm while most of the existing transparent spinel materials exhibit grain sizes above 10 µm
- The HIPed and polished samples showed IR transmissions up to 84 % in the 3 – 5 µm wavelength regions, which is at par with the best – reported transmission values.
- The samples exhibited hardness up to 16.20 GPa due to finer grain sizes while most of the reported spinel exhibit hardness closer to 13.0 GPa due to larger grain sizes.

5.3 Synthesis of optical – grade spinel powder

5.3.1 Specifications of major raw materials

High-purity boehmite and MgO powders were used as the starting precursors for this study. The average particle size of the boehmite powder as per the suppliers specification was around 2.5 µm. However, the given particle size belong to the hydrated compound which actually is much finer than the given values. It may be noted that the boehmite exhibit very high surface area of 180 m^2/ g confirming the ultra-fine nature of the powder. The chemical analysis shows that the boehmite contains 77 wt % of Al_2O_3 with traces of other elements such as Na, Fe and Si. Cautious selection of alumina precursor with minimum contamination avoids unnecessary inclusions that may adversely affect the final optical properties. Similarly, MgO powder having 99.95% purity was selected for the present study to synthesize the ultra-high pure, optical grade spinel powder. Table 5.1 summarizes the characteristics of the precursors supplied by different commercial suppliers.

Characteristics (as per the suppliers specifications)	**Boehmite**	**MgO**
Manufacturer	Disperal, Sasol, Germany	Alfa Aesar, USA
Particle size (d_{50})	2.5 µm	100 – 200 nm
BET surface area (m^2/g)	180	52
Chemical analysis	Al_2O_3 – 77%, Na_2O – 0.002%, Fe_2O_3 – 0.01%, SiO_2 – 0.012%	Ca – 0.029%, Fe – 0.004%, Na – 0.056%, Si – 0.011%

Table 5.1: Characteristics of starting powders

5.3.2 Process flow for spinel fabrication

Fig. 5.1 shows the complete flow chart for fabricating transparent spinel from the starting precursors. The process initiates with the simultaneous preparation of aqueous boehmite sol

and aqueous MgO suspension followed by homogenous dispersion of MgO suspension with the stable boehmite sol. The mixture further proceeds for successive processes such as drying, and calcination for the synthesis of spinel powder. The powder further mixed with optimized binders compacted uniaxially and further pressed cold isostatically for shaping followed by sintering and HIPing to obtain transparent spinel samples. The detail procedures of the fabrication are described in the following sections.

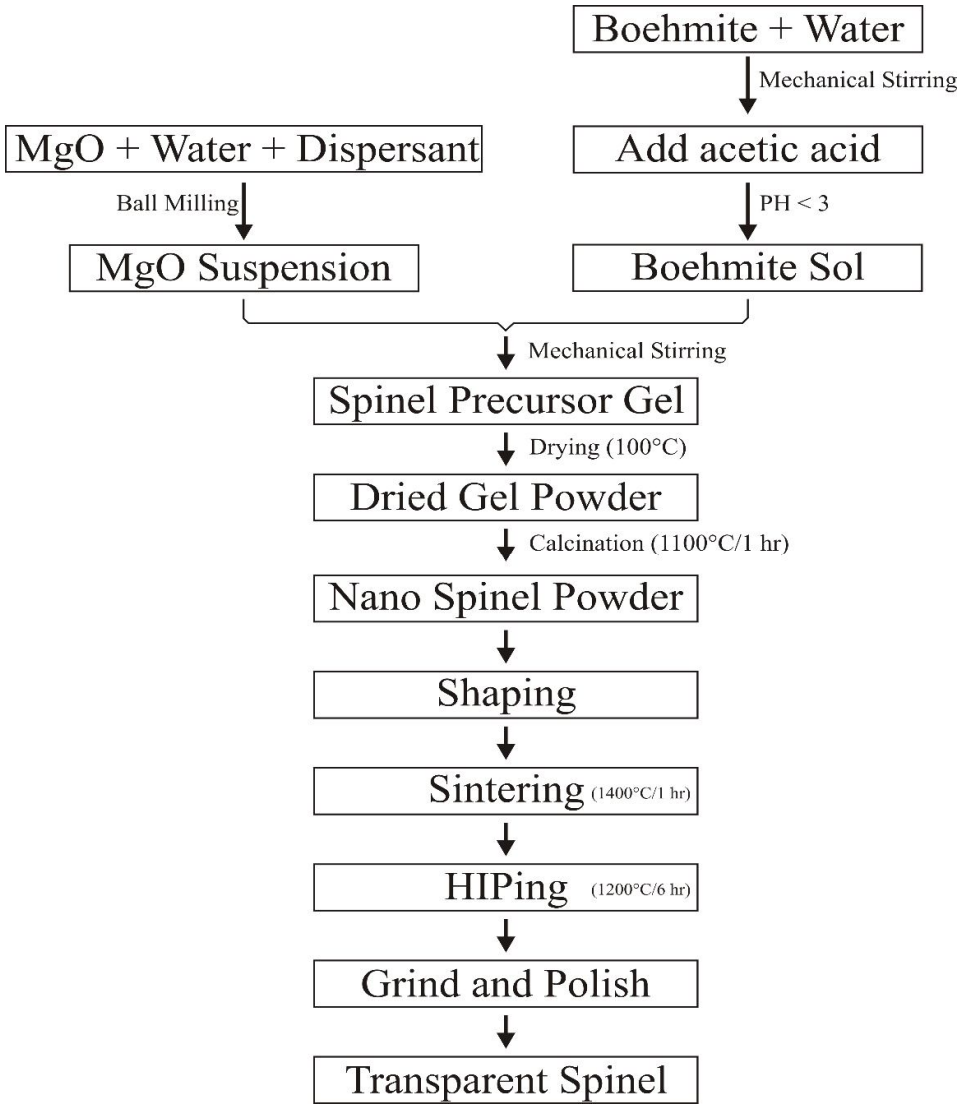

Fig 5.1 Flow chart for the fabrication of transparent spinel

5.3.3 Preparation of boehmite sol

Boehmite powder and water were mixed at 1:9 weight ratio in ambient conditions for a period of 1 hour using high speed mechanical stirrer at a speed of 800 rpm. Glacial acetic acid was added dropwise to this mixture to adjust the pH between 2 and 3 for peptization. Stirring was continued for another hour to obtain clear and stable boehmite sol. The sol was kept uninterrupted for a period of 24 hours for the settlement of any unreacted boehmite particles. The segregated unreacted particles were separated by transferring the supernatant clear sol to another container. 10 g of clear sol was dried at 100°C and calcined at 1200°C in air to find out the actual content of $\alpha - Al_2O_3$ in the sol. Approximately 76.5 wt % of alumina with respect to the weights of boehmite was obtained after calcination which is almost closer to the alumina content specified by the supplier.

5.3.4 Preparation of MgO suspension

Aqueous suspension of MgO was prepared by mixing MgO powder and water at a ratio of 60:40 wt % using a ball mill. Darvan 821A (R.T.Vanderbilt Co., Inc., Norwalk, CT, USA) of 1 wt% concentration with respect to the solids was used as a dispersant and 2mm alumina balls of purity above 99.9% was used as milling media. The charge ratio between the powder and the balls were maintained as 1:2 by weight and the milling was carried out in a polypropylene container for a period of 4 hours to obtain the stable aqueous MgO suspension.

5.3.5 Production of spinel powder

Stable boehmite sol having 50 mol% of alumina content was kept under constant stirring conditions for a period of 30 minutes using a high-speed mechanical stirrer. The milled MgO suspension having 50 mol% of MgO was slowly added to the boehmite sol. Stirring was continued a period of 2 hours to obtain the homogeneous spinel precursor gel. The gel was further dried at 100°C in a hot air oven for 12 hours to obtain the dried spinel precursor gel

granules. The granules were crushed using the pestle and mortar and sieved through a 100 mesh plastic sieve for obtaining the fine precursor gel powder. The powder was further calcined at temperatures between 600 and 1100°C for the synthesis of spinel powder. Disintegration of the calcined powders were carried out in a planetary mill for a period of 2 hours in ethanol medium. Planetary vials of 500 ml capacity and made of 99.9% pure alumina was used for the entire study. 2 wt% of polyvinyl pyrrolidone (Sigma Aldrich, U.S.A) was added as dispersant during milling. Alumina balls of 2 mm diameter having purity above 99.9% was used as grinding media to avoid milling contaminations. The milled slurry was dried at 70 – 80°C for 2 hours in the hot air oven to obtain the high purity, optical grade spinel powder.

5.4 Fabrication of transparent spinel samples

The optical grade spinel powder was pressed uniaxially to a size of 30 mm diameter and 5 mm thickness at 40 MPa pressure. The compacted pellets were further pressed cold isostatically at 160 MPa pressure for a period of 2 minutes. The pressed samples were sintered in air atmosphere for a period of 1 hour at temperatures between 1300°C to 1400°C with 25°C increment for each study. The heating and cooling rate was maintained as 5°C per minute for obtaining homogeneous densification. The main objective of varying sintering temperatures was to obtain samples with zero percent closed porosity or water absorption, which is the prerequisite condition for carrying out capsule free HIPing operations. The sintered samples with no open porosities were HIPed (American Isostatic Press Inc. U.S.A) at 1400°C for 4 hours at a pressure of 160 MPa to obtain transparent spinel samples. The samples after HIPing were ground and polished to a final thickness of 2 mm using diamond suspensions of grits sizes varying from 15 µm to 1.0 µm to obtain optically transparent spinel samples.

5.5 Characterization of powders and sintered specimens

The starting precursor powders such as boehmite and MgO were characterized for their microstructural features using FEG SEM (Carl Zeiss Microscopy GmbH, Oberkochen, Germany) and for phase analysis using XRD (D8, Bruker, Karlsruhe, Germany). The dried precursor gel comprising equimolar Al_2O_3 and MgO was subjected to TGDTA analysis (Netzsch, Germany) for its thermal response up to 1500°C in air atmosphere. The bonding characteristics of Al and Mg cations in the calcined spine powders and spinel bonding information were ensured through electromagnetic absorptions using FTIR (Vertex 70, Bruker Optik GmbH, Germany) analysis in the wavenumber region between 400 and 4000 cm^{-1}. Spinel phase formation at each stage of calcination temperatures from 600°C to 1100°C were analyzed using XRD analysis. Microstructural characteristics of spinel powders calcined at selected temperatures were investigated through FESEM and TEM (FEI, Technai G2, Netherlands) analyses. Spinel powders were further characterized for their particle size and size distribution using particle size analyzer (Nano SZ, Malvern Instruments Ltd, UK). Surface area of the spinel powders were characterized through BET surface analyzer (Gemini, Micromeritics, USA).

Sintered and HIPed spinel samples were characterized for their porosities and densities through Archimedes principle. Microstructural characteristics of polished and thermally etched dense samples were analyzed using FESEM. Thermal etching was carried out by heating the polished samples to the temperatures 100°C lower than their actual sintering temperatures with a hold of 1 hour at peak temperatures. The etched surfaces were further sputtered with gold ions for improving conductivity during SEM investigations. Hardness of the sintered and HIPed samples were measured by Vickers (Leco, St. Joseph, MI) indentation at 1 kg load. HIPed and polished spinel specimen having 2 mm thickness was measured for its real inline transmission properties in the IR wavelength region between 3 and 6μm through FTIR analysis.

5.6 Results and Discussions

5.6.1 Characteristics of initial precursors

Fig 5.2 shows the microstructural features of the starting raw materials. As shown in fig. 5.2a, the boehmite powders exhibit clustered particle morphology with random size distribution varying from 200 nm to as large as 8 – 10 µm. The hydroxyl molecules present in the boehmite (AlOOH) is the plausible reason for the vast size distribution. The duration of sol preparation vary based on the wideness of the size distribution and in the present study, an hour of mixing after acid peptization was found optimum to obtain a clear stable sol. The concentration of alumina from the sol was around 76.5% after calcination at 1200°C, which is relatively equal to the concentrations specified by the supplier. This indicates the stability and homogeneity of the synthesized boehmite sol. In case of MgO, the powders exhibit individual and monogamous cubic crystals having particle sizes distributed in the range of 100 – 200 nm. The powder is free from any agglomerations and random faceted morphologies that are beneficial for making stable aqueous suspensions.

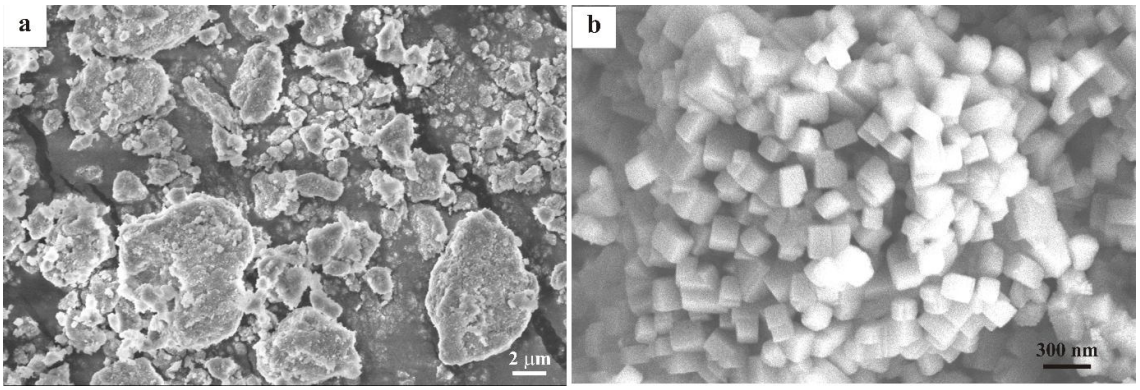

Fig. 5.2 Microstructural characteristics of starting materials such as (a) boehmite and (b) MgO powders

Fig. 5.3 shows the XRD patterns of as-received raw materials. Fig. 5.3a shows the characteristic peaks belong to boehmite phase and the broadness of the peaks indicates its amorphous nature. Figure 3b shows the XRD peaks corresponding to MgO phase and the sharpness of the peaks shows that the MgO is well crystallized. The patterns indicate that the raw materials are highly pure and free from any major contaminations.

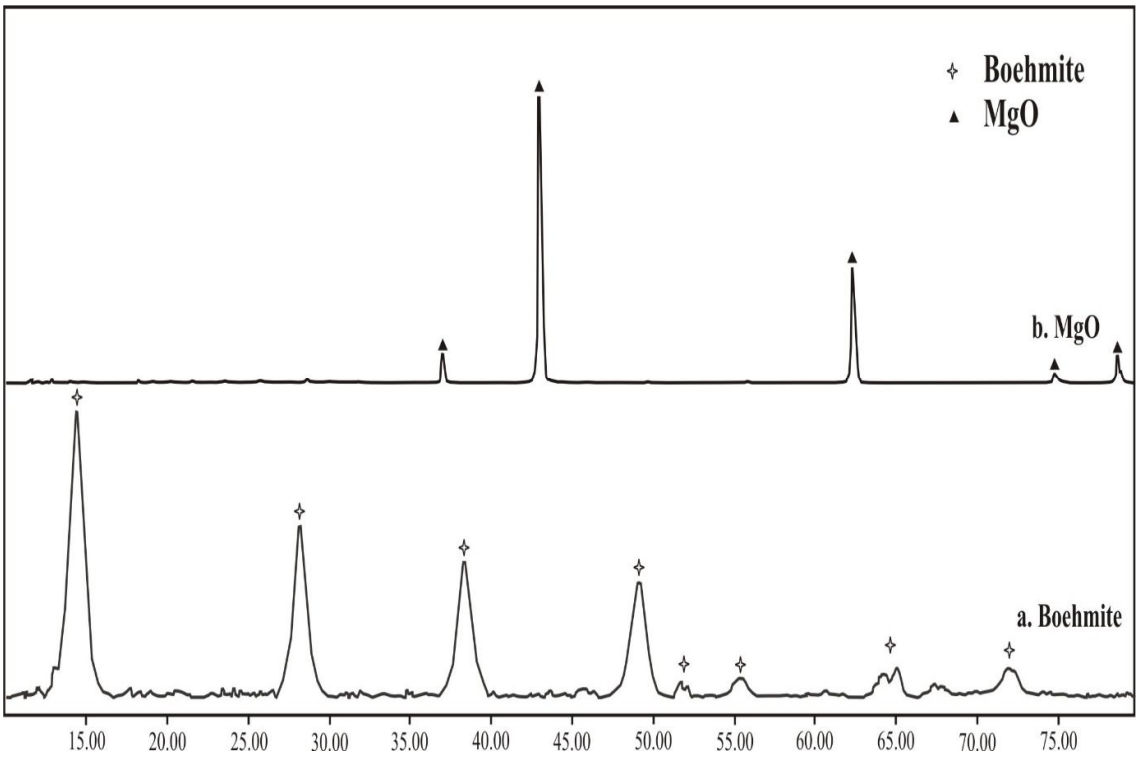

Fig. 5.3 XRD analyses for starting materials (a) boehmite and (b) MgO powders

5.6.2 Thermal analysis of spinel precursor gel

Fig 5.4 shows the thermal behavior of spinel precursor gel up to the temperatures of 1500°C in air atmosphere. The TG curve shows a weight loss up to 5 – 7% at temperatures between 150 and 200°C, which is ascribed to the evaporation of physically combined water. The primary loss at this stage seemed to be relatively lesser compared to the second stage of losses as the

precursor gel was dried at 100°C prior to this analysis. The secondary weight loss up to 20 – 25% at temperatures between 250 and 400°C corresponds to the loss of chemically combined water and removal of hydroxyl groups of alumina. The third stage of loss up to 2 – 3 % at temperatures up to 600°C was attributed to the loss of carbon from acetic acid that was used as a peptizing agent during the synthesis of boehmite sol. No major losses were further observed beyond 700°C.

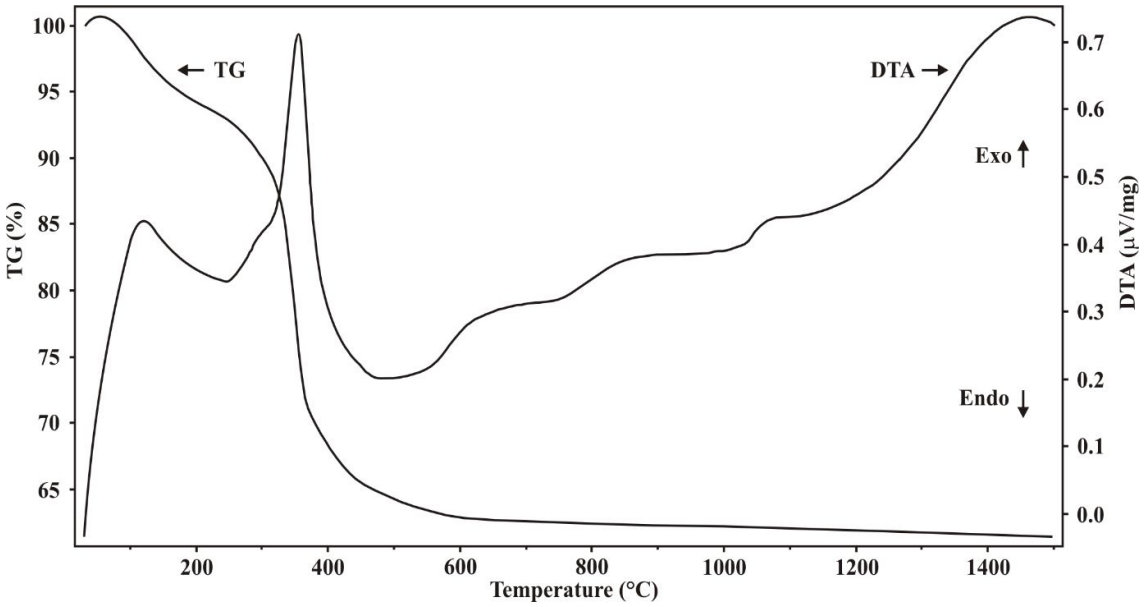

Fig. 5.4 TGDTA analysis of spinel precursor gel

The DTA curve shows a broader endothermic absorption at temperatures between 150 and 300°C, which is related to the loss of water molecules. The exothermic peak observed at temperatures between 350 and 360°C is ascribed to the formation of spinel phase. The phase formation at these temperatures was further confirmed through XRD analysis detailed in the subsequent section. Spinel phase formation via processes such as solid-state reactions between Al_2O_3 and MgO powders require temperatures generally above 1200°C and require even higher temperatures above 1500°C for further densification [33 – 41]. However, in the present study,

the spinel phase was obtained at temperatures <400°C. This is attributed to the exclusivity of the sol–gel process that facilitates intimate and homogenous mixing of starting materials that promotes early phase transformations at relatively lower temperatures compared to the solid-state reactions. Moreover, spinel powders produced at such low temperatures exhibit high surface area that facilitate extensive inter-particle diffusion and earlier densification during sintering.

Fig. 5.5 shows the physical appearance of precursor gel calcined at various temperatures up to 1200°C. As shown in fig. 5.5a, the dried gel undergo various physical transformations based on the calcination temperatures. No major changes were observed up to 400°C whereas the ignition of organic compounds from acetic acid was initiated at 500°C (fig. 5.5c) and their evaporation was mostly completed at temperatures less than 800°C as shown in fig. 5.5f. Further increment in the calcination temperatures beyond 900°C to 1200°C was not involved with any major physical transformations.

Fig. 5.5 Spinel precursor gel powders at various calcination temperatures

5.6.3 FTIR analyses of spinel powders

Fig. 5.6 shows the IR absorption spectrum indicating the bonding characteristics of Al and Mg cations in the wavenumber region between 400 and 4000 cm^{-1} for the spinel powders calcined at temperatures between 700°C to 1100°C.

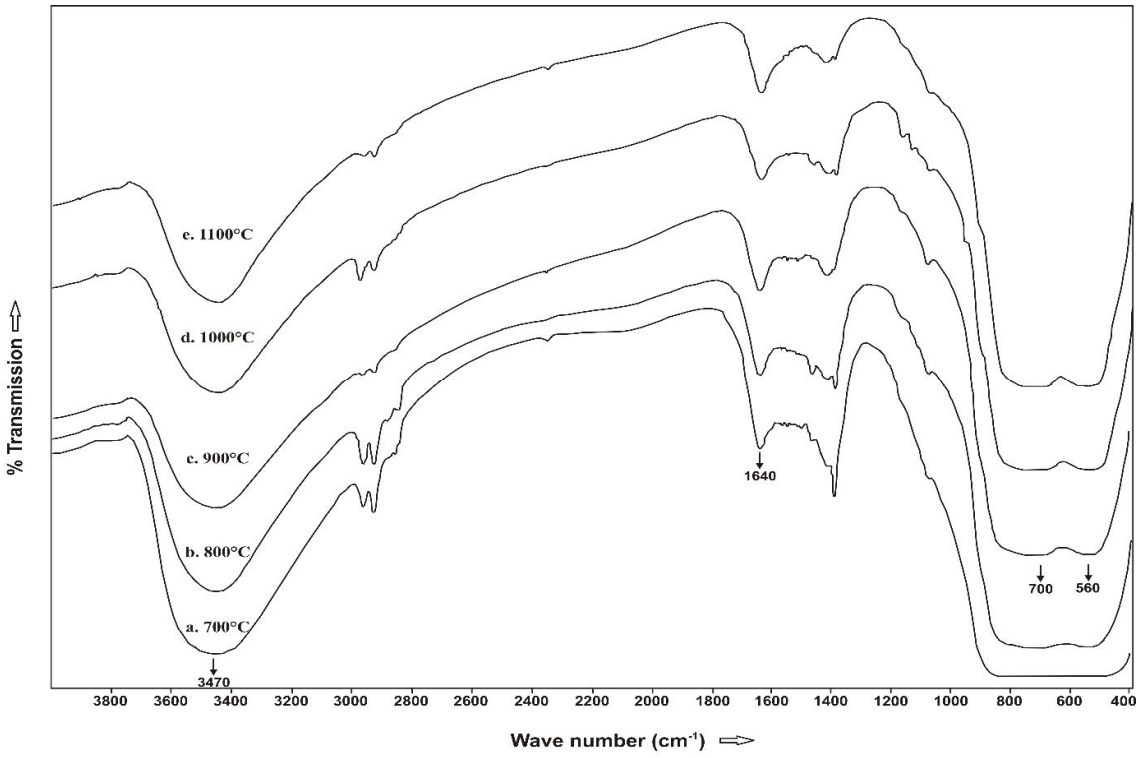

Fig. 5.6 IR absorption characteristics of spinel powders calcined at temperatures from 700°C to 1200°C

All the spinel powders synthesized from 700 to 1100°C exhibit a broadband absorption valley between 3400 and 3600 cm^{-1} centered at a wavenumber of ≈3470 cm^{-1} is corresponding to the valence vibration of water. In addition, the spectrums indicate a sharp absorption at 1640 cm^{-1} which is also a characteristic stretch of H-O-H bond [42]. The absorption of moisture from the atmosphere by the calcined particles would be the plausible reason for the formation of these hydroxyl bonds. The tendency of moisture absorption is an indication that the powder is ultra-fine and exhibiting high surface area. Fig. 5.6b indicates an initiation of a split formation in the

broadband spectrum at a wave number region between 500 and 800 cm^{-1} at 700°C and apparently enhance with an increment in the calcination temperatures as shown in fig. 5.6c and fig. 5.6d. The split gradually transforms into two individual absorption bands at 1100°C as appear in fig. 5.6e with their respective centers at 560 and 700 cm^{-1}. These bands are characteristic vibrations of Mg-O and Al-O groups of the spinel phase [43 – 44]. It may be noted that in the fig 5.6a, these bands are not obvious for the spinel powders calcined at 700°C. The steady increment in the formation of two absorption bands at 560 and 700 cm^{-1} from 800°C is an indication of the transformation of spinel from amorphous to crystalline state [45]. Therefore, the indication of phase formation at ≈ 400°C as per the TGDTA curve is presumably the formation of amorphous spinel.

5.6.4 Phase formation studies of the spinel powder

Fig. 5.7 shows the progress in the spinel phase formation from the precursors at various levels of calcination temperatures. Fig. 5.7a and 5.7b shows the diffraction peaks corresponding to the as-received boehmite and MgO powders respectively, which were used as the starting powders. The peaks corresponding to boehmite seem to be broader due to its amorphous condition and the sharp peaks belong to MgO state that they are crystalline. Fig. 5.7c shows the diffraction pattern of spinel precursor gel dried at 100°C. Though the precursor is composed of boehmite and MgO compounds, the pattern exhibited the peaks corresponding only to the boehmite phase. This is the indication of the process homogeneity where all the MgO particles were uniformly coated with boehmite sol, forming a core-shell structure during the mixing period. The phases of the gel remained unchanged up to the calcination temperature of 300°C as shown in fig. 5.7d. At 400°C, the starting phases were converted to spinel phase forming its predominant peaks corresponding to (311), (400), (440) planes as shown in fig. 5.7e. This is in good agreement with the TGDSC curve that exhibit an exothermic peak at 360°C to indicating the formation of spinel phase.

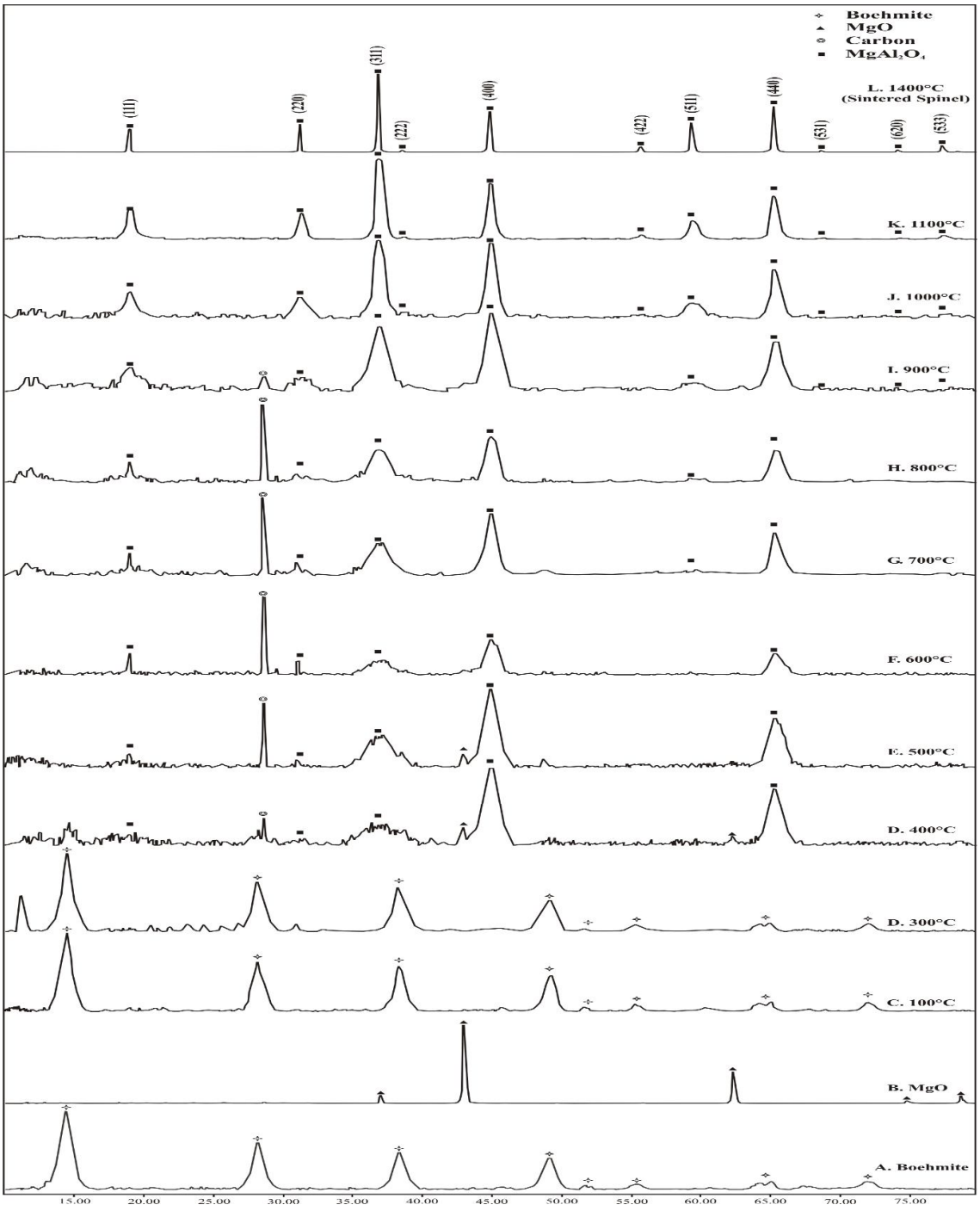

Fig. 5.7. XRD analysis of the spinel precursor powders at various calcination temperatures

Traces of peaks corresponding to MgO were still observed at this temperature and even at 500°C and 600°C as shown in fig. 5.7f and fig. 5.7g for further spinalization. In addition, a

peak corresponding to carbon possibly from acetic acid was also noticed in these temperature regions. All the peaks corresponding to MgO were completely disappeared and converted to spinel at 700°C as shown in fig. 5.7h. The peaks were still observed to be broader up to 800°C as seen in fig. 5.7i and started to sharpen from 900°C (fig. 5.7j) which is the indication of the crystalline refinement and growth of spinel particles. As shown in fig 5.7k for the pattern corresponding to the powder calcined at 1000°C, the particles were grown still further and the peaks belong to (111), (220) and (511) planes were also observed more obviously. At 1100°C, the powder exhibited all the peaks corresponding to phase pure spinel as shown in fig. 5.7l. Fig. 5.7m was included in this figure to show the pattern of the spinel after shaping and sintering at 1400°C for 1 hour. The pattern exhibits sharp and intense peaks indicating its high crystallinity and phase purity.

5.6.5 Microstructural and physical characteristics of spinel powder

Fig. 5.8 shows the progress in the particle morphologies of the spinel powders calcined at various temperatures between 700°C and 1100°C. The overall morphology of the powder throughout the calcination temperatures appeared to be homogenous with uniform particle size distribution. The powders calcined at temperatures between 700°C to 900°C exhibit ultra-fine particles that are not completely gained their individual shapes as shown in fig. 5.8a to fig. 5.8c. As indicated in XRD analyses, the particles at these temperatures undergo crystalline refinements and proceeding for inter-particle necking and growth. At the calcination temperatures of 1000°C, the particles gained their individual shapes and exhibiting round edged morphology as shown in fig. 5.8d. A further increment in calcination temperatures to 1100°C shows well crystallized spinel particles having particle sizes closer to 25 nm. The particle sizes of individual spinel crystallites were further confirmed through TEM analyses which shows the size closer to 20 nm as shown in fig. 5.8f.

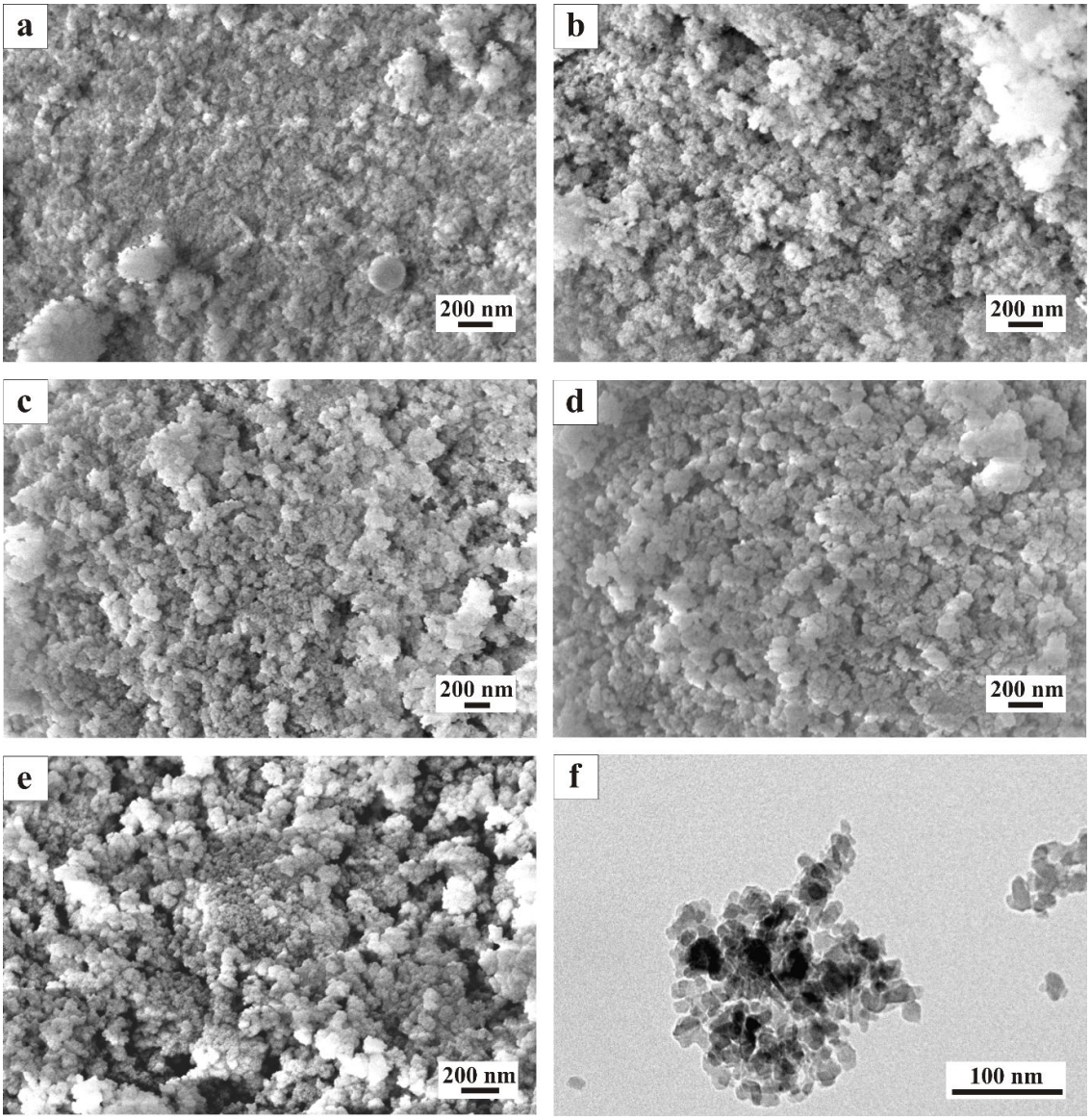

Fig. 5.8 SEM analysis of spinel powders calcined at various temperatures from (a) 700°C, (b) 800°C, (c) 900°C, (d) 1000°C and (e) 1100°C and (f) TEM micrograph of spinel powders calcined at 1100°C

Fig. 5.9 shows the BET surface area of spinel powders calcined at temperatures between 700°C and 1100°C for 1 hour. The powders calcined at 700°C exhibited very high surface area close

to 155 m^2/g. As indicated in the above sections, the amorphous status of the spinel at these temperatures would be the plausible reason for such high surface area. The surface area tends to reduce to 145 m^2/g and 129 m^2/g for the powders calcined at 800°C and 900°C respectively indicating the particle refinement and growth. The particles sizes were further improved at 1000°C indicating the surface area closer to 119 m^2/g. and eventually, the powder calcined at 1100°C and exhibiting well distinctive particles exhibited the surface area of 96 m^2/g size.

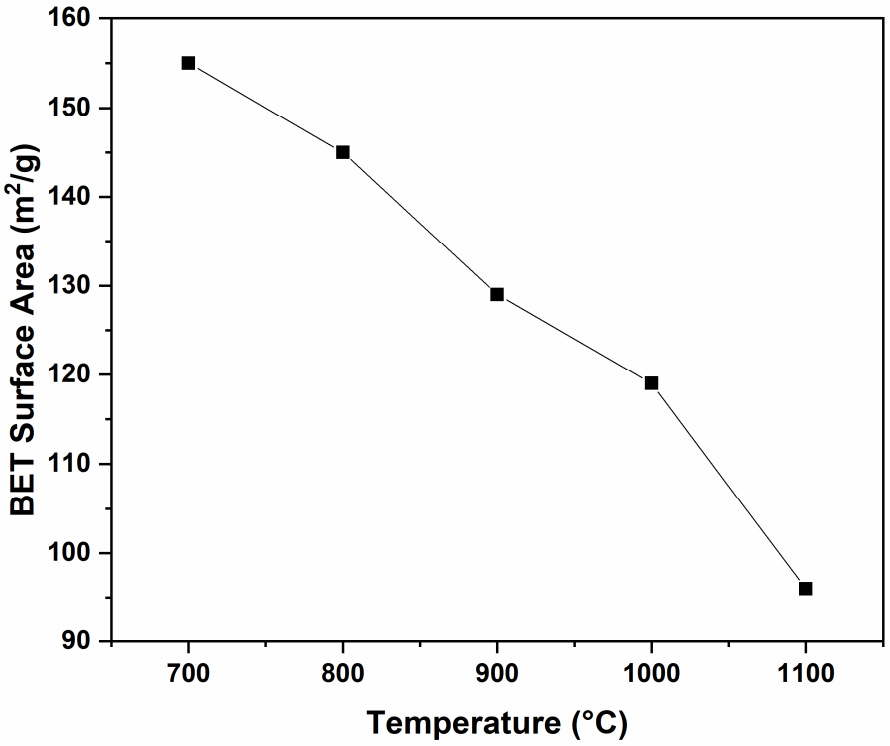

Fig. 5.9 Surface area of spinel powders Vs their calcination temperatures

The particle size corresponding to the surface area at 1100°C was calculated using the following formula:

$$D_{BET} = \frac{6}{\rho \times S_{BET}}$$

Where D – Particle diameter, ρ – Theoretical density of spinel (3.58 g/cc), S_{BET} – the specific surface area measured by the BET method. Accordingly, the particle diameter for the specific surface area of 96 m^2/g was found to be 17.5 nm. It was further confirmed through the TEM analysis where the average particle diameter of the spinel powder calcined at 1100°C was measured to be between 18 and 20 nm as observed from the TEM image shown in fig. 5.8f.

Fig. 5.10 shows the distribution pattern of the spinel particles calcined at 1100°C. The graph indicates the particles of larger sizes, which is actually in the agglomerated form.

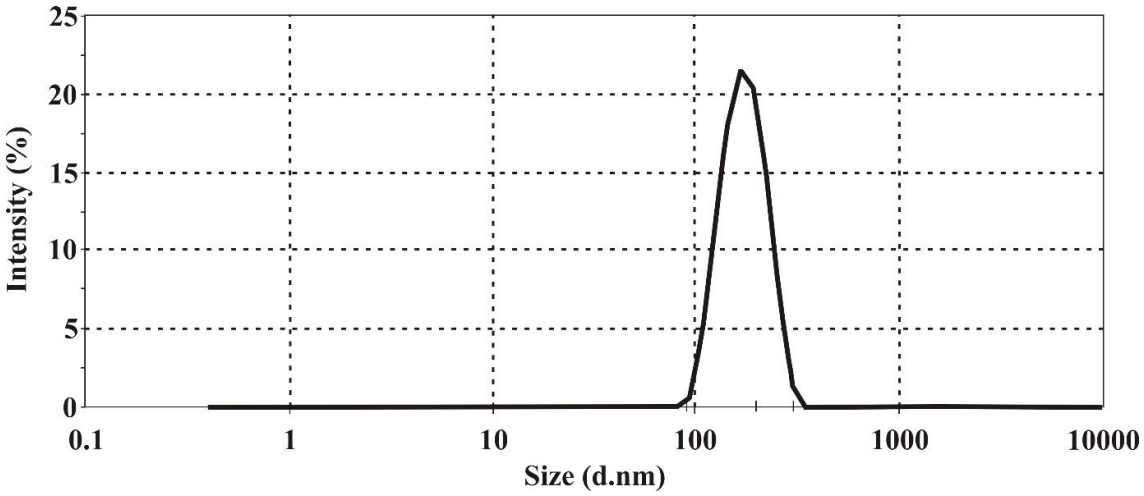

Fig. 5.10 Size distribution of spinel powder calcined at 1100°C

The nano particles of sizes less than 100nm usually exhibit strong inter-particle attraction leading to the formation of agglomerates and therefore not possible to prepare homogeneously dispersed suspensions consisting individual particles for the particle size analysis. Moreover, the chances of shielding of finer particles by the coarser agglomerates may drive the distribution curve to the coarser sides during the analysis [46 – 47]. In such cases, the analysis using laser diffraction principles usually indicate the distribution of agglomerates rather than the individual particle sizes. Accordingly, the fig. 5.10 shows the spinel agglomerates exhibit the size distribution ranging between 100 nm and 300 nm with an average d_{50} at 180 nm.

5.6.6 Physical and microstructural characteristics of dense spinel

Fig. 5.11 shows the plot between porosity and theoretical density of the spinel samples against their sintered temperature between 1300 and 1400°C for a period of 1 hour in air atmosphere.

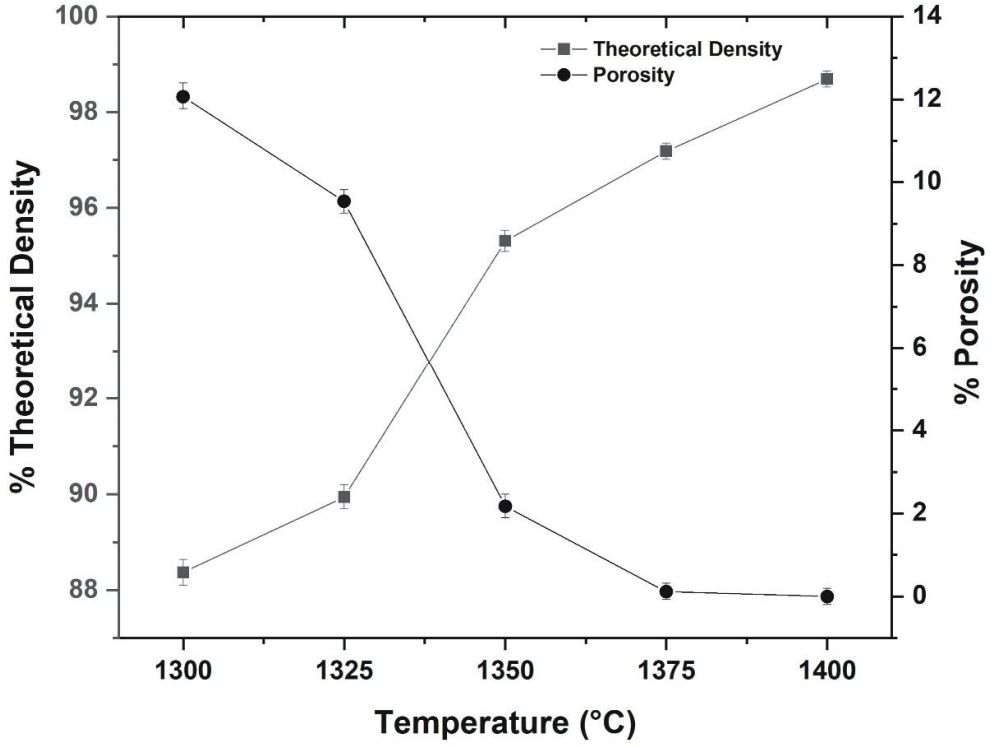

Fig. 5.11 Densification trend of spinel with respect to sintering temperatures

The sintered specimens of spinel contained large volume of open porosities between 10 – 12% up to the sintering temperatures of 1325°C with the corresponding theoretical densities around 88%. A steep increment in the densification was observed in the successive heat treatment at 1350°C. The levels of porosities were greatly reduced from 10% to around 2% at these temperature regions indicating the intense event of inter-particle necking and sintering. The densities at these stages was found to be around 95%. The samples sintered at 1375°C showed traces of open porosities while the samples wintered at 1400°C gained zero water absorption reaching around 97% – 98% relative densities. The rate of increments in the densities beyond

1350°C seem to be decreasing relative to the earlier rates indicating the densification at these stages is predominantly proceeding with grain growth. Goldstein *et al*. obtained similar densities for a dwelling period of 80 hours in air at 1400°C for their spinel bodies fabricated using powders derived through flame pyrolysis [23]. Their later studies with the coarser spinel powders improved the inter-particle coordination in the compacted bodies, which enhanced the sinterability to gain equivalent sintered densities at a shorter dwelling period of 3 hours [48]. Similarly, the powder synthesized through sol-gel technique in the present study exhibited remarkable densifications at temperatures around 1400°C with the mere holding period of 1 hour indicating the superior inter-particle cohesion and sinterability of the powders. On the other hand, Krell *et al.* reported that the powders produced through flame pyrolysis technique was 3000% costlier compared to the similar optical grade alumina powders having equivalent specifications [46].

Achievement of zero open porosities in the sintered bodies is a prerequisite of successful, subsequent clad-less HIPing operations for the complete elimination of last traces of porosities from the sintered microstructures. Accordingly, the samples sintered at 1400°C in the present study gained 100% relative density by subjected to HIPing at 1400°C under 160 MPa pressures for a dwelling period of 6 hours.

Fig. 5.12 shows the microstructural transformations of spinel samples as a function of sintering temperatures. Fig. 5.12a shows that the samples sintered at 1300°C attained initial stages of densification comprising the events of particle rearrangement and grain coarsening. The figure further shows the microstructure with larger volumes of interconnected continuous pore channels. The average grain size of the partially densified grains at this stage was found to be about 160 nm. The microstructure of the samples sintered at 1325°C as shown in fig. 5.12b, was found to be relatively denser with randomly distributed pore patches confirming the

continuation of grain coarsening. The grains at this temperature was grown to an average size of about 230 nm.

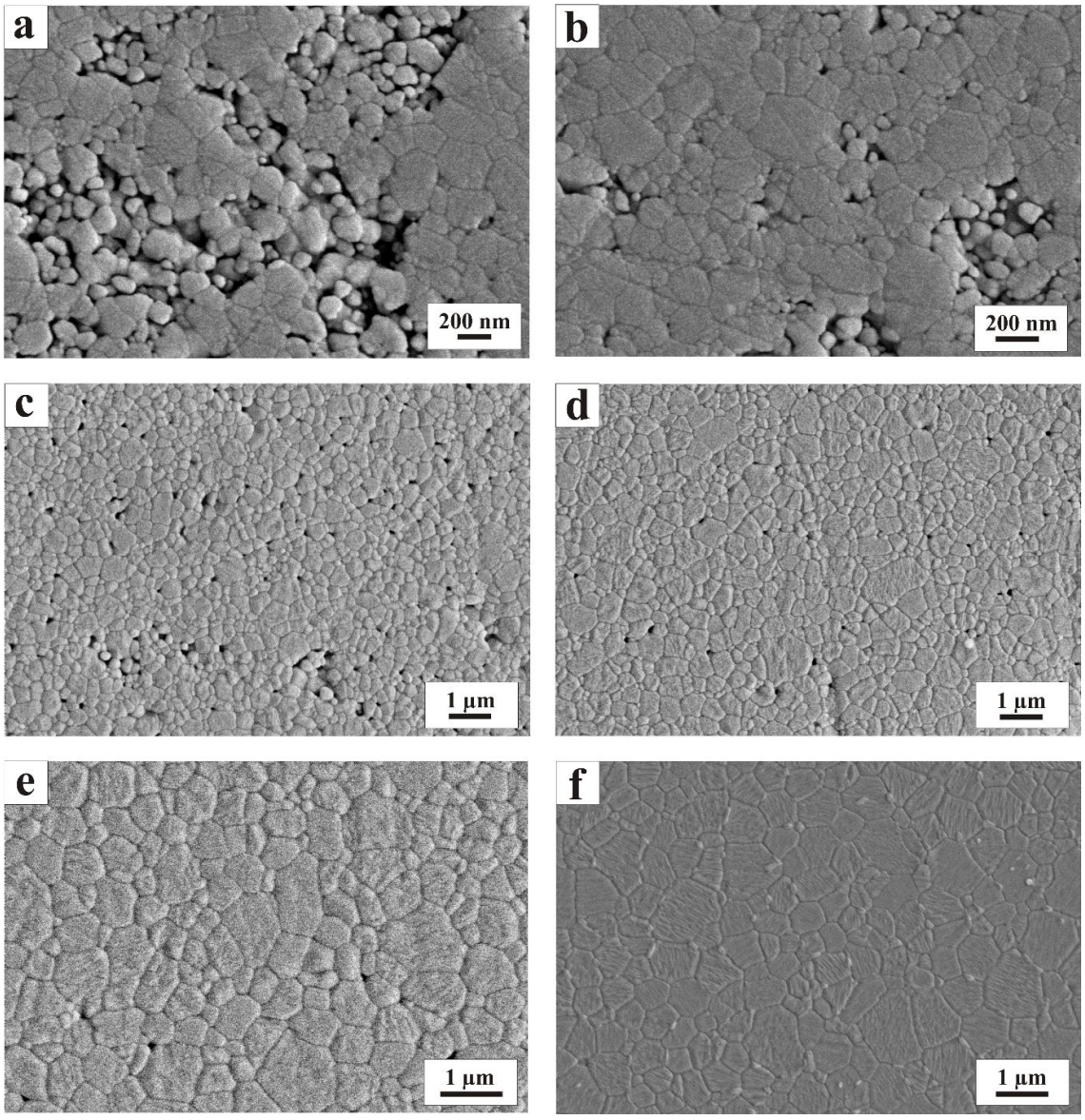

Figure 5.12 Microstructural transformations of spinel sintered at (a) 1300°C, (b) 1325°C, (c) 1350°C, (d) 1375°C. (e) 1400°C and (b) sintered at 1400°C and HIPed at 1200°C

Since the average sizes of the sintered grains at these temperature regions were around 200nm, the SEM images for these samples are presented in 200nm scale for a better resolution of grain

structures. The average sizes of the grains were further grown to about 306 and 382 nm for the sintering temperatures of 1350°C (fig. 12c) and 1375°C (fig. 12d) respectively. The pores in the microstructure were greatly eliminated in these temperature regions indicating the sintering entering to its second stages, which is majorly involved with grain coarsening.

Samples sintered at 1400°C resulted with highly dense microstructure as shown in fig. 5.12e with traces of closed porosities. The average grain size at this temperature was observed to be about 505 nm. The spinel bodies produced in the present method exhibit monogamous, equiaxed and finely distributed grains having minor volume of nano pores in the inter-granular sites as shown in figures from 5.12c to 5.12e. This harmony of controlled microstructure is corresponding to the event of uniform solid-state sintering of the green bodies composed of highly coordinated nano, round – edged powder particles exhibiting homogeneous nucleation and grain growth. In addition, the superior sinterability of the powders enabled such low-temperature densification without any assistance of sintering additives.

Fig. 5.12f shows the microstructure of the samples sintered at 1400°C and further pressed hot isostatically at 1400°C for 6 hours. The pressure assistance eliminated all traces of pores from the microstructure leading to the formation of theoretically dense body exhibiting optical transparency. The average grain sizes after HIPing was retained as 505 nm indicating the densification involved only with squeezing of pores through grain boundaries without any grain growth.

Fig. 5.13 shows the rate of grain growth for the spinel samples with respect to their sintering temperatures from 1300°C to 1400°C. The graph reveals the steady rate of grain growth revealing the homogenous and controlled diffusion and mass transfer throughout the sintering process. The growth rate was slightly steeper beyond 1375°C confirming the second stages of densification involving majorly with grain diffusion.

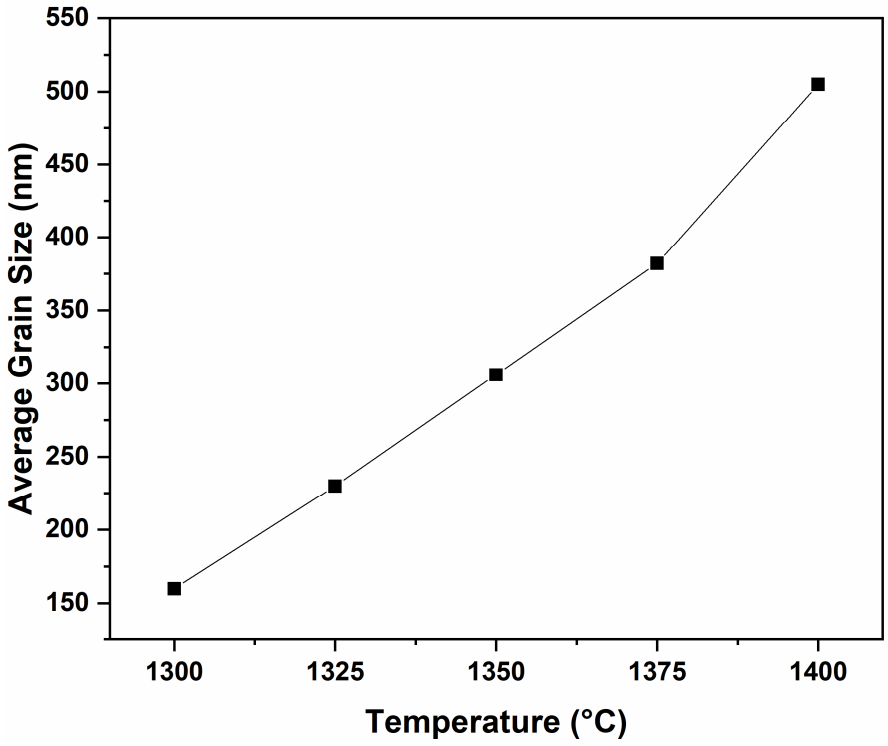

Fig. 5.13 Average Grain size of the spinel with respect to their sintering temperatures

Fig. 5.14 compares the hardness (HV_1) of the sintered samples related to their sintering temperatures from 1300°C to 1400°C. The samples sintered at 1300°C and 1325°C exhibited hardness of 787 ± 30 Kg/mm^2 and 850 ± 40 Kg/mm^2. A significant increment in hardness values were observed for the samples sintered at 1350°C and 1375°C reaching to 1316 ± 20 Kg/mm^2 and 1394 ± 10 Kg/mm^2 respectively. The hardness values were further increased to 1429 ± 10 Kg/mm^2 for the samples sintered at 1400°C which were enhanced to the heights of 1620 ± 10 Kg/mm^2 for the HIPed and transparent spinel samples.

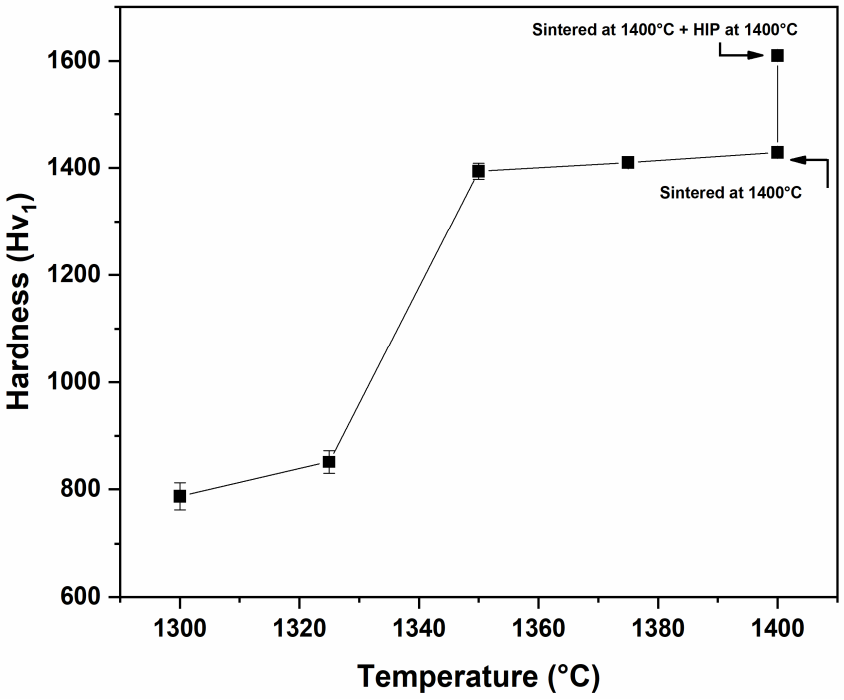

Fig. 5.14 Sintering Temperature Vs Hardness of spinel

The increment in the hardness values is attributed to improved densification and controlled microstructures with sub-micron grain sizes. The hardness values achieved in this study is at par with the best-reported sub-micron spinel [30, 32] and 40% superior to the values achieved for the coarse-grained conventional transparent spinel [5 – 10].

Fig 5.15a shows the photograph of a sintered, HIPed and polished transparent spinel sample having a thickness of 1.5 mm produced through the present method. The sample shows high degree of real inline optical transparency where the objects behind the spinel window is clearly visible to the naked eye. Moreover, fig. 5.15b shows the IR transmission pattern of the same showing broadband transparency up to 84 % between 2 and 5 µm region with no abnormal absorption throughout the wavelength window, proving the efficiency of the present process for fabricating optical grade window materials. The transmission values achieved for the submicron spinel fabricated in this study is at par with the best-reported values in the 2 and 5 µm wavelength regions [30, 32].

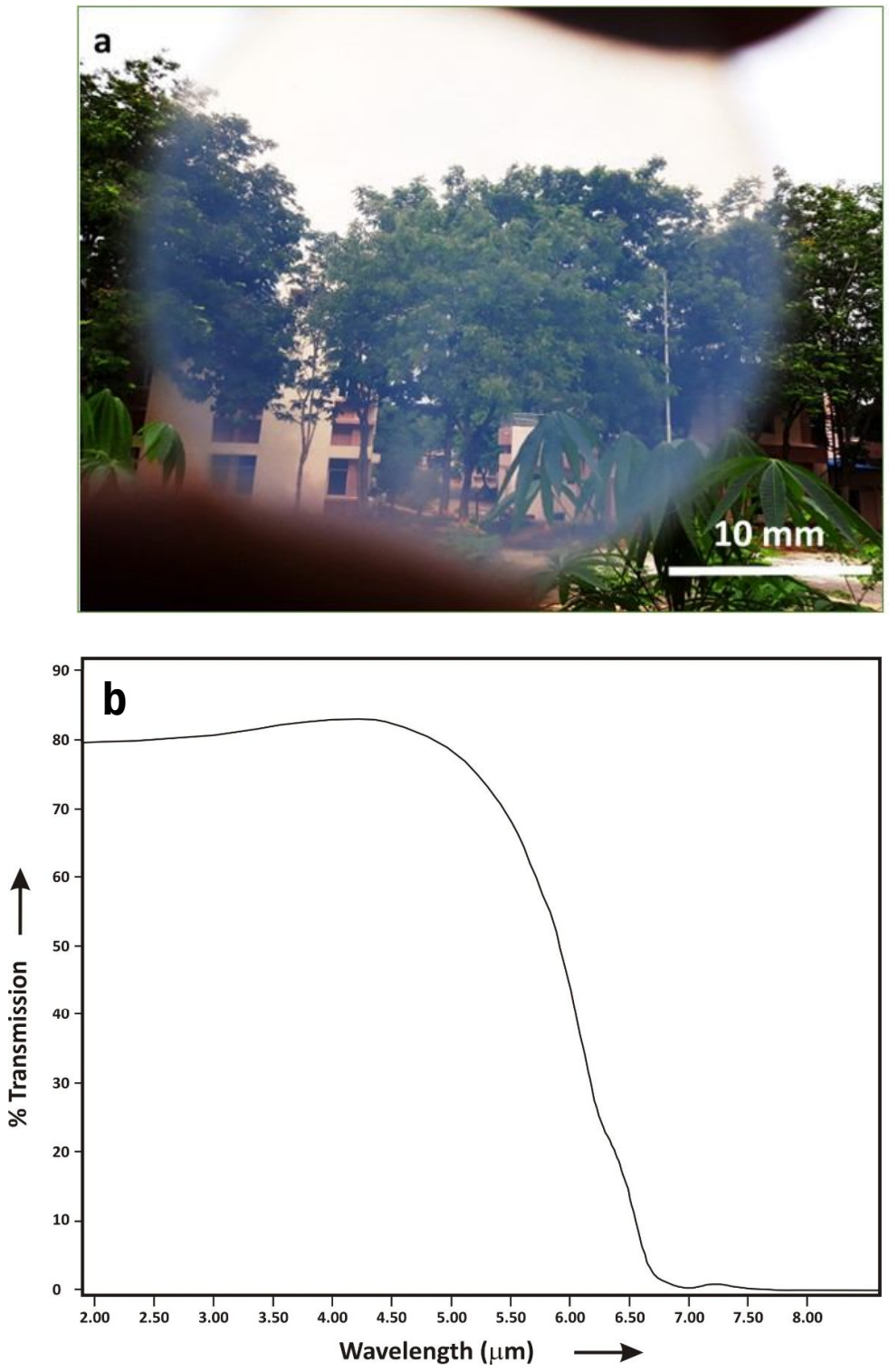

Fig. 5.15 (a)Transparent spinel from sol-gel derived powders, (b) Real inline transparency of the spinel

5.7 Summary

Highly reactive, nano spinel powder with superior control on molecular stoichiometry was prepared through a facile sol-gel methodology. The powders exhibited round edged morphology having uniform particle size distribution with an average size of about 30 nm. The powders with high inter – particle coordination enabled producing green samples with high degree of homogeneity without any flaws. The compacted green specimens exhibited excellent sinterability at temperatures between 1350 – 1400°C reaching sintered densities above 97% of its theoretical values without any assistance of sintering aids. The sintered specimens attained 100% densification and lead to the domain of exhibiting optical transparency upon further pressing hot isostatically at 1400°C under the pressures of 160 MPa. The sintered and HIPed specimens exhibited monogamous, equiaxed and uniform microstructures having sintered grain sizes in the submicron region with an average size of about 500nm. In consequence, the hardness of the final transparent material enhanced beyond 40% relative to the conventional coarse-grained spinel. On all of the above, the HIPed and polished spinel samples showed broadband optical transmissions up to 84% in the wavelength regions between 2 and 5 μm confirming the efficiency of the sol-gel derived spinel powders for fabricating transparent spinel components. Moreover, the present process of producing highly reactive nano spinel powder is relatively economical and the methodology followed for making transparent spinel are highly suitable for large-scale productions.

5.8 References

1. A. Goldstein and A. Krell, Transparent ceramics at 50: progress made and further prospects, J. Am. Ceram. Soc., 99 (2016) 3173 – 3197
2. A. Krell and J. Klimke, Effects of the homogeneity of particle coordination on solid-state sintering of transparent alumina, J. Am. Ceram. Soc., 89 (2006) 1985 – 1992

3. D. M. Chay, H. Palmour III, and W. W. Kreigel, Microstructure and room temperature mechanical properties of hot-pressed magnesium aluminate as described by quadratic multivariable analysis, J. Am. Ceram. Soc., 51 (1968) 10-16
4. A. Gatti, Development of a process for producing transparent spinel bodies, Final report contract N00019-69-C-0133, General electric co, Space division, Philedelphia, Pennsylvania, September 1969
5. R.J. Bratton, Translucent sintered $MgAl_2O_4$, J. Am. Ceram. Soc. 57 (1974) 283 - 286
6. D. W. Roy and J. L. Hastert, Method of manufacturing a transparent ceramic body, U.S. Pat. No. 3974249 – 264/ 65 (1976)
7. R. L. Gentilman, Fusion-Casting of Transparent Spinel, Am. Ceram. Soc. Bull. 60 (1981) 906-909
8. E. A. Maguire Jr. and R. L. Gentilman, Press Forging Small Domes of Spinel, Am. Ceram. Soc. Bull, 60 (1981) 255 – 256
9. D. W. Roy and J. L. Hastert, "Polycrystalline $MgAl_2O_4$ spinel for high temperature windows, Ceram. Engg. Sci. Proc., 4 (1983) 502 – 509
10. D. W. Roy and K. E. Green, "Transparent $MgAl_2O_4$ Spinel, A Broad Band Window Materials for Offensive Environments," Proc. SPIE, 1112 (1989) 2 – 8
11. M. E. Thomas, R. L. Joseph, and W. J. Tropf, Infrared Properties of Sapphire, Spinel and Yttria as a Function of Temperature, SPIE, 683 (1986) 41 – 48
12. T. M. Hartnett and R. L. Gentilman, Optical and mechanical properties of highly transparent spinel and AlON domes, Proc. SPIE, 505 (1984) 15-22
13. W. W. Ho, "Millimeter-Wave Dielectric Properties of Infrared Window Materials," Proc. SPIE, 750 (1987) 161-165.
14. C. M. Freeland, "High Temperature Transmission Measurements of IR Window Materials," Proc. SPIE, 929 (1988) 79-86.

15. A. Ghosh, K. W. White, M. G. Jenkins, A. S. Kobayashi, and R. C. Bradt, “Fracture Resistance of a Transparent Magnesium Aluminate Spinel,” J. Am. Ceram. Soc. 74, (1991) 1624-1630.
16. M. L. Huckabee, M. J. Paisley, R. L. Russell, and H. Palmour III, RCS–Taking the Mystery Out of Densification Profiles, Am. Ceram. Soc. Bull. 73 (1994) 82-86
17. J. A. Cox, D. Greenlaw, G. Terry, K. McHenry, and L. Fielder, Infrared and Optical Transmitting Materials, SPIE, 683 (1986) 49 – 62
18. M. C. L. Patterson, D. W. Roy, and G. Gilde, Improvements in Optical Grade Spinel; Ninth DoD EM Windows Symposium, May 2002, Huntsville, AL.
19. G. R. Villalobos, J. S. Sanghera, and I. D. Aggarwal, Degradation of magnesium aluminum spinel by lithium fluoride sintering aid, J. Am. Ceram. Soc., 88 (2005) 1321–1322
20. G. Gilde, P. Patel, and P. Patterson, Evaluation of hot pressing and hot isostatic pressing parameters on the optical properties of spinel, J. Am. Ceram. Soc., 88 (2005) 2747–2751
21. A. A. DiGiovanni, L. Fehrenbacher, D. W. Roy, Hard transparent domes and windows from magnesium aluminate spinel, Window and Dome Technologies and Materials IX, Proc. SPIE, 5786, 56–63 (2005).
22. T. J. Mroz, T. M. Hartnettb, J. M. Wahlb, L. M. Goldmanb, J. Kirschc, and W. R. Lindbergd, “Recent advances in spinel optical ceramic”, Window and Dome Technologies and Materials IX, Proc. SPIE, 5786, 64 – 70 (2005)
23. A. Goldstein, A. Goldenberg, Y. Yeshurun and M. Hefetz, “Transparent $MgAl_2O_4$ spinel from a powder prepared by flame spray pyrolysis”, J. Am. Ceram. Soc., 91 (2008) 4141–4144

24. P. Biswas, K. Rajeswari, P. Ramavath, R. Johnson and H. S. Maiti, Fabrication of transparent spinel honeycomb structures by methyl cellulose–based thermal gelation processing, J. Am. Ceram. Soc., 96 (2013) 3042–3045
25. R. Cook, M. Kochis, I. Reimanis and H. Kleebe, A new powder production route for transparent spinel windows: powder synthesis and window properties, Window and Dome Technologies and Materials IX, Proc. SPIE, 5786 (2005) 41 – 47
26. C.T. Wang, L. S. Lin and S. J. Yang, Preparation of $MgAl_2O_4$ spinel powders via freeze – drying of alkoxide precursors, J. Am. Ceram. Soc. 75 (1992) 2240 – 2243
27. S. S. Balabanov, V. E. Vaganov, E. M. Gavrishchuka, V. V. Drobotenko, D. A. Permin, and A. V. Fedin, Effect of magnesium-aluminum isopropoxide hydrolysis conditions on the properties of magnesium-aluminate spinel powders, Inorg. Mater. 50 (2014) 830 – 836
28. S.S. Balabanov, R.P. Yavetskiy, A.V. Belyaev, E.M. Gavrishchuk, V.V. Drobotenko, I.I. Evdokimov, A.V. Novikova, O.V. Palashov, D.A. Permin, V.G. Pimenov, Fabrication of transparent $MgAl_2O_4$ ceramics by hot-pressing of sol-gel-derived nano powders, Ceram. Inter. 41 (2015) 13366–13371
29. S. S. Balabanov, A. V. Belyaev, A. V. Novikova, D. A. Permin, E. Ye. Rostokina, and R. P. Yavetskiy, Densification peculiarities of transparent $MgAl_2O_4$ ceramics— Effect of LiF sintering additive, Inorg. Mater. 54 (2018) 1045 – 1050
30. A. Krell, J. Klimke, and T. Hutzler, Advanced spinel and sub - µm Al_2O_3 for transparent armor applications, J. Eur. Ceram. Soc.29 (2009) 275 - 281
31. A. Krell, T. Hutzler, and J. Klimke, Transparent Ceramics for Structural Applications, Ber. Dtsch. Keram. Ges., 84 (2007) E41– 49

32. T. Mroz and L. M. Goldman, A. D. Gledhill, D. Li and N. P. Padture, Nanostructured, infrared-transparent magnesium aluminate spinel with superior mechanical properties, Int. J. Appl. Ceram. Technol. 9 (2012) 83–90

33. M. Shimada, T. Endo, T. Saito and T. Sato, “Fabrication of transparent spinel polycrystalline materials”, Mater. Lett. 28 [4] 413–415 (1996)

34. N. Frage, M. Dariel, S. Meir and S. Kalabuchov, “Single-stage thermal process for manufacturing transparent sintered spinel”, U.S. Pat. No 2009/ 0297851 A1, Dec 3, (2009)

35. A. Krell, K. Waetzig and J. Klimke. Influence of the structure of $MgO{\cdot}nAl_2O_3$ spinel lattices on transparent ceramics processing and properties. J. Eur. Ceram. Soc. 32 (2012) 2887 – 2898.

36. L. Esposito, A. Piancastelli and P. Miceli, A thermodynamic approach to obtaining transparent spinel ($MgAl_2O_4$) by hot pressing. J. Eur. Ceram. Soc. 35 (2015) 651-661

37. D. Han, J. Zhang and P. Liu, Effect of polymorphism of Al_2O_3 on the sintering and microstructure of transparent $MgAl_2O_4$ ceramics. Opt. Mater. 71 (2017) 62-65.

38. D. Han, J. Zhang, P. Liu, G. Li and S. Wang, Densification and microstructure evolution of reactively sintered transparent spinel ceramics, Ceram. Inter. 44 (2018) 11101 – 11108

39. A. C. Sutorik, C. Cooper and G. Gilde, Visible light transparency for polycrystalline ceramics of $MgO.2Al_2O_3$ and $MgO.2.5Al_2O_3$ spinel solid solutions, J. Am. Ceram. Soc. 96 (2013) 3704 – 3707

40. A. F. Dericioglu and Y. Kagawa, “Effect of the Grain Boundary Micro-cracking on the Light Transmittance of Sintered Transparent $MgAl_2O_4$, J. Eur. Ceram. Soc., 23 (2003) 951– 959

41. A. F. Dericioglu, A. R. Boccaccini, I. Dlouhy, and Y. Kagawa, Effect of Chemical Composition on the Optical Properties and Fracture Toughness of Transparent Magnesium Aluminate Spinel Ceramics, Mater. Trans. 46 (2005) 996–1003
42. X. Guan, L. Li, J. Zheng, and G. Li, "$MgAl_2O_4$ nano particles: A new low – density additive for accelerated thermal decomposition of ammonium perchlorate", RSC Adv., 1 (2011) 1808 – 1814
43. B. Plesingarova, N Stevulov, M Luxov, E Boldi, and Z Arov, "Mechanochemical synthesis of magnesium aluminate spinel in oxide-hydroxide systems", J. Mat. Syn. Proc., 87 (2000) 2020 – 2024
44. S. Parvarinezhad, M. Salehi, and S. Kademinia, "Solid state synthesis of $MgAl_2O_4$ nano materials and solar light – induced photo-catalytic removal of malachite green", Inter. J. Nano. Dimens., 10 (2019) 89 – 104
45. S. Tripathy and D. Bhattacharya, "Rapid synthesis and characterization of mesoporous nanocrystalline $MgAl_2O_4$ via flash pyrolysis route", J. As. Ceram. Soc., 1 (2013) 328 – 332
46. A. Krell, T. Hutzler, J. Klimke and A. Potthoff, Fine-grained transparent spinel windows by the processing of different nano powders, J. Am. Ceram. Soc., 93 (2010) 2656–2666
47. M. R. Merac, H. Kleebe, M. M. Muller and I. E. Reimanis, Fifty years of research and development coming to fruition; unraveling the complex interactions during processing of transparent magnesium aluminate ($MgAl_2O_4$) spinel, J. Am. Ceram. Soc., 96 (2013) 3341–3365
48. A. Goldstein, A. Goldenberg, and M. Hefetz, Transparent polycrystalline $MgAl_2O_4$ spinel with submicron grains, by low temperature sintering, J. Ceram. Soc. Jpn. 117 (2009) 1281 – 1283

CHAPTER - VI

A novel approach of synthesizing nano Y_2O_3 powders for the fabrication of submicron IR transparent ceramics

6.1 Introduction

Polycrystalline transparent yttria (Y_2O_3) is widely known as an excellent optical material exhibiting transmissions in a wide range of electromagnetic radiations between 0.2 to 9 µm wavelengths. Y_2O_3 also exhibits high refractory properties and superior resistance to corrosion. Therefore, it is widely used for various applications such as host material for high power lasers and scintillators, envelopes for high-intensity-discharge lamps, IR transparent domes, and windows [1 – 2]. Y_2O_3 is the only material that shows full transmittance through the entire 3 – 5 µm mid wavelength infrared (MWIR) atmospheric band compared to the other competing IR transparent materials such as sapphire, submicron Al_2O_3, spinel, and AlON [3]. Besides, Y_2O_3 emit reduced re-radiation at elevated temperatures up to 1000°C and therefore becomes an exclusive choice for fabricating uncooled windows with reduced payloads. Low emittance from the Y_2O_3 heated domes or windows deliver improved signal to noise response to the seeker system and increase the acquisition ranges [4].

Successful fabrication of transparent grade ceramic materials involves various factors including selecting of right starting powders, shaping of defect-free green bodies, and controlling densification to eliminate the pores completely from the sintered bodies [5]. In the case of selecting starting Y_2O_3 powders, researchers either chose the commercial supplies [6 – 13] or utilized their own synthesized powders for the fabrication of green bodies. The in–house synthesis route received more attention between the two alternatives due to optical grade

commercial powders' high costs. In that context, investigators followed various synthesis techniques such as the dissolution of Y_2O_3 powder in acids followed by precipitation and calcination [14 – 17] and precipitation of yttrium salts [18 – 21].

In most conventional attempts [1 – 4, 6 – 7, 14, 22 – 26], Y_2O_3 bodies attained complete densification and optical transparency at temperatures between 1700°C to 2000°C. Such high – temperature processing enlarged the sintered grains to the sizes as large as up to 150 μm [22]. Transparent Y_2O_3 with such larger grain sizes exhibit low durability and flexural strength and hence, not suitable for advanced and high-performance dome applications [4]. As per the Hall-Petch relationship, ceramic materials with grain size lesser than one-micron exhibit higher mechanical properties. Therefore, presently, the focus of fabricating transparent Y_2O_3 is drifted towards reducing the grain sizes around one-micron or even to the submicron ranges to improve mechanical properties to combat the most aggressive missile trajectories. By adopting appropriate processing techniques such as initiating the fabrication with nano-sized (< 100 nm) Y_2O_3 powders and carefully achieving theoretical densities at lower temperatures, probably closer to 1400°C, it should be possible to retain the sintered grain sizes in the submicron regions.

In this context, Ikegami *et al*. [27 – 28] synthesized highly sinterable, Y_2O_3 nano powders from its hydroxide-based precursors. These powders exhibited round – edge morphology and showed enhanced sinterability compared to the conventionally utilized micron-sized powders. However, these powders contained contaminations of sulfur, as the process employed ammonium sulfate as a surface regulating agent for achieving round – edge morphology. These contaminations hindered Y_2O_3 from exhibiting theoretical transmissions. Apart from this orientation, Chen *et al*. [29] proposed a two-stage-sintering approach for sintering Y_2O_3 at lower temperatures. In this technique, the samples were heated at a higher temperature for few minutes, followed by drastic cooling to 100°C to 200°C lower than the higher temperature and

dwelled there for 20 to 40 hours until the body achieve complete densification. As per this technique, the high – temperature step activates the lattice diffusion between the neighboring particles, and the low – temperature step retains the lattice diffusion until the completion of densification.

Since the materials attained substantial densification at relatively lower temperatures, the sintered bodies retained their grain sizes in the submicron regions. Serivalsatit *et al.* [30 – 31] followed the footprints of Ikegami *et al*. [27 – 28] for the synthesis of sulfur - treated nano Y_2O_3 powders and utilized the two-stage–sintering technique combined with post HIPing to produce transparent Y_2O_3. Combination of both processing techniques effectively assisted in the fabrication of transparent Y_2O_3 with grain sizes around 300 – 400 nm with the optical transparency up to 80% in the 2.0 µm wavelength regions. This approach succeeded in retaining the sintered grain sizes in the submicron region. However, the prolonged dwelling periods of around 20 hours at the peak temperatures are neither energy-efficient nor suitable for continuous productions. Moreover, the material exhibited moderate fracture toughness. Y_2O_3 powders synthesized with sulfur additives induce liquid assisted densification [27 – 28], which in turn produce weaker grain boundaries that are vulnerable to the propagation of fractures. Apart from these approaches, low – temperature densification was explored using sintering techniques such as spark plasma sintering [32 – 34] and hot pressing [12 – 13, 35]. However, these methodologies produce only flat shapes and not suitable for large-scale productions and fabricating complex shapes such as domes. Alternatively, lowering the densification temperatures were attempted using various sintering additives including LiF [7, 36], Tm_2O_3 & ZrO_2 & Al_2O_3 [8], La_2CO_3 [17], Er and Yb ions, ZrO_2 & Ho ions and Tm & ZrO_2 [37 – 38]. These additives significantly improved the densification of Y_2O_3 and helped to attain superior transparencies. However, in most cases, these additives induced numerous absorption peaks at their corresponding wavelengths that may hamper the seekers'

performance.Sintering additives such as LiF entertain liquid assisted densification and affect the eventual mechanical properties similar to sulfate molecules.

Fig. 6.1 shows the overall summary [4, 7 – 8, 11 – 12, 14, 17 – 18, 20, 31, 36 – 37, 39 – 41] reporting the fabrication of transparent yttria having optical transmissions in the wavelength region between 1.0 and 8.0 µm. The evolution progressed towards constructing nanostructured material having optical transparency equivalent to single crystals, which is closer to 84% in the specified IR regions [7].

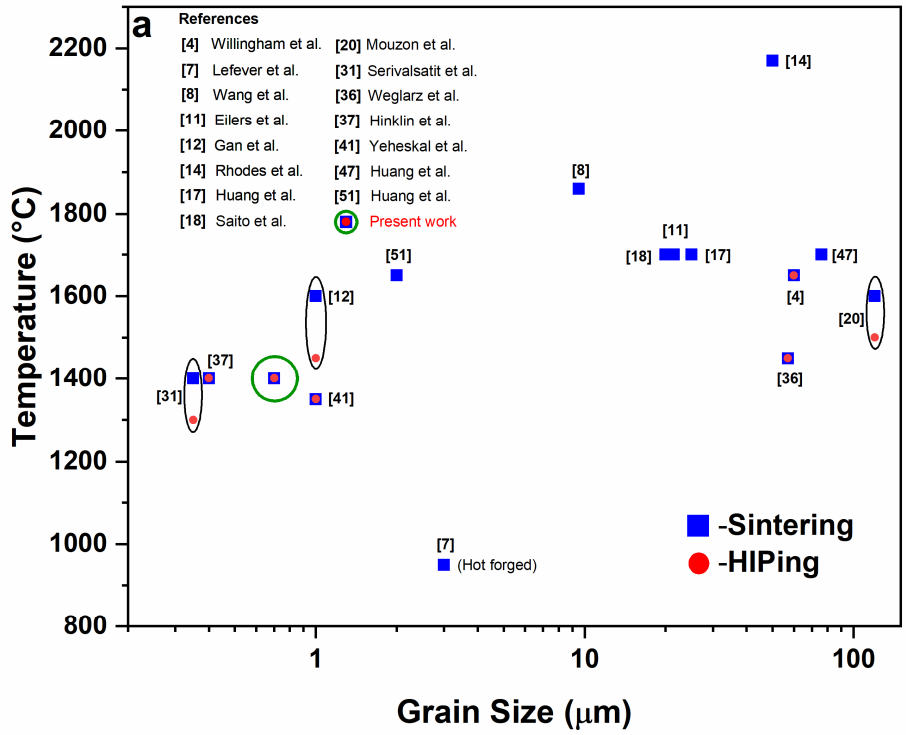

Figure 6.1a. Literature mapping of transparent Y_2O_3 in terms of its grain size Vs processing temperature

As shown in fig. 6.1a, very few have succeeded in retaining the final grain sizes under 1.0 µm [12, 31, 37, 39], and irrespective of the processing routes, all the methods invariably employed HIPing for controlling the grain sizes. Moreover, achieving densification at temperatures around 1400°C preserved sintered grain sizes in the submicron regions [31, 37].

Among, Hinklin et al. [37] employed commercial Y_2O_3 powders as starting powder, erbium atoms as sintering additives, and vacuum sintering for densification. Similarly, Serivalsatit et al. [31] utilized Sulphur-treated Y_2O_3 powders as starting material, erbium additives as sintering aid, and two-stage–vacuum sintering for densification. As discussed above, selecting commercial powders or attaining low-temperature densification through additives and two-stage-sintering techniques directly affects optical transparency and production costs. Also, samples sintered in a vacuum atmosphere usually require post-sintering-annealing treatments in the air atmosphere at temperatures above 1200°C for periods above 3 – 5 hours to regain the oxygen stoichiometry [37]. These additional procedures further increase the costs of the product.

Therefore, there is a need for an improved process to demonstrate the synthesis of sulfur-free, nano yttria powders suitable for fabricating sub-micron IR transparent Y_2O_3 materials. It would be advantageous if the process establishes low-temperature densification through economical sintering methods without any sintering additives to derive maximum benefits in optical transmissions and production costs.

Accordingly, in the present work, a facile synthesis methodology is developed to produce highly – reactive Y_2O_3 powders suitable for making sub-micron IR transparent Y_2O_3 materials. The process details the synthesis of round-edged Y_2O_3 powders without using any detrimental sulfate ions. Similarly, the method utilized an ambient atmosphere for densification at temperatures around 1350 – 1400°C and retained the sintered grain sizes in the submicron region as shown in fig. 6.1. Post sintering HIPing enhanced the densification to 100% theoretical densities and exhibited the high - inline transmissions equivalent to single crystal Y_2O_3 [7] as shown in fig. 6.1b. Besides, no annealing procedures were followed after HIPing as the process utilized the air atmosphere for pre-densification. This study further confirms the

physical, chemical, thermal, mechanical, and optical properties of the synthesized powders and the sintered samples through systematic characterization and analysis.

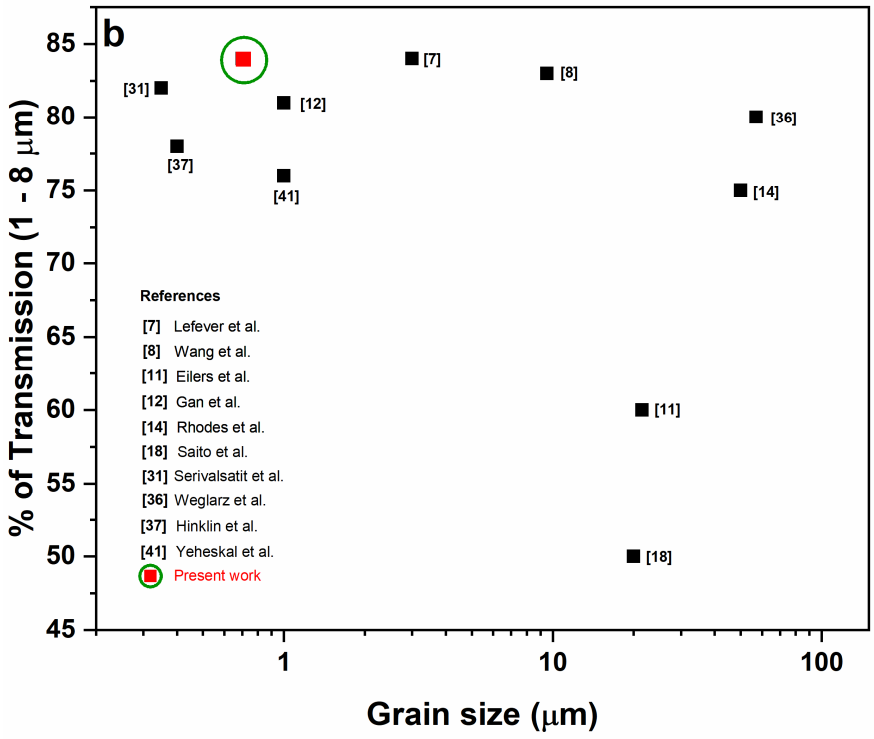

Figure 6.1b. Literature mapping of transparent Y_2O_3 in terms of its grain size Vs % of IR transmission

6.2 Highlights of the investigation

- Synthesis of highly reactive, Sulfur–free nano Y_2O_3 powders for the fabrication of submicron IR transparent yttria ceramics is reported for the first time

- Seeding of Y_2O_3 particles during the sol – gel process enabled achieving powders with round – edged morphology

- Effective inter-particle coordination and traces of Al_2O_3 inclusions accelerated densification at temperatures as low as 1400°C in air atmosphere.

- Low temperature densification is achieved through economical air sintering in the present study while similar densification is hitherto reported using expensive sintering techniques such as two – stage/ three – stage/ vacuum sintering
- Sintered and HIPed samples exhibited IR transmissions up to 84% in the 2.0–9.0 μm regions, equivalent to single crystal Y_2O_3
- The grain sizes were retained closer to 700 nm for the transparent yttria specimens
- Retaining the grain sizes in the submicron regions improved the hardness up to 8.9 GPa
- Achieving densification through solid – state sintering enhanced fracture toughness up to 3.0 $MPa.m^{1/2}$ which is twice the values reported for single crystal Y_2O_3

6.3 Experimental Procedure

6.3.1 Starting materials

Yttrium (III) nitrate hexahydrate (YNHH – 99.9%, Acros Organics, Fair Lawn, NJ) was used as a main precursor, and yttrium oxide powder (99.99%, Sigma Aldrich, St. Louis, MO) was used as seeding material. As-received yttrium oxide powder was milled in a planetary ball mill at 200 RPM using isopropyl alcohol as milling medium and 2.0 mm-sized alumina balls as grinding media. The ratio between powder and balls were maintained as 1: 2, and the milling was performed for six hours. The milled suspension was dried in a hot air oven at 70°C for four hours to obtain dried yttria powder and was used as a seed for the entire study.

6.3.2 Preparation of yttria sol

0.5 molar yttrium nitrate solution was prepared by dissolving YNHH in distilled water using a high-speed mechanical stirrer. The solution's initial pH was noted as four, and the pH of the solution was adjusted to 10 by adding liquid ammonia (40% solution, AR Grade, Finar, India) dropwise to form yttrium hydroxide (YOH) precipitate. The residue was washed in a Buckner

funnel using distilled water until the filtered water reaches a pH of seven. The washed residue was further dried in a hot air oven at 100°C for 12 hours to obtain the dried yttrium hydroxide powder. Ten grams of the precipitate powder was calcined at 1100°C for one hour in the air furnace to find the actual Y_2O_3 content in the precipitate powder. For the preparation of yttria sol, the dried YOH powder and distilled water were mixed at a 1:9 weight ratio using a high-speed mechanical stirrer for one hour. The mixture was further peptized by the dropwise addition of glacial acetic acid (AR Grade, Finar, India) to adjust the pH between two and three. The stirring was continued until the formation of transparent Y_2O_3 sol.

6.3.3 Preparation of Y_2O_3 seed suspension

Aqueous suspension of Y_2O_3 having 50 wt% solid content was prepared by dispersing milled yttria powder in distilled water using 1.0 wt% Darvan 821A (R.T. Vanderbilt Co. Inc., Norwalk, CT) as a dispersing agent. The mixture was ball milled at 50 rpm in a polypropylene jar using 2.0 mm size alumina balls for four hours to obtain stable aqueous seed suspension. The ratio between the balls the powder was maintained as 2: 1 by weight.

6.3.4 Synthesis of Y_2O_3 nano powder

Transparent Y_2O_3 sol was kept under constant stirring conditions using a high-speed mechanical stirrer. Stirring was continued for 30 minutes, and the seed suspension was slowly added to the sol. The weight ratio of Y_2O_3 between the sol and the seed suspension was maintained at 70:30. Stirring was continued for 30 minutes to obtain a homogenous suspension of the sol-seed mixture. Gelation was induced by the dropwise addition of liquid ammonia to adjust the pH to 10, and the gel was kept in the hot air oven at 100°C for 12 hours to obtain the dried gel. The dried gel was calcined at temperatures between 500°C and 1100°C in an air furnace for one hour to get single-phase Y_2O_3 powder. The calcined powder was further milled in the planetary mill for two hours at 200 RPM using isopropyl alcohol as a milling medium

and alumina balls as grinding media. Polyvinyl pyrrolidone (Sigma Aldrich, St. Louis, MO) having two percentage of 7ntrations by weight to Y_2O_3, was added during milling as a binder. The milled suspension was dried at 70°C in the hot air oven for obtaining the Y_2O_3 nano powders.

6.3.5 Fabrication of transparent Y_2O_3

The dried nano Y_2O_3 powders were compacted into pellets in a uniaxial press at 30 MPa pressure. The compacts were further sintered at temperatures between 1300℃ and 1400℃ for 1 hour in the atmospheric air furnace. The peak temperature was reached at a heating rate of 5°C/min, and the same was maintained for cooling to room temperatures. Sintered samples obtained complete densification through HIPing at 1400℃ for 6 hours at 160 MPa pressure to fabricate transparent Y_2O_3.

6.3.6 Characterization of powders and sintered specimens

As received and milled Y_2O_3 seed powders were analyzed for their microstructural features using FEG-SEM (Carl Zeiss Microscopy GmbH, Oberkochen, Germany) and the phase purity using XRD (Rigaku Corporation, Tokyo, Japan). Their particle size and size distribution were measured using a particle size analyzer (Nano SZ, Malvern Instruments Ltd, UK). The dried gel was tested for its thermal response in the TG-DTA analyzer (Netzsch STA 409C, Selb, Germany). The bonding characteristics between Y and O atoms at various calcination stages were studied using FTIR (Vertex 70, Bruker Optik GmbH, Germany) analyzer. Thin wafers of 20 mm diameter and 0.3 mm thickness composed of KBr and respective Y_2O_3 powders at 200: 1 mg ratios were prepared for the FTIR analysis. XRD followed phase formation studies of nano Y_2O_3 powders, and the microstructural characteristics of the calcined powders were analyzed by FESEM and TEM (FEI, Technai G2, Netherlands) analyses. Particle size and size

distribution of the powder was measured using a particle size analyzer, and the surface area of the powders was characterized through BET surface analyzer (Gemini, Micromeritics, USA).

The Y_2O_3 green compact's sintering behavior was followed through the single pushrod LVDT dilatometry studies (Netzsch, Germany) under 10°C/min heating rates in the air atmosphere. The compacted green samples of dimensions 10mm X 10mm X 10mm were used for this study. Porosities and densities were calculated using the Archimedes principle. Relative densities were calculated to the theoretical density of Y_2O_3 as 5.031 g/cc. Microstructural features of the samples concerning their densification temperatures were analyzed through FESEM. The average grain size of the sintered specimens was measured through the linear intercept method. Sintered and HIPed samples were tested for their hardness with the Knoops indentation under 100g load (Leco, St. Joseph, MI), and the fracture toughness (K_{IC}) was measured using the following Anstis principle [42].

$$K_{IC} = 0.016 (E/H)^{1/2} (P/C^{3/2}) \quad \text{---------- (1)}$$

E is Young's modulus, H is the hardness, P is the applied load, and C is the half-penny crack length formed at the indent's corners during the hardness test. The fracture was induced through Vickers indentation at 500g, and the crack length was measured using FESEM images. The Young's modulus of the transparent Y_2O_3 was calculated from the nano-indentation method [43]. The indentation load – depth curve obtained by testing the sample in a cyclic nano impact tester (Micro materials Inc., UK) using a Berkovich indenter at 40 g loading conditions. The average modulus was found to be 185.3±1.2 GPa from eight indentations. These values were similar to the values reported by Yeheskel *et al*. [39].

Thermal diffusivity and conductivity characteristics for the sintered (1400°C) and HIPed samples were studied using a laser flash technique. Thermal conductivity (λ) with the unit W/(m.K) is the measure of transport of energy in the form of heat through a body of mass due

to temperature gradients. The thermal conductivity of a material is calculated using the following equation

$\lambda = \rho . Cp . \alpha$ ---------- (2)

Where ρ is the specimen's density measured by the Archimedes principle, Cp is specific heat capacity, and α is thermal diffusivity. In the present study, the optically polished samples of dimensions 10mm X 10mm X 1 mm were used. The laser flash technique is a transient method that provides transitional thermal flow to the specimen and determines the characteristic of thermal conductivity concerning temperatures. In this study, a short laser energy pulse hits the top surface of a flat-faced, parallel-edged sample. The resulting change in temperature on the sample's lower body is measured through an infrared detector. The rise in temperature to time corresponds to the thermal energy diffusion along with the specimen's thickness. The conductivity measured in this study is an average of the values from three laser shots at each temperature. The thermal diffusivity α was calculated using the following equation

$\alpha(T) = 0.1388 \text{ X } (d^2/t_{1/2})$ --------- (3)

T is the temperature of measurement, d is the thickness of the specimen, and $t_{1/2}$ is the time needed for the specimen's rear side to reach half the maximum temperature [44].

HIPed and optically polished transparent Y_2O_3 samples of 1.4 mm thickness were analyzed for their transmission characteristics in the wavelength region between 2.0 and 9.0 μm through FTIR analysis. The entire fabrication procedure is shown as a flowchart in fig. 6.2.

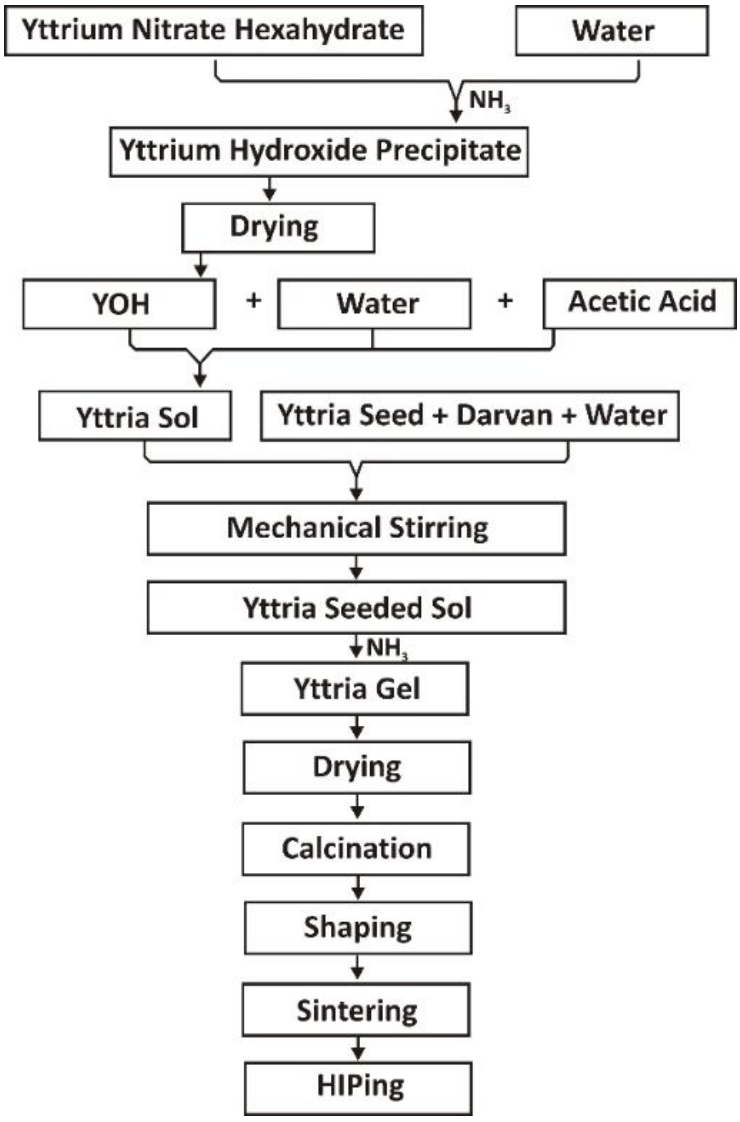

Figure 6.2. Process flow chart for fabricating transparent Y_2O_3

6.4 Results and Discussions

6.4.1 Physical characteristics of Y_2O_3 seeds

Fig. 6.3 shows the morphological characteristics of the yttria seeds used in this study. Fig. 6.3a shows the image of Y_2O_3 powder in the as-received condition. The morphology was in the form of large chunks having random shapes with a wide range of size distribution ranging between 1.0 – 10 µm with an average size closer to 3.0 µm, as shown in fig. 6.3b. Fig. 6.3c

shows the image of the Y_2O_3 seed particles milled for 6 hours. The initial coarser chunks were effectively reduced to the sizes around 100 nm to 200 nm with high homogeneity. Figure 6.3d shows the particle size distribution of the milled seed particles. The curve indicates the narrow size distribution of the milled particles with a mean size of around 120 nm.

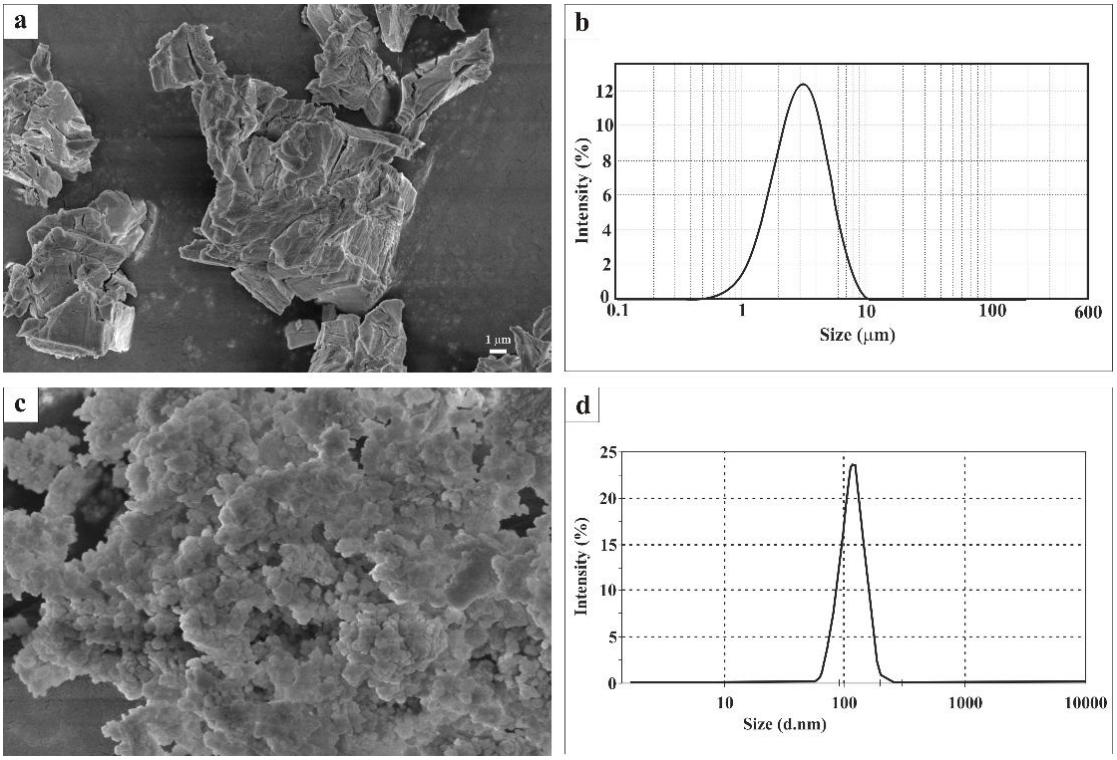

Figure 6.3. Characteristics of seed particles (a) Morphology and (b) PSD of as received Y_2O_3, (c) Morphology and (b) PSD after milling

6.4.2 Thermal analysis of dried yttria gel

Figure 6.4 shows the TGDT analysis of the dried sol-gel powder up to 1500°C in air atmosphere. The TG curve shows three significant weight losses at various stages of heat treatment. The initial decrement of 15% of weight up to 250°C, and the corresponding endothermic valley in the DTA curve was attributed to the loss of physically combined water. The gel exhibited significant weight loss up to another 35% at temperatures between 300 and 400°C due to the evaporation of chemically combined water. The second endothermic drop in

the DTA curve at these temperature regions also indicates the same event. Another minor loss of less than 6.0 % noticed up to 650°C ascribed to the loss of carbon from acetic acid used during the peptization process. The dried gel showed no further loss beyond 650°C. The gel powder exhibited an exothermic peak at 570°C, attributed to the phase formation of Y_2O_3.

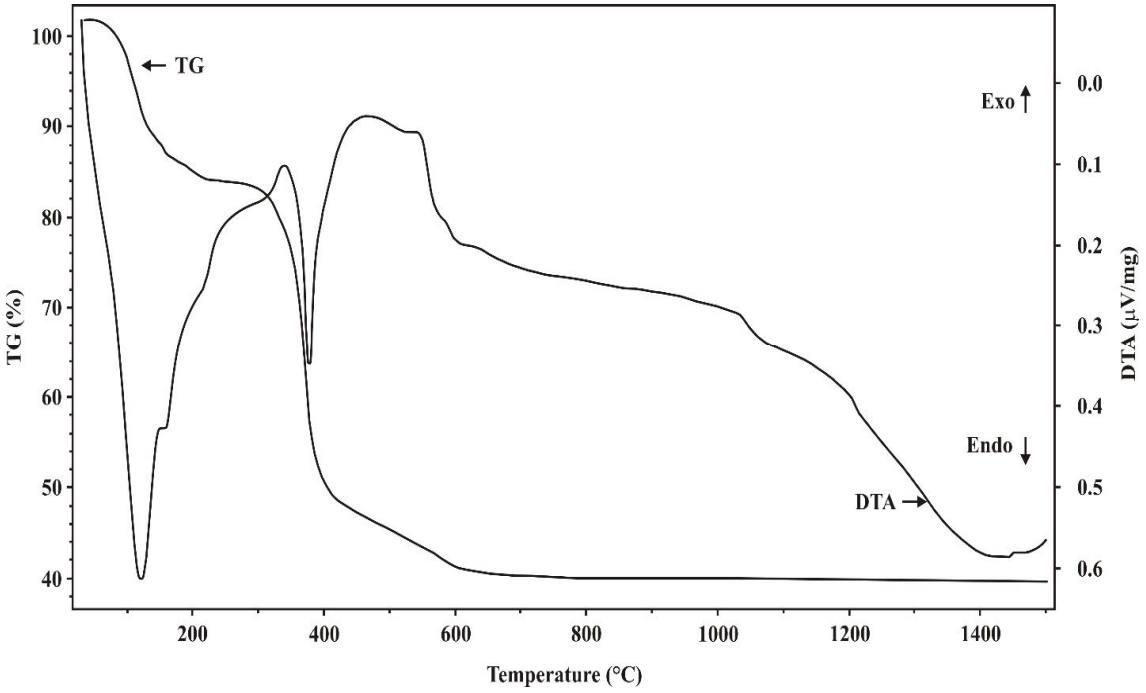

Figure 6.4. TGDTA analysis of dried yttria gel powder

6.4.3 Bonding characteristics of the yttria powder

Fig. 6.5 shows the IR spectrum of yttria powders calcined at different temperatures between 100°C and 1100°C. Fig. 6.5a shows the gel powder's characteristic curve dried at 100°C, exhibiting a broad absorption band between 3300 and 3600 cm^{-1} corresponding to water molecules' valence vibration [45]. The spectrum also shows another absorption at 1640 cm^{-1} attributed to another characteristic stretch for the H-O-H bond [46].

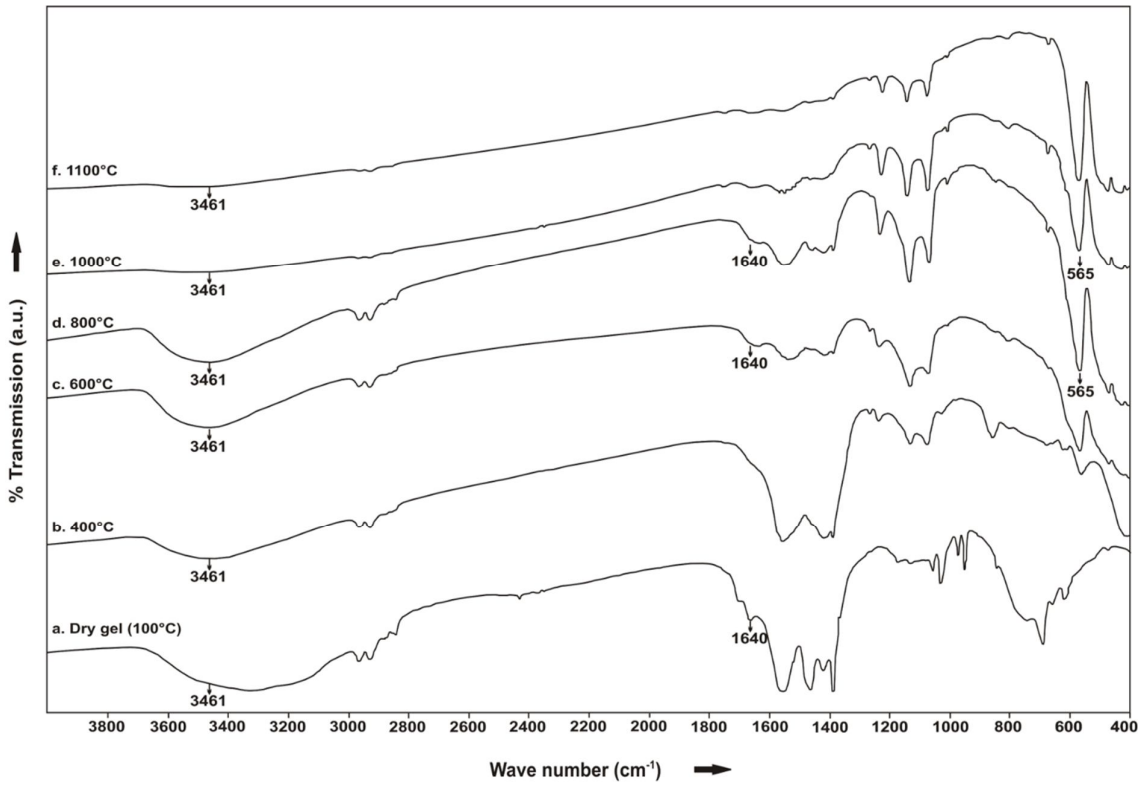

Figure 6.5. FTIR spectrum of Y_2O_3 powders at various stages of processing temperatures

The water absorption bands observed at 400°C (fig. 6.5b) to 800°C (fig. 6.5d) indicates that the powders calcined at these temperature regions absorbed moisture from the atmosphere due to their high surface area. However, these water molecule bonds were not observed for the powders calcined at 1000°C (fig. 6.5e) and 1100°C (fig. 6.5f), which indicates that the powder becomes non-reactive to the atmospheric moisture after its calcination beyond 1000°C. A sharp absorption peak at 565 cm^{-1} corresponding to the Y-O bond [30] was prominent for the powder calcined at 600°C, and its intensity grew more profound for the higher calcination temperatures. It indicates the phase transformation of Y_2O_3 from amorphous to crystalline to the increment in the calcination temperatures. Based on these observations, the dried gel powder was calcined at 1100°C to synthesize the nano Y_2O_3 powder.

6.4.4 Phase formation studies

Fig. 6.6 shows the progress in the phase formation of Y_2O_3 at various stages of calcination.

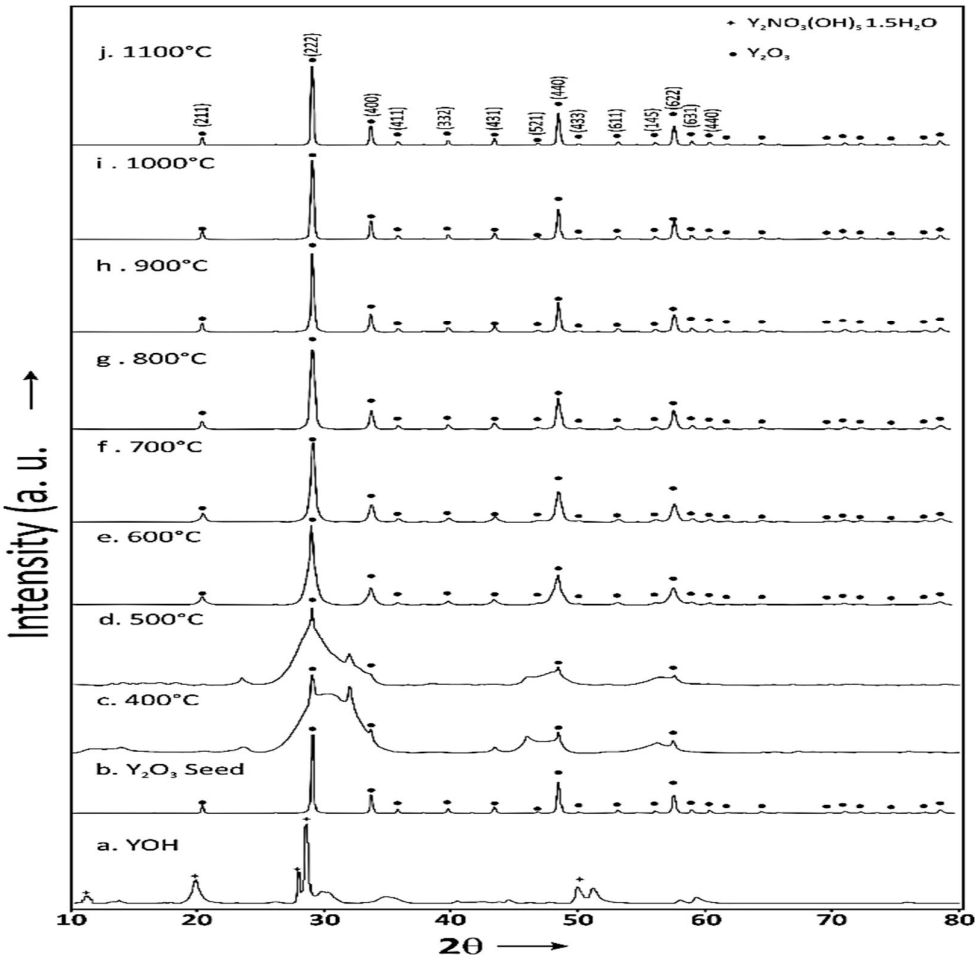

Figure 6.6. Phase transformation of Y_2O_3 as a function of calcined temperatures

Fig. 6.6a shows the XRD pattern corresponding to the precipitate powder obtained from YNHH and dried at 100°C. The peaks were matching with the yttrium hydroxide phase coordinating to the JCPDS No. 49-1107. Fig. 6.6b shows extremely sharp reflections from the milled seed particles. All the peaks correspond to the crystalline cubic Y_2O_3 phase, and no secondary phases were observed after milling operation. Fig. 6.6c and fig. 6.6d show the respective peaks gained from the Y_2O_3 gel powders calcined at 400°C and 500°C. The patterns exhibited broad peaks confirming the major portion of the powder as amorphous. However, few sharp peaks

corresponding to crystalline Y_2O_3 seeds were observed. All the amorphous phases were transformed into crystalline phases as the calcination temperature progressed to 600°C, as shown in fig. 6.6e and in good agreement with the TGDTA data corresponding to the phase transformation peak observed at 570°C. The reflections were still looking broader at this stage due to its ultra-fine particle sizes. Further heat treatments beyond 600°C sharpened the peaks indicating the Y_2O_3 crystals and particle growth refinement. At 1100°C, the powders exhibited all the reflections of (211), (222), (400), (440) planes corresponding to phase pure, crystalline cubic Y_2O_3 as observed in fig. 6.6j. The lattice parameter of the Y_2O_3 crystals at this temperature was found to be 10.582 Å.

6.4.5 Microstructural and physical characteristics of the Y_2O_3 nano powders

Fig. 6.7 shows the FESEM images of sol-gel derived Y_2O_3 powders heat-treated at various temperatures. Fig. 6.7a shows the gel's morphology dried at 100°C, composed of YOH coated Y_2O_3 seeds. The image confirms that the seed particles are homogeneously dispersed in the matrix of sol. Fig. 6.7b shows the appearance of Y_2O_3 powder calcined at 800°C. The powder seems to contain aggregates comprised of ultrafine Y_2O_3 particles progressing to obtain their individual shapes. The BET surface area of the powder at this temperature was found to be 67.55 m^2/g. On the further increment of calcination temperature to 1000°C, the particles grown larger and obtained their distinctive shapes, as shown in fig. 6.7c. The surface area at this temperature was found to be 59.27 m^2/g due to particle growth. The TEM image in fig. 6.7d reveals well distinctive particles exhibiting near – spherical morphology with average particle sizes closer to 40 – 50 nm. Fig. 6.7e shows the morphology of Y_2O_3 powder calcined at 1100°C. At this temperature, the powder consisted of well-crystallized, non – aggregated particles with very narrow size distribution having an average size of about 60 nm, as shown in the TEM image (fig. 6.7f). The surface area at this stage was found to be 45.76 m^2/g.

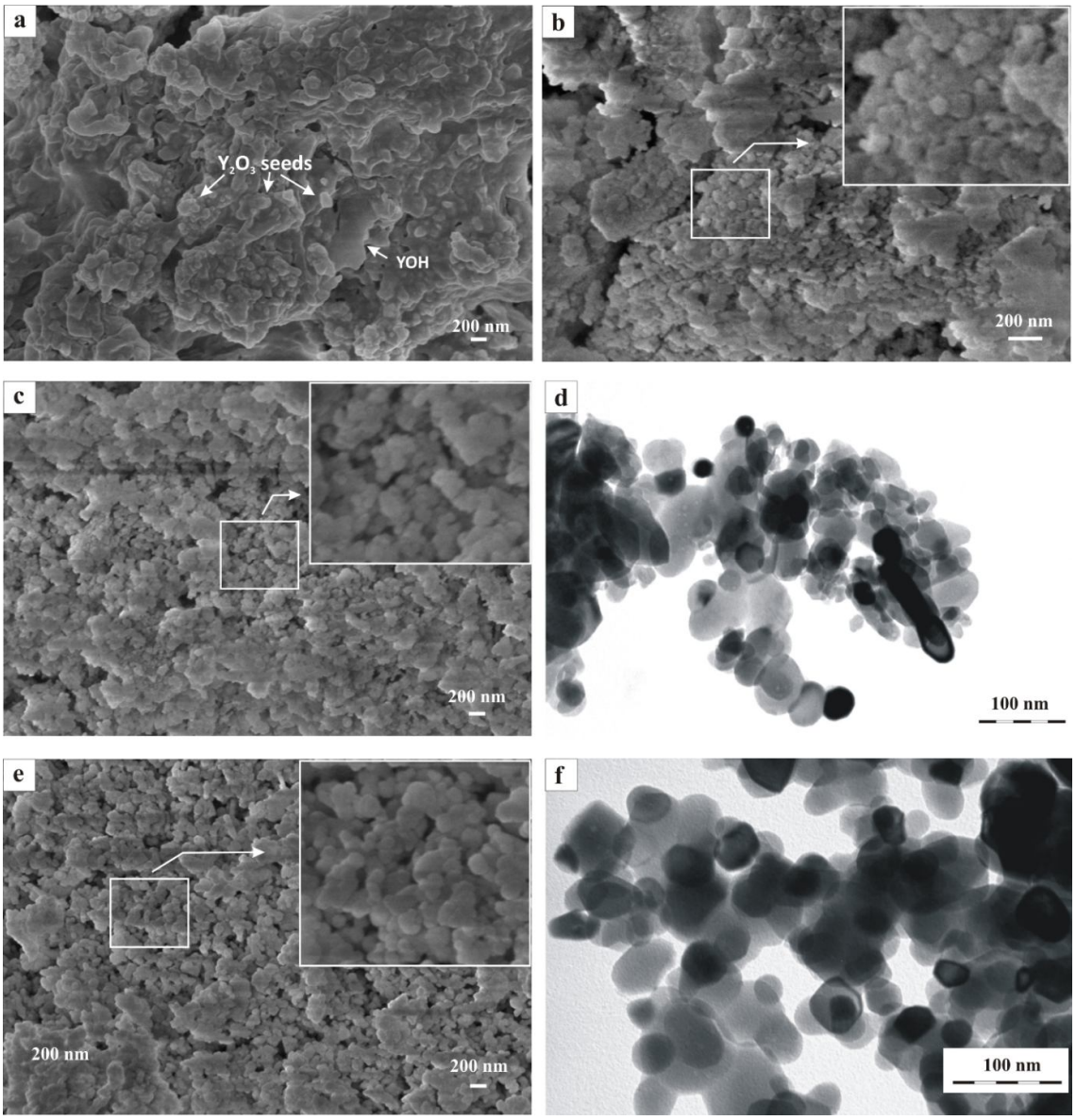

Figure 6.7. Microstructural features of Y_2O_3 powders. (a) Precursor gel dried at 100°C, (b) calcined at 800°C, (c) at 1000°C, (d) TEM image of powder at 1000°C, (e) at 1100°C, (f) TEM image of powder at 1100°C

In the earlier studies [16, 18, 47], Y_2O_3 powders synthesized through the calcination of as-synthesized YOH precipitate exhibited particles having flat surfaces and sharp edge morphology. YOH's physical characteristics are usually flaky and irregular, comprising larger flat agglomerates [27 – 28], as shown in fig. 6.8a and schematically in fig. 6.9a. The state of

aggregation, rigidity, thickness, and the morphology vary based on the precipitation process's pH and temperatures. Dupont *et al.* [48] and Wen *et al.* [16] obtained precipitates with distinctive characteristics based on the procedures followed for the synthesis. The sediments' physical structure crumble upon calcination at a temperature closer to 800 – 900 ℃, forming highly reactive powder particles.

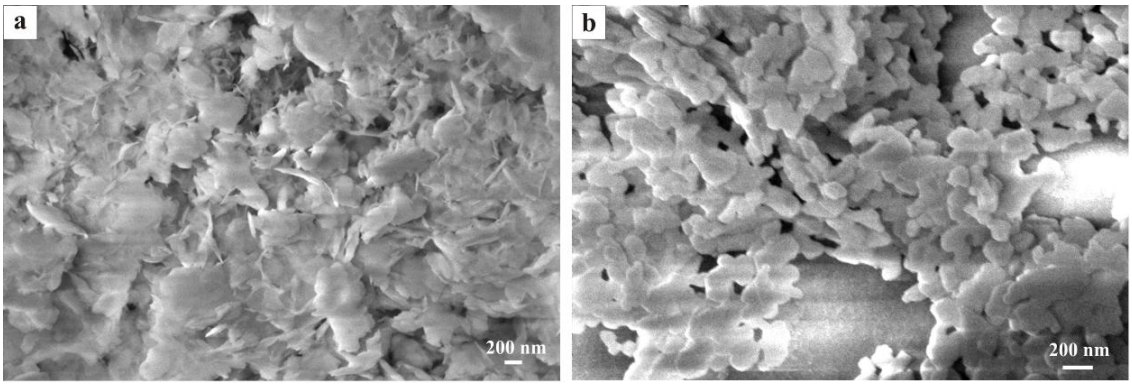

Figure 6.8. SEM micrograph of (a) YOH precipitates, (b) Y_2O_3 powder derived from direct calcination of YOH at 1100°C

The powder at this stage exhibit very high surface area and on the verge of obtaining crystallinity. The state of aggregation of these partially crystallized Y_2O_3 particles solely depends on the morphology of starting YOH precipitates and usually exhibits irregular accumulation, as shown in fig. 6.9b. Therefore, the powders exhibit inhomogeneous and vigorous inter-particle diffusion and particle growth on further calcination to 1100°C. As a result, the crystal planes orient randomly at the powders' surface, leading to uneven and sharp-edged particles, as shown in the fig. 6.7b and schematically in fig. 6.9c. Fig. 6.8b further shows that the particles from YOH precipitates grew relatively larger (200 nm) than the sizes obtained through present sol-gel method shown in fig. 6.7e.

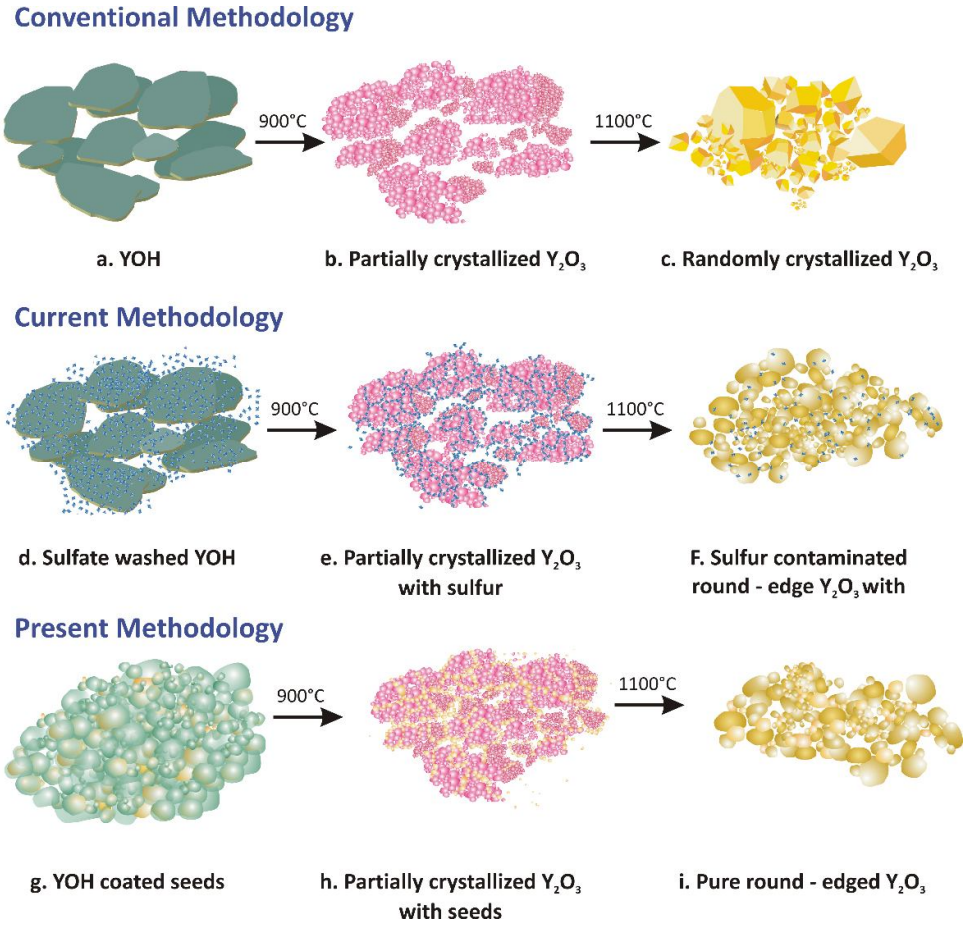

Figure 6.9. Schematic of synthesizing round – edged Y_2O_3 powders

Green bodies produced with such randomly crystallized powders exhibit low green densities due to the lack of inter-particle coordination. Consequently, they require very high temperatures for achieving complete densification. To prevent such formation of irregular morphologies, Saito *et al.* [18] washed the YOH precipitates with ammonium sulfate to introduce sulfate ions, as shown in fig. 6.8d. These sulfate ions hindered YOH's crumbling at 800 – 900°C, resisted their aggressive inter particle diffusion and aided the formation of finer aggregates as shown in fig. 6.9e. The sulfate ions further controlled crystal planes' orientation at the surface and produce round-edged Y_2O_3 particles at higher calcination temperatures [19],

as illustrated schematically in fig. 6.9f. Therefore, this suggestion was considered necessary for making round-edged yttria powders and followed by various investigators [16, 19, 29, 40] to fabricate transparent Y_2O_3 ceramics. However, Ikegami *et al.* [19] reported that the sulfur-treated Y_2O_3 form yttrium oxy-sulfide liquid due to Sulfur contaminations and steer the densification mode through liquid phase sintering. Transparent ceramics are highly sensitive for the secondary phases and their presence in minute quantities cause enough inline optical scattering and diminish the transmission levels due to their variance of refractive index [3]. Therefore, the present study neither followed the direct calcination of YOH nor utilized detrimental sulfate ions for synthesizing spherical Y_2O_3 powders. Instead, the YOH was dispersed into a translucent sol through acid peptization, followed by the addition of Y_2O_3 seeds. The successive gelation process effectively preserved the physical and molecular homogeneity of sol – seed mixture, as shown in fig. 6.9g. The peptization process enhanced the nucleation centers for homogenous nucleation and controlled the formation of Y_2O_3 particles. The seeds hindered the development of inhomogeneous aggregation of partially crystallized Y_2O_3 particles, as shown in fig. 6.9h. The seeding concept for nucleation and the development of aggregate – free nano powders were reported earlier for alumina and Y_2O_3 [49 – 50]. It has recently been reported that seeded alumina powders effectively controlled the sintered microstructure to fabricate submicron transparent alumina [51]. Similarly, in this study, the well-dispersed Y_2O_3 seed particles acted as active nucleation sites for the particle growth and enhanced the phase transformation kinetics. Eventually, the finely-aggregated Y_2O_3 particles exhibited controlled inter-particle diffusion, leading to particles' homogenous growth at higher calcination temperatures. Further, the organized arrangement of crystal planes at the surface assisted in isotropic, round-edged particles, as shown in fig. 6.9i.

The powders were further characterized for their crystallinity through high-resolution TEM analyses, as shown in fig. 6.10. The powders calcined at 1000°C exhibit a thin amorphous

external layer, as shown in fig. 6.10a, which indicates the need for further calcination at higher temperatures to gain complete crystallinity. On an additional increment of calcination temperature to 1100°C, the particles attained absolute crystallinity. The outer amorphous region disappeared after acquiring complete crystallinity, as shown in fig. 6.10b. The figure's insert shows the orderly aligned crystal planes up to the particle's edge confirming crystallinity. The selected area electron diffraction (SAED) pattern of the Y_2O_3 particle calcined at 1000°C in fig. 6.10c shows the clusters of hkl planes that are yet to obtain their respective sites, whereas, as shown in fig. 6.10d, the particle calcined at 1100°C exhibited well-defined positions of hkl planes corresponding to completely crystallized cubic yttria.

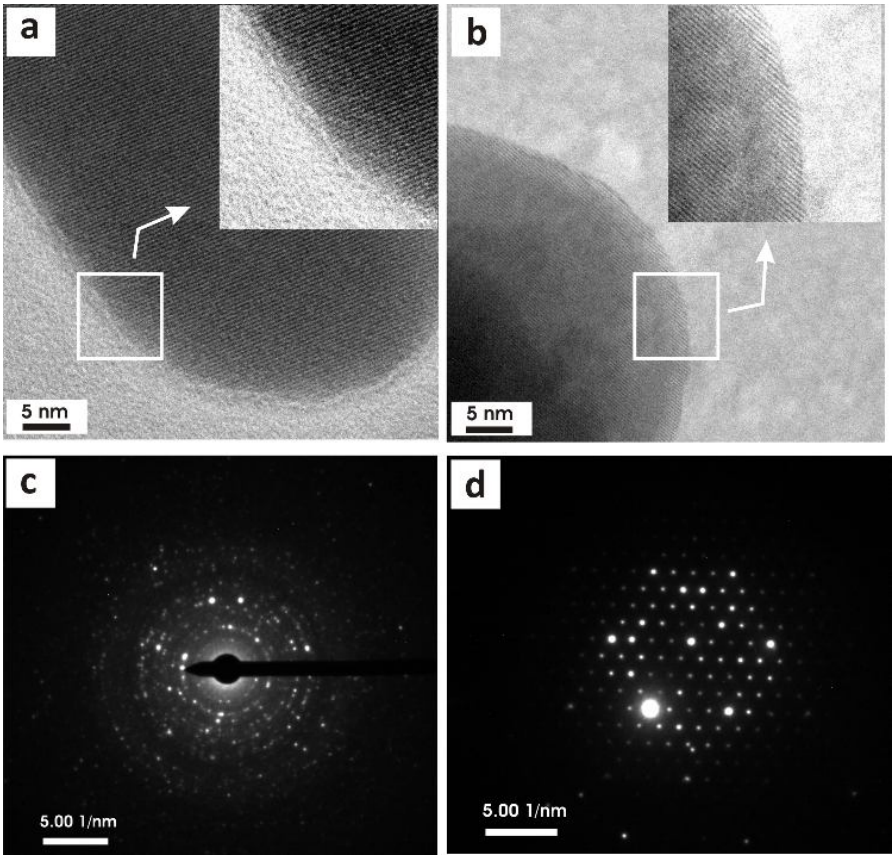

Figure 6.10. High-resolution TEM image of Y_2O_3 particle calcined at (a) 1000°C, (b) 1100°C and SAED pattern of particle calcined at (c) 1000°C, (d) 1100°C

6.4.6 Sintering characteristics of green Y_2O_3 specimens

Fig. 6.11 shows the dilatometry shrinkage and rate of shrinkage curves obtained for the green Y_2O_3 samples at the temperature region between 700°C and 1550°C heated under a constant heating rate of 10°C/min. No significant shrinkage was observed up to temperatures around 1100°C, and the onset of shrinkage was initiated at 1150°C. The shrinkage progressed faster beyond this temperature and reached its plateau region at temperatures closer to 1400°C. The rate of shrinkage curve reveals that the densification advanced rapidly due to high inter-particle diffusion of nanoparticles. The pattern explains that the powders produced in this study exhibited superior sinterability compared to the powders derived from flame pyrolysis, chemical vapor condensation [4], and precipitation [30 – 31]. The powders of these processing techniques have shown equivalent densification above 1500°C.

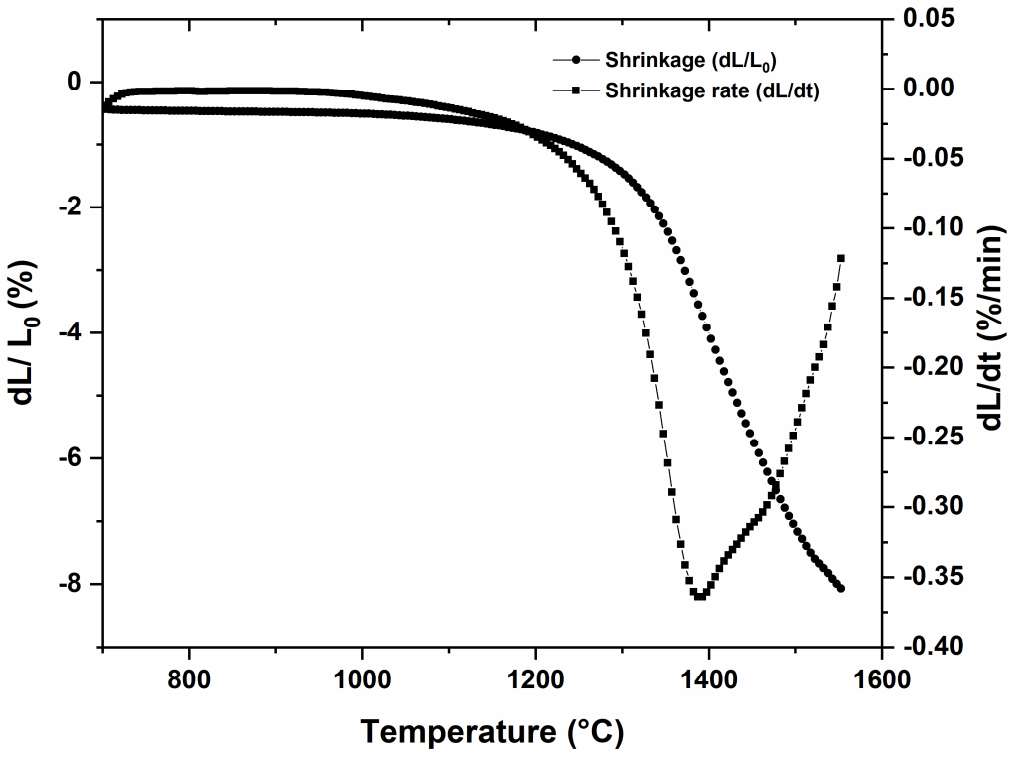

Figure 6.11. Sintering pattern of Y_2O_3 green compact

Fig. 6.12 shows the densification pattern of Y_2O_3 samples to their sintering temperatures for 1 hour in an air atmosphere. The samples sintered at 1300°C exhibited open porosities up to 12% with the corresponding theoretical density (T.D.) closer to 87%. With the further rise of sintering temperatures to 1325°C, the open porosities were significantly reduced from 12% to 2%, indicating the major densification events in these temperature regions. The sintered densities at this stage were found to be around 91% of T.D. At 1350°C, all the open pore channels were closed entirely, and the densities were increased to 96%. Additional increments in the sintering temperatures to 1375°C and 1400°C considerably improved the densification to exhibit T.D. up to 97.3% and 98.5%, respectively.

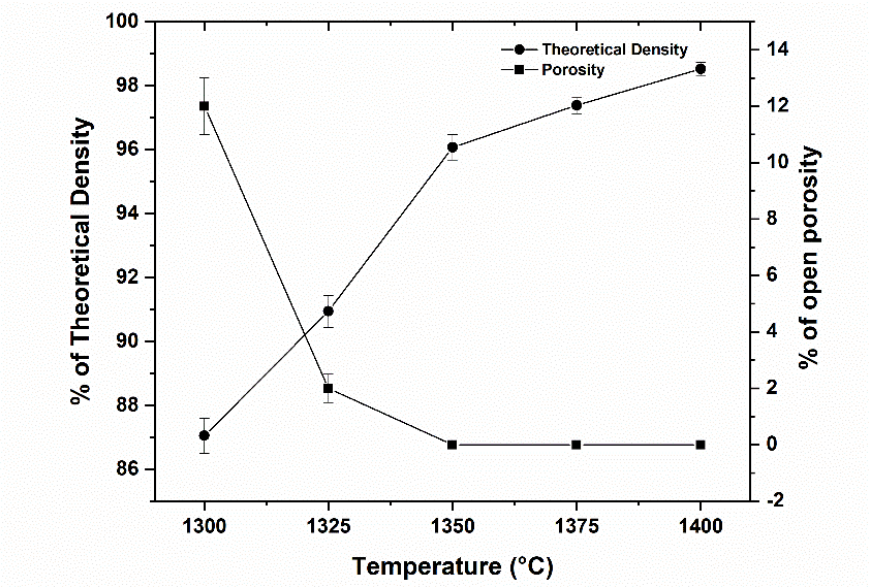

Figure 6.12. Densification of Y_2O_3 as a function of sintering temperature

The powder morphology, shaping routes, homogeneity in the green body and sintering methodology significantly influence the densification of materials. Most of the existing methods achieved complete densification of Y_2O_3 at temperatures above 1700°C [8, 14 – 16, 19, 26]. Wang *et al*. reported achieving 92 – 93 % of relative density at temperatures closer to 1750°C [38]. Huang *et al*. [41] reduced the densification temperature further to 1650°C by

sintering Y_2O_3 in an oxygen atmosphere. However, none of the high temperatures approaches obtained density above 98% at temperatures as low as 1400°C, as was obtained in the present study. Homogenously distributed round – edged particles and the seeds improved the inter-particle coordination in the green compacts and assisted the rapid solid-state densification. Serivalsatit *et al*. [30 – 31] attempted to reduce the maximum sintering temperature using erbium (Er) doping and utilize a two-stage sintering technique. The samples were initially heated to 1500°C with a hold for a few minutes and cooled down to 1400°C and dwelled for 20 hours to attain 98% density. Whereas, in our study, improved densification was achieved through a simple conventional air sintering at 1400°C in one hour. Further, the densification was realized without any doping assistance. It is the first time Y_2O_3 exhibiting superior air-densification at 1400°C to the best of our knowledge. This method is, therefore, highly beneficial in terms of increased production rate and reduced sintering costs. Further, the Y_2O_3 sintered at 1400°C reached 100% TD after HIPing at 1400°C under 160 MPa pressures.

Fig. 6.13 shows the microstructural features of thermally etched yttria samples as a function of sintering temperatures between 1300°C and 1400°C. Fig. 6.13a shows that the samples sintered at 1300°C containing a large volume of porosities having grain sizes distributed between 100 nm to 300 nm. The average sintered grain sizes at this stage were found to be around 229 ± 10 nm. Further increment in sintering temperatures to 1325°C showed a linear enhancement in the densification and enlarged the average grain sizes to 268 ± 15 nm, as revealed in fig. 6.13b. The grain sizes further enlarged to 450 ± 25 nm at 1350°C with isolated pores, as shown in fig. 6.13c. However, the samples attained near theoretical densification at temperatures beyond 1350°C. The microstructures were mostly free from pores and secondary phases, as shown in fig. 6.13d and 6.13e. The grains are equiaxed, distributed in narrow sizes, and explains the degree of controlled nucleation and grain growth. The average grain sizes of the specimens sintered at 1375°C and 1400°C were found to be around 540 ± 35 nm and 680 ± 40 nm,

respectively. Fig. 6.13f shows the microstructure of the sample pressed hot isostatically at 1400°C. The microstructure reveals no significant change in the grain sizes after HIPing. The HIPed transparent Y_2O_3 samples' average grain size was found to be 690 ± 30 nm, which is highly comparable with the transparent Y_2O_3 specimens sintered through prolonged two-stage sintering methods [30 – 31]. Moreover, is the smaller grain sizes reported hitherto for the transparent Y_2O_3 materials processed through air sintering techniques.

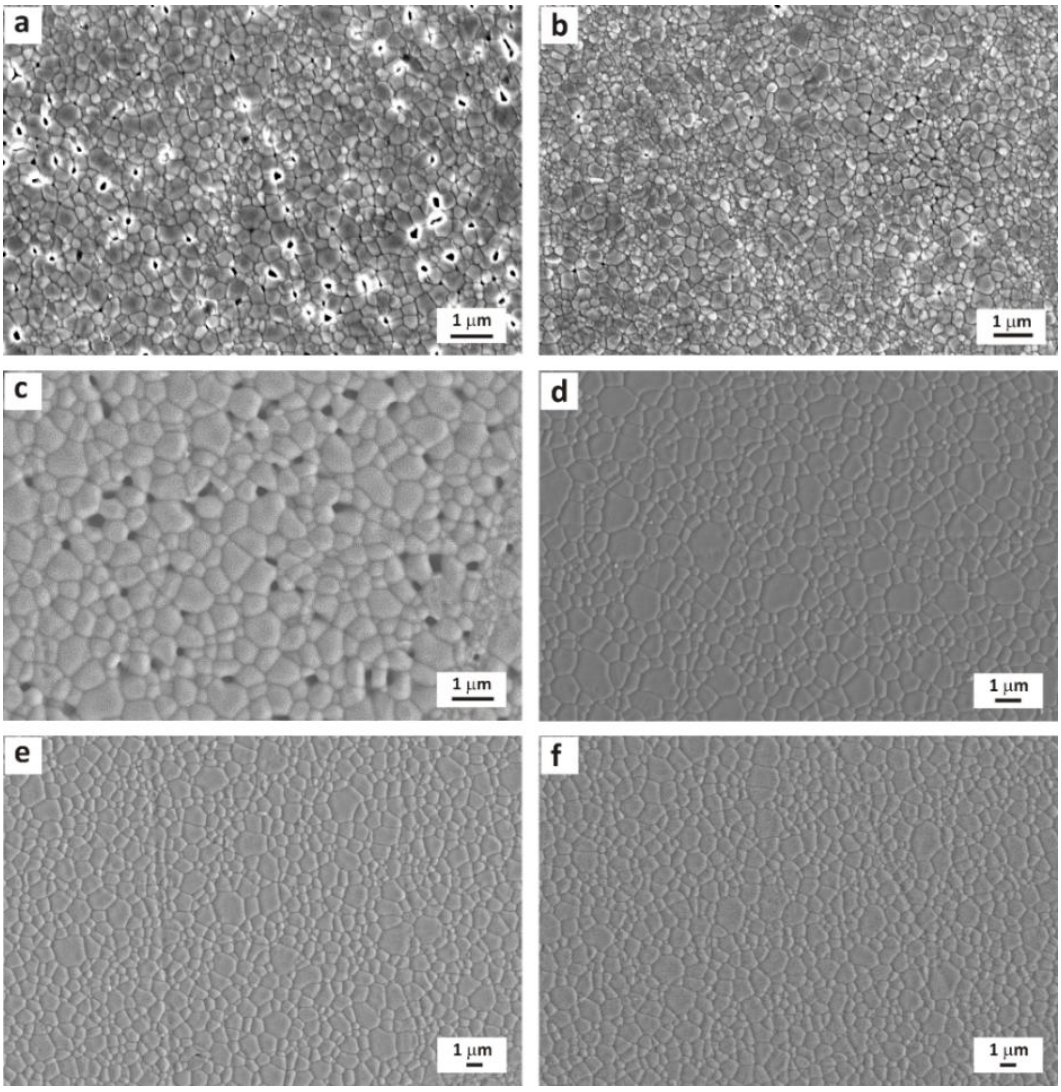

Figure 6.13. Microstructural characteristics of Y_2O_3 sintered at (a) 1300°C, (b) 1325°C, (c) 1350°C, (d) 1375°C, (e) 1400°C, (f) sintered and HIPed at 1400°C

Fig. 6.14 shows the rate of increment in the grain sizes concerning sintering temperatures. The pace of grain growth was initially slower at temperatures between 1300°C and 1325°C, where the densification occurred majorly due to lattice diffusion. The growth rate turned intense at temperatures beyond 1350°C as the densification at these regions were controlled by grain boundary diffusion.

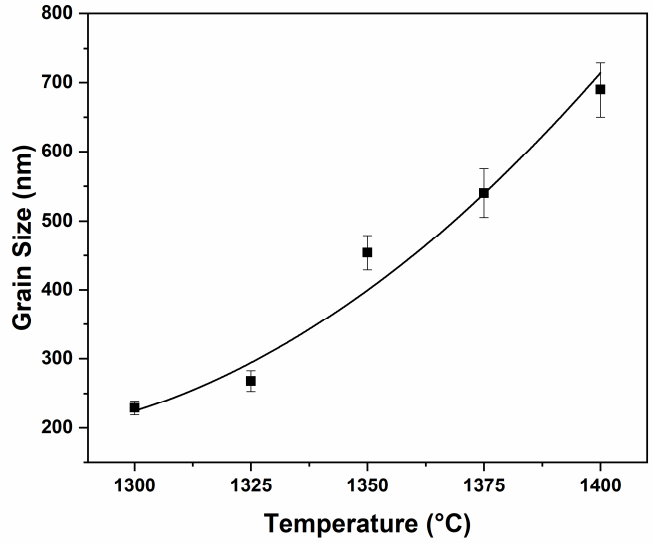

Figure 6.14. Rate of grain growth with respect to the sintering temperatures

Fig. 6.15a shows the Vickers indentation on the surface of polished and thermally etched transparent Y_2O_3 specimen and fig. 6.15b shows the crack propagation pattern. The fracture was majorly progressed through transgranular mode, which is an indication for rigid grain boundaries. Some of the approaches processed transparent Y_2O_3 using liquid forming additives such as LiF [7, 36] to obtain low-temperature densification. However, sintered bodies produced through such techniques generate weaker grain boundaries and exhibit low mechanical properties as the crack progress through intergranular fracture [52]. Obtaining densification through solid-state sintering develop dense grain boundaries resisting to fracture dislocations. Besides, controlling final grain sizes in the submicron region promotes deflections in the crack propagations and enhances the fracture toughness. The transparent Y_2O_3 produced in this study

exhibited fracture toughness up to 3.0 ± 0.05 MPa. $m^{1/2}$, which is thrice the values (~1.0 MPa. $m^{1/2}$) reported for single crystal yttria [53] and more than twice the values (1.39±0.07 MPa. $m^{1/2}$) reported for the fine-grained transparent Y_2O_3 fabricated through Sulphur-treated Y_2O_3 powders [31].

Also, Kaminskii *et al*. reported the fracture toughness up to 2.5 MPa. $m^{1/2}$ for their Y_2O_3 having mean grain size in the region between 1 – 2 µm [53]. The present improved values were due to the refinement of submicron grain sizes. The material also exhibited hardness up to 8.90 ± 0.2 GPa for the Knoop indentation under 100g loads, which is equivalent to the values obtained for the fine-grained transparent Y_2O_3 [31].

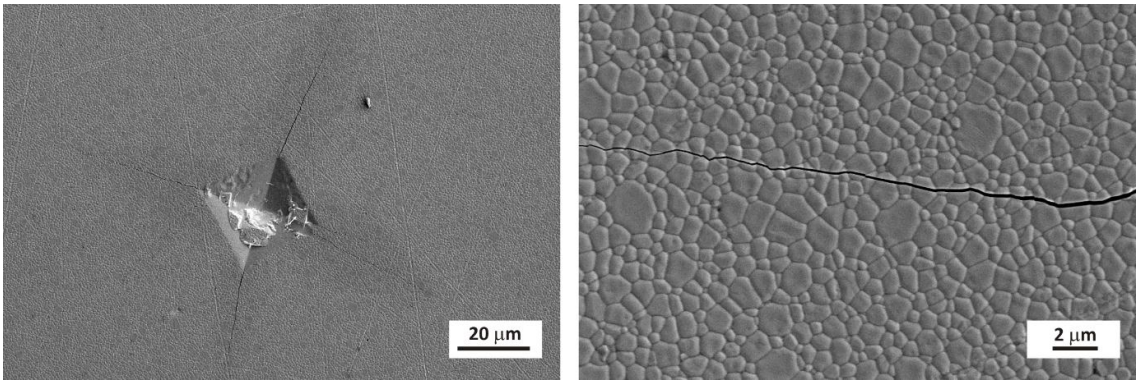

Figure 6.15. SEM image of (a) Vickers indentation and (b) crack propagation pattern

Fig. 6.16 shows the characteristics of the thermal diffusivities and conductivities of Y_2O_3 as a function of temperature between ambient temperature and 950°C. Noticeable increments in the values were observed between the sintered and HIPed versions due to the complete elimination of porosities after HIPing. The diffusivity of specimens sintered at 1400°C escalated from 4.33 ± 0.03 mm^2/s to 4.61 ± 0.03 mm^2/s after HIPing and the corresponding conductivity increased from 16.5 ± 1.3 W/m.K to 19. 5 ± 1.1 W/mK under ambient conditions. A similar trend was observed at higher temperatures as well. However, the overall thermal diffusion declined gradually with the increment in the tested temperature, and values of diffusivity and

conductivity of sintered specimens reached to1.37 ± 0.02 mm^2/s and 8.1 ± 0.1 W/m.K respectively. Similarly, the diffusivity of transparent HIPed specimens showed values close 1.5 ± 0.01 mm^2/s and the corresponding thermal conductivity was found to be to 8.7 ± 0.08 W/m.K at temperatures around 950°C. Hogan *et al.* [3] reported ambient thermal conductivity around 14.0 W/m.K and around 4.0 W/m.K at temperatures closer to 950°C for their transparent Y_2O_3.

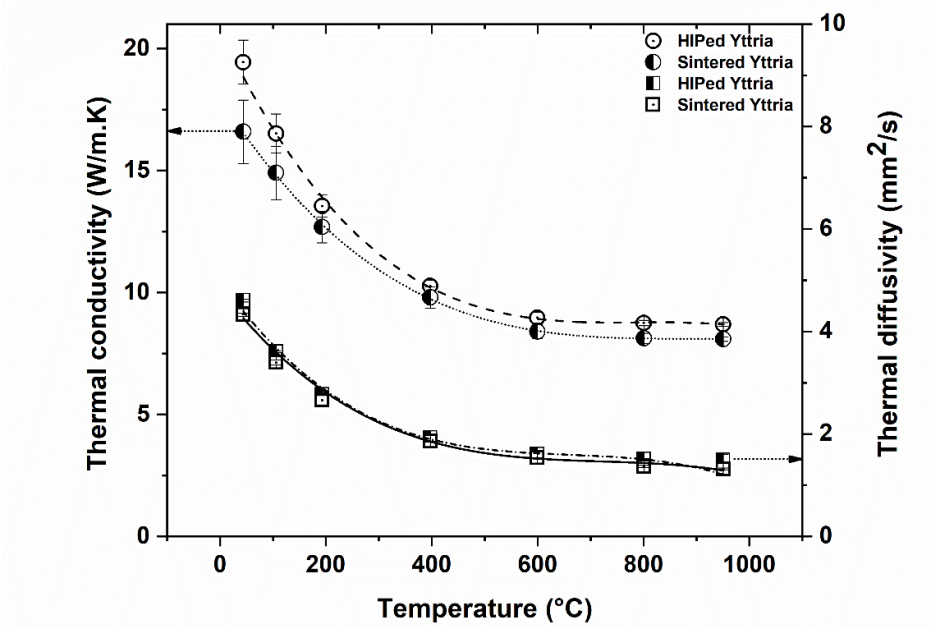

Figure 6.16. Thermal conductivity of sintered, sintered + HIPed Y_2O_3 specimens

The transparent Y_2O_3 produced in this study exhibited considerably higher thermal conductivities in similar temperature regions. The material with improved thermal conductivity shows enhanced resistance to thermal shocks. Therefore, the present material would be a promising candidate for solid-laser hosts that demands higher thermal conductivity and thermal shock resistance. In addition, the improved mechanical properties of the current material show its extension towards the uncooled missile window and dome applications to withstand the severe aerodynamic thermal shocks and sand erosion.

Fig. 6.17a shows the optical image of the IR transparent Y_2O_3 sample fabricated in this study. It was HIPed and ground to a thickness of 1.4 mm and polished at both sides. Fig. 6.17b shows

its real inline transparency in the wavelength regions between 2.0 and 9.0 µm. As shown in the figure, the material showed no evidence of optical absorption in the specified areas due to its dopant free formulations. Similarly, it exhibited high inline transparency reaching transmissions up to 84%, which is at par with the IR transmissions of single-crystal yttria and the best-reported polycrystalline transparent Y_2O_3 materials [3, 22, 54 – 55].

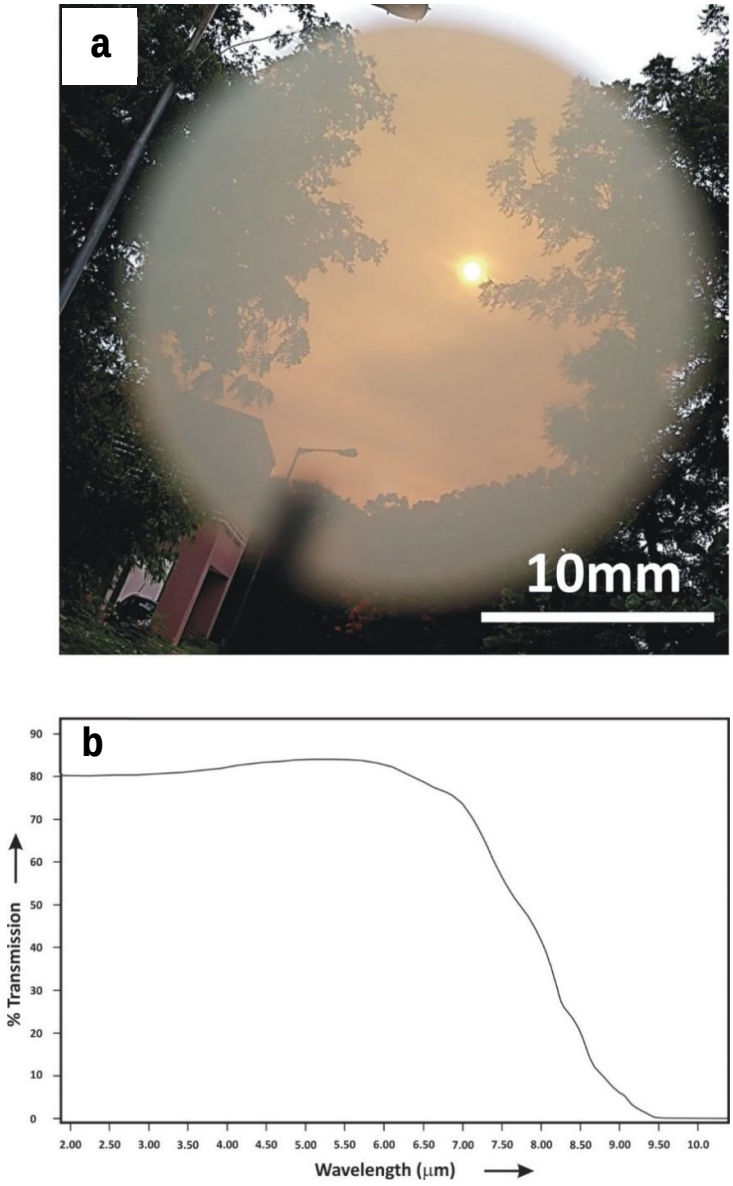

Figure 6.17. (a) Optical image of IR transparent Y_2O_3 produced in this study, (b) optical transmission spectra of air sintered and HIPed Y_2O_3

Table 6.1 shows the summary of physical and mechanical properties achieved in the present work, which are superior in terms of density, fracture toughness and IR transparency compared to the existing methods to produce submicron yttria. The material showed comparable hardness even with relatively larger grain sizes which is attributed to the defect free, solid-state densification.

Ref.	**Source of powder**	**Sintering method**	**Density** (% T.D.)	**Grain Size** (μm)	**Hardness** (GPa)	**Fracture Toughness** (MPa. $m^{1/2}$)	**Max. Transmission** (1 – 8 μm)
Present Work	In-house	Air sintering + HIP	100	0.69	8.9±0.20	3.0±0.05	84
[13]	Commercial	HP + HIP	>99.9	0.48	8.5±0.10	1.11±0.02	81
[31]	In-house (Precipitation process)	Two – stage/ Vacuum + HIP	>99.81	0.34	9.09±0.41	1.39±0.07	82
[37]	In-house (Flame Pyrolysis)	Vacuum + HIP	>98.0	0.40	-	-	75 – 78
[41]	Commercial	Vacuum + Canister HIP	>98.0	<1.0	-	-	75 – 76

Table. 6.1 Summary of properties of submicron transparent Y_2O_3 (Present Vs Reported)

6.5 Conclusions

Highly reactive, nano Y_2O_3 powders were synthesized using a facile sol-gel processing technique without using the commonly added sulfate ions. Optimized processing parameters enabled producing non-aggregated powders having average particle sizes closer to 60nm with round-edge morphology. The powders achieved complete crystallinity at 1100°C and the green compacts reached near theoretical densities at temperatures as low as 1400°C in the air without any sintering additives. Elimination of residual porosity through HIPing and constructing microstructures without secondary phases resulted in obtaining optically transparent Y_2O_3 having transparency up to 84%, which is equivalent to the transmissions of single-crystal yttria in the wavelength regions between 2.0 and 9.0 μm. Further, the samples showed hardness up to 8.90 ± 0.20 GPa, and fracture toughness up to 3.0 ± 0.05 MPa. $m^{1/2}$, which can be well correlated with the grain size of 690 ± 30 nm resulting from the powder's high-sinterability and low-temperature densification process employed. Laser flash measurements showed a thermal conductivity of 19.5± 1.1 W/m.K. The unique combinations of optical, mechanical, and thermal properties of the submicron Y_2O_3 samples produced in this study is a promising candidate for solid-laser hosts, IR transparent domes, and uncooled – thermal – window applications

6.6 References

1. C. Greskovich and J. P. Chernoch, Polycrystalline ceramic lasers, J. Appl. Phys. 44 (1973) 4599–4606.
2. C. Greskovich and S. Duclos, Ceramic scintillators, Annu. Rev. Mater. Sci. 27 (1997) 69–88.
3. P. Hogan, T. Stefanik, C. Willingham and R. Gentilman, Transparent yttria for IR windows and domes – past and present, ADM201976, 10thDoDEM Windows Symposium May 19, Norfolk, VV, 2004.
4. C.B. Willingham, J.M. Wahl, P.K. Hogan, L.C. Kupferberg, T.Y. Wong and A.M. De, Densification of nano-yttria powders for IR window applications, Window and Dome Technologies VIII, 5078 (2003) 179–188.
5. A. Krell and J. Klimke, Effects of the homogeneity of particle coordination on solid-state sintering of transparent alumina, J. Am. Ceram. Soc. 89 (2006) 1985–1992.
6. L. A. Brissette, P. L. Burnett, R. M. Spriggs and T. Vasilos, Thermomechanically deformed Y_2O_3, J. Am. Ceram. Soc. 49 (1966) 165–166.
7. R. A. Lefever and J. Matsko, Transparent yttrium oxide ceramics, Mater. Res. Bull. 2 (1967) 865–869.
8. J. Wang, J. Zhang, K. Ning, D. Luo, H. Yang, D. Yin, D. Tang and L. B. Kong, Densification of yttria transparent ceramics: The utilization of activated sintering, J. Am. Ceram. Soc. 99 (2016) 1671–1675.
9. J. Mouzon, A. Maitre, L. Frisk, N. Lehto and M. Oden, Fabrication of transparent yttria by HIP and the glass-encapsulation method, J. Eur. Ceram. Soc. 29 (2009) 311–316.
10. J. He, X. D. Li, J. G. Li and X. D. Sun, Colloidal stability of aqueous suspensions of nano-yttria powders, Int. J. Mater. Sci. Eng. 1 (2013) 28–31.

11. H. Eilers, Fabrication, optical transmittance and hardness of IR – transparent ceramics made from nano phase yttria, J. Eur. Ceram. Soc. 27 (2007) 4711–4717.
12. L. Gan, Y. J. Park, M. J. park, H. Kim, J. M. Kim, L. W. Ko and J. W. Lee, Facile fabrication of highly transparent yttria ceramics with fine microstructures by a hot – pressing method, J. Am. Ceram. Soc. 98 (2015) 1–3.
13. L. Gan, Y. J. Park, H. Kim, J. M. Kim, J. W. Ko and J. W. Lee, Mechanical properties of submicrometer – grained transparent yttria ceramics by hot pressing and hot isostatic pressing, Int. J. Appl. Ceram. Technol. 13 (2016) 678 – 684.
14. W. H. Rhodes, Controlled transient solid second-phase sintering of yttria, J. Am. Ceram. Soc. 64 (1981) 13–19.
15. H. Mingsheng, L. Jianbao, L. Hong, G. Gangfeng and L. Long, Fabrication of transparent polycrystalline yttria ceramics by combination of SPS and HIP, J. Rar. Ear. 24 (2006) 222–224.
16. L. Wen, X. Sun, Q. Lu, G. Xu and X. Hu, Synthesis of yttria nanopowders for transparent yttria ceramics, Opt. Mater. 29 (2006) 239–245.
17. Y. Huang, D. Jiang, J. Zhang and Q. Lin, Fabrication of transparent lanthanum-doped yttria ceramics by combination of two-step sintering and vacuum sintering, J. Am. Ceram. Soc. 92 (2009) 2883–2887.
18. N. Saito, S. Matsuda and T. Ikegami, Fabrication of transparent yttria ceramics at low temperature using carbonate-derived powder, J. Am. Ceram. Soc. 81 (1998) 2023–2028.
19. T. Ikegami, J. G. Li, T. Mori and Y. Moriyoshi, Fabrication of transparent yttria ceramics by the low-temperature synthesis of yttrium hydroxide, J. Am. Ceram. Soc. 85 (2002) 1725–1729.

20. J. Mouzon, T. Lindback and M. Oden, Influence of agglomeration on the transparency of yttria ceramics, J. Am. Ceram. Soc. 91 (2008) 3380–3387.
21. W. K. Jung, H. J. Ma, S. W. Jung and D. K. Kim, Effects of calcination atmosphere on monodispersed spherical particles for highly optical transparent yttria ceramics, J. Am. Ceram. Soc. (2017) 1–9.
22. R.L. Gentilman, M. Greenberg and T. Hartnett, Optically transparent yttrium oxide, U. S Pat. No. 4761390 (1988).
23. R. C. Anderson, GE has transparent ceramic, Chem. & Eng. News, Oct. 17 (1966) 38.
24. S. K. Dutta and G. E. Gazza, Transparent Y_2O_3 by hot pressing, Mat. Res. Bull. 4 (1969) 791–796.
25. Y. Tsukuda and A. Muta, Sintering of Y_2O_3 at high temperatures, J. Ceram. Soc. Jpn. 84 (1976) 585–589.
26. W. K. Jung, H. J. Ma, Y. Park and D. K. Kim, A robust approach for highly transparent Y_2O_3 ceramics by stabilizing oxygen defects, Scripta materialia 137 (2017) 1–4.
27. T. Ikegami, T. Mori, Y. Yajima, S. Takenouchi, T. Misawa and Y. Moriyoshi, Fabrication of transparent yttria ceramics through the synthesis of yttrium hydroxide at low temperature and doping by sulfate ions, J. Ceram. Soc. Jpn. 107 (1999) 297–299.
28. T. Ikegami, J. G. Li, T. Mori and Y. Moriyoshi, Fabrication of transparent yttria ceramics by the low-temperature synthesis of yttrium hydroxide, J. Am. Ceram. Soc. 85 (2002) 1725–1729.
29. I. W. Chen and X. H. Wang, Sintering dense nano crystalline ceramics without final-stage grain growth, Let. Nat. 404 (2000) 168–172.
30. K. Serivalsatit, B. Yazgan Kokuoz, B. Kokuoz, and J. Ballato, Nanograined highly transparent yttria ceramics, Opt. Lett. 34 (2009) 1033–1035.

31. K. Serivalsatit, B. Kokuoz, B. Y. Kokuoz, M. Kennedy and J. Ballato, Synthesis, processing and properties of submicrometer–grained highly transparent yttria ceramics, J. Am. Ceram. Soc. 93 (2010) 1320–1325.
32. H Zhang, B. N. Kim, K. Morita, H. Yoshida, K. Hiraga and Y. Sakka, Fabrication of transparent yttria by high-pressure spark plasma sintering, J. Am. Ceram. Soc. 94 (2011) 3206–3210.
33. L. An, A. Ito and T. Goto, Transparent yttria produced by spark plasma sintering at moderate temperature and pressure profiles, J. Eur. Ceram. Soc. 32 (2012) 1035–1040.
34. E. Korkmaz and F. Sahin, Fabrication of transparent yttria ceramics by spark plasma sintering, Act. Phys. Polo A. 131 (2017) 460–462.
35. B. Li, X. Zheng and Z. F. Fu, Fast densification of nanocrystalline yttria ceramics without grain growth, Inter. J. Sel. Hig. Temp. Syn. 24 (2015) 14–20.
36. H. Weglarz, A. Wajler, H. Tomaszewski, M. Mozdzonek and Z. Librant, Sintering studies of transparent yttria ceramics, Ceram. Mater. 63 (2011) 123–126.
37. T. R. Hinklin, S. C. Rand and R. M. Laine, Transparent, polycrystalline upconverting nanoceramics: Towards 3 – D displays, Adv. Mater. 20 (2008) 1270–1273.
38. J. Wang, K. Ning, J. Zhang, D. Luo, J. Ma, D. Yin, D. Tang and L. B. Kong, Rapid rate sintering of yttria transparent ceramics, J. Am. Ceram. Soc. 99 (2016) 1935–1942.
39. O. Yeheskel and O. Tevet, Elastic moduli of transparent yttria, J. Am. Ceram. Soc. 82 (1999) 136–144.
40. Y. Huang, D. Jiang, J. Zhang and Q. Lin, Precipitation synthesis and sintering of lanthanum doped yttria transparent ceramics, Opt. Mater. 31 (2009)1448–1453.
41. Y. Huang, D. Jiang, J. Zhang, Q. Lin and Z. Huang, Sintering of transparent yttria ceramics in oxygen atmosphere, J. Am. Ceram. Soc. 93 (2010) 2964–2967.

42. G. R. Anstis, P. Chantikul, B. R. Lawn and D. B. Marshall, A critical evaluation of indentation techniques for measuring fracture toughness: I, Direct crack measurements, J. Am. Ceram. Soc. 64 (1986) 533–538.
43. P. S. Babu, B. Basu and G. Sundararajan, Processing – structure – property correlation and decarburization phenomenon in detonation sprayed WC – 12 Co coatings, Acta. Mater. 56 (2008) 5012–5026.
44. T. W. Lian, A. Kondo, M. Akoshima, H. Abe, T. Ohmura, W. H. Tuan and M. Naito, Rapid thermal conductivity measurement of porous thermal insulation material by laser flash method, Adv. Powd. Technol. 27 (2016) 882–885.
45. F. Ribot, P. Toledano and C. Sanchez, X-ray and spectroscopic investigations of the structure of yttrium acetate tetrahydrate, Inorganica Chimica Acta, 185 (1991) 239–245.
46. X. Guan, L. Li, J. Zheng, and G. Li, $MgAl_2O_4$ nano particles: A new low – density additive for accelerating thermal decomposition of ammonium perchlorate, RSC Adv. 1 (2011) 1808–1814.
47. Z. Huang, X. Sun, Z. Xiu, S. Chen and C. T. Tsai, Precipitation synthesis and sintering of yttria nanopowders, Mater. Lett. 58 (2004) 2137–2142.
48. A. Dupont, A. Largeteau, C. Parent, B. L. Garrec and J. M. Heintz, Influence of the yttria powder morphology on its densification ability, J. Eur. Ceram. Soc. 25 (2005) 2097–2103.
49. M. Kumagai and G. L. Messing, Controlled transformation and sintering of a boehmite sol – gel by α – alumina seeding, J. Am. Ceram. Soc. 68 (1985) 500–505.
50. P. K. Sharma, M. H. Jilavi, R. Nar and H. Schmidt, Seeding effect in hydrothermal synthesis of nanosize yttria, J. Mater. Sci. Lett. 17 (1998) 823–825.

51. R. Senthil Kumar, A. K. Khanra and R. Johnson, Processing and properties of sintered submicron IR transparent alumina derived through sol–gel method, J. Sol. Sci. Technol. 86 (2018) 374–382.
52. M. Ramisetty, S. Sastri, U. Kashalikar, L. M. Goldman and N. Nag, Transparent polycrystalline cubic spinels protect and defend, J. Am. Ceram. Soc. Bull. 92 (2013) 20–25.
53. A. A. Kaminskii, M. Sh. Akchurin, R. V. Gainutdinov, K. Takaichi, A. Shirakava, H. Yagi, T. Yanagitani and K. Ueda, Microhardness and fracture toughness of Y_2O_3 – and $Y_2Al_5O_{12}$ – Based nanocrystalline laser ceramics, Russian academy of sciences, crystallography reports, 50 (2005) 869–873.
54. K. A. Wickersheim and R. A. Lefever, Infrared transmittance of crystalline yttrium oxide and related compounds, J. Opt. Soc. Amer. 51 (1961) 1147–1148.
55. Y. Nigara, Measurement of the optical constants of yttrium oxide, Jpn. J. Appl. Phys. 7 (1968) 404–408.

CHAPTER - VII

Aqueous sol-gel processing of precursors for the synthesis of aluminum oxynitride powder and fabrication of transparent AlON ceramics

7.1 Introduction

Aluminum Oxynitride (AlON), an emerging transparent ceramic material with excellent mechanical properties, attracts attention in various fields of application, such as bulletproof armors, windows for super market scanners, IR windows and domes, laser windows, ceramic semiconductors, low-cost substitute for sapphire, and ceramic lamp envelops [1 – 2]. As per the Al_2O_3/ AlN phase diagram [3], the reaction between Al_2O_3 and 28 – 40 mol% of AlN at temperatures above 1700°C form single phase γ – AlON. Researchers synthesized γ – AlON through several methods, such as solid state reactions between Al_2O_3 and AlN [4 – 11], Al_2O_3 and BN [12], carbothermal nitridation of α or γ – Al_2O_3 [13 – 19], alumino-thermic reactions [20 – 21], nitridation between γ – Al_2O_3 and aluminum metal [22], gas-phase reaction with aluminum chloride [23], carbothermal reduction synthesis of gibbsite [24], and wet chemical syntheses [25 – 26].

Among the various approaches, synthesis of AlON was mostly carried out using Al_2O_3 and AlN due to process simplicity, the availability of high pure Al_2O_3, and AlN starting powders and formation of phase pure AlON with minimum contaminations. AlN, due to its severe tendency of hydrolysis in water, is generally dispersed in a non-aqueous medium such as isopropyl alcohol, methanol, or ethanol. AlN reacts with water and deteriorates into AlOOH, $Al(OH)_3$ and NH_3 compounds. These reactions crumple the requisite molecular ratio between

Al_2O_3 and AlN and hinder the eventual formation of γ – AlON phase. Miller *et al.* attempted to address this problem by limiting the exposure period of AlN in water to 2 hours during mixing [27]. However, the article have not reported the stability of AlN during shaping and drying periods. Few investigations reported the use of a surface modification treatment of AlN powders to arrest the reactions of hydrolysis. Various chemicals such as ortho phosphoric acid, polyphosphoric acid, butyl acid phosphate, sebacic acid, citric acid etc. have been employed for the surface modification process [28 – 32]. Such process extended the incubation period of AlN in water for few hours to even weeks. Senthil Kumar *et al.* employed this surface passivation technique to produce AlON with defect free microstructures by fabricating AlON in two phases. In the first phase, AlON powder was synthesized by reacting Al_2O_3 and AlN. In the second phase, the aqueous slip was produced using the surface-modified AlON powder and the green bodies were fabricated through slip casting method. The casted samples were further sintered at temperature above 1900°C to produce dense AlON ceramics. Though this process describes the shaping of AlON through aqueous processing, a non-aqueous medium was still the choice for the synthesis of AlON powder [33].

Synthesizing AlON powders through aqueous processing route would be more economical and friendly to environment. However, no investigations hitherto reported using of aqueous medium for synthesizing AlON powders using Al_2O_3 and AlN.

Therefore, in the present study, an attempt has been made to produce γ – AlON powders using the precursors processed through a simple aqueous sol-gel route. Investigations were carried out on the interaction mechanism of AlN during the sol – gel processing of AlON. The entire procedure of synthesizing AlON powder through the present method is shown in Fig. 7.1. AlON powders produced through this technique are comparatively economical. This is because the source of Al_2O_3 utilized in this process is less expensive than the commercially available high pure Al_2O_3 powders, which were generally used in most of the existing AlON processing

methods. Perhaps for the first time, AlON precursors were successfully processed through aqueous sol-gel procedures and the AlON powders were eventually synthesized with an average particle size in the submicron region. In addition, the powder was compacted and sintered for exploring its suitability for the fabrication of transparent AlON. The results showed that the powder is useful for the making of transparent AlON materials.

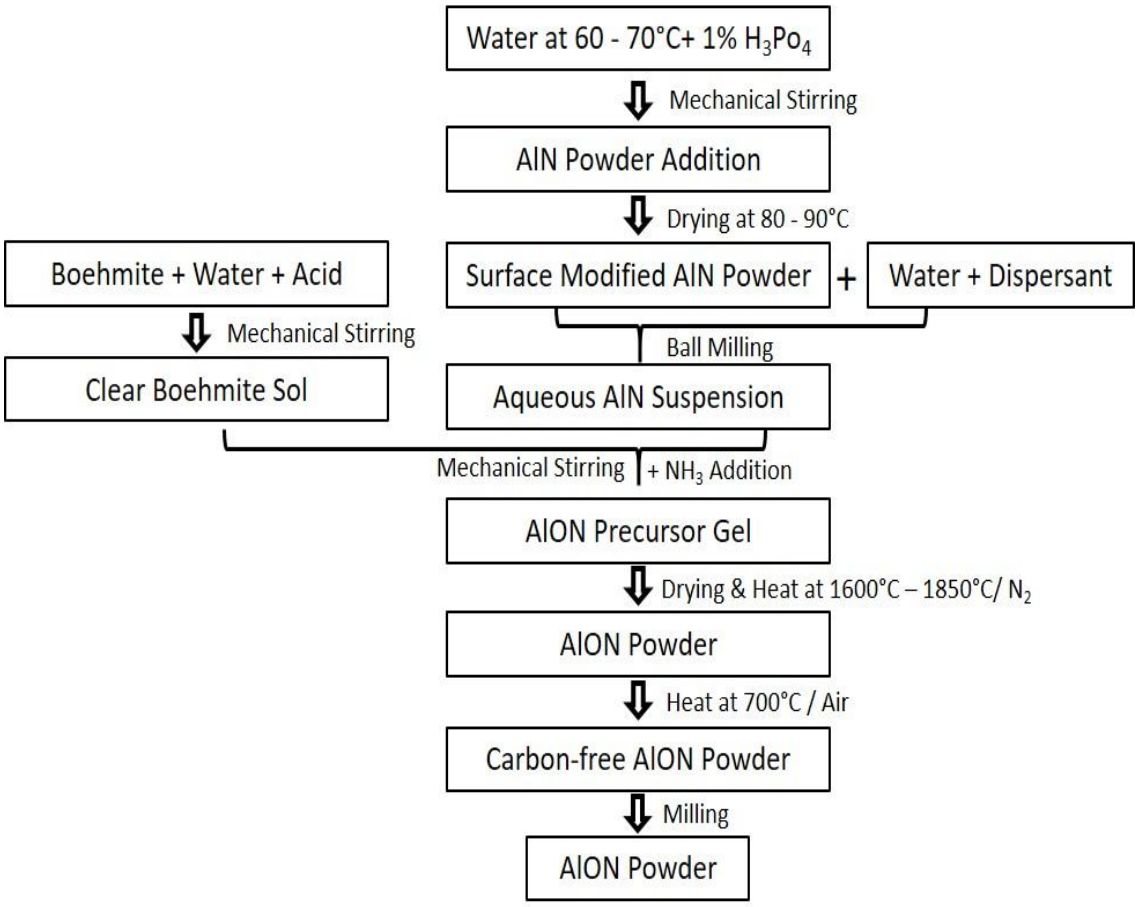

Fig. 7.1 The entire flow process for the synthesis of AlON powder

7.2 Highlights of the study

- For the first time, aluminum oxynitride (ALON) powders were synthesized using the precursors processed through aqueous sol–gel procedures

- Hydrolysis reactions of as received AlN powder in aqueous boehmite sol collapsed the molecular stoichiometry for AlON
- Surface modification treatment for AlN powders circumvented its hydrolysis tendency and retained its phase integrity during sol-gel processing
- Heat treating the sol-gel derived precursor mixture at 1850°C produced single phase AlON powder having particle size closer to 490 nm
- Sintering of compacted specimens at 1950°C in flowing nitrogen atmosphere for 6 hours produced transparent AlON
- The samples exhibited inline transmissions up to 82% in the 3 – 5 μm wavelength regions and Vickers hardness up to 1350 Kg/mm^2

7.3 Experimental Procedure

Commercially available boehmite and AlN powders were used as major raw materials for this study. The properties of these materials as per the manufacturer specifications are shown in Table 7.1. The starting powders were analyzed for their microstructural characteristics using FEG-SEM (Carl Zeiss Microscopy GmbH, Oberkochen, Germany).

Type of powder	Boehmite	AlN
Manufacturer	Disperal, Sasol Germany GmbH, Hamburg, Germany	Grade - C, H.C. Starck, Germany
Particle Size (d_{50})	2.5 μm	1.12μm
BET Surface Area	180 m^2/g	4.06 m^2/g

Table 7.1. Technical specifications of raw materials (as per the supplier specification)

7.3.1 Preparation of Boehmite sol

100 g of boehmite powder was mixed with 900 g of distilled water using high speed mechanical stirrer at ambient conditions for one hour. The peptization of boehmite in water was carried out by dropwise addition of glacial acetic acid (Standard Reagents, India). The acid was continually added to adjust the pH between 2 and 3, and the mixture was stirred for another 2 hours to obtain stable boehmite sol. The sol was kept idle for a period of 12 hours afterward, to allow any unreacted boehmite particles to settle. The supernatant clear sol was transferred to another container and used for the entire study. The evaluation of α-Al_2O_3 content from the stable sol was measured by heat-treating 10 g of clear sol at 1200°C for 1 hour in air atmosphere. The α-Al_2O_3 content in the stable sol was found to be 7.6 wt. % with respect to the weight of the sol.

7.3.2 Surface modification of AlN powders

The surface treatment of AlN powder was carried out by dispersing 100 g of as-received (raw/ pristine) AlN powder in 200 ml of water containing 1% orthophosphoric acid (98% H_3PO_4, Qualigens, India) using high speed mechanical stirrer at 60 – 70 °C. Stirring was continued for 30 minutes, and the mixture was filtered for the removal of excess water. The filtered material was dried in hot air oven at 80 – 90 °C for 12 h to obtain the surface modified AlN powder that is resistant to hydrolysis.

7.3.3 Preparation of AlN aqueous suspension

Aqueous suspension of AlN with 70 wt% solid content was prepared by dispersing surface modified AlN powder in distilled water using 1 wt% Darvan 821A (R.T. Vanderbilt Co. Inc., Norwalk, CT) as a dispersing agent. The mixture was ball milled in a polypropylene jar for 4 h using 2mm diameter Al_2O_3 balls as the grinding media to obtain stable aqueous AlN suspension.

7.3.4 AlN reaction studies during AlON powder processing

One hundred grams of boehmite sol were mixed with 30 – 35 mol% of stable AlN aqueous suspension to synthesize stoichiometric AlON precursor mixture. The mixture was continuously stirred using magnetic stirrer for 5 h. The pH and viscosity (MCR 51, Anton Paar GmbH, Graz, Austria) of the mixture were measured for every 30 min. For comparison, a mixture of boehmite sol and pristine AlN powder was also prepared, and its pH and viscosity measurements were recorded over time. The mixtures obtained at the end of these experiments were dried at 80 – 90 °C in a hot air oven. Both the dried AlON precursor mixtures were analyzed for their morphology using FEG-SEM.

The reaction of AlN in boehmite sol was examined through FTIR analysis (Vertex 70, Bruker Optik GmbH, Germany). For this experiment, the dried precursor powders were mixed with KBr powder at a 1:99 weight ratio and compacted to thin pellets having a thickness of about 0.2 – 0.3 mm through uniaxial pressing. The pellets were analyzed for its optical absorption behavior in the wave number region between 4000 – 400 cm^{-1}.

7.3.5 Sol – gel preparation of precursor powder

Stable boehmite sol was kept under constant stirring conditions using high speed mechanical stirrer and 30 – 35 mol % of surface modified AlN powder in the form of 70 wt% solid loaded aqueous suspensions was slowly added to the sol. Stirring was continued for 1 h to obtain a homogeneous suspension of sol-AlN mixture. Ammonium hydroxide was added by drops after the mixing period to adjust the pH between 13 and 14 for effecting gelation. The precursor gel was dried in a hot air oven at 80 – 90 °C for 12 h. The dried gel was subjected to TG-DTA analysis (Netzsch STA 409C, Selb, Germany) in the nitrogen atmosphere for understanding its thermal behavior. The dried precursor gel was heat treated at temperatures from 1600 to 1850 °C in a graphite furnace for 1 h in a flowing nitrogen atmosphere to obtain single phase AlON

powder. The powder was further heat treated in air at 700 °C for 2 h to remove carbon residues. The powder was milled further in a planetary mill for 2 h to disintegrate any hard agglomerates. A 500 ml alumina vial was used as the milling container and 2 mm alumina balls of purity above 99.9 % were used as the milling media. AlON phase formation studies were carried out using XRD and powder morphology was characterized by FEG-SEM. Particle size was analyzed by a laser diffraction technique (Malvern Instruments SARL, Orsay Cedex, France) and surface area was analyzed using the BET surface analyzer (ASAP; Micromeritics Norcross, GA).

7.4 Results and discussions

Fig. 7.2 shows the morphological characteristics of the starting raw materials used in the present study. Fig. 7.2a shows the morphology of as-received boehmite powder. It is evident that the boehmite particles of sizes less than 100 nm are agglomerated with a wide range of size distribution from 0.5 µm to 2 µm. The AlN particles, as shown in fig. 7.2b appear to have irregular angular morphology with particle sizes ranging from 200 nm and 3 µm with an average size of about 1 µm (as per the supplier's specification).

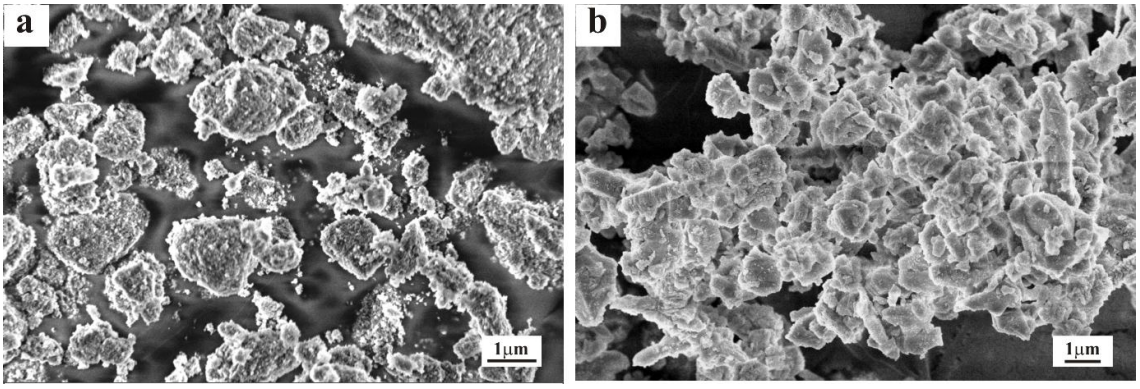

Fig. 7.2 Microstructural characteristics of starting raw materials

7.4.1 Reaction studies of AlN during the synthesis of precursor mixture

Fig. 7.3a shows the plot between pH and time against the addition of pristine AlN powder in boehmite sol. The pH of sol was around 2.8 during the addition of pristine AlN powder and started to increase within the first 2 hours. The rapid change in pH indicates that the pristine AlN powder undergoes hydrolysis in the aqueous sol and disintegrates into AlOOH, $Al(OH)_3$ and NH_3 compounds as discussed in the introduction section. The pH reached up to 6.9 within the next 3 hours of mixing due to the continuous formation of NH_3 from the hydrolysis reactions. On the other hand, during the addition of surface modified AlN in boehmite sol, the pH of the sol remained constant over the entire 5 hours of mixing. The stability in the pH value indicates that the surface treated AlN remained unaffected during the synthesis period of precursor mixture. A similar trend was observed in the case of viscosity measurements as well, as shown in Fig. 7.3b. The viscosity of the sol started to increase within 2 hours of addition of pristine AlN powder and reached to 0.45 Pa. s from the initial value of 0.01 Pa. s within 5 h of mixing period. The change in viscosity indicates the initiation of gelation of stable sol due to the formation of NH_3 from pristine AlN powders. In contrast, the viscosity of the sol-AlN mixture remained unchanged throughout the 5 h of mixing and indicated no sign of gelation. The stability in viscosity measurements confirms that there was no formation of NH_3 from surface treated AlN powders. In other words, the AlN phase remained intact during the sol-gel processing of precursor mixture.

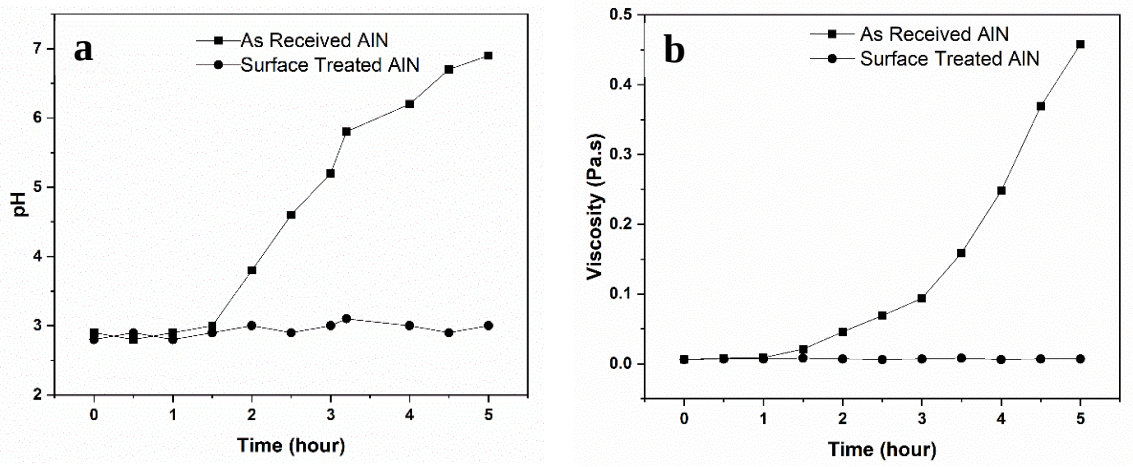

Fig. 7.3 Comparison of changes in (a) pH and (b) Viscosity against the addition of pristine and treated AlN in sol

7.4.2 FTIR studies on reaction behavior of AlN in sol

Fig. 7.4 shows the characteristic spectra of AlN at various stages of processing of precursor mixture. Fig. 7.4a exhibits the IR absorption spectrum of pristine AlN powder. A broad absorption band was observed in the range between 500 and 900 cm^{-1} wavelength region with an additional small absorption peak at 1325 cm^{-1}. The absorption peaks in these regions correspond to Al – N bonds [34 – 35]. Fig. 7.4b shows the spectrum of pristine AlN powder subjected to a hydrolysis reaction in distilled water for 5 hours. The pattern shows absorption peaks at 1070 cm^{-1}, 1635 cm^{-1} and a broad band absorption spectrum between 3100 and 3600 cm^{-1} in addition to its intrinsic Al – N bonds. The peaks corresponding to Al – N bonds seem to be weaker due to the loss of nitrogen during hydrolysis reactions. The peaks at 1070 cm^{-1} and 1635 cm^{-1} correspond to Al – OH and water respectively. The broad band spectrum appeared between 3100 and 3600 cm^{-1} correspond to $Al(OH)_3$ species [36 – 37]. To confirm that these bonds are corresponding to hydroxyl groups of Al_2O_3, as-received boehmite powder was subjected to FTIR analysis, which is shown in Fig. 7.4c.

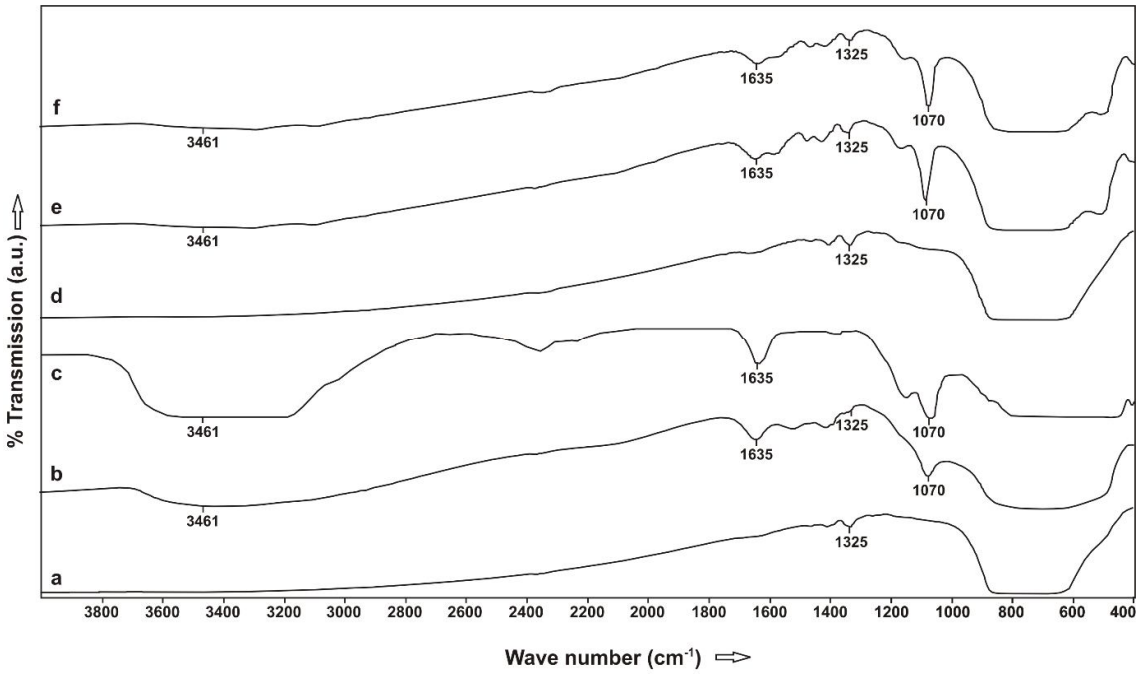

Fig. 7.4 FTIR analysis of AlN interaction against aqueous sol

It is observed that the absorption peaks of hydrolyzed AlN are matching with the hydroxyl groups of boehmite. However, as shown in fig. 7.4d, these hydroxyl bonds are not formed in the surface modified AlN powders even after 5 h in water, which confirms the effectiveness of the surface modification process at preventing hydrolysis. Fig. 7.4e shows the pattern observed for the precursor mixture composed of pristine AlN and boehmite sol. The spectrum contains the characteristic hydroxyl peaks at 1070 cm^{-1} and 1635 cm^{-1} in addition to the peaks related to Al – N bonds. The formation of these hydroxyl peaks was majorly due to the presence of boehmite in the precursor gel. However, hydrolysis reactions of pristine AlN also presumably contributed to the formation of the hydroxyl peaks. The spectrum observed for the precursor mixture prepared using surface treated AlN (fig. 7.4f) also exhibit absorption curve like fig. 7.4e. The pattern exhibited bonds corresponding to both Al – N and the hydroxyl groups of Al_2O_3. However, as per the absorption pattern exhibited by the surface treated AlN in fig. 7.4d, it can be presumed that the hydroxyl bonds observed in fig. 7.4f merely correspond to boehmite

and not to AlN powders. The wavenumbers corresponding to the observed absorption peaks are tabulated in Table 7.2.

IR absorption Wavenumber (cm^{-1})	Species	Reference
500 - 900	Al-N	32
1070	δ Al - OH	35
1325	Al-N	33
1635	H_2O/OH of Al	35
3100 - 3500	$Al(OH)_3$	34
3461	Bayerite	34

Table 7.2: IR absorption frequencies and its corresponding species

7.4.3 Thermal behaviour of dried precursor gel

Fig. 7.5 shows the TG-DTA analysis of dry precursor gel powder. The TG curve shows loss of weight in two stages at temperatures around 150 °C and between 470 and 480 °C. The initial weight loss at 150 °C was due to the loss of physically combined water. Minor drop in weight was observed at this temperature as the precursor powder was dried at 90 °C before the TG-DTA analysis. The subsequent weight loss up to 480 °C was probably due to the loss of chemically bonded water. The weight loss at these regions was also accompanied by the initiation of phase transition from boehmite to $\gamma - Al_2O_3$. No major change in weight was observed beyond these temperatures. The DTA plot shows the endothermic peaks at 150 °C and at 470 °C to 480 °C corresponding to the loss of physically and chemically combined water respectively. Also, the initiation of exothermic reaction coincides at 480 °C representing the formation of $\gamma - Al_2O_3$. Another exothermic peak at 1220 °C corresponds to the phase transformation of γ to $\alpha - Al_2O_3$.

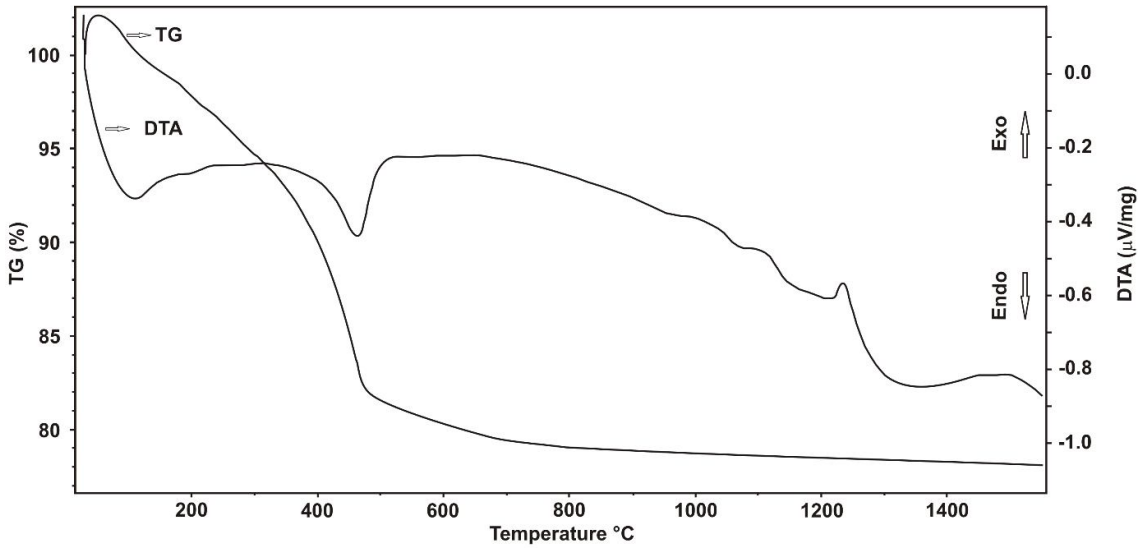

Fig. 7.5. TGDTA analysis of dried precursor gel

7.4.4 Microstructural analysis of AlN powder

As discussed in the introduction section, AlN tends to undergo hydrolysis reaction with water to form hydrates of Al_2O_3 such as AlOOH, $Al(OH)_3$ and NH_3 compounds through the following reactions.

$AlN + 2H_2O \rightarrow AlOOH + NH_3$ ---------- (1)

$NH_3 + H_2O \rightarrow NH_4^+ + OH^-$ ---------- (2)

$AlOOH + H_2O \rightarrow Al(OH)_3$ ---------- (3)

Fig. 7.6a shows the surface characteristics of pristine AlN powder after the hydrolysis reaction. The surface of hydrolyzed AlN particles indicates the formation of needle like boehmite compounds. Studies suggest that the extent of the hydrolysis of AlN particles depends on the period of their exposure with water and the amount of water available for reaction [38].

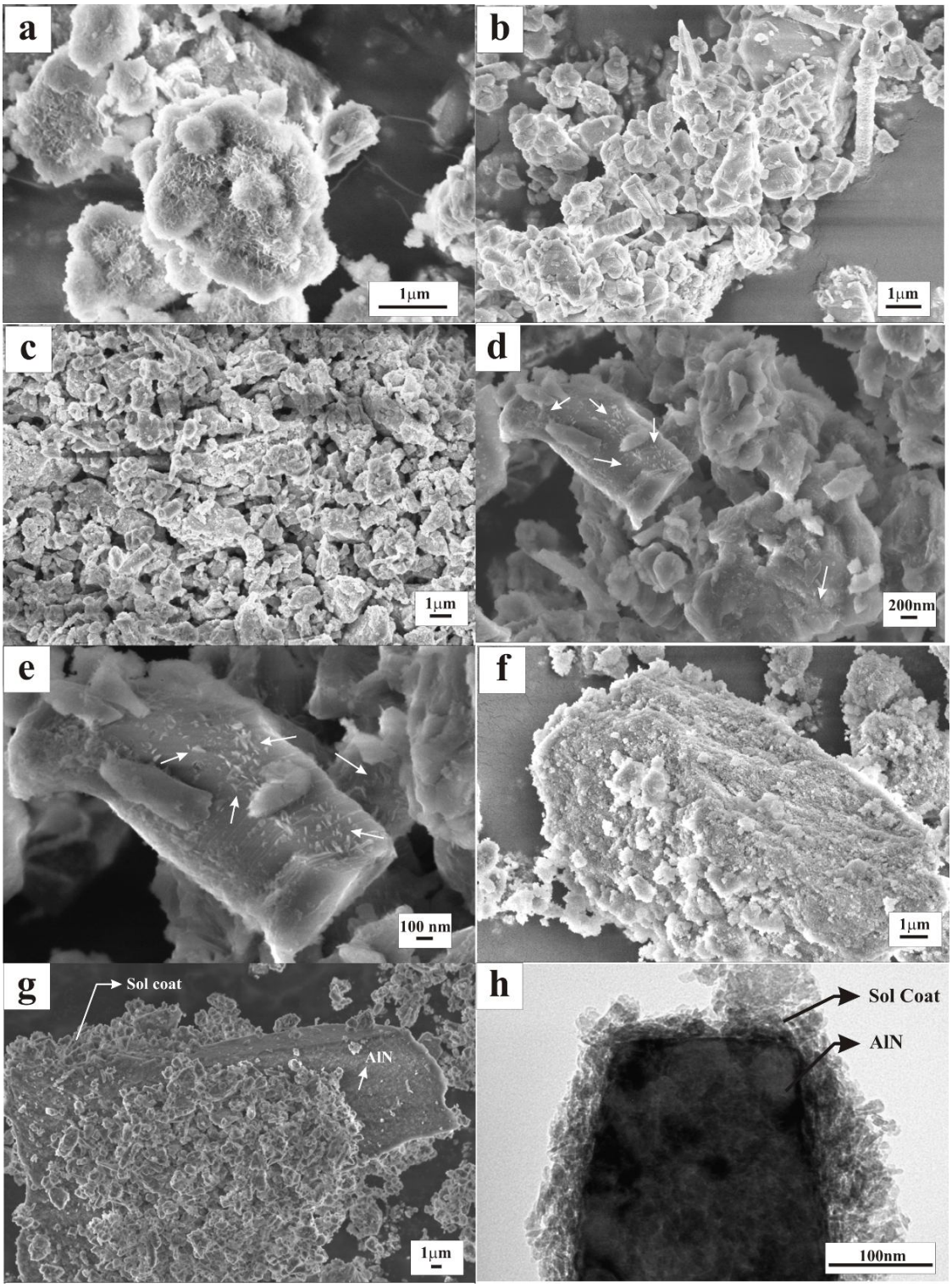

Fig. 7.6 Microstructural characteristics of pristine and treated AlN at various stages of powder processing

In general, aqueous sol-gel based powder synthesis routes involve water in substantial proportions. Therefore, it is not a favorable environment to employ pristine AlN powder due to its strong tendency towards hydrolysis. This situation would be a plausible reason for why no aqueous sol-gel based studies have been attempted for the synthesis of AlON powder involving AlN powder since. Surface modification treatment presented in this study stabilized the AlN in aqueous medium by guarding its surface against hydrolysis reactions. Fig. 7.6b shows the microstructure of surface modified AlN particles resided in water for at least 5 h. The exterior shows no indication of reactive compounds as noticed in Fig. 7.6a and exhibit similar surface characteristics as observed in the pristine AlN powder shown in Fig. 7.2b.

Fig. 7.6c shows the microstructure of dried precursor gel prepared with boehmite sol and pristine AlN aqueous suspensions. It can be seen from the figure that all the AlN particles were uniformly coated with boehmite sol forming a core-shell structure. As discussed above, the pristine AlN particles would have undergone hydrolysis reactions beneath the sol coat. To expose the surface of hydrolyzed AlN, the core-shell structure of the powder was disintegrated in a pestle and mortar and subjected for the SEM characterization. As shown in Fig. 7.6d, the surface of AlN that was used in pristine conditions exhibited needle like structures (indicated by arrows) confirming the event of hydrolysis reactions. The presence of needle like structures is clearly shown in Fig. 7.6e. Fig. 7.6f shows the morphology of dried precursor gel prepared using surface modified AlN powder. A core-shell structure with a uniform coat of sol over the surface of AlN was observed in this case as well. Therefore, this powder also was disintegrated for the exposure of AlN surface and its microstructure was observed as shown in Fig. 7.6g. It is shown that surface modified AlN exhibited no foot prints of needle like structures. The TEM image of the dried precursor gel (Fig. 7.6h) shows the actual core-shell structure which is composed of surface modified AlN particle and boehmite coat.

7.4.5 AlN interaction mechanism – A schematic study

The aforementioned microstructural features are schematically illustrated in fig. 7.7 for a better insight of the surface interaction mechanism of AlN particle in the aqueous processing of precursor mixture. Fig. 7.7A demonstrates the reactions of pristine AlN particle and fig. 7.7B shows the reactions of surface modified AlN particle. Fig. $7.7A_1$ shows a typical morphology of pristine AlN particle. In an aqueous medium, it undergoes hydrolysis, forming needle-like compounds of AlOOH and $Al(OH)_3$, as shown in fig. $7.7A_2$. The hydrolysis reaction initiates at the surface of the AlN particle and progress towards its core, based on several variables (such as particle size, reaction period, water content, reaction temperature, etc.). Fig. $7.7A_3$ shows the cross section of the hydrolyzed AlN particle. It can be observed that the hydrolysis reaction initiated on the surface of AlN and progressed towards the core, forming the crust of hydrated Al_2O_3. The phase of the AlN particle at its center remained intact, which may or may not undergo further reactions with respect to the aforementioned variables of hydrolysis. Fig. $7.7A_4$ shows the typical particle morphology of AlN covered with homogeneous boehmite coat. A portion of sol coat was skinned off to expose the hidden surface of pristine AlN particle as shown in Fig. $7.7A_5$ where the surface of AlN underwent hydrolysis could be observed under the boehmite sol coat. Fig. $7.7A_6$ shows the cross section of the core-shell particle illustrated in Fig. $7.7A_5$. The AlN particle underwent hydrolysis reaction to an unpredictable depth and thus the molecular stoichiometry between AlN and Al_2O_3 was destroyed.

On the other hand, as illustrated in Fig. 7B, the pristine AlN particle (Fig. $7B_1$) was treated with orthophosphoric acid molecules. The surface treatment provided a phosphate shield over the pristine AlN surface consisting of various possible compounds of $P(OAl)(OH)_3$, $P(OAl)_2(OH)_2$ and $P(OAl)(OP)(OH)_2$ [39] as shown in Fig. $7.7B_2$. These hydrophilic layers surrounds the AlN surface, extends its residence period in water up to 30 hours [38], and protect the phase.

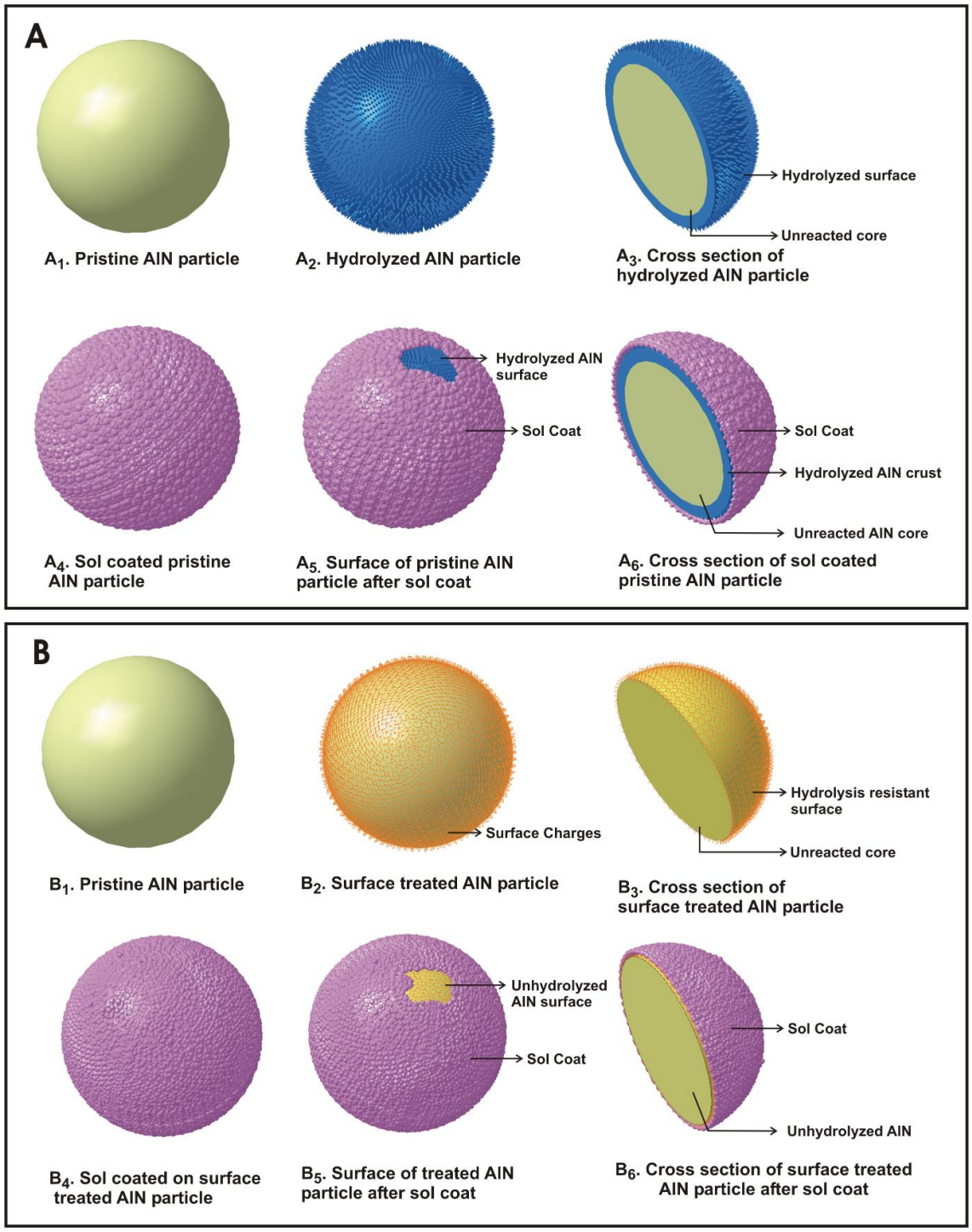

Fig. 7.7 Schematic representation of AlN – boehmite sol interaction-mechanism

The cross section of the surface modified AlN particle (fig. 7.7B_3) illustrates its phase stability from the surface to the core with no traces of hydrolysis reactions. As shown in fig. 7.7B_4, a surface modified AlN particle also exhibits uniform coating of boehmite sol. However, it maintained phase integrity without hydrolysis as shown in fig. 7.7B_5. The cross section of the core-shell structure (fig. 7.7B_6) also indicates that the molecular composition between AlN and boehmite remained unchanged to form phase pure AlON upon further calcination.

Moreover, as per the report by *Bakas et al.*, [40] aluminum phosphate compounds formed through the surface treatments decomposes at calcination temperatures above 1600°C forming Al_2O_3 and P_2O_5 gas. As the Al_2O_3 further reacts to form AlON and P_2O_5 leaves the system, the aluminum phosphate compounds were reported to be non-detrimental to the purity of the final AlON phase.

The phosphate treatment was employed in our earlier reports [33] on the processing of aqueous slip casting of AlON powders. The treatment did not show any detrimental effects on the processing and we have successfully fabricated optically transparent AlON ceramics using phosphate bonded AlON powders.

7.4.6 Phase transformation studies of AlON powder

Fig. 7.8 shows the XRD pattern of dried precursor gel at various heat treatment temperatures. Fig. 8a shows the XRD pattern of precursor gel dried at 80 °C, indicating the peaks corresponding to boehmite and AlN. The peaks corresponding to AlN are of low intensity, as the AlN particles are coated with boehmite sol. At a calcination temperature of 1000 °C, all the boehmite phases transformed to $\gamma - Al_2O_3$ as shown in fig. 7.8b. The pattern also showed peaks corresponding to AlN phase. All the $\gamma - Al_2O_3$ peaks were completely converted to $\alpha - Al_2O_3$ with an increment in the calcination temperature to 1600 °C, as shown in fig. 7.8c. A further extension of calcination temperature to 1700 °C initiated the phase formation of γ – AlON as

observed in fig. 7.8d. As the temperature progressed to 1800 °C, all the α – Al_2O_3 peaks completely disappeared forming γ – AlON as a major phase, as observed in fig. 7.8e. At this temperature, traces of AlN were still observed which will further react at high temperatures to form complete AlON phase. As expected, at 1850 °C, all the traces of AlN phases also reacted further to form 100% γ – AlON. The lattice parameter of AlON synthesized at 1850 °C was calculated as 0.7956 nm, which agrees with the reported values [41].

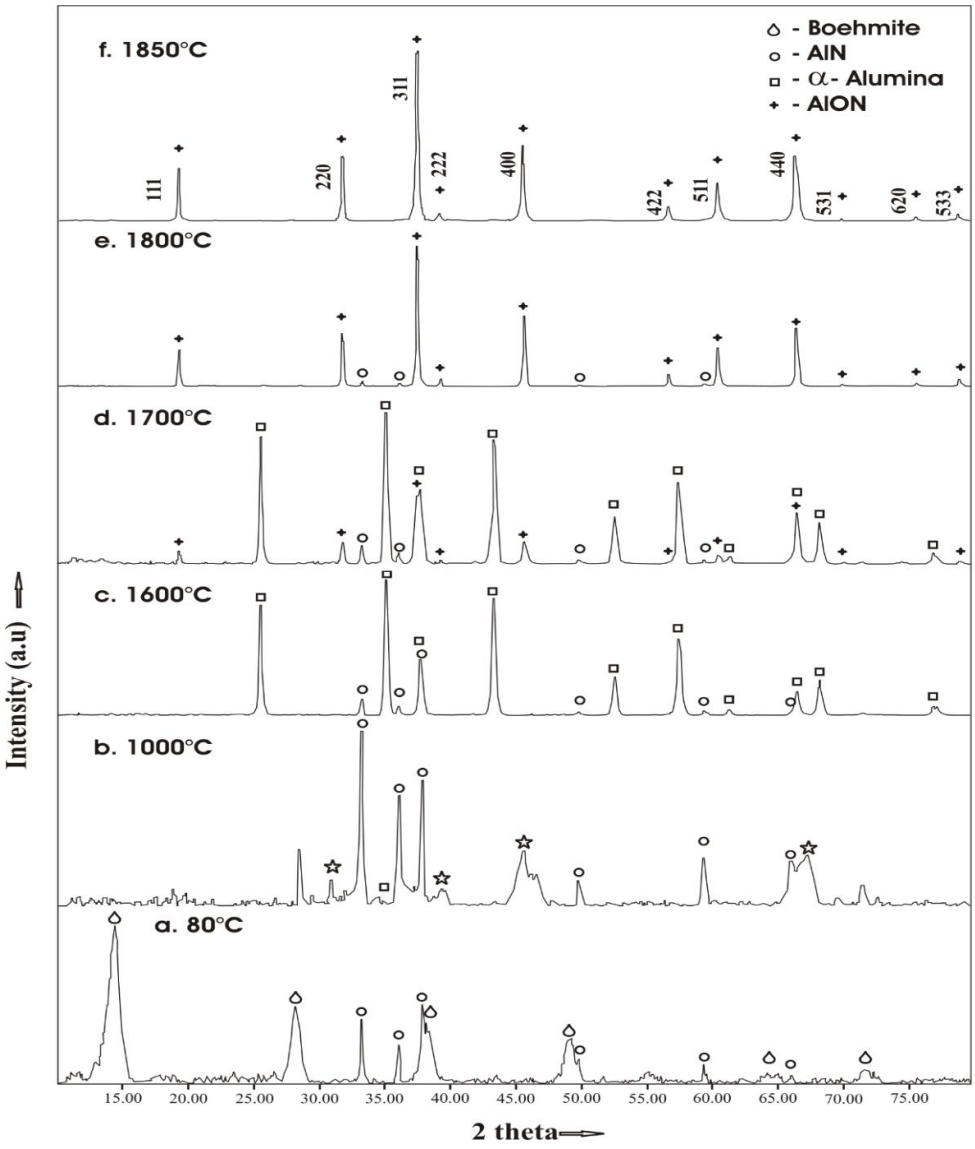

Fig. 7.8 Phase formation studies with respect to calcination temperatures

7.4.7 Characterization of sol-gel derived AlON powder

Fig. 7.9a shows the microstructural features of AlON powder synthesized in this study. As shown, particles were un-agglomerated with typical angular morphology. Fig. 7.9b shows the TEM microstructure confirming the size of the powder in the submicron region. The particle size analysis of the powder indicates that the particles were distributed in a narrow size distribution, with the size ranging between 200 nm and 1µm with an average size of 490 nm, as shown in fig. 7.9c. The BET surface area of the synthesized AlON powder was found to be 10.20 m^2/g.

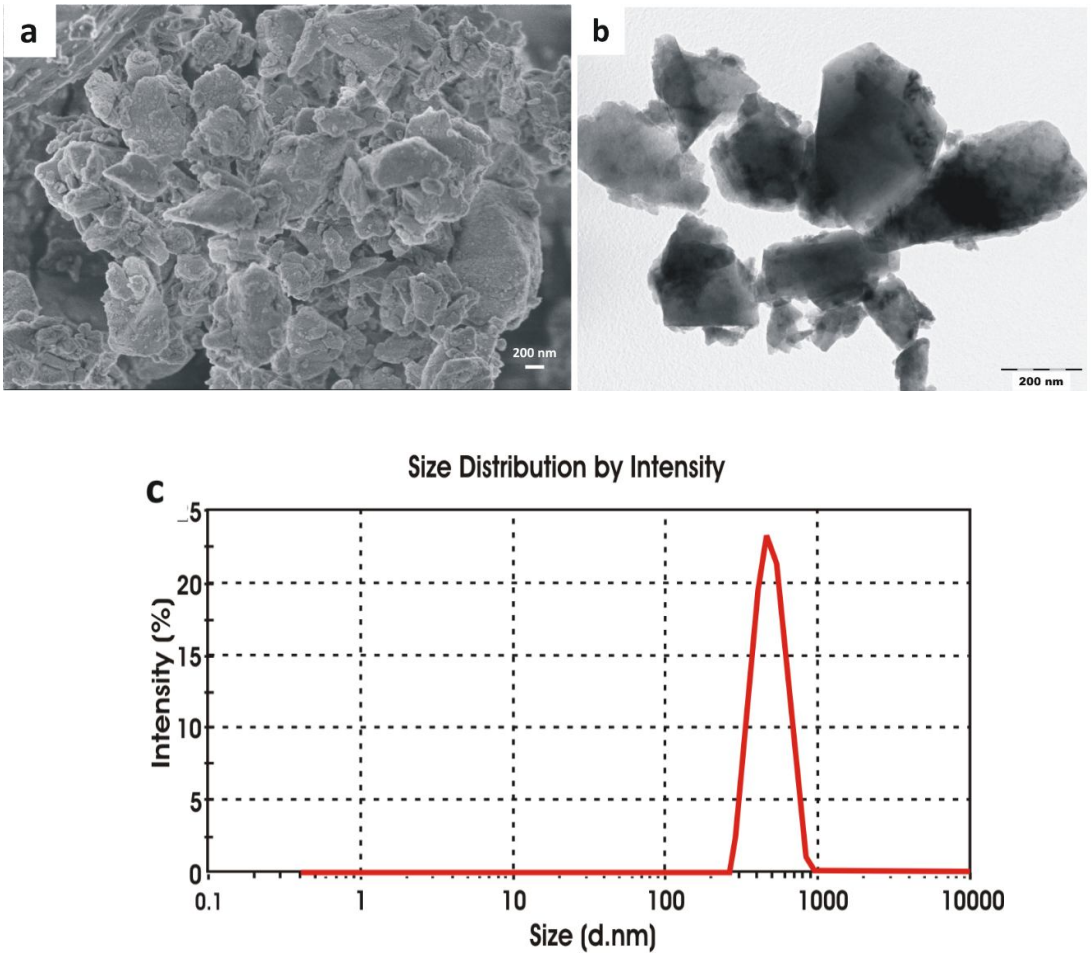

Fig. 7.9 Microstructural and particle analysis of sol-gel derived AlON powder

7.4.8 Fabrication of transparent AlON samples

The AlON powder synthesized in this study was further mixed with 0.1% La_2O_3 and compacted through uniaxial pressing followed CIPing at 200 MPa. The samples were further sintered at 1950°C in a flowing nitrogen atmosphere for 6 hours for the fabrication of transparent AlON. Figure 7.10a shows transparent AlON sample produced in this study. The figure also shows the fracture microstructure of the sintered AlON (fig. 7.10b) and the optical transmission properties of the polished AlON sample up to 2mm thickness (fig. 7.10c). The figure shows that the microstructure is free from any traces of porosities with the grain sizes ranging up to 150 – 200 µm. The microstructure also revealed that the fracture occurred through intergranular and transgranular mode. The transparent sample exhibited transmissions up to 82% in the 3 – 5 µm wavelength regions, which is closer to the values indicated in the best – reported literatures [33, 41]. The sample also exhibited Vickers hardness up to 1350 ± 20 Kg/mm^2 under 10 Kg loading conditions and fracture toughness was found to be 2.2 ± 0.2 MPa.m$^{1/2}$, which were also equivalent to the reported values [33].

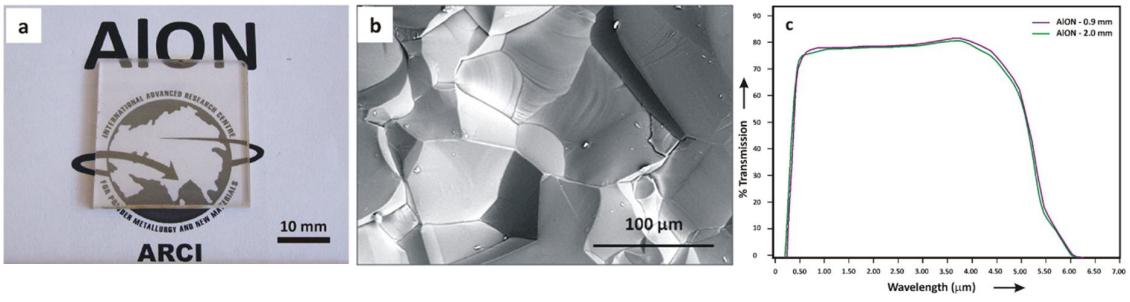

Fig. 7.10 (a) 2mm thick transparent AlON produced in this study, (b) SEM image of fractured surface of transparent AlON, (c) Inline optical transmission of AlON samples having thicknesses of 0.9mm and 2.0mm

7.5 Summary and conclusions

Single phase γ-AlON powder was successfully synthesized through an aqueous sol-gel processing technique. Aqueous boehmite sol and AlN powders were used as precursors for the synthesis. A surface modification treatment was carried out for preventing the hydrolysis of pristine AlN before its addition in boehmite sol. The interaction mechanism between AlN and boehmite sol during the processing period was examined in detail through pH, viscosity, FTIR and microstructural analyses. The sol mixture was then further gelled, dried and calcined at temperatures between 1600°C and 1850 °C in nitrogen atmosphere for the formation of γ-AlON, after which the calcined powder was further calcined at 700 °C in air for the removal of carbon contaminations. The resultant powder was found to be 100 % phase pure γ-AlON with a particle size range of 200 nm to 1μm and an average size of 490 nm. The process proposed here for the synthesis of AlON powder is facile, scalable, and environmentally friendly. In addition, the transparent AlON samples produced using the sol – derived AlON powders showed transmissions up to 82 % in the 3 – 5 μm wavelength regions which is closer to the values reported in the literatures.

7.6 References

1. J. M. Wahl, T. M. Hartnett, L. M. Goldman, R. Twedt, C. Warner, Recent advances on AlON optical ceramic; in window and dome technologies and materials IX, Vol. 5786, Proceedings of SPIE, Edited by R. W. Tustiston. SPIE, Bellingham, WA, (2005) 71 – 82
2. G.C. Wei, Transparent ceramic lamp envelope materials, J. Phys. D: Appl. Phys. 38 (2005) 3057 – 3065

3. J. W. McCauley and N. D. Corbin, High temperature reactions and microstructures in the Al_2O_3 – AlN system, Progress in nitrogen ceramics, ed. F.L. Rley, Martinus Nijhojj Pub., The Netherlands, 65 (1983) 111 – 118
4. R.L. Gentilman, E.A. Maguire and L.E. Dolhert, Transparent aluminum oxynitride and method of manufacture, U.S. Pat. No. 4 720 362 (1988)
5. H. Fukuyama, W. Nakao, M. Susa and K. Nagata, New synthetic method of forming aluminum oxynitride by plasma arc melting, J. Am. Ceram. Soc. 82 (1999) 1381 – 1387
6. J. P. Cheng, D. Agarwal and R. Roy, Microwave synthesis of aluminum oxynitride, J. Mater. Sci. Lett. 18 (1999) 1989 – 1990
7. Y. W. Kim, H. C. Park, Y. B. Lee, K. D. Oh, R. Stevens, Reaction sintering and microstructural development in the system Al_2O_3-AlN, J. Eur. Ceram. Soc. 21 (2001) 2383 – 2391
8. W. Xidong, W. Fuming and L. Wenchao, Synthesis, microstructures and properties of γ – aluminum oxynitride, Mater. Sci. Engg. A 324 (2003) 245 – 250
9. P. J. Patel, G. Gilde and J. W. McCauley, Transient liquid phase reactive sintering of aluminum oxynitride (AlON), U. S. Pat. No. 7045091 B1 (2006)
10. J. W. McCauley and N. D. Corbin, Phase relations and reaction sintering of transparent cubic aluminum oxynitride spinel (AlON) 62 (1979) 476 – 479
11. R.L. Gentilman, E.A. Maguire and L.E. Dolhert, Transparent aluminum oxynitride and method of manufacture, U.S. Pat. No. 4 520 116 (1985)
12. J. C. Labbe, A. Jeanne, G. Roult, Synthesis of gamma phase AlON by reaction of the BN/alumina system, Ceram. Int. 18 (1992) 81 – 84
13. W.Rafaniello and B.Cutler, Preparation of sinterable cubic aluminum oxynitride by carbothermal nitridation of aluminium oxide, J. Am. Ceram. Soc. 10 (1981) C-128

14. X. Jin, L. Gao, J. Sun, Y. Liu and L. Gui, Highly transparent AlON presuurelessly sintered from powder synthesized by a novel carbothermal nitridation method, 95 (2012) 2801 – 2807
15. G. Ruan, H. Xu, Z. Zhang, M. Yin, G. Xu and X. Zhan, New method of synthesizing aluminum oxynitride spinel powders, J. Am. Ceram. Soc. 96 (2013) 1706 – 1708
16. X. Xie, Y. Wang, J. Qi, S. Wang, Z. Feng, G. Hou, W. Liu, W. Zhang, Q. Xu , T. Lu, Ethanol – water derived sucrose coated Al_2O_3 for sub-micrometer AlON powder synthesis, J. Am. Ceram. Soc. 99 (2016) 2601 – 2606
17. Z. Feng, J. Qi, X. Huang, X. Guo, Y. Yu, X. Cao, Y. Wang, D. Wu, C. Meng and T. Lu, Planetary ball milling of AlON powder for highly transparent ceramics, J. Am. Ceram. Soc. 102 (2019) 2377 – 2389
18. Y. Wang, Q. Li, S. Huang, X. Cheng, P. Hou, Y. Wang, G. Chen and S. Yi, Preparation and properties of AlON powders, Ceram. Inter. 44 (2018) 471 – 476
19. V. Sabaghi, F. Davar, M. H. Teherian, Ultrasonic – assisted preparation of AlON from alumina / carbon core – shell nano particle, Ceram. Inter. 45 (2019) 3350 – 3358
20. D. Zientara, M. M. Bucko and J. Lis, AlON – based materials prepared by SHS technique, J. Eur. Ceram. Soc. 27 (2007) 775 – 779
21. N. Zhang, B. Liang, X. Y. Wang, H. M. Kan, K. W. Zhu, X. J. Zhao, The pressureless sintering and mechanical properties of AlON ceramic, Mater. Sci. Eng., A, 528 (2011) 6259 – 6262
22. J. Zhou, Z. Liao, J. Qi, W. Pang, Y. Wen, A new method for the preparation of transparent AlON ceramic, Key Eng. Mater. 368, 441 (2008)
23. N. D. Corbin, Aluminum oxynitride spinel: a review, J. Eur. Ceram. Soc. 5 (1989) 143 – 154

24. L.Yawei, L.Nan and Y.Runzhang, Carbothermal reduction synthesis of aluminum oxynitride spinel powders at low temperatures, J. Mater. Sci. Lett 16 (1997) 185 – 186
25. A.B. Galakhov, V.A. Zelenskii, L.V. Vinogradov, V.I. Antipov, M.I. Alymov, Synthesis of aluminum oxynitride from starter organic compounds, Ref. Ind. Ceram. 53 (2012) 269 – 271
26. M.R. Loghman-Estarki, F. Davar, S. Ghorbani, M. Zendehdel, M.H. Taherian, Synthesis and characterization of aluminum oxyntiride (AlON) from the nano sized precursor, Ceram. Inter. 42 (2016) 16861 – 16866
27. L.Miller and W.D.Kalpan, Water-based method for processing of aluminum oxynitride (AlON), Int. J. Appl. Ceram. Technol. 5 (2008) 641 – 648
28. M. Uenishi, Y. Hashizume, and T. Yokote, Aluminum nitride powder having improved water resistance, U. S. Pat. No. 4 923 689, 1990
29. I. Ganesh, N. Thiyagarajan, D. C. Jana, P. Barick, G. Sundararajan, and J. M. F. Ferreira, Dense β –SiAlONs consolidated by a modified hydrolysis-assisted solidification route, J. Eur. Ceram. Soc. 28 (2008) 879 – 885
30. Y. Shimizu, J. Hatano, T. Hyodo, and M. Egashira, Ion- exchange loading of yttrium acetate as a sintering aid on aln powder via aqueous processing, J. Am. Ceram. Soc. 83 (2000) 2793 – 2797
31. K. Krenel and T. Kosmac, Protection of AlN against hydrolysis using aluminium dihydrogen phosphate,'' J. Eur. Ceram. Soc. 21 (2001) 2075 – 2079
32. K. E. Horward, ''Method for aqueous processing of AlN and compositions therefrom, U. S. Pat. No. 5 234 676, 1993
33. R. Senthil Kumar and R. Johnson, Aqueous slip casting of Aluminum oxynitride, J. Am. Ceram. Soc. 99 (2016) 3220 – 3225

34. R. A. Nyquist, R. O. Kagel, Handbook of infrared and Raman spectra of inorganic compounds and organic salts, Academic Press, New York, (1971) 48 – 495
35. E. Ponthieu, P. Grange, B. Delmon, L. Lonnoy, L. Leclercq, R. Bechara, J. Grirnblot, Proposal of a composition model for commercial AlN powders, J. Eur. Ceram. Soc. 8 (1991) 233 – 241
36. D. H. Lee, R. A. Condrate S., An FTIR spectral investigation of the structural species found on alumina surfaces, Mater. Lett. 23 (1995) 241 – 246
37. Ph. Colomban, Structure of oxide gels and glasses by infrared and Raman scattering, J. Mater. Sci. 24 (1989) 3002 – 3010
38. R. Senthil Kumar, U. S. Hareesh, P. Ramavath and R. Johnson, Hydrolysis control of alumina and AlN mixture for aqueous colloidal processing of aluminum oxynitride, Ceram. Inter. 37 (2011) 2583 – 2590
39. M. Oliveira, S. Olhero, J. Rocha, J.M.F. Ferreira, Controlling hydrolysis and dispersion of AlN powders in aqueous media, J. Colloid Interface Sci, 261, 456 (2003)
40. Bakas M, Chu H (2010) Pressureless reaction sintering of AlON using aluminum orthophosphate as a transient liquid phase. In: JJ. Swab, D. Singh, J. Salem (Eds), Advances in Ceramic Armor V, The American Ceramic Society, John Wiley and Sons, Inc., Hoboken, New Jersey
41. T. M. Hartnett, S. D. Bernstein, E. A. Maguire and R. W. Tustison, Optical properties of AlON (Aluminum Oxynitride), Infrared Phys. Technol. 39 (1998) 203 – 211

CHAPTER - VIII

Summary and Conclusions

8.1 Summary

The entire work on synthesizing various optical grade ceramic powders useful for manufacturing transparent ceramic materials are summarized as follows. Table 8.1 shows the gist of various properties achieved for the powders and dense materials during the present study.

8.1.1 Transparent Al_2O_3

Optical grade nano Al_2O_3 powders have been synthesized through a facile sol – gel processing methods. Appropriate quantity of α – Al_2O_3 seeds added to the stable boehmite sol enhanced the phase transformation and produce α – phase Al_2O_3 at temperatures closer to 1050°C. The powders exhibited high homogeneity in terms of particle size and size distribution with an average size of about 20 – 40 nm. α – Al_2O_3 seeds enhanced low-temperature θ to α transformation and improved the inter – particle coordination and the packing factor. Flawless green bodies with high degree of homogeneity was prepared using uniaxial compaction followed by cold isostatic pressing at 200 MPa pressures. Sintering of the green samples at temperatures around 1400°C in air atmosphere improved the sintered density above 97% of T.D. Hot isostatic pressing of sintered samples at 1350°C at a pressures of 195 MPa improved the densities to 100% of T.D. The samples after HIPing exhibited grain sizes in the submicron region. The HIPed and polished sample having 0.9 mm thickness exhibited broadband transmission from 82 % to 87% between 2 and 5 μm regions. The specimen produced in this study exhibited transmissions equivalent to single crystal sapphire in the specified IR regions.

In addition, the mechanical properties of the was found to be superior than the single crystal sapphire.

8.1.2 Transparent spinel

Highly reactive $MgAl_2O_4$ spinel nano powder ($MgO.nAl_2O_3$, $n \approx 1$) was synthesized through a facile and novel aqueous sol-gel processing techniques. Homogeneously mixed precursors of alumina and MgO obtained phase transformation to single phase cubic spinel at temperatures closer to 400°C. The powder was further calcined to 1100°C to obtain complete crystallinity. The average particle size of the spinel powder was found to be around 20 nm. Shaping of green articles followed uniaxial pressing and cold isostatic pressing routes. Samples sintered at 1400°C in air atmosphere exhibited densities above 98% of T.D. The densities were further increased to 100% T.D. after HIPing at 1400°C at 160 MPa pressures. The average sintered grain sizes after HIPing was found to be around 500 nm which is exceptional compared to values reported for most of the existing spinel materials. The hardness values were reached to the heights of 1620 Kg/mm^2 which is highly comparable to the best values reported. Above all, the optically polished HIPed spinel specimens of 1.5 mm thickness showed transmissions up to 84% in the 2 – 5 µm wavelength regions.

8.1.3 Transparent Y_2O_3

High purity and highly reactive nano yttria powders having an average particle size of 60 nm and the surface area of 59 m^2/g was synthesized through a novel sol – gel methodology. The particles with round edge morphologies were synthesized without any addition of sulfate ions which is a common additive used in most of the existing powder processing techniques for obtaining spherical morphology. The powders exhibited exceptional reactivity and showed excellent sintering activities at temperatures as low as 1400°C in air atmospheres. In addition, the outstanding densification is achieved at these temperatures through conventional sintering

procedures without any assistance of sintering additives. HIPing was carried out at 1400°C at 160 MPa pressures for obtaining 100% densification. The completely sintered material showed grain sizes in the submicron regions. Optically polished, 1.4 mm thick specimens showed IR transparency up to 84% in the 2.0 and 9.0 μm regions which is the equivalent transmissions reported for single crystal yttrium oxide. Further, the samples showed hardness up to 8.90 ± 0.20 GPa, and fracture toughness up to 3.0 ± 0.05 MPa. $m^{1/2}$, which can be well correlated with the grain size of 690 ± 30 nm resulting from the powder's high-sinterability and low-temperature densification process employed. Laser flash measurements showed a thermal conductivity of 19.5± 1.1 W/m.K. The unique combinations of optical, mechanical, and thermal properties of the submicron Y_2O_3 samples produced in this study is a promising candidate for solid-laser hosts, IR transparent domes, and uncooled – thermal – window applications

8.1.4 Aluminum oxynitride powder

Aqueous sol – gel techniques were successfully employed for the synthesis of single phase γ – AlON powders using precursors such as alumina and AlN. Hydrolysis tendency of AlN was found altering the requisite molecular ratio of alumina and AlN in aqueous medium and hindered the phase formation of AlON. Therefore, AlN powders were subjected to a surface modification treatment to circumvent the hydrolysis tendency and enhance their incubation period in water. Such surface treated AlN powders were found stable in the aqueous sol – gel processing and produced single phase γ – AlON on further calcination at 1850°C. The resultant AlON powders exhibited particle size in the submicron region. The process developed in this study for the synthesis of AlON powder is facile, scalable, and environmentally friendly. The powder was found to be suitable for producing transparent AlON materials having IR transmissions up to 82 % in the 3 – 5 μm wavelength regions.

Properties	**Al_2O_3**	**Spinel**	**Y_2O_3**	**AlON**
Synthesis Methodology	Aqueous Sol - Gel	Aqueous Sol - Gel	Aqueous Sol - Gel	Aqueous Sol - Gel
Precursors	Boehmite, α – Al_2O_3	Boehmite, MgO	YNHH, Y_2O_3	Boehmite, AlN
Phase formation temperature (°C)	1050	360	570	1850
Calcination temperature (°C)	1100	1100	1100	1850
Final Phase	α – Al_2O_3	$MgAl_2O_4$	Y_2O_3	γ – AlON
Average particle size (nm)	Bi-modular (20 – 40 nm and 100 – 200nm)	20	60	490
BET Surface Area (m^2/g)	70.47	96	59	10.2
Shaping Technique	Uniaxial compaction + CIP	Uniaxial compaction + CIP	Uniaxial compaction + CIP	Uniaxial compaction + CIP
Sintering temperature (°C)	1400	1400	1400	1950
Sintered density (% T.D.)	97.0	98.0	98.5	100
HIPing temperature (°C)	1350	1400	1400	N/A
Average Grain Size (nm)	800	505	490	1500 – 2000
Hardness (Kg/mm^2)	Hv_{10} – 20.5	$Hv_{1\_}$ 16.2	Hk_{100} – 9.0	Hv_{10} – 13.5

% of IR transmission in 2 – 7 µm wavelength	87.0	84.0	84.0	82
Transparent Specimen			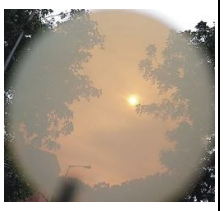	

Table 8.1 Overall summary of the properties of powders and sintered specimens achieved for the spectrum of transparent ceramic materials derived through sol – gel powders produced in the present study.

8.2 Overall Conclusions

- Ultra – high pure optical grade ceramic powders were produced through a facile, novel and economical aqueous sol – gel procedures
- Powders of Al_2O_3, spinel and Y_2O_3 having ultra – fine particle sizes suitable for producing submicron transparent articles were synthesized
- A novel aqueous sol – gel procedure is developed for synthesizing AlON powders
- All the materials exhibited excellent sintering characteristics and obtained complete densification at temperatures around 1400°C
- Materials with excellent hardness values were obtained due to high control in the sintered grain sizes
- High performance transparent ceramic materials such as Al_2O_3, spinel, Y_2O_3 and AlON have been successfully fabricated with excellent optical transparency in the 3 – 5 µm wavelength regions.

8.3 Scope for the future works

- The current study focused on developing transparent ceramics that are exhibiting excellent transmissions in the IR region. However, their application areas can be extended towards transparent armors if the materials are developed with superior transmissions in the visible regions.
- The hardness values of currently presented nano yttria require increment from 900 Kg/mm^2 to the values above 1000 Kg/mm^2 in order to extend its applications having harsher aerodynamic environments.
- Enhancing the mechanical properties by further reducing the sintered grain sizes to 300 – 400 nm by adding suitable pinning agents without negotiating with the optical transparency.
- Altering the sintering procedures from conventional approach to other methods such as pressure assisted sintering, two stage sintering and hydrogen sintering to obtain enhanced optical and mechanical properties.
- Adapting the current sol – gel approach to develop optical grades powders of ZrO_2, YAG, $ZnAl_2O_4$ etc. and produce the respective transparent ceramic materials.

8.4 List of Publications

1. **R. Senthil Kumar,** A. K. Khanra and R. Johnson, Processing and properties of sintered submicron IR transparent alumina derived through sol-gel method, J. Sol. Sci. Tech., 86 (2018) 374 – 382

2. **R. Senthil Kumar,** S. Erkulla, A. K. Khanra and R. Johnson, Aqueous sol–gel processing of precursors and synthesis of aluminum oxynitride powder therefrom, J. Sol. Sci. Tech., 93 (2020) 100 – 110

3. **R. Senthil Kumar,** K. H. Sai Priyanka, A. K. Khanra and R. Johnson, A novel approach of synthesizing nano Y_2O_3 powders for the fabrication of submicron IR transparent ceramics, Ceram. Inter. 47 (2021) 16986 – 16999

8.5 List of lectures delivered at conferences

1. Presented an oral lecture on “Development of aluminum oxynitride for armor applications”, at the International conference on advanced materials and processes for defense applications organized by DRDO on 25th December 2019 at Hyderabad Marriott Hotel & Convention Centre, Hyderabad

2. Presented an oral lecture on “Processing and properties of sintered submicron IR transparent yttria ceramics derived through sol-gel method”, at the International conference on advances in minerals, metals, materials, manufacturing and modelling (ICAM 5) organized by Department of Metallurgical and Materials Engineering, NIT Warangal on 26th December 2019 at NIT Warangal, Warangal